

**UCLA**

**UCLA Electronic Theses and Dissertations**

**Title**

Modeling transition metal surface reconstruction in CO gas environment

**Permalink**

<https://escholarship.org/uc/item/6v37h997>

**Author**

Sumaria, Vaidish Pravin

**Publication Date**

2023

Peer reviewed|Thesis/dissertation

UNIVERSITY OF CALIFORNIA

Los Angeles

Modeling transition metal surface reconstruction in CO gas environment

A dissertation submitted in partial satisfaction  
of the requirements for the degree  
Doctor of Philosophy in Chemical Engineering

by

Vaidish Pravin Sumaria

2023



© Copyright by  
Vaidish Pravin Sumaria  
2023

## ABSTRACT OF THE DISSERTATION

Modeling transition metal surface reconstruction in CO gas environment

by

Vaidish Pravin Sumaria

Doctor of Philosophy in Chemical Engineering

University of California, Los Angeles, 2023

Professor Philippe Sautet, Chair

Transition metals play a key role as catalysts in applications ranging from chemical and energy production to environmental remediation. Ample evidence indicates that catalyst structures do not remain unchanged during use. Instead, substantial restructuring occurs due to the rearrangement of the metal atoms to make new structures. This restructuring has major consequences on catalytic properties, sometimes beneficial and sometimes not. Understanding how surface-active sites evolve under reaction conditions is of central importance to designing improved catalysts but presents experimental and theoretical challenges. In this dissertation we use Density Functional Theory (DFT) with Machine Learning based interatomic potentials, atomistic thermodynamics, and global optimization in combination with in-situ experimental observations to uncover the mechanism of such restructuring processes. We primarily focus our attention to CO-induced Pt reconstruction, but also discuss the on-going work on Cu restructuring.

We developed an adsorbed CO bond length-based correction to solve the GGA-level DFT errors in describing the Pt/CO system. This corrected both the site prediction and adsorption energy relative to experiments and helped reproduce experimental in-situ STM imaging

results at high coverage. Using a NN-based potential trained on a large number of reference DFT data, we perform large scale global optimizations to understand CO organization on stepped Pt surfaces. (111) steps lead to formation of quasi-hexagonal structure of CO on terrace with a 2:1 ratio of top:bridge sites occupied, while (100) steps lead to a majority of multiply bonded CO on the terrace.

By improving this NN-based potential further, we explored the mechanism of step reconstructing. High CO coverage at a Pt step edge triggers the formation of atomic protrusions which then detach from the step edge to create subnano-islands on the terraces. The undercoordinated sites on these islands are stabilized by the strongly bound CO adsorbate. Using the computational study, we discover that small ( $< 12$  atoms) islands are metastable, while islands with 12 atoms and more are thermodynamically stable, in agreement with the experimental observation.

Finally using a similar approach, we have developed an accurate NN-based potential for Cu/CO system which we are using to understand its reconstruction in operando conditions.

The dissertation of Vaidish Pravin Sumaria is approved.

Dante Simonetti

Carlos Morales-Guio

Anastassia Alexandrova

Philippe Sautet, Committee Chair

University of California, Los Angeles

2023

To my parents, my brother and all my friends who have been a constant support  
thoughtout this journey.

## TABLE OF CONTENTS

<b>1</b>	<b>Research Background</b>	<b>1</b>
1.1	Adsorbate induced catalysts restructuring	3
1.1.1	Experimental Overview	3
1.1.2	Computational Overview	6
1.2	Thesis Objective	8
<b>2</b>	<b>Optimal packing of CO at high coverage on Pt(111) and Pt(100)</b>	<b>11</b>
2.1	Introduction	11
2.1.1	Experimental overview of CO adsorption structures on Pt surface	11
2.1.2	“Pt/CO Puzzle”	12
2.1.3	Overview of the corrections developed in the literature	15
2.2	Methods	16
2.2.1	Computational Details	16
2.2.2	Experimental Details	21
2.3	Results and Discussion	22
2.3.1	CO adsorption energy correction scheme	22
2.3.2	Pt(111) surface stability	24
2.3.3	Pt(100) surface stability	33
2.4	Conclusion	41
<b>3</b>	<b>High Dimensional Neural Network Potential</b>	<b>43</b>
3.1	Introduction	43

3.2	Feed-forward Neural Networks . . . . .	44
3.3	High Dimensional Neural Network Potential . . . . .	47
3.3.1	Symmetry Functions . . . . .	49
3.3.2	Forces from HDDNP: Energy Gradients . . . . .	57
3.3.3	Training Neural Networks based Potentials . . . . .	58
3.4	Conclusion . . . . .	63
<b>4</b>	<b>CO organization at ambient pressure on stepped Pt surfaces . . . . .</b>	<b>64</b>
4.1	Introduction . . . . .	64
4.2	Methods . . . . .	68
4.2.1	First Principle Calculation Details . . . . .	68
4.2.2	Training a High Dimensional Neural Network Potential . . . . .	69
4.2.3	Basin Hopping Monte Carlo (BHMC) Simulation . . . . .	71
4.3	Results and Discussions . . . . .	75
4.3.1	Pt(553) . . . . .	76
4.3.2	Pt(557) . . . . .	81
4.3.3	Pt(643) . . . . .	85
4.4	Conclusion . . . . .	88
<b>5</b>	<b>Atomic scale mechanism of platinum catalyst restructuring under the pres- sure of CO gas . . . . .</b>	<b>90</b>
5.1	Introduction . . . . .	90
5.2	Methods . . . . .	93
5.3	Results . . . . .	96
5.3.1	In situ imaging of restructuring at nanoscale . . . . .	96

5.3.2	Grand canonical simulations of elementary restructuring processes . . .	98
5.3.3	Mechanism of island formation on terraces . . . . .	100
5.3.4	Kinetics of Pt restructuring under CO pressure . . . . .	103
5.4	Discussion . . . . .	104
5.5	Conclusion . . . . .	108
<b>6</b>	<b>Cu surface activation induced by CO adsorption-driven nanocluster de-</b>	
	<b>composition . . . . .</b>	<b>110</b>
6.1	Introduction . . . . .	110
6.2	Methods . . . . .	111
6.3	Results . . . . .	113
6.3.1	HDNNP Accuracy . . . . .	113
6.3.2	Restructuring events on different Cu surfaces . . . . .	114
6.4	Conclusion . . . . .	120
<b>7</b>	<b>Conclusion . . . . .</b>	<b>121</b>
<b>A</b>	<b>Supplementary Information for Chapter 2 . . . . .</b>	<b>156</b>
A.1	Coverage effect on CO bond distance based adsorption energy correction . . .	156
A.2	Atomistic Thermodynamics Approach . . . . .	157
A.2.1	Ideal Gas . . . . .	157
A.3	Harmonic Oscillator (HO) approximation . . . . .	160
A.4	Vibrational Frequency . . . . .	160
A.5	Relationship between correction and vibrational frequency . . . . .	161
A.6	Various surface terminations considered . . . . .	162



A.6.1	Pt(111)	162
A.6.2	Pt(100)	175
A.6.3	Generalized Correction	180
A.6.4	Simulated STM imaging	182
A.6.5	Surface Stability Diagram without Energy Correction	183
A.7	Vibrational Frequencies Pt(111)	185
A.8	Vibrational Frequencies Pt(100)	194
<b>B</b>	<b>Supplementary Information for Chapter 4</b>	<b>199</b>
B.1	LEME structures data	199
B.1.1	Pt(553)	199
B.1.2	Pt(557)	203
B.1.3	Pt(643)	209
B.2	CO-Surface vs CO-CO lateral interaction	211
B.2.1	CO-Surface Interaction	211
B.3	Neural Network Evaluation	212
B.3.1	Pt(553)	212
B.3.2	Pt(557)	213
B.3.3	Pt(643)	214
B.3.4	Pt(111)	215
B.3.5	Low Coordination adsorption sites	216
<b>C</b>	<b>Supplementary Information for Chapter 5</b>	<b>217</b>
C.1	Stepped Surfaces	217

C.2	STM images . . . . .	218
C.3	Methods . . . . .	218
C.3.1	Density Functional Theory Calculations . . . . .	218
C.4	Effect of Pressure . . . . .	224
C.4.1	Pt(553) . . . . .	224
C.4.2	Pt(557) . . . . .	228
C.4.3	Pt(111) + Islands . . . . .	232
C.5	Reconstruction in absence on CO . . . . .	235
C.6	$\Delta E_{chem}$ vs $\Delta E_{metal}$ . . . . .	238
C.7	NEB - Diffusion . . . . .	241
C.8	Data Availability . . . . .	241

## LIST OF FIGURES

1.1	Schematic figure showing the “Ideal Catalyst” in Ultra-High Vacuum (UHV) conditions and “Real Catalyst” at realistic reaction conditions. The figure described the various experimental microscopy and spectroscopy methods used in these conditions as well as the advances made in computational techniques to solve the “pressure gap” and describe catalysts in operando conditions. . . . .	2
1.2	STM images of Pt(557), Pt(111), and Cu(111) in CO at 25°C at a time about 40 minutes after exposure to CO. (a) Pt(557) in UHV. (b) Pt(557) in $5 \times 10^{-8}$ Torr CO; Terrace edges are curvy. (c) Pt(557) in 0.1 Torr CO; the whole surface is broken up into homogeneously distributed Pt nanoclusters. (d) Pt(111) in 0.1 Torr CO after 2 hours; (e) Cu(111) in 0.1 Torr CO. Adapted from Science 327, 850 (2010) and Science 351, 475 (2016). . . . .	4
2.1	Adsorption energies ( $E_{ads}$ eV) for CO adsorbed on the top, fcc and hcp hollow sites on Pt(111) surface calculated with various XC functionals. The range of energy marked between the dashed lines indicates the experimental single crystal calorimetry value for the adsorption energy. Data regenerated from Janthon et al. <sup>156</sup> . . . . .	14
2.2	Blyholder model of CO chemisorption. The model describes two main components: (a) $\sigma$ donation - $5\sigma$ Highest Occupied Molecular Orbital (HOMO) donates electron density to the substrate and (b) $2\pi^*$ Backbonding where anti-bonding $2\pi^*$ Lowest Unoccupied Molecular Orbital (LUMO) receives electronic density from the substrate. . . . .	15
2.3	Adsorption energy of CO on (a) Pt(100) and (b) Pt(111) ( $\Delta E_{CO}^{ad}$ ) calculated for ML=0.25 plotted against the singlet-triplet excitation energy $\Delta E_{S-T}$ for the various pseudopotentials mentioned in the table 2.1 . . . . .	19

2.4	Adsorption energy of CO on (a) Pt(100) and (b) Pt(111) ( $\Delta E_{CO}^{ad}$ ) calculated for ML=1.00 plotted against the singlet-triplet excitation energy $\Delta E_{S-T}$ for the various pseudopotentials mentioned in the table 2.2 . . . . .	19
2.5	Correction in CO adsorption energy ( $\Delta$ ) plotted against the adsorbed CO bond distance ( $d_{CO}$ ) for various sites (top, bridge and hollow/hcp) for Pt(100) and Pt(111). The corrections are measured by extrapolating the dependence of the adsorption energy ( $E_{CO}^{ad}$ ) on the CO singlet-triplet excitation energy ( $\Delta E_{S-T}$ ) for the various sites on (100) and (111) surfaces of Pt to the coupled cluster and CI calculated value for $\Delta E_{S-T}$ . CO coverage is 0.25 ML. The red dots ( $\bullet$ ) and the red line represent the data and the correction as a function of CO bond distance for Pt(111) which is given as $\Delta = 5.13 d_{CO} - 5.83$ where $d_{CO}$ is in $\text{\AA}$ and $\Delta$ in eV. Similarly, the blue squares ( $\square$ ) represent the correction for the Pt(100) surface and can be expressed as $\Delta = 4.8 d_{CO} - 5.44$ . Both the fits have a mean absolute error (MAE) of smaller than 4 meV per CO. The structures (on Pt(111) and Pt(100)) for which the corresponding correction is calculated are shown. . . . .	22
2.6	Thermodynamic surface stability diagram depicting the most stable CO coverage as a function of temperature and pressure on Pt(111). The various colors represent the calculated most stable surface terminations as labelled in the figure and shown in table 2.4. The black dashed line represents the pressure range studied using STM at 300 K by Longwitz et. al. where the superposition of the quasi-hexagonal (and hexagonal) lattice of CO on the hexagonal lattice of Pt(111) appears in the range of coverage from 0.5 to 0.68 ML. . . . .	26
2.7	Thermodynamic surface stability diagram depicting the most stable CO coverage as a function of the temperature and pressure on Pt(100). Above $\theta \geq 0.75$ , we see formation of the $c(n \times 2)$ unit cells with $(n-2)CO$ ( $n=4,6,8$ ) which are observed in STM images discussed in the paper. The red and blue dots on the plot represent the different pressures at room temperature where HP-STM images were obtained. 33	33

2.8	Over-layer structure of CO at different pressure on Pt(100) surface observed by in-situ HP-STM at room temperature. (a) $2.7 \times 10^{-6}$ Pa CO, which indicates formation of $c(4 \times 2)$ -6CO over-layer corresponding to $\theta = 0.75$ . Red circles show location of adsorbed CO molecules. (b) $6.6 \times 10^4$ Pa CO, which indicates formation of $c(8 \times 2)$ -14CO over-layer corresponding to $\theta = 0.875$ . (c) $1 \times 10^5$ Pa CO. In (b) and (c), red and yellow rectangles show locations of quasi-top CO molecules and quasi-bridge CO molecules, respectively. White arrows indicate direction of scan profiles which are shown on the right side. Settings for STM acquisition are: (a) 0.50 nA, 0.60 V; (b) 1.00 nA, 0.60 V; (c) 0.85 nA, 0.90 V. . . . .	39
3.1	Schematic of a small feed-forward neural network. The network is used to establish a relationship between the atomic structure (input layer) and the energy of structures (output layer). Between the input and output layer, the FFNN has 2 hidden layers with 5 and 4 nodes respectively which defines the functional forms of the NN as expressed by the equation 3.2. The fitting parameters (weights of the NN, $a_{ij}^{kl}$ ) are represented using arrows. For clarity, bias nodes and weights are now shown here. . . . .	45
3.2	Schematic of a High Dimensional Neural Network Potential. Each Cartesian coordinate $R_i$ is first converted to its invariant form using symmetry functions $G_i$ which is fed to the atomic neural networks to obtain atomic energy $E_i$ . The sum of these atomic contributions yields the short-range energy $E$ . . . . .	48
3.3	Plots showing the functional form of various cutoff functions in Table 3.1 . . . . .	50
3.4	Effect of $\eta$ and $\mu$ on the radial symmetry function value $G^{rad}$ . . . . .	51
3.5	Angular contributions of the angular symmetry function $G^4$ (similar effect on $G^5$ . The plot corresponds to a example triatomic system, for a many-atoms system, a summation over the angular terms is used. . . . .	52

3.6	Radial part of the angular symmetry functions shown for the case $\mathbf{R} = \mathbf{R}_{ij} = \mathbf{R}_{ik} = \mathbf{R}_{jk}$ and $R_c = 7\text{\AA}$ . The solid curves represent the radial part of angular functions of type $G^4$ and dashed curves correspond to the radial parts of type $G^5$ . . . . .	53
3.7	Comparison of the total angular functions $G^4$ and $G^5$ for atom $i$ in a triatomic molecule. The interatomic distances $\mathbf{R}_{ij}$ and $\mathbf{R}_{ik}$ are fixed at $0.8R_c$ and the symmetry function values are plotted as a function of the angle $\Theta_{ijk}$ centered at $i$ . Function $G^4 \approx 0$ for angles $70^\circ < \Theta_{ijk} < 290^\circ$ because of the resulting large distance $\mathbf{R}_{jk}$ in the additional cutoff function $f_c(R_{jk})$ . . . . .	54
3.8	Polar plots depicting the influence of the parameters $\lambda$ and $\zeta$ on a single term of the sum in Eq. 3.7. All Gaussian functions are set to $\eta = 0.01$ . Changing the sign of the phase $\lambda$ moves the maximum of the angular density between $0^\circ$ and $180^\circ$ . Increasing the parameter $\zeta$ focuses the function on a smaller range of angles close to the respective maxima. . . . .	56
3.9	Schematic explain how early stop method if implemented to avoid the overfitting problem while training NNPs . . . . .	60
3.10	Schematic of the iterative training process used to improve the accuracy and generality of the Neural Network Potentials. . . . .	61
4.1	Basin Hopping Algorithm flowchart. . . . .	72
4.2	Flow-chart showing the algorithm for (a) Metropolis criterion - which decides the acceptance/ rejection of MC move and (b) adjusting temperature during the BH simulation where (a) is the acceptance ratio for the BH simulation. . . . .	73

4.3	Clustering mutation algorithm implemented with the Basin Hopping algorithm. The dark gray balls represent carbon atoms and red balls represent oxygen atoms. The light gray balls are the substrate platinum atoms. The blue lines define the Voronoi tessellation and the yellow dots represent the centers for the Voronoi clusters. Atoms within one cluster are moved randomly in the same direction as seen in the model implementation. . . . .	74
4.4	Ball Models of various clean surfaces considered. (a) Pt(553) top view, (b) Pt(553) side view, (c) Pt(557) top view, (d) Pt(557) side view, (e) Pt(643) top view, Pt(643) side view. Colors represent the z-position of the atoms. Black balls represent the step edge and others represent the terrace. . . . .	75
4.5	(a) Adsorption free energy per unit surface area $\Delta G_{ads}$ (at T=300K, P=1 atm) plotted against CO coverage ( $\theta$ ) on Pt(553). Yellow markers represents the structures defending the Low energy minima ensemble. (b) and (c) represent the coverage of CO on the Pt step-edge and terrace as a function of the $\Delta G_{ads}$ respectively. <span style="color: red;">●</span> represents top site, <span style="color: blue;">●</span> represents bridge site, <span style="color: green;">●</span> represents hollow sites and <span style="color: black;">●</span> represents the total coverage. The density of different sites at various coverages is represented by the histogram attached to the right ordinate axis. The density of structures as a function of $\Delta G_{ads}$ is represented by the histogram on the top abscissas axis. In plots (b) and (c), to distinguish the points, we move the red points (top sites) on the y-axis by -0.005, green points (hollow sites) have been moved by +0.005 and black points (total coverage) have be moved by +0.01. . . .	76

- 4.6 Various structures of CO orientations patterns observed in the LEME for Pt(553). (a) represents structures with  $\theta = 0.56$ ; (b)-(e) represent structures with  $\theta = 0.6$ ; (f)-(h) with  $\theta = 0.63$ ; (i) with  $\theta = 0.65$ . The Pt atoms are shown using a colormap (color-bar representing z-position of the Pt atom). For a given pattern, the lowest energy orientation of CO is shown using the solid black and red balls representing the positions of C and O respectively and the ensemble of structures are represented by the “cloud” of pink and grey balls. . . . . 77
- 4.7 (a) Adsorption Free energy per unit area ( $\Delta G_{ads}$ ) plotted against CO coverage ( $\theta$ ) on Pt(557). Yellow markers represents the structures defining the LEME.(b) and (c) represent the coverage of CO on the Pt step-edge and terrace as a function of the  $\Delta G_{ads}$  respectively. ● represents top site, ● represents bridge site, ● represents hollow sites and ● represents the total coverage. The points in (b) and (c) have been moved in a similar fashion as Fig. 4.5 to distinguish the points better. . . . . 81
- 4.8 Various structures of CO orientations patterns observed in the LEME for Pt(557). (a) represents structures with  $\theta = 0.61$ ; (b) with  $\theta = 0.625$ ; (c) with  $\theta = 0.64$ ; (d-f) with  $\theta = 0.66$ , (g) with  $\theta = 0.69$ , (h) with  $\theta = 0.71$ , and (i) with  $\theta = 0.72$ . The Pt atoms are shown using a colormap (color-bar representing z-position of the Pt atom). For a given pattern, the lowest energy orientation of CO is shown using the solid black and red balls representing the positions of C and O respectively and the ensemble of structures are represented by the “cloud” of pink and grey balls. . . . . 82



4.9	(a) Adsorption Free energy per unit area ( $\Delta G_{ads}$ ) plotted against CO coverage ( $\theta$ ) on Pt(643). Yellow markers represents the structures defining the LEME.(b) and (c) represent the coverage of CO on the Pt step-edge and terrace as a function of the $\Delta G_{ads}$ respectively. ● represents top site, ● represents bridge site, ● represents hollow sites and ● represents the total coverage. The points in (b) and (c) have been moved in a similar fashion as Fig. 4.5 to distinguish the points better. . . . .	85
4.10	Various structures of CO orientations patterns observed in the LEME for Pt(643). (a) represent structures with $\theta = 0.5$ ; (b) with $\theta = 0.55$ ; (c) with $\theta = 0.6$ and (d) with $\theta = 0.65$ . The Pt atoms are shown using a colormap (color-bar representing z-position of the Pt atom). For a given pattern, the lowest energy orientation of CO is shown using the solid black and red balls representing the positions of C and O respectively and the ensemble of structures are represented by the “cloud” of pink and grey balls. . . . .	87
5.1	STM images of a Pt(111) surface at room temperature in gaseous CO. (a-h) STM images of the same region taken sequentially at different times: (a) $t_0 = 0$ , (b) $t_1 = 10$ , (c) $t_2 = 12$ , (d) $t_3 = 14$ , (e) $t_4 = 16$ , (f) $t_5 = 23$ , (g) $t_6 = 25$ , (h) $t_7 = 27$ min after the CO pressure was brought up to $1.5 \times 10^{-6}$ Torr at room temperature; the size of each image (a-h) is 15 nm×20 nm; the acquisition time of each image is 1-2 minutes. In (a-h), the progressive detachment of a subnanometer cluster was observed experimentally. (i) STM image under a CO pressure of 0.1 Torr; size of the image is 30 nm×40 nm; nanoclusters with a size of 0.5-0.8 nm appeared as bright spots on terraces of Pt(111). . . . .	97

5.2	Simulation of elementary surface restructuring events at the Pt(557) step edge: (a) Restructuring energy under a CO pressure of 0.0007, 0.5 or 450 Torr for step rearrangement (structures b-e), step atom extraction (structures f-h) and island formation keeping the step unmodified (structures i-k). The parallelogram shown in white line marks a unit cell. . . . .	99
5.3	(a) Simulation of elementary surface restructuring events at the Pt(553) step edge: (a) Restructuring energy under a CO pressure of 0.0007, 0.5 or 450 Torr, for step rearrangement (structures b-e), step atom extraction (structures f-h) and island formation keeping the step unmodified (structures i-k). . . . .	101
5.4	(a) Comparing the formation energies of Pt islands of increasing sizes from 1 to 19 atoms on a Pt(111) terrace under a CO pressure of 0.007, 0.5 or 450 Torr. (b-e) show the representative structures at a CO pressure of 450 Torr. . . . .	102
5.5	Kinetic reaction pathway for a restructuring event on Pt(553); (a) Reaction energy profile for the detachment of one Pt atom from the Pt(553) step edge (b-h) and its diffusion on the terrace (h-k) at a CO pressure of 450 Torr. . . . .	103
6.1	Various Cu facets used with GCBH to generate data for training the HDNNP: (a) 100, (b) 111, (c) 410, (d) 1021, (e) 430, (f) 533, (g) 711, (h) 843. All the balls represent Cu atom. The balls with lighter color (yellow) show the step edges and the darker colors represent the terrace. The color gradient shows the different height of the atoms in the unit cell. . . . .	113
6.2	Parity plot comparing the Neural network predicted energy (per atom) and forces with the reference DFT calculations for the initial dataset generated. . . . .	114
6.3	Parity plot comparing the Neural network predicted energy and forces with the reference DFT calculations for larger stepped surface unit cells dataset generated using GCBH simulations. . . . .	115

6.4	GCBH results for Cu(553) (a) Stability diagram that shows a heat map of the relative formation energy $g^{rel} = E - n_{CO} \times \mu_{CO} - n_{Cu} \times \mu_{Cu}$ as a function number of Cu and CO in the system. The relative adsorption Gibbs free energy for a specific Cu/CO pair is labeled within the heat map. The four lowest energy structures (with $g^{rel} = 0, 0.17, 0.2, 0.58$ ) found from the analysis are shown in increasing energy order from (b)-(e) respectively. The simulation is performed using 1 atm and 25°C conditions. . . . .	116
6.5	GCBH results for Cu(533) (a) Stability diagram that shows a heat map of the relative formation energy $g^{rel} = E - n_{CO} \times \mu_{CO} - n_{Cu} \times \mu_{Cu}$ as a function number of Cu and CO in the system. The relative adsorption Gibbs free energy for a specific Cu/CO pair is labeled within the heat map. The four lowest energy structures (with $g^{rel} = 0, 0.08, 0.14, 0.15$ ) found from the analysis are shown in increasing energy order from (b)-(e) respectively. The simulation is performed using 1 atm and 25°C conditions. . . . .	117
6.6	GCBH results for Cu(537) (a) Stability diagram that shows a heat map of the relative formation energy $g^{rel} = E - n_{CO} \times \mu_{CO} - n_{Cu} \times \mu_{Cu}$ as a function number of Cu and CO in the system. The relative adsorption Gibbs free energy for a specific Cu/CO pair is labeled within the heat map. The four lowest energy structures (with $g^{rel} = 0, 0.02, 0.03, 0.03$ ) found from the analysis are shown in increasing energy order from (b)-(e) respectively. The simulation is performed using 1 atm and 25°C conditions. . . . .	118
6.7	(a) Comparing the formation energies of Cu islands of increasing sizes from 1 to 19 atoms on Cu(111) terrace. (c-h) Showing the representative structures at 1 atm and 25°C are shown in the figure. . . . .	119

A.1	The suggested correction in adsorption energy ( $\Delta$ ) plotted against the adsorbed CO bond distance ( $d_{CO}$ ) for various sites (top, bridge and hollow/hcp) for Pt(100) and Pt(111). The corrections developed using adsorption energy data for coverage of 0.25 ML and 1.00 ML have been compared. . . . .	156
A.2	CO bond length based correction as a function of vibrational frequency and the vibrational frequency as a function of CO bond length for Pt(111). . . . .	161
A.3	CO bond length based correction as a function of vibrational frequency and the vibrational frequency as a function of CO bond length for Pt(100). . . . .	162
A.4	Pt(111) surface stability diagram using the generalized correction for both the surfaces. . . . .	180
A.5	Pt(100) surface stability diagram using the generalized correction for both the surfaces. . . . .	181
A.6	Simulated STM image of $(\sqrt{19} \times \sqrt{19})R23.4^\circ$ -13CO structure containing. The STM is generated using the partial charge densities and p4vasp software. The bright features in the image are attributed to CO adsorbed on the top (or quasi-top) site. The faded, less bright spot represents the bridge site. . . . .	182
A.7	Simulated STM image of $c(8 \times 2)$ structure containing 6 top/quasi-top and 8 bridge/quasi-bridge CO molecules per unit cell. The STM is generated using the partial charge densities and p4vasp software. . . . .	182
A.8	Surface stability diagram for Pt(111) representing the stable surface terminations as a function of pressure and temperature without applying the energy corrections. This figure can be compared with figure 2 of the main text. . . . .	183
A.9	Surface stability diagram for Pt(100) represents the stable surface terminations as a function of pressure and temperature without applying the energy corrections. This figure can be compared with figure 3 of the main text. . . . .	184

B.1	CO orientation on Pt(553) at $\theta = 0.65$ in the LEME structure . . . . .	199
B.2	Configurations used to compare adsorption energy of CO on step edge and the terrace. . . . .	211
B.3	Parity plot comparing the reference DFT energies and forces with the neural network estimates for Pt(553) . . . . .	212
B.4	Parity plot comparing the reference DFT energies and forces with the neural network estimates for Pt(557) . . . . .	213
B.5	Parity plot comparing the reference DFT energies and forces with the neural network estimates for Pt(643) . . . . .	214
B.6	Parity plot comparing the reference DFT energies and forces with the neural network estimates for Pt(111) . . . . .	215
B.7	Parity plot comparing the reference DFT energies and forces with the neural network estimates for structures with low coordination adsorption sites . . . . .	216
C.1	Model showing clean Pt(553) surface with (111) terraced and (111) type steps. (a) Top view, (b) Side view . . . . .	217
C.2	Model showing clean Pt(557) surface with (111) terraced and (100) type steps. (a) Top view, (b) Side view . . . . .	218
C.3	Pt(111) in $5 \times 10^{-8}$ Torr CO. Size: 100 nm x 100 nm. . . . .	219
C.4	Parity plot showing the training (6153 structures) and validation (13379 structures) data. . . . .	222
C.5	HDNNP accuracy: Energy Error histogram. . . . .	223
C.6	(a) Energetics of elementary surface reconstruction steps explored for Pt(553) step edge including step wandering (b-e), step atom extraction (f-h) and island extraction from bulk (i-k). Structures shown at 0.5 Torr . . . . .	226

C.7 (a) Energetics of elementary surface reconstruction steps explored for Pt(553) step edge including step wandering (b-e), step atom extraction (f-h) and island extraction from bulk (i-k). Structures shown at 0.0007 Torr . . . . .	227
C.8 (a) Energetics of elementary surface reconstruction steps explored for Pt(557) step edge including step wandering (b-e), step atom extraction (f-h) and island extraction from bulk (i-k). Structures shown at 0.5 Torr . . . . .	228
C.9 (a) Energetics of elementary surface reconstruction steps explored for Pt(557) step edge including step wandering (b-e), step atom extraction (f-h) and island extraction from bulk (i-k). Structures shown at 0.0007 Torr . . . . .	229
C.10 (b) Comparing the formation energies of Pt islands of increasing sizes from 1 to 19 atoms on Pt(111) terrace. (b-e) Showing the representative structures at 0.5 Torr. . . . .	232
C.11 (b) Comparing the formation energies of Pt islands of increasing sizes from 1 to 19 atoms on Pt(111) terrace. (b-e) Showing the representative structures at 0.0007 Torr. . . . .	233
C.12 Pt reconstruction energy for Pt(553) in absence of CO . . . . .	235
C.13 Pt reconstruction energy for Pt(557) in absence of CO . . . . .	236
C.14 Pt reconstruction energy for Pt(111) with islands in absence of CO . . . . .	237
C.15 $\Delta E_{chem}$ vs $\Delta E_{metal}$ for Pt(553). (A) - step wandering, (D) - Step atom extraction and (NR) - Island with NR step . . . . .	238
C.16 $\Delta E_{chem}$ vs $\Delta E_{metal}$ for Pt(557). (A) - step wandering, (D) - Step atom extraction and (NR) - Island with NR step . . . . .	239
C.17 $\Delta E_{chem}$ vs $\Delta E_{metal}$ for Pt(111). (A) - step wandering, (D) - Step atom extraction and (NR) - Island with NR step . . . . .	240

C.18 Reaction energy diagram for 1 atom Pt diffusion on the terrace of Pt(553) at 450

Torr. . . . . 241

## LIST OF TABLES

2.1	Pseudopotential details. Core radii ( $R_c$ ) are in $a_0$ . $\Delta E_{S-T}$ (eV) is the singlet-triplet excitation energy of CO. $\Delta E_s$ (eV) represents the adsorption energies of CO on the 's' site at a coverage of 0.25 ML. . . . .	18
2.2	Pseudopotential details. Core radii ( $R_c$ ) are in $a_0$ . $\Delta E_{S-T}$ (eV) is the singlet-triplet excitation energy of CO. $\Delta E_s$ (eV) represents the adsorption energies of CO on the 's' site at a coverage of 1.00 ML. . . . .	18
2.3	CO adsorption energies (in eV, including the ZPE correction) on Pt(111) and Pt(100) for top, bridge, and hollow adsorption sites as predicted by the PBE exchange-correlation functional, after applying the correction to the PBE energies (Corr.) and experimentally obtained value (Expt.). . . . .	24
2.4	Stable surface structures observed in Fig. 2.6 (and shown in table 2.5). The table outlines the types of unit cells, the CO coverage, the average adsorption energy per CO (including $\Delta ZPE$ ) and the average adsorption Gibbs free energy per CO per unit area of the cell at 300K and 1 atm pressure. Low energy competing metastable structures are also indicated with -a, -b or -c added label . . . . .	25
2.5	Low energy structures for CO on Pt(111) for various coverages. This includes stable structures found in the surface stability diagram of Fig. 2 (using the same numeric ID) and low energy metastable structures with surface energy at most 5 meV/Å <sup>2</sup> less stable (indicated with the added -a and -b labels). . . . .	29
2.6	Stable surface structures observed in Fig. 2.7 (and shown in table 2.7). The table outlines the types of unit cells, the CO coverage, the average adsorption energy per CO (including $\Delta ZPE$ ) and the average adsorption Gibbs free energy per CO per unit area of the cell at 300K and 1 atm pressure. Low energy metastable structures are also (indicated with -a or -b added label). . . . .	36



2.7	Low energy structures for CO on Pt(100) for various coverages. This includes stable structures in the surface stability diagram of Fig. 2.6 (using the same numeric ID) and low energy metastable structures with surface energy at most 5 meV/Å <sup>2</sup> less stable (indicated with the added -a and -b labels) . . . . .	38
3.1	Cutoff function types used in the construction of symmetry functions . . . . .	50
A.1	Average CO adsorption energies ( $\Delta E_{CO} = E_{CO_n@slab} - E_{slab} - n_{CO} \times E_{CO} + \Delta ZPE$ ) calculated for the various structures considered for Pt(111). The structures, unit cell, CO coverage and average adsorption energies have been listed in the table. .	162
A.2	Average CO adsorption energies ( $\Delta E_{CO} = E_{CO_n@slab} - E_{slab} - n_{CO} \times E_{CO} + \Delta ZPE$ ) calculated for the various structures considered for Pt(100). The structures, unit cell, CO coverage and average adsorption energies have been listed in the table. .	175
B.1	Pt(553) LEME structures data: Free energy per unit area (G/A), Coverage of CO on the terrace top site ( $\theta_t(T)$ ), bridge site ( $\theta_t(B)$ ), hollow site ( $\theta_t(H)$ ) and on the step edge top site ( $\theta_e(T)$ ), bridge site ( $\theta_e(B)$ ), hollow site ( $\theta_e(H)$ ), total coverage of CO on the terrace ( $\theta_t$ ) and on the step edge ( $\theta_e$ ) and the surface area of the unit cell (A) . . . . .	199
B.2	Pt(557) LEME structures data: Free energy per unit area (G/A), Coverage of CO on the terrace top site ( $\theta_t(T)$ ), bridge site ( $\theta_t(B)$ ), hollow site ( $\theta_t(H)$ ) and on the step edge top site ( $\theta_e(T)$ ), bridge site ( $\theta_e(B)$ ), hollow site ( $\theta_e(H)$ ), total coverage of CO on the terrace ( $\theta_t$ ) and on the step edge ( $\theta_e$ ) and the surface area of the unit cell (A) . . . . .	203

B.3	Pt(643) LEME structures data: Free energy per unit area ( $G/A$ ), Coverage of CO on the terrace top site ( $\theta_t(T)$ ), bridge site ( $\theta_t(B)$ ), hollow site ( $\theta_t(H)$ ) and on the step edge top site ( $\theta_e(T)$ ), bridge site ( $\theta_e(B)$ ), hollow site ( $\theta_e(H)$ ), total coverage of CO on the terrace ( $\theta_t$ ) and on the step edge ( $\theta_e$ ) and the surface area of the unit cell ( $A$ ) . . . . .	209
B.4	Comparison the adsorption energy of CO on the step edge and the terrace. . . . .	211
C.1	Symmetry functions used for HDNNP input layer generation . . . . .	220
C.2	$\Delta E_{rec}$ separated into $\Delta E_{metal}$ and $\Delta E_{chem}$ at different CO pressures for various reconstruction models studied for Pt(553) . . . . .	224
C.3	Number of CO per unit cell on Pt(553) at different CO pressure and considered reconstruction models (SW - Step Wandering, SE - Step atoms Extraction, NR - Islands with NR step) . . . . .	225
C.4	$\Delta E_{rec}$ separated into $\Delta E_{metal}$ and $\Delta E_{chem}$ at different CO pressures for various reconstruction models studied for Pt(557) . . . . .	230
C.5	Number of CO per unit cell on Pt(557) at different CO pressure and considered reconstruction models. (SW - Step Wandering, SE - Step atoms Extraction, NR - Islands with NR step) . . . . .	231
C.6	$\Delta E_{rec}$ separated into $\Delta E_{metal}$ and $\Delta E_{chem}$ at different CO pressures for various reconstruction models studied for Pt(111) with different island sizes. . . . .	233
C.7	Number of CO per unit cell on Pt(111) at different CO pressure and considered island sizes. . . . .	234

## ACKNOWLEDGMENTS

Firstly, I would like to thank my supervisor Dr. Philippe Sautet for his invaluable supervision, support and tutelage during the course of my PhD degree. He not only helped me advance academically but also encouraged my interest in getting industrial experience in the last five years. I really couldn't have asked for a better advisor.

Additionally, I would like to thank our experimental collaborators Dr. Franklin Feng Tao and Dr. Luan Nguyen for their immense contribution to my research. I would also like to acknowledge the members of my dissertation committee, Dr. Anastassia Alexandrova, Dr. Dante Simonetti and Dr. Carlos Morales-Guio for their advice and support.

I would also like to thank all the members of Sautet Lab for their help, discussions, and collaborations over the years. A lot of research ideas were developed during our group meetings.

Finally, just as importantly, I would like to thank my parents, my brother and all my friends who supported me through the ups and downs of this PhD journey.

Several chapters in this dissertation contain material adapted from published, submitted, and unpublished manuscripts with multiple contributing authors, as noted in the following.

Chapter 2 contains figures, tables, and text reprinted (adapted) with permission from the article *ACS Catal.* 2020, 10, 16, 9533–9544 Copyright 2020 American Chemical Society. DOI: <https://pubs.acs.org/doi/10.1021/acscatal.0c01971> It was authored by Vaidish Sumaria, Luan Nguyen, Franklin Feng Tao and Philippe Sautet. PS and FT conceptualized and supervised the work in the article. VS performed the computational studies and LN performed the experimental work. This work was funded by the NSF (grant no. 1800601 and 1800577). This work used computational and storage services associated with the Hoffman2 Shared Cluster provided by the UCLA Institute for Digital Research and Education's Research Technology Group. The authors want to thank XSEDE (TG-CHE170060) SDSC's

Comet Supercomputer and Bridges PSC for the computer time. XSEDE is supported by National Science Foundation grant number ACI-1548562.

Chapter 4 contains figures and text reprinted (adapted) with permission from the article *Chem. Sci.*, 2021, 12, 15543-15555 by Vaidish Sumaria and Philippe Sautet. DOI: <https://doi.org/10.1039/D1SC03827C>. V. S. performed DFT calculations, HDNNP training and data analysis for the work. P. S. supervised the project and both the authors discussed the results and helped in writing the manuscript. This work was funded by NSF, Grant no. 1800601. This work used computational and storage services associated with the Hoffman2 Shared Cluster provided by the UCLA Institute for Digital Research and Education's Research Technology Group. The authors want to thank XSEDE (TG-CHE170060) SDSC's Expanse Supercomputer and Bridges PSC for the computation time.

Chapter 5 contains figures and text reprinted (adapted) with permission from the article *J. Am. Chem. Soc.* 2023, 145, 1, 392–401 Copyright 2023 American Chemical Society authored by Vaidish Sumaria, Luan Nguyen, Franklin Feng Tao and Philippe Sautet. DOI: <https://www.doi.org/10.1021/jacs.2c10179>. PS and FT conceptualized and supervised the work in the article. VS performed the computational studies and LN performed the experimental work. This work was funded by the NSF through Grants NSF-CHE-1800601 and NSF-CHE-1800577. The computer time was funded by the Extreme Science and Engineering Discovery Environment (XSEDE), which is supported by National Science Foundation grant number TG-CHE170060. Specifically, it used the Bridges, Bridges-2 (Pittsburgh Supercomputing Center (PSC)), and SDSC Expanse computer systems. The STM images were collected from the high-pressure scanning tunneling microscope funded by the University of Notre Dame through a faculty start-up fund.

## VITA

- 2012-2016 B.Tech. (Chemical Engineering), University of Petroleum & Energy Studies, Uttarakhand, India
- 2016-2017 M.S. (Chemical Engineering), Carnegie Mellon University, Pittsburgh, PA, USA
- 2021-2021 Computational Chemistry Intern, Phaseshift Technologies
- 2022-2022 Computational Materials Science Intern, Robert Bosch LLC

## AWARDS

- 2022 Dissertation Year Fellowship

## PUBLICATIONS

*Vaidish Sumaria*, Luan Nguyen, Franklin Feng Tao, and Philippe Sautet. “Atomic scale mechanism of platinum catalyst restructuring under a pressure of reactant gas.” In Revision (2022).

*Vaidish Sumaria*, and Philippe Sautet. “CO organization at ambient pressure on stepped Pt surfaces: first principles modeling accelerated by neural networks.” *Chemical science* 12, no. 47 (2021): 15543-15555.

*Vaidish Sumaria*, Luan Nguyen, Franklin Feng Tao, and Philippe Sautet. “Optimal packing of CO at a high coverage on Pt (100) and Pt (111) surfaces.” ACS Catalysis 10, no. 16 (2020): 9533-9544.

Dilip Krishnamurthy, *Vaidish Sumaria*, and Venkatasubramanian Viswanathan. “Quantifying robustness of DFT predicted pathways and activity determining elementary steps for electrochemical reactions.” The Journal of Chemical Physics 150, no. 4 (2019): 041717.

*Vaidish Sumaria*, Dilip Krishnamurthy, and Venkatasubramanian Viswanathan. “Quantifying confidence in DFT predicted surface pourbaix diagrams and associated reaction pathways for chlorine evolution.” ACS Catalysis 8, no. 10 (2018): 9034-9042.

Dilip Krishnamurthy, *Vaidish Sumaria\**, and Venkatasubramanian Viswanathan. “Maximal predictability approach for identifying the right descriptors for electrocatalytic reactions.” The journal of physical chemistry letters 9, no. 3 (2018): 588-595.

# CHAPTER 1

## Research Background

Transition metals are workhorses of catalytic reactions. In addition to their use as catalysts in various chemical production processes, the search for renewable energy solutions and sustainable production processes has renewed interest in understanding their role in these chemical processes.<sup>1</sup> Pt, Pd, and Ni find applications in the hydrogenation of alkenes.<sup>2-4</sup> Haber-Bosch process used for commercial ammonia production is catalyzed by Fe.<sup>5,6</sup> Catalytic converters which are used as an automobile exhaust emission control device to convert nitrogen oxides to N<sub>2</sub> and carbon, hydrocarbons and CO to CO<sub>2</sub> require Pt and Pd catalysts.<sup>7,8</sup> Rh, Ru, Pt, Pd, and Ir have been used for steam reforming, catalytic thermal decomposition (pyrolysis), and as dry reforming catalysts for industrial manufacturing of H<sub>2</sub> gas.<sup>9-13</sup> Along with these thermal catalytic applications, transition metals are also used for sustainable electrochemical processes including oxygen reduction,<sup>14,15</sup> hydrogen evolution,<sup>15,16</sup> CO<sub>2</sub> reduction.<sup>15,17,18</sup> With so many important industrial processes relying on transition metals, it is important to have a fundamental understanding of how these catalyst work in order to develop new catalyst design strategies. Over the last two decades, significant progress has been made in understanding these catalytic processes due to the combination of theoretical and experimental research. This combined strategy has helped yield a framework for understanding these processes at the atomic scale, reaction mechanisms, and trends that can provide guidance toward the development of improved catalysts.

Experimental surface science methods applied in heterogeneous catalysis can be expressed using a plot between a realistic environment defined by T,P (or the chemical potential) and

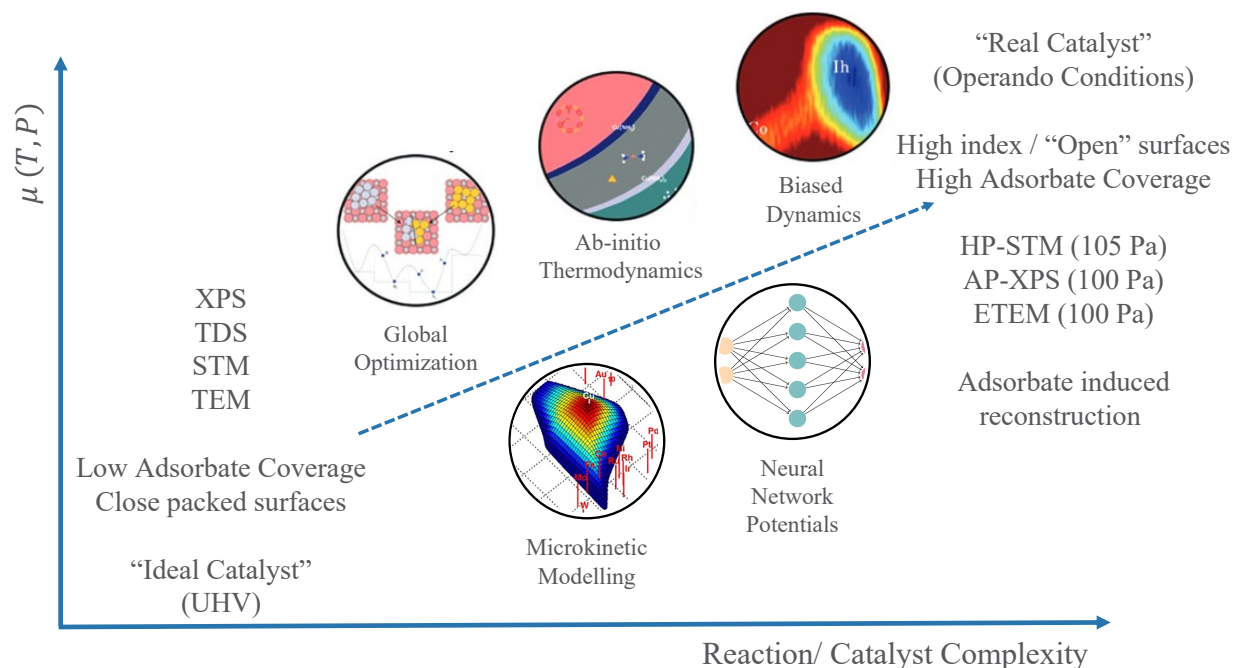


Figure 1.1: Schematic figure showing the “Ideal Catalyst” in Ultra-High Vacuum (UHV) conditions and “Real Catalyst” at realistic reaction conditions. The figure described the various experimental microscopy and spectroscopy methods used in these conditions as well as the advances made in computational techniques to solve the “pressure gap” and describe catalysts in operando conditions.

catalyst or reaction complexity as shown in Fig. 1.1. In ultra-high vacuum regions, closed-pack surfaces (111, 100) are more stable. At these conditions, unless the temperature is very low, adsorbate coverage remains low. On the other hand, at high temperature/pressure conditions for real catalysts – high index or open surfaces are stabilized by the possible high coverage of adsorbates. At the UHV conditions, a number of surface science spectroscopy techniques like Auger Electron Spectroscopy (AES), Photo-emission spectroscopy (PES), X-ray photoelectron spectroscopy (XPS), Thermal desorption spectroscopy (TDS) and other microscopy techniques like Scanning Tunnelling Microscopy (STM) and Transmission Electron Microscopy (TEM) are used to image and understand surfaces. To address the so-called “pressure gap”, there have been advancements to improve these similar techniques to be able to use at high pressure. For example HP-STM which works for pressures as high as 1 bar, ambient pressure XPS, and environmental TEM can handle pressures of about  $10^{-3}$  bar



pressures. To move from simple Density Functional Theory (DFT) calculations describing the UHV conditions to the real conditions, a lot of techniques have been developed. Global optimization methods like Grand Canonical Basin Hopping (GCBH) and Genetic Algorithm (GA) in combination with ab-initio thermodynamics are used to find the ideal local environment of the systems that is most stable with respect to the system structure as well as the temperature and pressure conditions of the reaction. Further complex biased molecular dynamics can be introduced at high temperatures where the description of the system can more ideally be represented by some statistical descriptor over an ensemble of structures. At the same time, microkinetics can be used at any level between UHV and high pressures to understand reaction kinetics. With increasing complexity, Neural Network based potentials can be used to study large systems with the least computational cost.

Industrial catalysts operate in the “Real catalyst” region usually consisting of small particles exposing different atomic terminations that exhibit a high concentration of step edges, kink sites, and vacancies at the edge of the facets, which are thought to be the catalytically active sites. On such surfaces, the high coverage of adsorbate can induce reconstruction in the catalyst surface. A brief overview of experimental and theoretical studies exploring this reconstruction has been presented in the following sections.

## **1.1 Adsorbate induced catalysts restructuring**

### **1.1.1 Experimental Overview**

Atomic packing and coordination at the surface of a catalyst are key parameters in fundamentally understanding catalytic performance.<sup>19–41</sup> There are now clear evidences that catalysts might not remain as prepared during a catalytic reaction;<sup>19–26,42–52</sup> their structures and/or compositions evolve in the presence of the reactants and/or major reaction intermediates. How the surface of a metal catalyst is restructured in a gas phase of the reactant(s) is hence the key for identifying catalytic active sites, fundamentally understanding catalytic

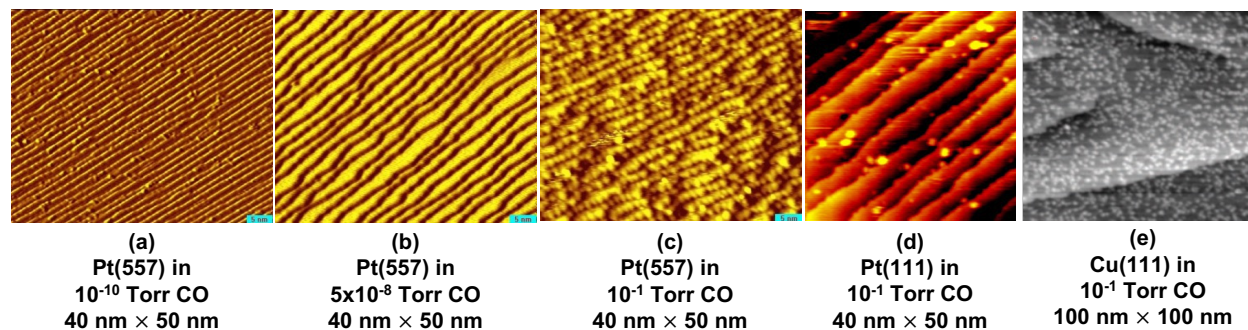


Figure 1.2: STM images of Pt(557), Pt(111), and Cu(111) in CO at 25°C at a time about 40 minutes after exposure to CO. (a) Pt(557) in UHV. (b) Pt(557) in  $5 \times 10^{-8}$  Torr CO; Terrace edges are curvy. (c) Pt(557) in 0.1 Torr CO; the whole surface is broken up into homogeneously distributed Pt nanoclusters. (d) Pt(111) in 0.1 Torr CO after 2 hours; (e) Cu(111) in 0.1 Torr CO. Adapted from Science 327, 850 (2010) and Science 351, 475 (2016).

mechanisms and predicting novel, more active, more selective or more durable catalysts.

Literature extensively reports the surface adsorption of small molecules such as CO, O<sub>2</sub>, CH<sub>4</sub>, NO;<sup>3,35-37,48,53,54</sup> however, there are few explorations of the origin of the restructuring of a catalyst surface under reaction conditions due to the limited access to surface-sensitive techniques operational for a catalyst exposed to a gas. In the last few years, due to the development of in-situ/ operando study techniques, the surface structure of some model catalysts under reaction conditions has been studied.<sup>22,24,25,55-58</sup> Using Scanning Tunneling Microscopy (STM), restructuring of the Pt(557) stepped surface consisting of (111) terraces and (100) steps under a gas phase of CO at 0.1-1 Torr has been observed.<sup>55</sup> Terrace edges of Pt(557) become curly in  $5 \times 10^{-8}$  Torr of CO at 25°C (Fig. 1.2(b)). At 0.1 Torr of CO, the whole surface is massively broken into nanoclusters, with a homogeneous size of 2.6 nm and a periodic packing (Fig. 1.2(c)). The reconstruction was also observed by Ambient Pressure X-ray Photoelectron Spectroscopy (AP-XPS), where the much larger fraction of Pt 4f<sub>7/2</sub> XPS peak at 71.8 eV is attributed to under-coordinated Pt atoms at edge of Pt nanoclusters formed during reconstructions.<sup>55</sup> Once the CO pressure around these nanoclusters is decreased to  $\sim 10^{-8}$  Torr, CO coverage is lowered to about 0.5 monolayers (ML) and Pt nanoclusters “disappear” through “coalescing” into terraces. This suggests that the reorganization of Pt-Pt

bonds at the surface and the observed massive restructuring are driven by the high coverage and are reversible. On the other hand, for Pt(111), where the density of steps is lower, there is no obvious change of the surface structure after 40 minutes of exposure to CO at a pressure of  $5 \times 10^{-8}$  Torr and a small number of nanoclusters (size  $\sim 1.5$  nm) were observed in 0.1 Torr of CO after a couple of hours.

The stable Pt(100) clean surface consists of a quasi-hexagonal overlayer, or hex-Pt(100) on top of the square symmetry (100) lattice resulting in a 20% higher density than the bulk-terminated structure.<sup>59,60</sup> Due to the weak interaction between the hex-reconstructed layer and the underlying square symmetry of Pt(100), hex-Pt(100) is more prone to further reconstruction upon CO adsorption. When exposed to  $10^{-5}$  Torr of CO at room temperature, hex-Pt(100) reconstructs to form numerous islands from the Pt atoms expelled from the hexagonal structure of diameter in the 0.5–3.5 nm range and covering about 45% of the surface.<sup>61</sup> The incommensurate structure of the top layer compared with the bulk is not solely the cause of reconstruction. Zhu et al. showed that adsorption of other molecules, such as ethylene, does not affect the hex-Pt(100) up to 1 Torr.<sup>62</sup> Although in the presence of  $5.10^{-6}$  Torr of ethylene, the interaction of only a few CO molecules with a partial pressure less than  $10^{-8}$  Torr on the surface leads to formation of 2.3x1.4 nm Pt islands.<sup>62</sup> Au(100) has a similar hex overlayer that reconstructs in the presence of CO.<sup>63</sup>

Salmeron et al. used low energy energy diffraction (LEED) and Auger electron spectroscopy to show that on a Pt(110)-(1x2) surface, a short 4 minute exposure of CO at  $10^{-7}$  Torr at 25°C causes a rapid reconstruction to Pt(110)-(1x1) structure.<sup>64</sup> Using high resolution scanning tunneling microscopy (STM) images, Gritsch et al. showed that the “nucleation and growth” mechanism proposed for the Pt(100) reconstruction also applies to this transformation.<sup>65</sup> Thostrup et al. followed the reconstruction on an atomic scale for CO pressure over 12 orders of magnitude, until 1 bar pressure, using high pressure STM (HP-STM) studies. From their observations, they conclude that the gain in CO binding energy when CO binds to low-coordinated metal atoms governs the surface reconstruction on the Pt(110) surface.<sup>66</sup>

Similar reconstruction of Pt(311)-(1×2)→(1×1) was reported using LEED studies.<sup>67</sup>

Copper is another metal used as a catalyst in many chemical and energy transformations reactions.<sup>68-77</sup> Although the binding energies of CO on the Cu(111) surface are lower than that on Pt(557) by 0.5 eV the whole Cu(111) terraces are reconstructed for Cu nanoclusters of size 3 nm at 0.2 Torr CO and 25°C (Fig. 1.2(e)).<sup>24,55,78</sup> As both Pt(557) and Cu(111) can significantly restructure at 0.1-0.2 Torr of CO, the adsorption energy of CO on a metal surface does not determine alone whether this surface can be restructured or not under a pressure of CO. Compared to the formation of a large density of Cu nanoclusters on the Cu(111) surface in 0.2 Torr CO at a time scale of less than one hour, only a low coverage of clusters is formed on the terraces of Pt(111).<sup>24</sup>

On Ni(100), using STM images, Klink et al. show that above a critical coverage, CO induces a reconstructed phase resulting in a lateral clockwise-counterclockwise displacement of the Ni atoms.<sup>79</sup> This shows that similar facets of different materials reconstruct in different ways when exposed to CO. LEED structural study shows that CO at a coverage 0.3-0.75 leads to missing row reconstruction in Pd(110).<sup>80,81</sup> STM imaging has also helped observe the reconstruction of Co(11-20) surface at room temperature led by anisotropic migration of Co atoms.<sup>82</sup> Apart from CO, other adsorbates are also studied in the literature that induce surface restructuring in transition metals. Oxygen has showed to induce reconstruction on Ag(111),<sup>83</sup> Ni(100),<sup>84</sup> Ni(111),<sup>85</sup> Cu(100)<sup>86</sup> and Cu(110).<sup>87</sup> Similarly, several STM studies have revealed carbon-induced clock reconstruction of both Ni(100) and Ni(111).<sup>88-90</sup> and EELS and LEED studies show hydrogen induced reconstruction in Ni(110),<sup>91-93</sup> Ni(111),<sup>94</sup> and W(100).<sup>95</sup>

### 1.1.2 Computational Overview

A few studies have addressed surface restructuring from the angle of computational chemistry methods. Banerjee et al have shown from DFT calculations that the presence of CO and C adsorbates on Co(0001), relevant to the conditions of Fischer-Tropsch catalysis, pro-

notes the formation of steps.<sup>96-98</sup> Kaghazchi et al have studied the roughening of Ru, Os, and Re surfaces covered by N adsorbates with similar methods.<sup>28</sup> On Co(11-20), DFT calculations show that [0001]-directed, zigzag added row of Co atoms is energetically favorable and that the initial restructuring occurs preferentially through carbonyl-type species where the migrating Co atom is bonded to two CO molecules.<sup>82</sup> Harrison et al. using first principles studies showed that for Cu(100)/O system, the missing row reconstruction provides an alternative mode of compressive stress relief to that of a clock reconstruction in a c(2×2) overlayer phase.<sup>86</sup> In all these studies the range of restructuring is however limited and hard to directly compare with the realistic conditions in which in-situ experiments show large-scale reconstructions.

Loffreda et al. used computational atomistic thermodynamics, isotherm models, and kinetics, to show that high CO pressures (between 10 and 100 Torr) removes the (1×2) missing-row reconstruction on Au(110).<sup>20</sup> Their model suggests that high pressure of CO allows formation of Au-CO clusters which diffuse along the empty troughs that generates the unreconstructed Au(110)-(1×1) surface. Similarly on Au(111), Piccolo et al. show using DFT calculations that the chemisorption of CO is favored on low-coordinated sites such that CO binds strongest to the adatoms, followed by kink sites, step edge and least strongly to the terrace. This supports the RAIRS data suggesting the formation of step and kink sites at pressures as low as 1 Torr.<sup>99</sup> DFT investigation has also shown that CO adsorption induces segregation in bimetallic alloys. In a Cu<sub>3</sub>Pd(111) surface and in Au/Pd bimetallic surfaces, CO adsorption leads to Pd skin formation.<sup>100,101</sup>

Gezelter and coworkers used classical force fields and molecular dynamics simulations to probe step wandering and step doubling on CO-covered Pt and Au surfaces.<sup>102</sup> They parameterized the PtCO interactions using experimental data and plane-wave density functional theory (DFT) calculations. Various mechanisms for CO-mediated step wandering and step doubling were investigated on the Pt(557) surface. However, the triangular clusters that had been seen by Tao et al. using in-situ STM were not observed in these simulations.<sup>55</sup>

They also studied CO-induced reconstruction using similar techniques for Pt/Pd alloyed catalysts. They showed that the different binding preferences of CO adsorbed to the two metals can help explain the observed stabilization of the Pd surface structures as well as the roughening of the Pt step edges. They concluded that since the adsorbed CO acts to lower the surface energy of the Pt, it accelerated the formation of Pt-islands which is kinetic in nature.<sup>103</sup> Similarly, Beurden et al. used modified embedded-atom method to describe the mechanism and dynamics of CO-Induced Lifting of the Pt(100) surface.<sup>104</sup> Although these works give immense insights into the reconstruction process, (mean) embedded atom method ((M)EAM) potentials used to describe the metal-metal interactions and Lennard-Jones type potentials used to describe the Pt-CO interactions have limited accuracy. The parameters used in the model are modified to ensure that the Pt-CO interaction is favoring the on-top site on Pt(111) to match experimental results, yet they significantly overestimate the CO binding energy which can impact the results presented.<sup>103</sup>

## 1.2 Thesis Objective

In this dissertation, we seek to understand the mechanism of adsorbate induced surface restructuring, under a pressure of gas using first principles calculations, Machine Learning based atomic potentials and global optimization techniques. Within the dissertation, we discuss the Pt/CO system in detail.

Chapter 2 focuses on developing a correction for the so-called “Pt/CO Puzzle” which discusses why Semilocal exchange correlation functionals are known to provide incorrect adsorption site and overestimated adsorption energy for CO on Pt. We develop a simple first-principles correction for the adsorption energy of CO on Pt(111) and Pt(100) using the bond length of adsorbed CO as a descriptor. Using the developed correction and atomic thermodynamics, we develop surface stability diagrams showing the stable CO configurations on the Pt(111) and Pt(100) surface as a function of reaction conditions (temperature and pressure). High

coverage ( $\theta > 0.5$ ) configurations of CO on Pt(111) lead to the formation of superimposed hexagonal/quasi-hexagonal lattice of CO on hexagonal Pt(111) layer which matches the experimental STM imaging. For Pt(100) at  $\theta \geq 0.75$ , the CO molecules adopt a one dimensional coincidence lattice and we observe the formation of  $(n \times 2)$  unit cells ( $n=4,6,8$ ) with  $(2n-2)$  CO molecules in each cell on top/quasi-top and bridge/quasi-bridge positions creating a skewed hexagonal lattice to reduce CO-CO repulsion with increasing coverage.

Chapter 3 deals with understanding the development on High Dimensional Neural Network Potential (HDNNP) using reference Density functional theory data. The neural-network representation of DFT potential-energy surfaces using HDNNP provides the energy and forces as a function of all atomic positions in systems of arbitrary size and is several orders of magnitude faster than DFT calculations. The detailed iterative process of training such a potential is discussed in this chapter which includes data generation, input parameterization, NN-architecture choice, optimization algorithms, overfitting, etc.

Chapter 4 aims at understanding the adsorption of CO in ambient conditions ( $T=300$  K,  $P=1$  atm) on step and kink sites at Pt surfaces which have a crucial importance in catalysis. To thoroughly and efficiently explore the potential energy surface (PES), we develop a NN potential and use a modified Basin Hopping method to perform global optimization. We show that for the considered facets of Pt surfaces, low coordination Pt sites (steps) are always fully covered by on-top CO molecules. We show that the step structure and the structure of CO molecules on the step dictate the arrangement of CO molecules on the lower terrace. Overall, this effort provided a detailed analysis of the influence of step edge structure, kink sites, and terrace width on the organization of CO molecules on non-reconstructed stepped surfaces, yielding initial structures for understanding restructuring events driven by CO at high coverages and ambient pressure.

Chapter 5 illustrates the mechanism of Pt catalysts reconstruction in reactive conditions. Understanding how catalyst active sites dynamically evolve at the atomic scale under reaction conditions is a prerequisite for an accurate determination of catalytic mechanisms

and predictably developing catalysts. By combining in-situ time-dependent observation and machine learning-accelerated first-principle atomistic simulations we uncover the mechanism of restructuring of Pt catalysts under a pressure of carbon monoxide (CO). We show that a high CO coverage at a Pt step edge triggers the formation of atomic protrusions of low-coordination Pt atoms, which then detach from the step edge to create subnano-islands on the terraces, where undercoordinated sites are stabilized by the CO adsorbates.

Finally 6 discusses CO-induced reconstruction on Copper. Although the binding energy of CO on the Cu surface is lower than that on Pt by 0.5 eV, the whole Cu surface is reconstructed into Cu nanoclusters even at low pressures of CO at room temperature. We discuss how the low cohesive energy of Cu compared to Pt could be a reason for this massive reconstruction observed. This work is still an on-going research and we present some preliminary results.



## CHAPTER 2

# Optimal packing of CO at high coverage on Pt(111) and Pt(100)

### 2.1 Introduction

#### 2.1.1 Experimental overview of CO adsorption structures on Pt surface

Adsorption of carbon monoxide on transition metals is frequently regarded as a benchmark system owing to its importance in CO oxidation,<sup>105-108</sup> water-gas shift reaction<sup>109-112</sup> and Fischer Tropsch synthesis<sup>3,113-115</sup> and hence has been a subject of many studies, both experimental and theoretical. The determination of the CO adsorption site, coverage and assembly structure on the different transition metal surfaces is a key information for these reactions. It is especially important to understand the structure and coverage of CO at ambient pressure relevant to catalytic conditions. Moreover, the simplicity and known adsorption properties of CO, make it the perfect candidate as a probe molecule in surface science. As a result, adsorption of CO on platinum surfaces (Pt(100) and Pt(111)) is considered as a model system in the field and has been studied using wide range of experimental techniques, some of them enabling to access near ambient to high pressure conditions, including low energy electron diffraction (LEED), X-ray photoemission spectroscopy (XPS), scanning tunnelling microscopy (STM), temperature programmed desorption (TPD), calorimetry, work function measurements, Extended X-ray absorption fine structure (EXAFS) etc.<sup>116-137</sup> CO adsorption on Pt(111) has been studied both in UHV conditions at low temperature and

at atmospheric pressure and room temperature. Interestingly, different structures are seen. In UHV at low temperature, CO initially forms a  $(\sqrt{3} \times \sqrt{3})R30^\circ$ -1CO structure at 1/3 ML coverage, occupying the top site, followed by a well ordered  $c(4 \times 2)$ -2CO (or equivalently  $(\sqrt{3} \times 2)$ rect-2CO) structure at  $\theta=0.5$  ML with equal population of top and bridge sites.<sup>120,121,138,139</sup> The CO arrangement is not hexagonal in this structure. At higher coverage, a set of compressed, but still non-hexagonal, structures is found ( $c(\sqrt{3} \times 5)$ rect-3CO,  $\theta=0.6$  ML;  $(\sqrt{3} \times 3)$ rect-4CO,  $\theta=0.67$  ML ;  $c(\sqrt{3} \times 7)$ rect-5CO,  $\theta=0.71$  ML).<sup>140</sup> In contrast, at room temperature and atmospheric pressure, STM images show the formation of a hexagonal CO lattice superpositioned on Pt(111) to construct the so called Moiré pattern structures, for example the  $(\sqrt{19} \times \sqrt{19})R23.4^\circ$ -13CO commensurate structure at  $\theta=0.68$  ML.<sup>141</sup> The presence of this different set of CO structures for different conditions is puzzling and the stable or metastable nature of these structures is unclear until now. On the other hand, the situation for CO adsorption at low coverage on Pt(100) is somewhat more confused. Bradshaw et al. showed using vibrational spectroscopy that at 90 K CO occupies the bridge site until 0.5 ML ( $c(2 \times 2)$  structure), while at room temperature an equal mixture of bridge and top site is seen.<sup>135</sup> Hence the bridge site should correspond to a slightly lower internal energy. At high coverage, adsorbed CO on Pt(100) is reported using STM images to adopt a  $c(5\sqrt{2} \times \sqrt{2})R45^\circ$ -3CO unit cell ( $\theta = 0.6$  ML) with 2:1 bridge to top site ratio,<sup>134</sup> followed by a  $(3\sqrt{2} \times \sqrt{2})R45^\circ$ -4CO ( $\theta = 0.67$  ML) unit cell with a 1:1 bridge to top site ratio and a  $c(4 \times 2)$ -3CO unit cell ( $\theta = 0.75$  ML) with 2:1 bridge to top site adsorption ratio, using LEED.<sup>135</sup> In parallel, synergistic efforts have been applied on the computational aspects of studying the Pt/CO system.<sup>142-146</sup> A recent work by Gunasooriya et al. used the vdW-DF non-local functional to model ordered CO structures on Pt(111) at the high coverage limit.<sup>142</sup>

### 2.1.2 “Pt/CO Puzzle”

Understanding surface phenomena in heterogeneous catalysis theoretically has been vastly improved owing to the advancement in density functional theory with the semilocal (GGA)

and hybrid exchange-correlation (XC) functionals. Despite these successes, a few cases of performing these electronic structure calculations are known to be problematic in determining the correct adsorption site. This challenge is famously known for the Pt(111)/CO system and is coined as “The Pt(111)/CO Puzzle.”<sup>144,147–150</sup> The widely used semilocal XC functionals - PW91, PBE, and RPBE predict chemisorption energies for CO on Pt significantly higher than an experimental determination by single crystal calorimetry by approximately 0.37, 0.37, and 0.17 eV respectively.<sup>78,151</sup> More importantly, all these functionals favor the more coordinated bridge and hollow sites over the top site for Pt(111). On the other hand, more accurate hybrid functionals (PBE0,<sup>152</sup> B3LYP<sup>153</sup>) have been able to predict the correct adsorption site, but provide a CO adsorption energy which is even more overestimated than semilocal functionals, in relation with an overestimated Pt d-bandwidth. Blyholder model,<sup>154,155</sup> describes CO chemisorption on metal surfaces from CO molecular orbitals. Fig. 2.1 shows CO adsorption energies on top, fcc, and hcp sites of Pt(111) predicted using various exchange-correlation functionals. As seen from the figure, almost all functionals favor the hollow fcc site over the experimentally preferred top site. M06-L meta-GGA functional only predicts the correct adsorption site and reproduces rather well the experimental adsorption energy.

The commonly used Blyholder model (Fig. 2.2) used for explaining CO interaction with the transition metals suggests interactions of the two CO frontier orbitals, the  $5\sigma$  highest occupied molecular orbital (HOMO) and the  $2\pi^*$  lowest unoccupied molecular orbital (LUMO), with the metal states. The bonding  $5\sigma$  orbital (HOMO) donates electron density to the substrate (known as  $\sigma$ -donation) and the anti-bonding  $2\pi^*$  orbital (LUMO) receives electron density from the substrate (known as  $2\pi^*$ -backbonding). The extent of back bonding increases with the metallic coordination of the adsorption site (hence is more important for hollow-site) whereas the highly directional  $5\sigma$  metal interaction is stronger for the low coordination site, i.e. top site.<sup>157–159</sup> Semilocal XC functionals such as PBE tend to underestimate the HOMO-LUMO gap for CO<sup>144,146,160</sup> and place the unfilled CO  $2\pi^*$  orbital too low in

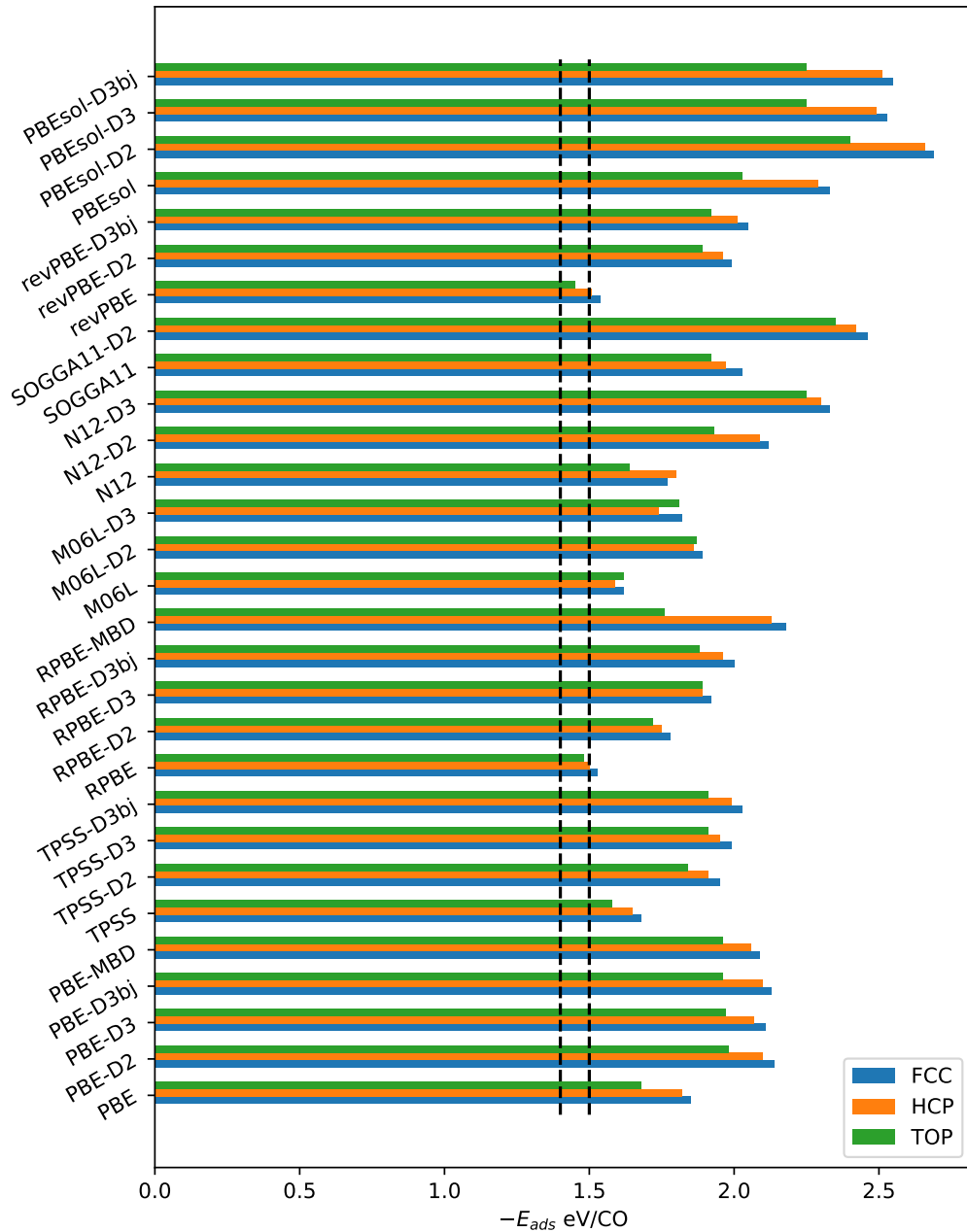


Figure 2.1: Adsorption energies ( $E_{ads}$  eV) for CO adsorbed on the top, fcc and hcp hollow sites on Pt(111) surface calculated with various XC functionals. The range of energy marked between the dashed lines indicates the experimental single crystal calorimetry value for the adsorption energy. Data regenerated from Janthon et al.<sup>156</sup>

energy which makes it too close in energy to the metal d band, resulting in an unrealistic strengthening of the  $2\pi^* - d$  band bonding interactions (backbonding) which favors multiply

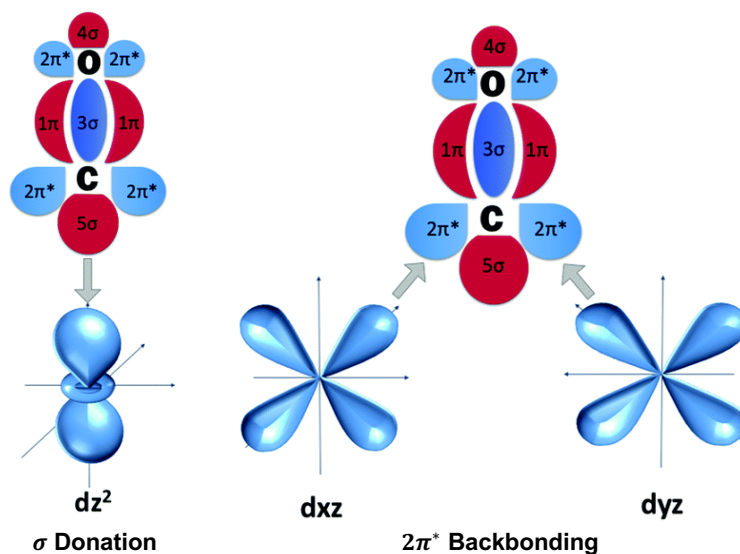


Figure 2.2: Blyholder model of CO chemisorption. The model describes two main components: (a)  $\sigma$  donation -  $5\sigma$  Highest Occupied Molecular Orbital (HOMO) donates electron density to the substrate and (b)  $2\pi^*$  Backbonding where anti-bonding  $2\pi^*$  Lowest Unoccupied Molecular Orbital (LUMO) receives electronic density from the substrate.

bonded sites.

### 2.1.3 Overview of the corrections developed in the literature

In order to obtain a better agreement with experiments, several studies have developed energy correction schemes to shift the CO LUMO to higher energies, which results in reducing the backbonding and favouring the experimentally observed top site for adsorption. The first method was developed by Kresse et al. where by using potentials with different core radii, they discovered that there exists a linear relationship linking the difference between top and hollow site adsorption energies for CO on Pt(111) and the gas-phase energy of the CO  $2\pi^*$  orbital.<sup>144</sup> They developed a GGA+U inspired method to tune the CO  $2\pi^*$  orbital energy and re-institute the correct top-site for CO adsorption on Pt(111). Following this work, another method developed by Mason et al. argued the use of GGA+U, since the U parameter is not known *a priori*.<sup>158</sup> They showed that the CO adsorption energy is not only dependent on the LUMO level of the free CO molecules but can also be equivalently linearly

related to the CO singlet-triplet excitation energy ( $\Delta E_{S-T}$ ). By extrapolating these linear relationships to the Configuration Interaction (CI) calculated value of  $\Delta E_{S-T}$ , a correction to the GGA energy for a respective adsorption site (top, bridge or hollow) was developed. This method was also shown to be universally working for a variety of metal surfaces.<sup>158</sup> Finally it was shown that the suggested correction for the adsorption energy also scales with the CO stretching frequency (which is a function of the adsorption site), which can yield a simpler correction scheme. This idea was elaborated later by Abild-Pedersen et. al., who suggested that the adsorption energy correction ( $\Delta$ ) for RPBE XC functional can be simply expressed as  $\Delta = 1.8 - 0.0008 \times \nu_{CO}$ , where  $\nu_{CO}$  is the internal stretch vibration frequency of CO in  $\text{cm}^{-1}$ .<sup>145</sup> Gajdoš et. al showed that a linear correlation exists between the CO stretching frequency and C-O bond length which is independent of the coordination of the CO molecule.,<sup>146</sup> which suggests that a relationship could also exist between the adsorption energy correction and the C-O bond length.

## 2.2 Methods

### 2.2.1 Computational Details

#### 2.2.1.1 DFT Calculation

Calculations were performed using the Vienna Ab-initio Simulation Package using the general gradient approximation (GGA) Perdew-Burke-Erzenhof (PBE) functional. Two set of calculations were performed: (i) Developing the correction scheme for CO adsorption on Pt surfaces, (ii) Using the developed correction scheme to compute the landscape of the adsorbed CO on Pt surfaces at various pressure and temperature conditions. The calculations for CO adsorption correction scheme are modeled using 1/4 and 1 mono-layer coverage of adsorbed CO on a six Pt layer slab, separated by 12 Å vacuum from its periodic image in the z direction. The two bottom layers of the unit cell were kept fixed, and the top four

layers with the adsorbates were allowed to relax with a force criterion of  $<0.01$  eV/Å. A fermi smearing width of 0.2 eV was applied using the Methfessel-Paxton method (order 2). A 3x3 surface supercell was considered for Pt(111) and Pt(100) and their Brillouin zones were sampled using a 7x7x1 k-point mesh. A 0.25 ML and 1 ML coverage was modeled on a 2x2 and 1x1 surface for both Pt(111) and Pt(100) and the k-points were scaled suitably. The calculation settings used to develop the surface stability diagram are the same as described above. The k-points are suitably scaled for the various unit cells used. We consider the adsorption of CO molecules on various sites with different coverages.

### 2.2.1.2 Correction development

The corrections have been obtained using the scheme developed by Mason et al.<sup>158</sup> This involves the following steps: (i) Using various pseudopotentials for C and O listed in Table 2.1 for  $\theta = 0.25$  ML and Table 2.2 for  $\theta = 1.00$  ML) we find the scaling relations between the CO adsorption energy on top, fcc and hcp (or hollow) site on Pt(111) (and Pt(100)) and the CO singlet-triplet excitation energy,  $\Delta E_{S-T}$  (Fig. 2.3 for  $\theta = 0.25$  ML, Fig. 2.4 for  $\theta = 1.00$  ML) (ii) These scaling relations are then extrapolated to find the adsorption energy at  $\Delta E_{S-T} = 6.095$  eV (excitation energy value reproduced using Coupled-cluster and CI calculations which are comparable with the experimental values.)<sup>161</sup> (iii) The correction is defined as the difference between the extrapolated value of the adsorption energy and the energy obtained using the normal PAW settings for C and O.

Table 2.1: Pseudopotential details. Core radii ( $R_c$ ) are in  $a_0$ .  $\Delta E_{S-T}$  (eV) is the singlet-triplet excitation energy of CO.  $\Delta E_s$  (eV) represents the adsorption energies of CO on the 's' site at a coverage of 0.25 ML.

PP	$R_c(\text{O})$	$R_c(\text{C})$	$\Delta E_{S-T}$	Pt(111)			Pt(100)		
				$\Delta E_{top}$	$\Delta E_{bridge}$	$\Delta E_{hcp}$	$\Delta E_{top}$	$\Delta E_{bridge}$	$\Delta E_{hollow}$
n	1.52	1.50	5.548	-1.68	-1.82	-1.84	-1.97	-2.16	-1.64
s	1.85	1.85	5.278	-1.75	-1.96	-2.01	-2.04	-2.30	-1.85
GW_new	1.6	1.6	5.665	-1.65	-1.77	-1.79	-1.94	-2.11	-1.59
h	1.1	1.1	5.681	-1.65	-1.77	-1.78	-1.94	-2.11	-1.58
GW	1.52	1.5	5.619	-1.65	-1.78	-1.80	-1.94	-2.12	-1.60

Table 2.2: Pseudopotential details. Core radii ( $R_c$ ) are in  $a_0$ .  $\Delta E_{S-T}$  (eV) is the singlet-triplet excitation energy of CO.  $\Delta E_s$  (eV) represents the adsorption energies of CO on the 's' site at a coverage of 1.00 ML.

PP	$R_c(\text{O})$	$R_c(\text{C})$	$\Delta E_{S-T}$	Pt(111)			Pt(100)		
				$\Delta E_{top}$	$\Delta E_{bridge}$	$\Delta E_{hcp}$	$\Delta E_{top}$	$\Delta E_{bridge}$	$\Delta E_{hollow}$
n	1.52	1.5	5.548	-0.908	-0.836	-0.751	-1.319	-1.532	-0.587
s	1.85	1.85	5.278	-1.014	-0.979	-0.914	-1.428	-1.679	-0.758
GW_new	1.6	1.6	5.665	-0.913	-0.836	-0.744	-1.322	-1.527	-0.578
h	1.1	1.1	5.681	-0.907	-0.824	-0.732	-1.316	-1.516	-0.565
GW	1.52	1.50	5.619	-0.915	-0.837	-0.750	-1.325	-1.532	-0.584



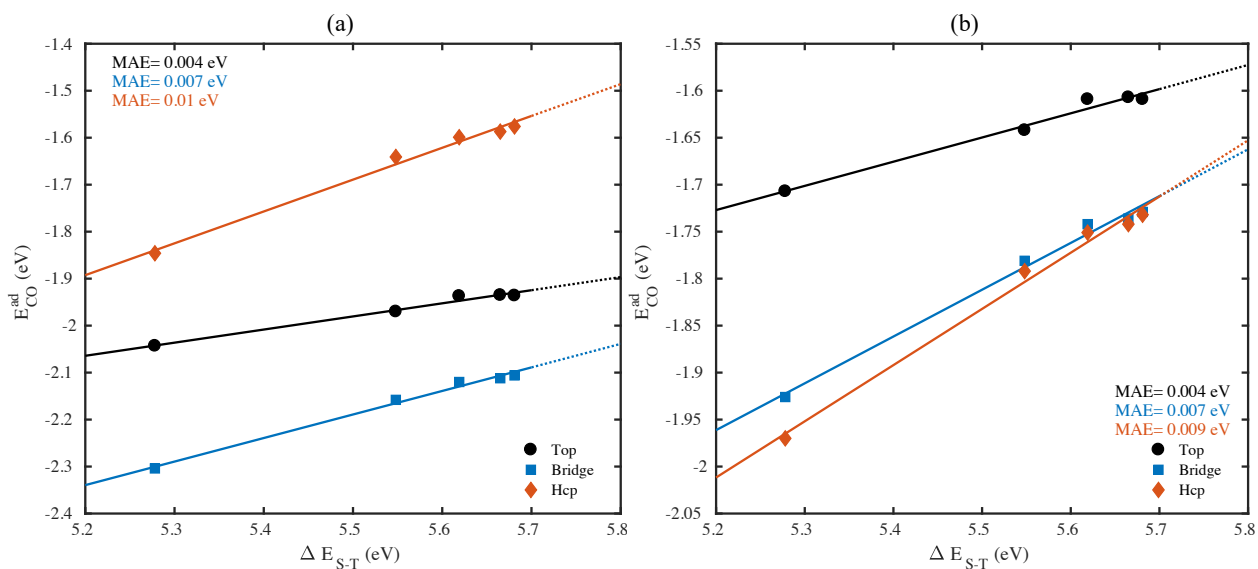


Figure 2.3: Adsorption energy of CO on (a) Pt(100) and (b) Pt(111) ( $\Delta E_{CO}^{ad}$ ) calculated for ML=0.25 plotted against the singlet-triplet excitation energy  $\Delta E_{S-T}$  for the various pseudopotentials mentioned in the table 2.1

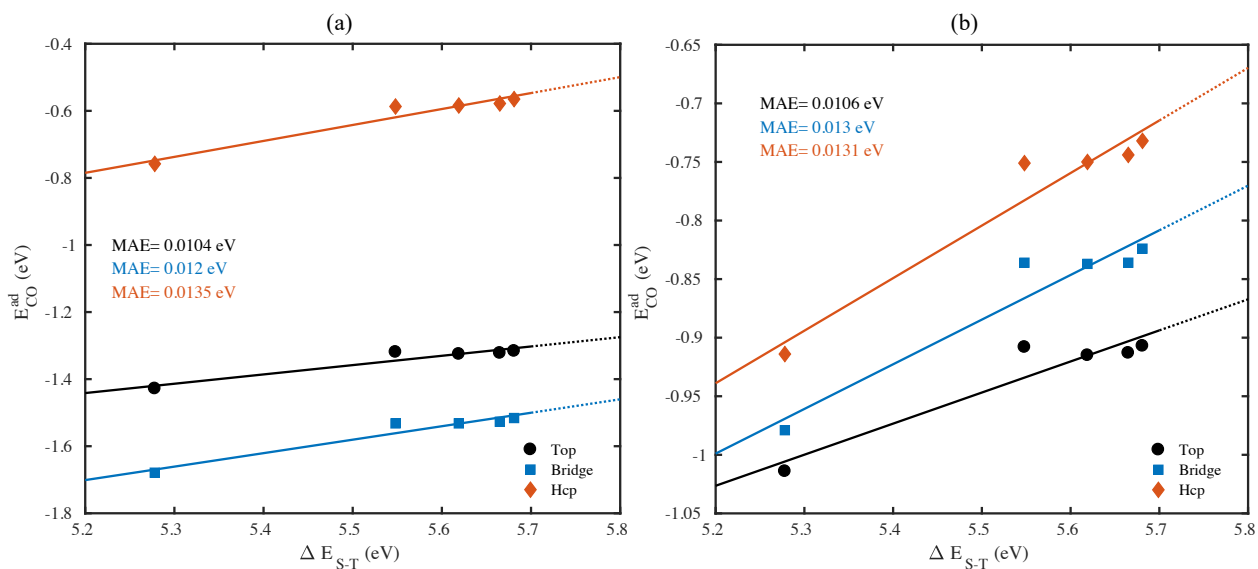


Figure 2.4: Adsorption energy of CO on (a) Pt(100) and (b) Pt(111) ( $\Delta E_{CO}^{ad}$ ) calculated for ML=1.00 plotted against the singlet-triplet excitation energy  $\Delta E_{S-T}$  for the various pseudopotentials mentioned in the table 2.2

### 2.2.1.3 Surface Stability

To create the surface stability diagram, we systematically select structures manually inspired by an extensive literature review of the available experimental data including hypothetical structures, or proposed variants. Using a number of surface science studies including LEED, STM, EELS, RAIRS, XPS and TPD results we generate a sequence of ordered structures with increasing CO coverage. The symmetry of configurations at low coverage also helps sample various structures manually. For Pt(111) we use a number of different unit cells including p(2x2), p(3x3), p(4x4), p(5x5),  $(\sqrt{3} \times \sqrt{3})R30^\circ$ ,  $(\sqrt{7} \times \sqrt{7})R19.1^\circ$ ,  $(2\sqrt{3} \times 2\sqrt{3})R30^\circ$ ,  $(\sqrt{13} \times \sqrt{13})R14^\circ$ ,  $(\sqrt{19} \times \sqrt{19})R23.4^\circ$ ,  $(\sqrt{21} \times \sqrt{21})R10.8^\circ$ ,  $(3\sqrt{3} \times 3\sqrt{3})R30^\circ$ , c(4x2),  $(\sqrt{3} \times 3)\text{rect}$ , c( $\sqrt{3} \times 5$ )rect, c( $\sqrt{3} \times 7$ )rect with CO adsorbed on multiple of symmetric (top, bridge, fcc and hcp) and quasi-symmetric sites. Since at high coverage, STM images show formation of rotated hexagonal CO layers on the Pt(111) surface, we put a special attention to methodically generate a family of such “Moiré pattern” adsorption structures..<sup>141</sup> For Pt(100), at low coverages ( $\theta \leq 0.67$ ), we utilize known experimental results to explore adsorption of CO on various unit cells including c(2x2), c(3x3), c( $2\sqrt{2} \times \sqrt{2}$ )R45°, c( $3\sqrt{2} \times \sqrt{2}$ )R45°, c( $5\sqrt{2} \times \sqrt{2}$ )R45°. At higher coverage ( $\theta \geq 0.75$ ), we show later that CO arranges on an elongated c(nx2) unit cell which helps us explore systematically a number of different coverages on c(nx2) unit cell with n=4,5,6,7,8,9,10.

The Gibbs free energy for gas-phase CO and for adsorbed CO on the surface is obtained from the DFT energies with ZPE and entropy corrections determined from frequency calculations performed for all the considered structures using the Harmonic Oscillator approximation. By displacing the atoms of adsorbate in each direction by a small positive and negative displacement, we determine six frequencies per CO which include the typical CO stretch frequency and five low-frequency models associated with the Pt-C stretching, frustrated rotation, and translation. Low-frequency modes have a large effect on the entropy, hence we use Truhlar approximation by defining a cutoff frequency of 100 cm<sup>-1</sup> such that all the

frequencies below the cut-off are uniformly shifted up to the cut-off value before entropy calculation. The configurational entropy does not affect the results for temperatures below 1000 K, hence has been ignored in this analysis. All the reported values of adsorption energies have been corrected using the respective calculated zero-point energies. The details of atomistic thermodynamics approach used has been included in the Appendix section A.2.

## **2.2.2 Experimental Details**

### **2.2.2.1 Sample Preparation**

Sample preparation was performed in a high pressure scanning tunneling microscope (HP-STM) system which consists of a HP-STM chamber and sample preparation chamber equipped with a sputter ion gun, mass spectrometer and electron beam heater. The Pt(100) single crystal (9mm diameter and 1 mm thickness) was purchased from MaTeck GmbH. Sample cleaning procedure consists of Ar<sup>+</sup> sputtering ( $4 \times 10^{-4}$  Pa Ar at 1000 eV and 10 mA of emission current) at room temperature for 15 minutes, annealing at 800K under O<sub>2</sub> atmosphere of  $2.7 \times 10^{-6}$  Pa, and annealing at 1200K in UHV for 5 minutes. This procedure was repeated for 5 to 10 cycles. In the last cycle, an additional reduction step at 800K in  $2.7 \times 10^{-6}$  Pa H<sub>2</sub> was performed. The sample cleanness was checked by STM.

### **2.2.2.2 High-Pressure Scanning Tunneling Microscope (HP-STM)**

Surface structure of Pt(100) under UHV and CO environment (at different pressures) was studied using a HP-STM system. Details information about this system can be found in the literature.<sup>162</sup> In short, the sample was placed inside the HP-STM cell (approximately 15mL in volume) with the cell door remained open for surface checking under UHV environment. For in-situ experiment, the HP-STM cell door was closed and CO gas was flown through the cell and over the sample during STM image acquisition. The sample could be heated simultaneously by an IR laser (810 nm) irradiation on the back of the sample. The sample

temperature was monitored using a K-type thermocouple spot-welded onto the back of the sample.

## 2.3 Results and Discussion

### 2.3.1 CO adsorption energy correction scheme

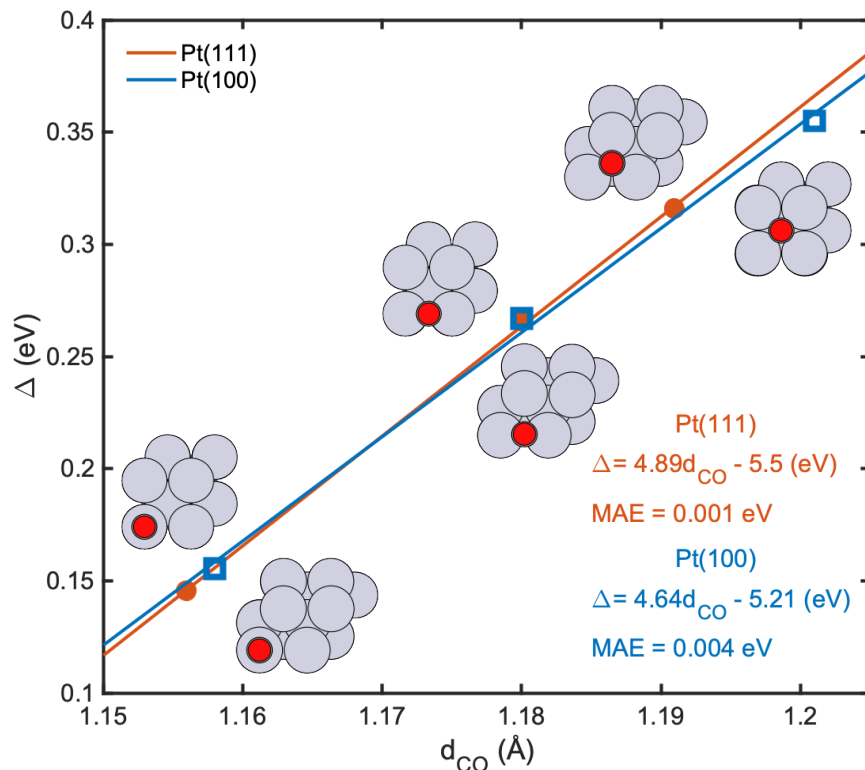


Figure 2.5: Correction in CO adsorption energy ( $\Delta$ ) plotted against the adsorbed CO bond distance ( $d_{CO}$ ) for various sites (top, bridge and hollow/hcp) for Pt(100) and Pt(111). The corrections are measured by extrapolating the dependence of the adsorption energy ( $E_{CO}^{ad}$ ) on the CO singlet-triplet excitation energy ( $\Delta E_{S-T}$ ) for the various sites on (100) and (111) surfaces of Pt to the coupled cluster and CI calculated value for  $\Delta E_{S-T}$ . CO coverage is 0.25 ML. The red dots ( $\bullet$ ) and the red line represent the data and the correction as a function of CO bond distance for Pt(111) which is given as  $\Delta = 5.13 d_{CO} - 5.83$  where  $d_{CO}$  is in Å and  $\Delta$  in eV. Similarly, the blue squares ( $\square$ ) represent the correction for the Pt(100) surface and can be expressed as  $\Delta = 4.8 d_{CO} - 5.44$ . Both the fits have a mean absolute error (MAE) of smaller than 4 meV per CO. The structures (on Pt(111) and Pt(100)) for which the corresponding correction is calculated are shown.

Fig. 2.5 shows the calculated correction for the CO adsorption energy on Pt(111) and Pt(100) for the top, bridge, and hollow site, at a coverage of 0.25 ML. This correction scales with a very small error to the bond length of the adsorbed CO (MAE equal or smaller than 4 meV). The difference between the correction developed using the two coverages (0.25 and 1 ML) is small (Fig. A.1) and hence we use the relations developed for  $\theta = 0.25$  ML for all our calculations, irrespective of the coverage. Selecting the relation at 1ML coverage does not change the results presented here.

From previous studies, it has been shown that both  $5\sigma$ -metal d and  $2\pi^*$ -metal d interactions are bonding and the donation from  $5\sigma$  orbital is dominant for CO adsorbed on the top site. In contrast, the back-donation to the  $2\pi^*$  is dominant for the hollow sites.<sup>144,155,163,164</sup> Accordingly the inaccurate DFT-GGA  $\Delta E_{S-T}$  (or the incorrect placement of  $2\pi^*$  orbital) will require the smallest correction for the top site, followed by the bridge and other poly-coordinated sites (threefold hcp/fcc site for Pt(111) and fourfold hollow site for Pt(100)). This explains the trend we see in the Fig. 2.5, where the correction required increases with C-O bond distance which is lowest for top site and highest for hcp/hollow site. Another observation is that within the range of C-O bond distance plotted in Fig. 2.5 (1.15-1.25 Å), the correction calculated at a given value of  $d_{CO}$  is fairly constant between Pt(100) and Pt(111) with a max difference of 0.015 eV between the two surfaces. This suggests that we can also develop a general correction scheme that is universal across different facets of Pt which is slightly more approximate but simpler to use. Nevertheless, in the current work, we proceed with using the respective corrections for Pt(111) and Pt(100). There also exists a scaling relationship between CO vibrational stretch frequency and CO bond distance which can be used to develop a scaling between the correction and the frequency. These scaling relationships have been shown in the in Fig. A.2 and A.3 for Pt(111) and Pt(100) respectively. Table 2.3 shows a comparison of the CO adsorption energies obtained experimentally using single crystal adsorption calorimetry (SCAC) and PBE corrected energies. The predicted energies are lowered in absolute value by up to 0.3 eV and brought within 0.15 eV error of

Pt(111) (0.25 ML)				Pt(100) (0.25 ML)			
	PBE	Corr.	Expt.		PBE	Corr.	Expt.
Top	-1.58	-1.42	-1.27 ± 0.13 <sup>145,165</sup>	Top	-1.86	-1.70	-1.57 ± 0.1 <sup>132</sup>
Bridge	-1.74	-1.46	-	Bridge	-2.07	-1.80	-
FCC 3-fold Hollow	-1.77	-1.45	-	4-fold Hollow	-1.60	-1.23	-

Table 2.3: CO adsorption energies (in eV, including the ZPE correction) on Pt(111) and Pt(100) for top, bridge, and hollow adsorption sites as predicted by the PBE exchange-correlation functional, after applying the correction to the PBE energies (Corr.) and experimentally obtained value (Expt.).

the experimental values. On Pt(111) after correction, the adsorption energies of the top, bridge, and hollow sites are very similar. On Pt(100), the bridge site remains 0.1 eV more stable than the top site, and the 4-fold hollow site is significantly less stable (by 0.57 eV). We will discuss the site’s dependence on energy again below.

### 2.3.2 Pt(111) surface stability

In experimental conditions of heterogeneous catalysis, the structure of the catalytic interface is far from that in vacuum.<sup>166</sup> Thus to understand the adsorption landscape, we determine the (T, P) surface stability diagram which covers the surface phases from Ultra High Vacuum and low temperatures to realistic catalytic conditions. Such a thermodynamics-based approach in conjunction with ab-initio calculations has been successfully utilized to study Pd hydrogenation catalysts,<sup>167</sup> model RuO<sub>2</sub> structure in O<sub>2</sub> and CO environment,<sup>168</sup> oxygen adsorption on Ag(111),<sup>169</sup> CO and O<sub>2</sub> induced reconstruction in Pd/Ag(111) surface alloy<sup>170</sup> etc. This method involves comparing the surface stability for systems with a varying number of adsorbates. This is achieved by either comparing the unit surface energy or adsorption energy per unit area for the systems. In this work, we use the adsorption energy per unit area since we are more interested in the CO binding energies rather than energies for the overall formation of these surfaces. Since the exact procedure used is similar to that in previous

works, we don't discuss it here again but include the complete analysis in the section A.2.

Fig. 2.6 depicts the thermodynamically most stable state of CO on the Pt(111) surface (lowest adsorption Gibbs energy per unit area) as a function of operating temperature and pressure, as predicted after applying the aforementioned correction in the DFT, calculated adsorption energies. In total, 61 potential structures were generated (including the bare Pt(111) surface), spanning a coverage between 0 and 1 ML (Table A.1). We put special attention to systematically generating, among others, all CO adsorption configurations resulting from the matching between an arbitrary (rotated) supercell of Pt(111) and another (rotated) supercell of a hexagonal CO layer, hence generating a family of ‘‘Moiré pattern’’ adsorption structures. Among these 61 structures, 6 are the most stable ones in a region of the (T,P) diagram of Fig. 2.6 and are also presented in table 2.4. Some structures are very

ID	Structure	Coverage	$\Delta E_{CO}^{avg}$ (eV)	$\Delta G_{CO}/A$ (eV/Å <sup>2</sup> )
I	Bare Pt(111) surface	$\theta = 0.00$	-	
II	$(\sqrt{3} \times \sqrt{3})R30^\circ$ -1CO (T)	$\theta = 0.33$	-1.50	-5.03e-02
II-a	$(\sqrt{21} \times \sqrt{21})R10.8^\circ$ -7CO	$\theta = 0.33$	-1.43	-4.64e-02
III	$c(4 \times 2)$ -2CO (2T-2B)	$\theta = 0.50$	-1.39	-6.67e-02
III-a	$(4 \times 2)$ -2CO (3T-1B)	$\theta = 0.50$	-1.34	-6.32e-02
IV	$(2\sqrt{3} \times 2\sqrt{3})R30.0^\circ$ -7CO (3T-3B-1H )	$\theta = 0.583$	-1.34	-7.16e-02
IV-a	$(2\sqrt{3} \times 2\sqrt{3})R30.0^\circ$ -7CO (4T-2B-1H )	$\theta = 0.583$	-1.31	-7.42e-02
IV-b	$(\sqrt{13} \times \sqrt{13})R14.0^\circ$ -7CO	$\theta = 0.54$	-1.36	-7.00e-02
IV-c	$(\sqrt{7} \times \sqrt{7})R19.1^\circ$ -4CO	$\theta = 0.571$	-1.34	-7.24e-02
V	$(\sqrt{19} \times \sqrt{19})R23.4^\circ$ -13CO (1)	$\theta = 0.684$	-1.23	-7.53e-01
V-a	$(\sqrt{19} \times \sqrt{19})R23.4^\circ$ -13CO (2)	$\theta = 0.684$	-1.21	-1.39e-01
V-b	$(\sqrt{3} \times 3)$ rect-4CO	$\theta = 0.677$	-1.23	-7.40e-02
V-c	$c(\sqrt{3} \times 7)$ rect-5CO	$\theta = 0.677$	-1.23	-7.40e-02
VI	$p(2 \times 2)$ -3CO	$\theta = 0.750$	-1.16	-7.47e-02

Table 2.4: Stable surface structures observed in Fig. 2.6 (and shown in table 2.5). The table outlines the types of unit cells, the CO coverage, the average adsorption energy per CO (including  $\Delta ZPE$ ) and the average adsorption Gibbs free energy per CO per unit area of the cell at 300K and 1 atm pressure. Low energy competing metastable structures are also indicated with -a, -b or -c added label

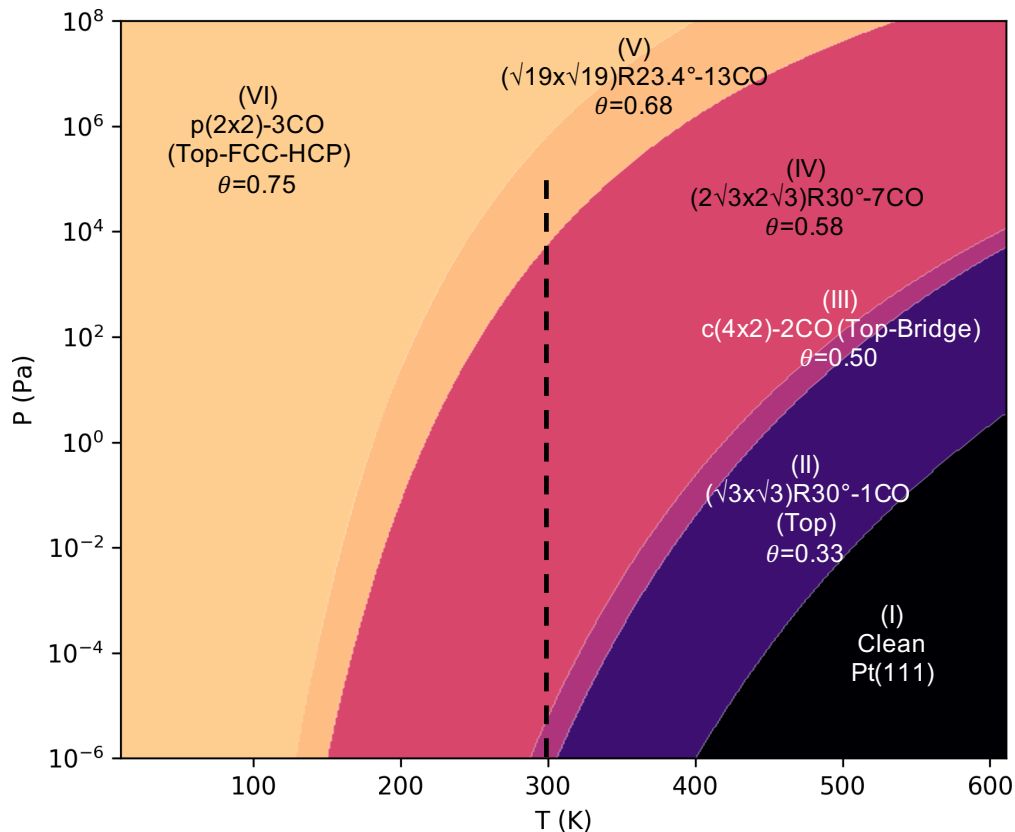


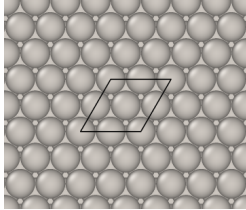
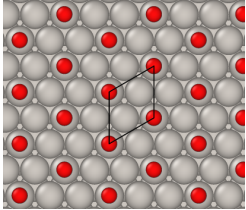
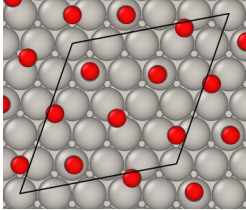
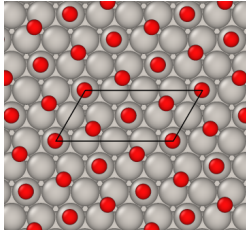
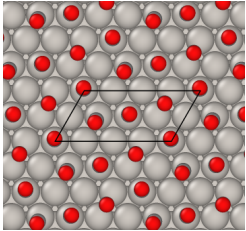
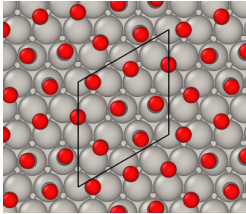
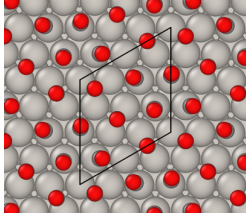
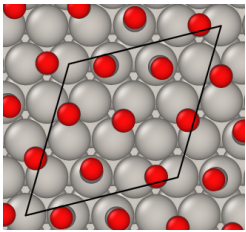
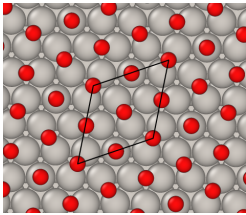
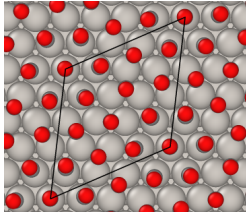
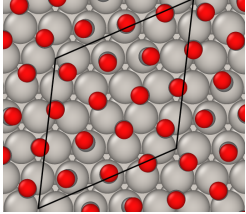
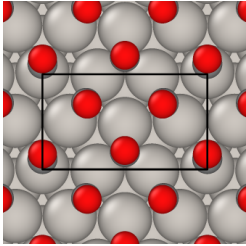
Figure 2.6: Thermodynamic surface stability diagram depicting the most stable CO coverage as a function of temperature and pressure on Pt(111). The various colors represent the calculated most stable surface terminations as labelled in the figure and shown in table 2.4. The black dashed line represents the pressure range studied using STM at 300 K by Longwitz et. al. where the superposition of the quasi-hexagonal (and hexagonal) lattice of CO on the hexagonal lattice of Pt(111) appears in the range of coverage from 0.5 to 0.68 ML.

close in energy to these most stable ones. We also include in table 2.4 the structures whose surface free energy is at most  $5 \text{ meV}/\text{\AA}^2$  less stable than the most stable one found in any point of the diagram. Due to inaccuracies in the calculations, it is indeed not possible to exclude that these structures could be found experimentally stable. As expected, with the increase in the chemical potential of CO ( $\sim -2.7 \text{ eV}$  at 600K and  $10^{-6} \text{ Pa}$ , to  $\sim 0 \text{ eV}$  at 100K and  $10^8 \text{ Pa}$ ), we see that the coverage of CO on Pt(111) increases. An interesting feature of the stable structures emerging from our results is that CO tends to form a quasi-hexagonal structure on the Pt(111) surface at high coverages. These hexagonal CO patterns either match the Pt hexagonal orientation on the (111) surface or are rotated at an angle to create



a so-called family of “Moiré patterns”.

At low-pressure and high-temperature conditions, we find that it is thermodynamically not favorable to have CO adsorbed on the surface (bottom right corner of Fig. 2.6). With increasing pressure and decreasing temperature, CO first arranges on a  $(\sqrt{3} \times \sqrt{3}) R30^\circ$  unit cell with CO only on the top site (structure (II) in Table 2.5). The very small preference in the internal energy for the bridge site (Table 2.4) is counterbalanced by a larger vibrational entropy at the top site, resulting in a most stable top site. This matches the experimentally observed structure first seen in UHV conditions upon dosing CO at a  $1/3$  ML ( $\theta = 0.33$ ) coverage.<sup>120</sup> At 300 K, for  $-1.43 < \Delta\mu_{CO}(T, P) < -1.08$  eV, the  $(\sqrt{21} \times \sqrt{21})R10.8^\circ$ -7CO structure ((II-a) in Table 2.5) is only 4 meV/Å<sup>2</sup> less stable than the  $(\sqrt{3} \times \sqrt{3}) R30^\circ$  structure. On  $(\sqrt{21} \times \sqrt{21})R10.8^\circ$ -7CO unit cell, CO arranges on a combination of top and bridge sites to form a hexagonal pattern. Further, an increase in the pressure and decrease in temperature results in half-monolayer coverage with  $c(4 \times 2)$ -2CO unit cell that consists of an equal population of top and bridge sites (structure (III) in Table 2.5) which agrees with the experimental studies using LEED, EELS, and STM.<sup>121,171-173</sup> At this same coverage at 300 K, for a small range of chemical potential of CO ( $-1.08 < \Delta\mu_{CO}(T, P) < -1.01$  eV), a metastable  $c(4 \times 2)$ -2CO structure with 3 CO on top (and quasi top) site and one CO on bridge site (structure (III-a) in Table 2.5) is found 3.5 meV/Å<sup>2</sup> higher in energy. The CO layer in this stable mixed top-bridge structure is strongly deviating from a hexagonal arrangement. One CO molecule is surrounded by 6 other CO molecules, but the structure is markedly distorted with neighbors at a  $\sqrt{3}$  separation (4.881 Å) and others at  $\sqrt{7}/2$  (3.727 Å). This is the last structure of this type on the diagram of figure 2.6 and all other structures found stable at higher coverage will all be (quasi) hexagonal.

<p>(I) Clean</p> 	<p>(II) <math>(\sqrt{3} \times \sqrt{3})R30^\circ</math>-1CO (T)</p> 	<p>(II-a) <math>(\sqrt{21} \times \sqrt{21})R10.8^\circ</math>-7CO</p> 
<p>(III) <math>c(4 \times 2)</math>-2CO (2T-2B)</p> 	<p>(III-a) <math>c(4 \times 2)</math>-2CO (3T-1B)</p> 	<p>(IV) <math>(2\sqrt{3} \times 2\sqrt{3})R30.0^\circ</math>-7CO (3T-3B-1H)</p> 
<p>(IV-a) <math>(2\sqrt{3} \times 2\sqrt{3})R30.0^\circ</math>-7CO (4T-2B-1H)</p> 	<p>(IV-b) <math>(\sqrt{13} \times \sqrt{13})R14.0^\circ</math>-7CO</p> 	<p>(IV-c) <math>(\sqrt{7} \times \sqrt{7})R19.1^\circ</math>-4CO</p> 
<p>(V) <math>(\sqrt{19} \times \sqrt{19})R23.4^\circ</math>-13CO</p> 	<p>(V-a) <math>(\sqrt{19} \times \sqrt{19})R23.4^\circ</math>-13CO</p> 	<p>(V-b) <math>(\sqrt{3} \times 3)</math>rect-4CO (1T-3B)</p> 

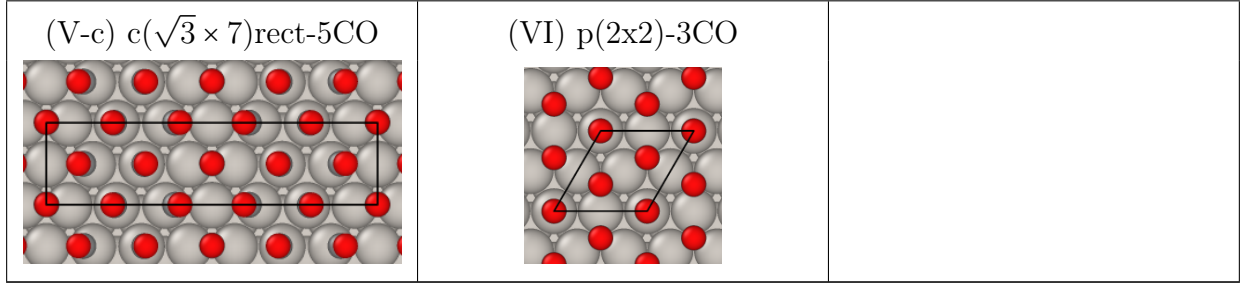


Table 2.5: Low energy structures for CO on Pt(111) for various coverages. This includes stable structures found in the surface stability diagram of Fig. 2 (using the same numeric ID) and low energy metastable structures with surface energy at most  $5 \text{ meV}/\text{\AA}^2$  less stable (indicated with the added -a and -b labels).

The next domain corresponds to structure IV and enters the conditions studied by Longwitz et al.<sup>141</sup> using STM at room temperature. We will hence follow the dotted black line on Fig. 2. Along this line (at 300 K), in the pressure range  $10^{-5}$  to  $6 \times 10^3$  Pa, corresponding to  $-1.01 \lesssim \Delta\mu_{CO}(T, P) \lesssim -0.47$ , we find the  $(2\sqrt{3} \times 2\sqrt{3})R30^\circ\text{-7CO}$  structure as most stable (structure (IV) in table 2.5). On this unit cell CO molecules occupy 3 (quasi) top, 3 bridge, and 1 HCP site forming a quasi-hexagonal arrangement. On the same unit cell, another structure with CO occupying 4 (quasi)top, 2 bridge, and 1 HCP site (structure IV-a in table 2.5) is only  $0.5 \text{ meV}/\text{\AA}^2$  less stable than the former structure, thus quasi-isoenergetic. STM images show in this pressure range a Moiré pattern image corresponding to a superstructure rotated by  $30^\circ$  with respect to the Pt lattice, in good agreement with our theoretical geometry, but with a lattice vector length increasing continuously from 3.2 to 4 times the Pt-Pt distance and CO coverage from 0.56 to 0.65 ML, explained by the incommensurate nature of the imaged structure, instead of constant values of  $3.46 \text{ \AA}$  and 0.58 ML in our case. The CO dense row is rotated by  $10\text{-}15^\circ$  with respect to Pt rows, which agrees well with our  $11.63^\circ$  value. Our computed structure can hence be viewed as a (necessarily) commensurate approximate of an otherwise incommensurate phase evolving with pressure. In this chemical potential range ( $-1.01 \lesssim \Delta\mu_{CO}(T, P) \lesssim -0.47$ ), we also see some slightly less stable structures with coverages between 0.5 ML and 0.58 ML. At  $\theta = 0.54$ , the  $(\sqrt{13} \times \sqrt{13})R14^\circ\text{-7CO}$  structure ((IV-b) in

Table 2.5) is at most  $9.5 \text{ meV}\text{\AA}^2$  less stable, at  $\theta = 0.57$ , the  $(\sqrt{7} \times \sqrt{7})R19.1^\circ\text{-4CO}$  structure ((IV-c) in Table 2.5) is at most  $2 \text{ meV}/\text{\AA}^2$  less stable compared to the predicted structure at 0.58 ML. These low-energy metastable structures have not been seen experimentally, to our knowledge. At a pressure above  $6 \times 10^3 \text{ Pa}$ , the overlayer switches to another higher coverage superposition structure  $(\sqrt{19} \times \sqrt{19})R23.4^\circ\text{-13CO}$  ((V) in Table 2.5), with coverage of  $\theta = 0.684$  (13 CO on a 19 surface Pt atoms), which remains stable until  $6 \times 10^5 \text{ Pa}$ , corresponding to the CO chemical potential interval of  $-0.47 \lesssim \Delta\mu_{\text{CO}}(T, P) \lesssim -0.34$ . The coincidence lattice places the CO adsorbate on various adsorption sites ((quasi)top, bridge, fcc, hcp), but 7 of the 13 CO molecules are on the top or quasi-top sites. This commensurate structure is clearly seen in the STM experiment at RT and  $9.6 \times 10^4 \text{ Pa}$ .<sup>141</sup> The simulated STM image (Fig. A.6) of this structure also compares well with the experiment. As shown earlier by Bocquet et al. in the case of low coverage CO, the bright spot on the image corresponds to CO on the top/quasi-top site and the lesser bright spot corresponds to the bridge/quasi-bridge/hollow site.<sup>143</sup> On the same unit cell, another orientation of CO with 5 of the 13 CO on the top or quasi-top sites ((V-a) in Table 2.5) is observed to be slightly less stable with an energy difference of only  $1.4 \text{ meV}/\text{\AA}^2$ . Starting from the previously described incommensurate Moiré pattern rotated by  $30^\circ$  (at  $\theta = 0.5$ ), the experimental structure undergoes a rotational phase transition at  $\theta \sim 0.6\text{-}0.65 \text{ ML}$ , with a decrease of the superstructure angle with respect to the Pt lattice from  $30^\circ$  to  $23.4^\circ$  and the stabilization of the lattice vector length at 4.36 times the Pt-Pt distance. This is in very good agreement with the calculated structural parameters for the  $(2\sqrt{3} \times 2\sqrt{3})R30^\circ\text{-7CO}$  and  $(\sqrt{19} \times \sqrt{19})R23.4^\circ\text{-13CO}$  coincidence lattices. Hence, for coverage above 0.5 ML, structures calculated to be most stable correspond to the quasi-hexagonal ones seen by the room temperature atmospheric pressure experiments. Let us now compare with the non-hexagonal structures found in UHV and high pressure.

At a coverage of 0.6, three different models have been proposed for a  $c(\sqrt{3} \times 5)\text{rect-3CO}$  unit cell with bridge:top occupation ratio of 2:1 (proposed by Petrova and Yakovkin,<sup>174</sup> shown in Table A.1 ID: 38) and 1:2 (proposed by Persson et al.<sup>140</sup> and Avery et al.<sup>116</sup> having

different CO relative positions, shown in Table A.1 ID: 39,40 respectively). Structures 39 and 40 are found to be quasi-isoenergetic and more stable than 38. Gunasooriya et. al using computational thermodynamics shows that the structures with a bridge:top ratio of 1:2 are stable.<sup>142</sup> However, our calculations show that the  $(\sqrt{19} \times \sqrt{19})R23.4^\circ$ -13CO overlayer is significantly more stable (with an energy difference of  $16.8 \text{ meV}/\text{\AA}^2$  at 300K) compared to the  $c(\sqrt{3} \times 5)$ -3CO structure, and the later is thus not visible in the surface stability diagram. Similarly, at a coverage of 0.67, on the basis of LEED and HREELS studies, Avery<sup>116</sup> suggested the formation of a  $(\sqrt{3} \times 3)$ rect-4CO type unit cell with 1:3 bridge:top site occupation (shown in table 2.5 V-b). On the same unit cell, Biberian and van Hove<sup>123</sup> showed a 3:1 bridge:top occupation using LEED and TPD studies (Table A.1, structure 50). Our results find the Avery structure slightly more stable than that of Biberian and van Hove, in agreement with the calculations by Gunasooriya et. al. On comparing the  $(\sqrt{19} \times \sqrt{19})R23.4^\circ$ -13CO with the  $(\sqrt{3} \times 3)$ rect-4CO structure, we find the former structure is numerically more stable but only by a small energy difference of  $3 \text{ meV}/\text{\AA}^2$ .<sup>142</sup> At a higher coverage of 0.714 ML, Persson et. al showed LEED studies that suggest a  $c(\sqrt{3} \times 7)$ rect-5CO (shown in table 2.5 V-c).<sup>140</sup> Comparing this structure with the  $(\sqrt{19} \times \sqrt{19})R23.4^\circ$ -13CO structure shows that the latter is only  $2.4 \text{ meV}/\text{\AA}^2$  (maximum) more stable. Hence, CO on Pt(111) at high coverage can present two types of structures (hexagonal and non hexagonal) with very similar stability. Our calculation find the hexagonal Moiré pattern type structures to be more stable, but non-hexagonal structures (as  $(\sqrt{3} \times 3)$ rect-4CO and  $c(\sqrt{3} \times 7)$ rect-5CO) come very close in energy, quasi degenerate. This explains the fact that these two types of structures can be found in different experimental conditions.

At low temperatures and very high  $\mu_{CO}(T, P) \gtrsim -0.34$  (at 300K), we find a (2x2) structure with 3 CO molecules on a top, an fcc and an hcp hollow site. Such a structure, has been reported in aqueous acidic medium for Pt(111) using STM along with IRAS<sup>175</sup> and for Pd(111) using computational results as well as RAIRS/HREELS spectra.<sup>176</sup> From all the considered coverages of CO, we find that the adsorption saturates at this coverage of 0.75 ML.

Comparing this structure with  $c(\sqrt{3}\times 7)\text{rect}-5\text{CO}$  (0.714 ML), in the chemical potential range ( $\mu_{\text{CO}}(T, P) \gtrsim -0.34$  (at 300K)) where the former is stable, we find that 0.75 ML structure is only  $4.8 \text{ meV}/\text{\AA}^2$  (maximum) more stable. This once again reinforces the possible presence of quasi degenerate hexagonal and non-hexagonal packing of CO at high coverages on Pt(111). The effect the developed correction scheme has a marked effect on the stability diagram of Pt(111). The stability diagram without the suggested correction has a very different appearance (supporting information fig. A.8). Low coverage phases appear before  $1/3$  ML, and the fcc hollow site is the preferred site over the experimentally observed top site. Without the applied corrections, the  $c(4\times 2)$  0.5 ML coverage domain does not appear, which also disagrees with the experimental findings. At  $\theta = 0.58$ , the  $(2\sqrt{3}\times 2\sqrt{3})R30^\circ-7\text{CO}$  Moiré pattern is predicted but for a much smaller range of temperature and pressure; and the  $(\sqrt{19}\times \sqrt{19})R23.4^\circ-13\text{CO}$  structure at  $\theta = 0.68$  is not seen, at the benefit on a strongly extended domain for the high coverage  $p(2\times 2)$  (0.75 ML), which appears at 300 K for a pressure of CO 8 orders of magnitude lower than when including the correction. Hence application of the correction has a major qualitative effect on the predicted stability diagram and markedly improves the agreement with experimental results. Using the generalized correction,  $\Delta = 4.77d_{\text{CO}} - 5.37 \text{ eV}$ , valid for both Pt(111) and Pt(100), results in the same stability diagram, showing that a single surface independent correction appears sufficient.

### 2.3.3 Pt(100) surface stability

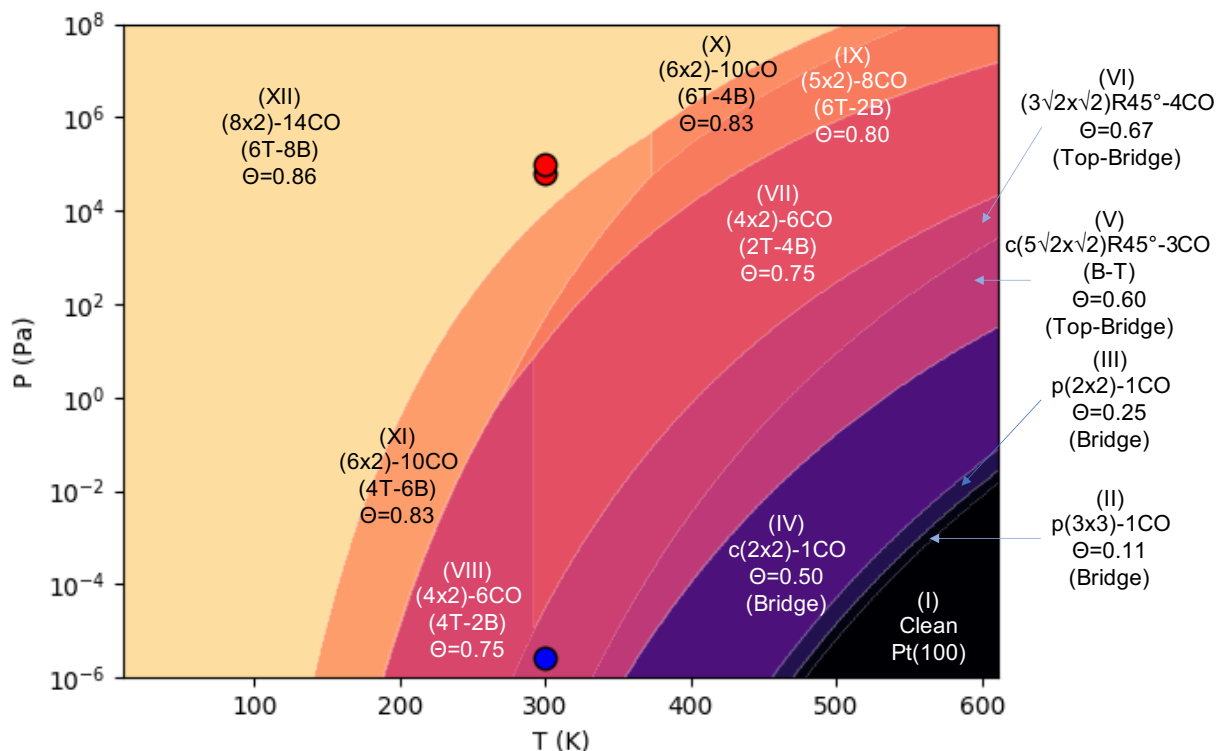


Figure 2.7: Thermodynamic surface stability diagram depicting the most stable CO coverage as a function of the temperature and pressure on Pt(100). Above  $\theta \geq 0.75$ , we see formation of the  $c(n \times 2)$  unit cells with  $(n-2)\text{CO}$  ( $n=4,6,8$ ) which are observed in STM images discussed in the paper. The red and blue dots on the plot represent the different pressures at room temperature where HP-STM images were obtained.

Fig. 2.7 depicts the most thermodynamically stable state of the CO on Pt(100) surface as a function of temperature and CO pressure, while adsorption energies and geometries are provided in table 2.6 and 2.7 respectively. 29 structures have been generated in total (including the bare Pt(100) surface), and 12 appear on the stability diagram (Table A.2). For high temperature and low pressure the clean surface is the most stable (bottom right corner of Fig. 2.7). Increasing the chemical potential  $\Delta\mu_{\text{CO}}(T, P)$  (reducing the temperature or increasing the pressure), we find two narrow stable domains corresponding to low coverage adsorption of CO at 0.11 and 0.25 ML. CO is calculated to adsorb slightly more favorably on

the bridge site. The first wide domain of stability corresponds to the  $c(2 \times 2)$ -1CO structure ( $\theta=0.5$  ML) with both CO on bridge sites. The difference in energy between CO on top vs CO on bridge site (structure IV and IV-a in table 2.6) is again small  $2.5 \text{ meV}/\text{\AA}^2$ . IRAS experiments for low coverage CO adsorption (until 0.5 ML) on Pt(100) at 90 K gives rise to a single band at  $1874 \text{ cm}^{-1}$ , assigned to bridge bonded CO, in good agreement with the calculated frequency of  $1863 \text{ cm}^{-1}$ .<sup>135</sup> A band at  $2075 \text{ cm}^{-1}$ , assigned to top site CO, only appears at higher exposure. Low coverage adsorption at 300 K gives rise to two bands, one at  $2067 \text{ cm}^{-1}$ , for top site, and another at  $1870 \text{ cm}^{-1}$ , for bridge-site CO. From these experiments, Martin et al. concluded that the ratio of bridge to linear site occupancy at low coverages is temperature-dependent with a favored  $c(2 \times 2)$  (or equivalently  $(\sqrt{2} \times \sqrt{2})R45^\circ$  0.5 ML structure with bridge sites at low temperature, and a superposition of bridge site and top sites domains at high temperature.<sup>135</sup> This agrees with a slightly more stable energy for bridge site at low coverage. For this 0.5 ML coverage, a  $(2\sqrt{2} \times \sqrt{2})$  unit cell can provide a different arrangement of bridge sites which is almost degenerate (IVb in table 2.7). A  $p(2 \times 2)$ -2CO unit cell with equal population of top and bridge site (Table A.2 structure 11) is also compared with the symmetric  $c(2 \times 2)$ -1CO structures, and the former structure is found only  $4 \text{ meV}/\text{\AA}^2$  less stable.

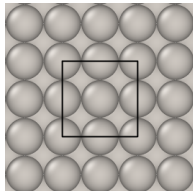
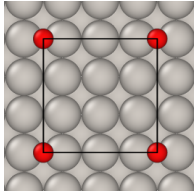
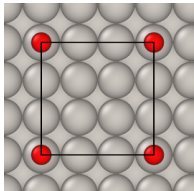
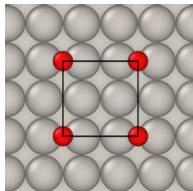
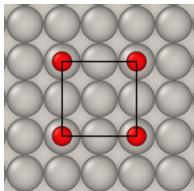
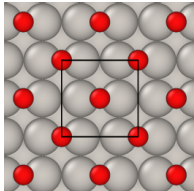
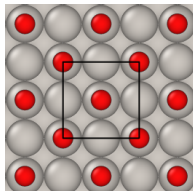
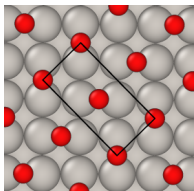
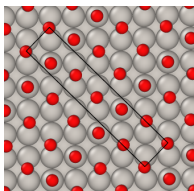
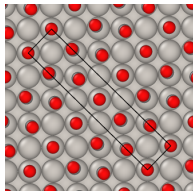
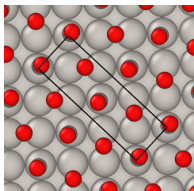
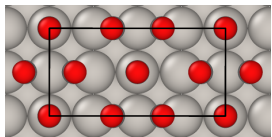
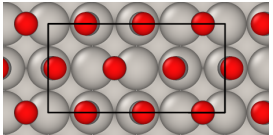
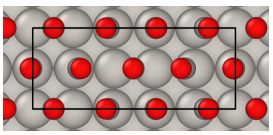
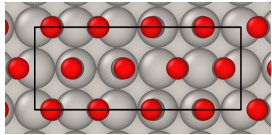
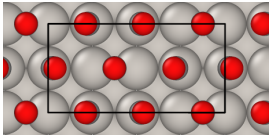
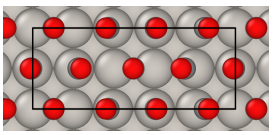
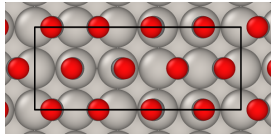
The next stable surface on the diagram (Figure 2.7) we find is the  $c(5\sqrt{2} \times \sqrt{2})R45^\circ$ -3CO unit cell with  $\theta=0.6$  ML. On this unit cell, we compare two different CO adsorption: (i) 4 CO on bridge site and 2 on Top and (ii) all 6 CO on the top site ((V) and (V-a) in Table 2.7). When compared at 300 K, the former structure is only  $6 \text{ meV}/\text{\AA}^2$  more stable than the latter corresponding to an overall average adsorption energy difference on  $0.07 \text{ eV}/\text{CO}$ . STM images and LEED analysis confirm the formation of this  $c(5\sqrt{2} \times \sqrt{2})R45^\circ$ -3CO unit cell with a 2:1 bridge to top ratio of CO occupation.<sup>134,135</sup> On increasing the chemical potential further, CO coverage increases to 0.67 ML on a  $(3\sqrt{2} \times \sqrt{2})R45^\circ$  unit cell with equal ratio of CO on bridge and top sites. This agrees with the experimental analysis from LEED.<sup>135,177</sup> For  $\theta \geq 0.75$ , a specific structural pattern was seen for the formation of a dense layer of CO



on Pt(100): the registry of a deformed quasi hexagonal CO layer on the Pt(100) surface. We observed the formation of elongated  $(n \times 2)$  unit cells with  $[(n \times 2) - 2]$  CO adsorbed on a combination of top, quasi-top and bridge sites in Fig. 2.8. Some structures are centered ( $c(n \times 2)$ ) but for simplicity in the presentation, we will call all of them  $(n \times 2)$ . At  $\theta = 0.75$  a  $(4 \times 2)$ -6CO unit cell with 6 CO is observed to be stable. Two different configurations of CO on the surface are observed - (i) 2 CO on top, 4 CO on quasi-bridge site (ii) 4 CO on quasi-top, 2 CO on bridge site (structures VII and VIII shown in table 2.7). The former is stable at low pressures below 300 K and the later is stable at higher pressures above 300 K. Such an arrangement of CO molecules on the surface results from a compromise between the CO-surface interaction and the repulsive lateral interactions between the CO molecules. It can be seen that any two CO molecules on the short direction of the unit cell are on different sites (bridge or top), which allows for a reduced repulsion of the adsorbates. In addition, this over-layer CO structure was confirmed by in-situ HP-STM result as seen in Fig. 2.8(a). Gaseous CO was introduced into the HP-STM cell and maintained at  $2.7 \times 10^{-6}$  Pa ( $2.7 \times 10^{-8}$  mbar) during image acquisition. At this condition, STM image of Pt(100) shows formation of a domain of  $(4 \times 2)$ -6CO over-layer structure, in conditions which are at the border of the calculated region of the phase diagram (red dot in Fig. 2.7). Red circles in Fig. 2.8(a) indicate the location of adsorbed CO molecules. The structure present some imperfect order but the assignment is supported by the average CO-CO distance of the CO over-layer (experimental value 0.328 nm, model value 0.338 nm) (Fig. 2.8(a) and model VII of table 2.7).

ID	Unit Cell	Coverage	$\Delta E_{CO}^{avg}$ (eV)	$\Delta G_{CO}/A$ (eV/Å <sup>2</sup> )
I	Bare Pt(100) surface	$\theta = 0.00$	-	-
II	p(3×3)-1CO (B)	$\theta = 0.11$	-1.82	-0.019
II-a	p(3×3)-1CO (T)	$\theta = 0.11$	-1.71	-0.018
III	p(2×2)-1CO (B)	$\theta = 0.25$	-1.80	-0.042
III-a	p(2×2)-1CO (T)	$\theta = 0.25$	-1.70	-0.039
IV	c(2×2)-1CO (B)	$\theta = 0.50$	-1.76	-0.081
IV-a	c(2×2)-1CO (T)	$\theta = 0.50$	-1.71	-0.078
IV-b	(2√2 × √2)R45°-2CO (B)	$\theta = 0.50$	-1.75	-0.081
V	c(5√2 × √2)R45°-3CO (B-T)	$\theta = 0.60$	-1.68	-0.092
V-a	c(5√2 × √2)R45°-3CO (T)	$\theta = 0.60$	-1.61	-0.086
VI	(3√2 × √2)R45°-4CO	$\theta = 0.67$	-1.64	-0.098
VII	(4×2)-6CO (2T-4B)	$\theta = 0.75$	-1.58	-0.104
VIII	(4×2)-6CO (4T-2B)	$\theta = 0.75$	-1.57	-0.104
IX	(5×2)-8CO (6T-2B)	$\theta = 0.8$	-1.52	-0.106
IX-a	(5×2)-8CO (4T-4B)	$\theta = 0.8$	-1.51	-0.105
IX-b	(5×2)-8CO (2T-6B)	$\theta = 0.8$	-1.50	-0.103
X	(6×2)-10CO (6T-4B)	$\theta = 0.83$	-1.49	-0.106
XI	(6×2)-10CO (4T-6B)	$\theta = 0.83$	-1.48	-0.106
XII	(8×2)-14CO (6T-8B)	$\theta = 0.875$	-1.44	-0.107
XII-a	(8×2)-14CO (8T-6B)	$\theta = 0.875$	-1.44	-0.106

Table 2.6: Stable surface structures observed in Fig. 2.7 (and shown in table 2.7). The table outlines the types of unit cells, the CO coverage, the average adsorption energy per CO (including  $\Delta ZPE$ ) and the average adsorption Gibbs free energy per CO per unit area of the cell at 300K and 1 atm pressure. Low energy metastable structures are also (indicated with -a or -b added label).

(I) Clean Pt(100) 	(II) p(3x3)-1CO (B) 	(II-a) p(3x3)-1CO (T) 
(III) p(2x2)-1CO (B) 	(III-a) p(2x2)-1CO (T) 	(IV) c(2x2)-1CO (B) 
(IV-a) c(2x2)-1CO (T) 	(IV-b) $(2\sqrt{2} \times \sqrt{2})R45^\circ$ -2CO 	(V) $c(5\sqrt{2} \times \sqrt{2})R45^\circ$ -3CO (B-T) 
(V-a) $c(5\sqrt{2} \times \sqrt{2})R45^\circ$ -3CO (T) 	(VI) $(3\sqrt{2} \times \sqrt{2})R45^\circ$ -4CO 	(VII) (4x2)-6CO (2T-4B) 
(VIII) (4x2)-6CO (4T-2B) 	(IX) (5x2)-8CO (6T-2B) 	(IX-a) (5x2)-8CO (4T-4B) 
(IX-b) (5x2)-8CO (2T-6B) 	(X) (6x2)-10CO (6T-4B) 	(XI) (6x2)-10CO (4T-6B) 

(XII) (8x2)-14CO (8T-6B)	(XII-a) (8x2)-14CO (6T-8B)	

Table 2.7: Low energy structures for CO on Pt(100) for various coverages. This includes stable structures in the surface stability diagram of Fig. 2.6 (using the same numeric ID) and low energy metastable structures with surface energy at most  $5 \text{ meV}/\text{\AA}^2$  less stable (indicated with the added -a and -b labels)

The next stable configuration of adsorbed CO is found on  $(5 \times 2)$ -8CO with a coverage of 0.8 ML. At this coverage we find three different configurations of CO on the surface that are identical in energy - CO adsorbed on (i) 6T-2B (ii) 4T-4B (iii) 2T-6B, where T represents top and quasi top site and B represents the bridge and quasi-bridge site of adsorption (structures IX, IX-a, IX-b in Table 2.7). When compared at 300K, the Gibbs free energy difference between these structures is less than  $2 \text{ meV}/\text{\AA}^2$ , making them computationally identical. We observe that this structure is only stable at pressures above 1 Pa and temperatures above RT.

With increasing chemical potential, coverage increases and CO molecules arrange in a similar manner on a longer unit cell -  $(6 \times 2)$ -10CO, corresponding to a coverage of 0.83 ML. At this coverage, in a similar way to the  $(4 \times 2)$  unit cell case, we find that two configurations of CO molecules on the surface have similar adsorption energies - (i) 6 CO on top (and quasi-top) + 4 CO on quasi-bridge CO (ii) 4 CO on quasi-top + 6 CO bridge and quasi-bridge (structures X and XI in table 2.7. The former orientation is only stable at high temperatures ( $T > 370 \text{ K}$ ) and high pressures ( $P > 6 \times 10^4 \text{ Pa}$ ). At the quasi-top/quasi-bridge site the adsorbed CO are tilted from the normal z-axis by a  $\pm 5.5^\circ$  angle. Such a behaviour of “fan out” helps

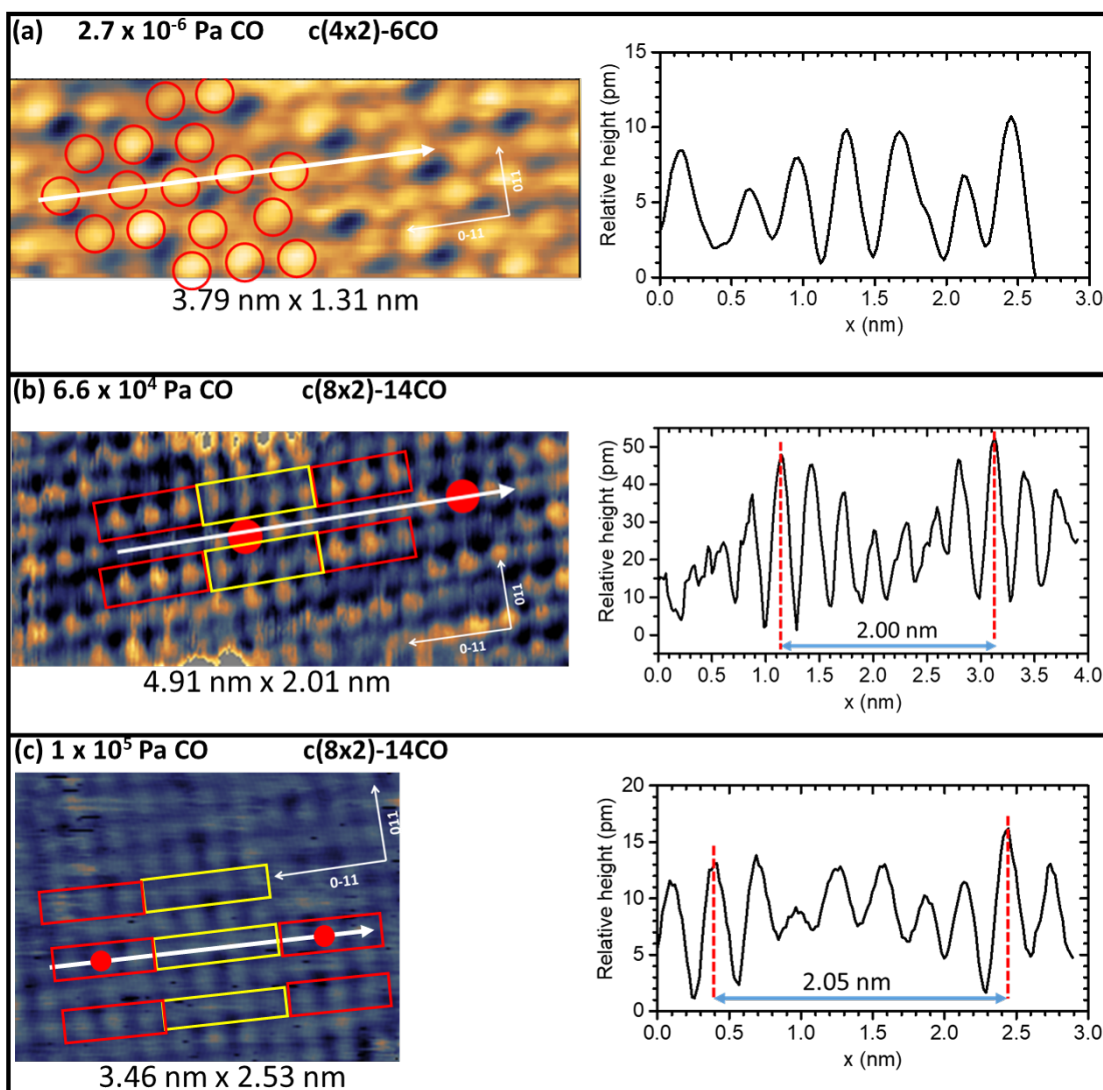


Figure 2.8: Over-layer structure of CO at different pressure on Pt(100) surface observed by in-situ HP-STM at room temperature. (a)  $2.7 \times 10^{-6}$  Pa CO, which indicates formation of  $c(4 \times 2)$ -6CO over-layer corresponding to  $\theta = 0.75$ . Red circles show location of adsorbed CO molecules. (b)  $6.6 \times 10^4$  Pa CO, which indicates formation of  $c(8 \times 2)$ -14CO over-layer corresponding to  $\theta = 0.875$ . (c)  $1 \times 10^5$  Pa CO. In (b) and (c), red and yellow rectangles show locations of quasi-top CO molecules and quasi-bridge CO molecules, respectively. White arrows indicate direction of scan profiles which are shown on the right side. Settings for STM acquisition are: (a) 0.50 nA, 0.60 V; (b) 1.00 nA, 0.60 V; (c) 0.85 nA, 0.90 V.

to incorporate more adsorbate on the surface and similar observation was made previously on 2D nano-clusters on reconstructed hex-Pt(100) surface in CO environments by Tao. et.

al.<sup>61</sup>

Finally we see that the coverage saturates at 0.875 ML where two iso-energy CO configurations, (i) 8 quasi-top, 6 quasi-bridge and (ii) 6 quasi-top, 8 quasi-bridge CO adsorbed on a  $(8 \times 2)$  unit cell are stable (structures XII and XII-a in Table 2.7). The quasi-top adsorbed CO are tilted at an angle of  $\pm 6^\circ$  and the quasi-bridge adsorbed CO are tilted at an angle of  $\pm 5.2^\circ$  with respect to the normal z-axis.

Beyond the already discussed low pressure conditions, a high CO pressure was studied experimentally to confirm the predictions from theory (Fig. 2.8(b) and (c)). Two experiments were performed at rather similar near ambient pressure ( $6.6 \times 10^4$  Pa and  $10^5$  Pa). At  $6.6 \times 10^4$  Pa, they formed a  $(8 \times 2)$ -14CO over-layer structure, in agreement with the computed stability diagram (blue dots in Fig. 2.7). Two groups of bright protrusion in the STM can be identified (red rectangles = 3 higher protrusions, yellow rectangles = 4 lower protrusion) in Fig. 2.8(b) and 2.8(c), indicating the presence of quasi-top and quasi-bridge CO. DFT Simulated STM image of this structure (Fig. A.6) shows brighter contrast of CO on top/quasi-top site compared to CO on bridge/quasi-bridge sites. Therefore, based on the contrast of the experimental STM image (fig. 2.8(b) and 2.8(c)), it can be deduced that configuration (i) (6 quasi-top, 8 quasi-bridge), of the two iso-energetic CO configurations mentioned earlier, is the one being observed experimentally. Interestingly, configuration (ii) (8 quasi-top, 6 quasi-bridge) was not observed in STM images.

On further examination of high coverage ( $\theta \geq 0.75$ ) structures for Pt(100), CO arranges in a skewed hexagonal matrix with average CO-CO distances smaller than that observed on Pt(111). On Pt(111), at  $\theta = 0.75$ , CO arranges on a  $p(2 \times 2)$  unit cell with CO on top, FCC and HCP site creating a perfect hexagonal lattice with C-C distance of 3.25 Å. In comparison, for Pt(100), the average C-C distance for CO on  $(4 \times 2)$ ,  $(6 \times 2)$  and  $(8 \times 2)$  is 3.22 (2.22% smaller), 3.18 (3.4%) and 2.93 (11.02%) respectively. The superimposed distorted hexagonal configuration of CO on Pt(100) reduces the repulsion between adjacent CO molecules and therefore decreases the energy. Hence for a given condition (for example standard condition

at room temperature) the density of chemisorbed CO molecules is larger on Pt(100) (0.11 in CO/Å<sup>2</sup>) than on Pt(111) (0.099 in CO/Å<sup>2</sup>). This is due to the lower Pt-Pt coordination on Pt(100) resulting in a larger CO adsorption energy, that is able to compensate a stronger CO-CO repulsion energy and lead to a larger CO density at equilibrium. It's worth highlighting that using the generalized correction,  $\Delta = 4.77d_{CO} - 5.37$  eV, results in essentially the same stability diagram (Fig. A.5) as using the separately fitted correction terms for Pt(100) surface ( $\Delta = 4.74d_{CO} - 5.34$  eV).

## 2.4 Conclusion

The adsorption of CO on Pt(111) and Pt(100) was studied using an atomistic first-principles thermodynamic model and high-pressure scanning tunneling microscopy. In order to correct the site preference and for the overestimated adsorption energy, we developed an energy correction scheme based on the C-O bond distance. The magnitude of the correction is the smallest for the top site, followed by the bridge and other poly-coordinated sites (threefold hcp/fcc site for Pt(111) and fourfold hollow site for Pt(100)). Using the energy correction scheme, we construct the thermodynamic stability diagram that describes the surface terminations as a function of temperature and pressure. The formation of dense CO layers on Pt(111) and Pt(100) follows two different modes. On Pt(111) (at  $\theta=0.25$  ML) all the adsorption sites (top, bridge, hollow) are rather equivalent in stability. In order to optimize adsorption and minimize repulsion CO molecules organize in a 2D hexagonal pattern and the adsorbate density depends on the pressure. This CO hexagonal pattern is set in registry with the surface by the coincidence of a rotated supercell of Pt(111) with a rotated supercell of the CO hexagonal lattice. From this ideal starting position, CO molecules slightly relax laterally, with small tilts in the vertical direction, and slightly deform the hexagonal pattern. A systematic computational exploration of such hexagonal coincidence structures shows that the  $(2\sqrt{3} \times 2\sqrt{3})R30^\circ$ -7CO at 0.583 ML and the  $(\sqrt{19} \times \sqrt{19})R23.4^\circ$ -13CO at 0.684 ML are

the stable arrangement appearing in the calculated thermodynamic diagram. These calculated structures are in very good agreement with experimental data, as seen for example with the simulated STM image (refer Fig. A.6). Non-hexagonal CO adlayers ( $(\sqrt{3}\times 3)\text{rect-4CO}$  and  $c(\sqrt{3}\times 7)\text{rect-5CO}$  arrangement) however appear as low energy metastable structures, explaining why in UHV at low temperature, these non-hexagonal layers can be observed in place of the Moiré pattern coincidence lattices.

On Pt(100), the bridge and top sites have similar stability, but the hollow site is less stable. The CO molecules hence adopt a 1D coincidence lattice, with  $n-1$  CO molecules placed on a dense row of  $n$  Pt atoms, with an ensemble of top sites molecules followed by an ensemble of bridge site ones. The structures relax with slight off-vertical rotations on the CO molecules, illustrated as a “fan-out” movement. These “fan-out” displacements lead to reduced repulsion between CO molecules on adjacent adsorption sites. These CO rows are staggered in the perpendicular direction, forming elongated  $(n\times 2)$  unit cells. Our STM experiments at ambient CO pressure and room temperature on Pt(100) clearly confirm these theoretical predictions, with the formation of a highly dense  $(8\times 2)\text{-14CO}$  structure (coverage of 0.875 ML). These high-coverage structures of CO provide structural data for studying the catalytic reactivity and restructuring events occurring on these Pt surfaces in reactions involving high CO pressures.



## CHAPTER 3

# High Dimensional Neural Network Potential

### 3.1 Introduction

Machine Learning has influenced many science and engineering fields which includes catalysis and surface science. Machine learning models rely on fitting flexible and often non-linear models that are trained on reference data to reproduce some desired information. With the rapid development of various machine learning techniques, availability of open source software like scikit-learn, TensorFlow, Pytorch etc., and the advancement of computational hardware capable of performing immense calculations substantially at a reduced cost, machine learning has led to a renaissance in how science and “big data” is approached.

Density functional theory (DFT) has been a workhorse of first-principles-based simulation in catalysis and surface science. Techniques like *Ab initio* Molecular Dynamics (AIMD), Grand Canonical Basin Hopping (GCBH), Genetic Algorithm, etc. used to explore the potential energy surface (PES) for a given adsorbate-catalyst system involve computationally expensive DFT simulations. Despite the availability of efficiently implemented DFT simulation codes and fast computers, a large number of interesting problems remain inaccessible by *ab initio* simulations due to the high computational expense. To circumvent this high computational cost, classical physics-based atomic potentials which are mathematical functions that describe the interactions between atoms or molecules are developed. Most empirical potential development starts with a physically motivated functional form and contains some parameters which are fitted to experimental or *ab initio* data. While the physically informed

nature and computational efficiency of these potentials are appealing, they may lack the numerical accuracy required, and they are difficult to systematically improve. To prioritize the overall accuracy in reproducing the known reference data, fitting can be performed using an unbiased and purely mathematical functional form over the physically motivated classical potentials. For such potentials, it is important to verify the transferability and generalization carefully. Multiple mathematical functional forms including splines,<sup>178</sup> Taylor expansions,<sup>179–181</sup> Gaussian based methods<sup>182</sup> and many more have been suggested in the literature. In the last decade, more emphasis has been given to another class of very flexible functions given by artificial neural networks (NNs). In principle, these NN can fit any real-valued function with arbitrary accuracy<sup>183,184</sup>

A neural network is a type of machine learning model that is inspired by the structure and function of the brain. It is composed of layers of interconnected “neurons” which process and transmit information. In a neural network, data flows through the network and is processed by the neurons in each layer. The neurons apply weights to the input data and then apply an activation function to produce an output. The output is then passed on to the next layer, and this process is repeated until the final output is produced. There are many different types of neural networks, including feedforward neural networks, convolutional neural networks, and recurrent neural networks, to name a few. The training on the reference data is done iteratively using different algorithms. In case of NN potentials, the high dimensional function to be fit is the Potential Energy Surface (PES) and the goal is that the NN can create a functional correlation between the atomic configuration and the energy (and forces on the atoms) for a given system.

## 3.2 Feed-forward Neural Networks

Fig. 3.1 shows a schematic architecture of a small NN. It consists of a number of nodes, or neurons, arranged in layers. The node in the output layer provides the function value

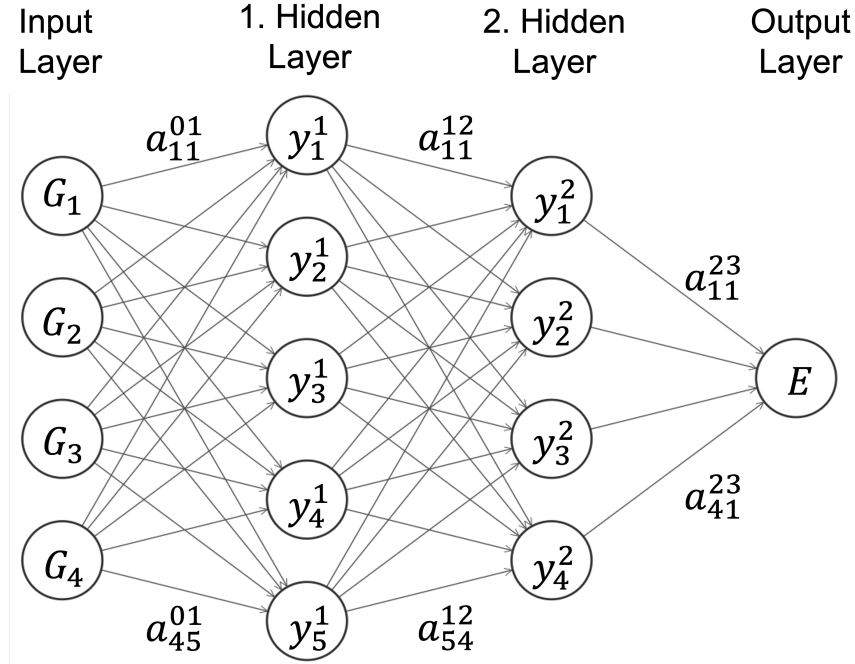


Figure 3.1: Schematic of a small feed-forward neural network. The network is used to establish a relationship between the atomic structure (input layer) and the energy of structures (output layer). Between the input and output layer, the FFNN has 2 hidden layers with 5 and 4 nodes respectively which defines the functional forms of the NN as expressed by the equation 3.2. The fitting parameters (weights of the NN,  $a_{ij}^{kl}$ ) are represented using arrows. For clarity, bias nodes and weights are now shown here.

of the NN, the energy  $E$  (and forces). In a feedforward neural network, data flows in only one direction: from the input layer to the output layer, without looping back. There are no feedback connections, which means that the output of a layer does not affect that layer itself. The input layer consists of nodes that represent the input data. The input layer is defined by some suitable coordinates  $\mathbf{G} = G_i$  that define the atomic positions. The output layer consists of nodes that represent the output data, i.e., energy and forces. Between the input and output layers, there may be one or more hidden layers that consist of nodes that process the data. A larger number of nodes leads to a bulky but more flexible NN. Each node in a layer receives input from the nodes in the previous layer, processes the input using an activation function, and produces an output that is passed to the next layer. The activation function determines whether the node should "fire" and pass on its output or

"not fire" and produce no output. The weights of the connections between the nodes are adjusted during training to optimize the output of the network. The process of adjusting the weights to minimize the error between the predicted output and the actual output is known as back-propagation.

In Fig. 3.1,  $a_{ij}^{kl}$  refers to the weight connecting node  $i$  in layer  $k$  with node  $j$  in layer  $l$ . The input layer corresponds to the layer superscript 0. Additionally, except for the input layer, each node  $i$  in layer  $j$  is connected to a bias node by the bias weight  $b_i^j$  (not shown). The bias node always has value one and the bias weights can be used as an adjustable offset to shift the input of the nodes. The value  $y_i^j$  of node  $i$  in layer  $j$  is then calculated as:

$$y_i^j = f_i^j \left( b_i^j + \sum_k a_{ki}^{j-1,j} \cdot y_k^{j-1} \right) \quad (3.1)$$

In the special case  $j-1 = 0$ , the  $y_k^{j-1}$  correspond to the  $G_k$ . The function  $f_i^j$  is called activation function of the NN. This is a nonlinear function providing the capability to fit arbitrary functions. Without the activation function, the energy would simply reduce to a linear combination of the coordinates. There are multiple activation functions that can be used to develop the NN which includes: hyperbolic tangent, sigmoid, linear, Rectified linear unit (ReLU), Softplus, Gaussian etc. For the output layer, linear activation function ( $f(x) = x$ ) is used. The full analytic form of the feed-forward neural network, shown schematically in Fig. 3.1, is then given by:

$$E = f_1^3 \left( b_1^3 + \sum_{l=1}^4 a_{l1}^{23} \cdot f_l^2 \left( b_l^2 + \sum_{k=1}^5 a_{kl}^{12} \cdot f_k^1 \left( b_k^1 + \sum_{j=1}^4 a_{jk}^{01} \cdot G_j \right) \right) \right). \quad (3.2)$$

To calculate the number of variables in a feed forward neural network, we need to know the number of inputs, the number of hidden layers, the number of neurons in each hidden layer, and the number of outputs. The number of variables in a feedforward neural network is equal to the sum of the following: (1) The number of weights between the input layer and

the first hidden layer: this is equal to the number of inputs times the number of neurons in the first hidden layer (2) The number of weights between each pair of subsequent hidden layers: this is equal to the number of neurons in the current hidden layer times the number of neurons in the next hidden layer (3) The number of weights between the last hidden layer and the output layer: this is equal to the number of neurons in the last hidden layer times the number of outputs. (4) The number of bias terms in the network which is equal to the number of neurons in the network, not including the input layer. For Fig. 3.1 with the feed-forward NN architecture of 4-5-4-1, the total number of variables can be calculated as:  $4 \times 5 + 5 \times 4 + 4 \times 1 + 9 = 53$ . Such Feed Forward NN based potentials have been reported in the literature for small gas phase molecules<sup>185-194</sup> and has also been used to develop PES for interaction of small molecules with (frozen) surfaces.<sup>195-202</sup>

### 3.3 High Dimensional Neural Network Potential

Although feed-forward NN potentials are useful in training low dimensional PES, there are several limitations to this method that do not allow training potential for a high-dimensional PES which involve thousands of degrees of freedom:

- Since each degree of freedom is represented by an input node, the size of the NN increases significantly making the method less efficient.
- The number of input nodes cannot be changed once a NN potential has been fitted. Therefore, in principle for each system size a separate potential would have to be constructed. This is not feasible.
- Exchanging the positions of any two atoms of the same chemical element does not change the structure. Since feed-forward NNs do not use arbitrary order of coordinates, this invariance of the NN energy output is not reflected in this architecture of the NN potential.

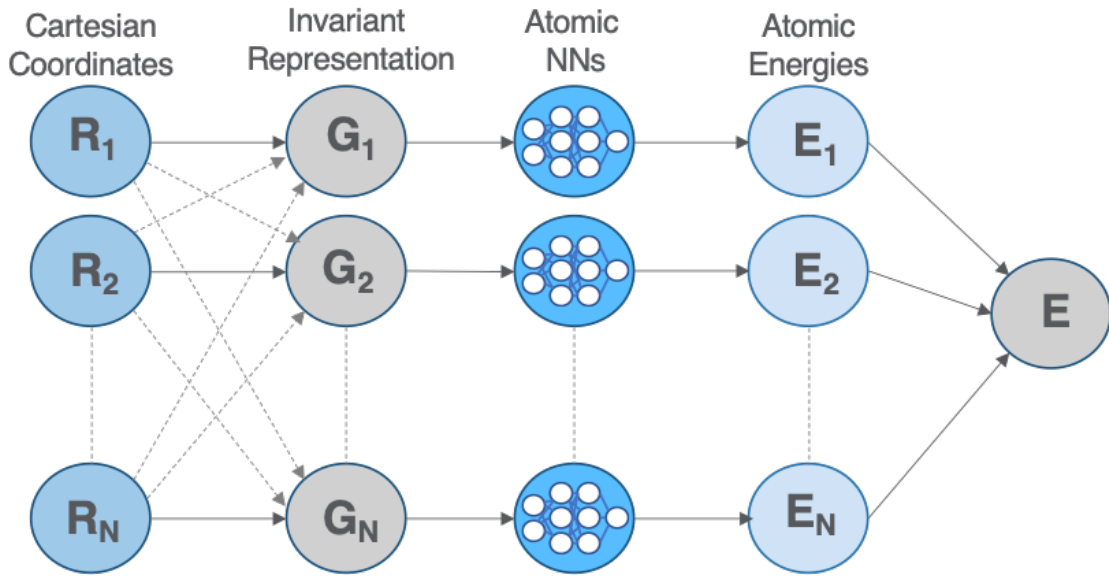


Figure 3.2: Schematic of a High Dimensional Neural Network Potential. Each Cartesian coordinate  $R_i$  is first converted to its invariant form using symmetry functions  $G_i$  which is fed to the atomic neural networks to obtain atomic energy  $E_i$ . The sum of these atomic contributions yields the short-range energy  $E$ .

- All input nodes are connected to the NN by numerically different weight parameters.

Thus, in case of permutations in the input vector a different output is obtained.

J. Behler and M. Parrinello had an elegant solution to solve all these above mentioned problems with the feed-forward NN potentials. They conceptualized construction of a different architecture of the NN such that the NN representing the total energy can be replaced by a set of atomic NNs as shown in Fig. 3.2.<sup>203–205</sup> Each atomic NN then provides the contribution  $E_i$  of an atom to the total energy of the system, such that:

$$E = \sum_i E_i \quad (3.3)$$

### 3.3.1 Symmetry Functions

To solve the structural invariance problem as discussed above, the first step in generating this high dimensional neural network potential is converting the Cartesian coordinates ( $R_i$ ) of atoms in the system to a set of symmetry function values ( $G_i$ ). The symmetry function values of each atom reflect the local environment that determines its energy. As a result, some properties that symmetry functions should follow:

- Two structures with different energies must yield different sets of symmetry function values, while identical local environments must give rise to the same set
- Symmetry function values must be invariant with respect to a rotation or translation of the system.
- The number of symmetry functions must be independent of the coordination of the atom because the coordination number of an atom can change in a MD simulation, while the structure of the atomic NN must not be changed if the NN is to remain applicable generally.

In order to define the energetically relevant local environment a cutoff function  $f_c$  of the interatomic distance  $R_{ij}$ . The cutoff function has the following functional form:

$$f_c(R) = \begin{cases} f(x) & \text{for } R \leq R_c \\ 0 & \text{for } R > R_c \end{cases} \quad (3.4)$$

where  $f(x)$  is defined in Table 3.1 and plotted in Fig. 3.3 and  $R_c$  is the cutoff radius. A cutoff radius ( $R_c$ ) of 6-8 Å is generally used in the literature.

No.	Cutoff Type	f(x)
1	cos	$0.5 \times [\cos(\pi x) + 1]$
2	tanh	$\tanh^3(1 - x)$
3	exp	$\exp(1 - 1/(1 - x^2))$
4	Poly <sub>1</sub>	$(2x - 3)x^2 + 1$
5	Poly <sub>2</sub>	$((15 - 6x)x - 10)x^3 + 1$
6	Poly <sub>3</sub>	$(x(x(20x - 70) + 84) - 35)x^4 + 1$
7	Poly <sub>4</sub>	$(x(x((315 - 70x)x - 540) + 420) - 126)x^5 + 1$

Table 3.1: Cutoff function types used in the construction of symmetry functions

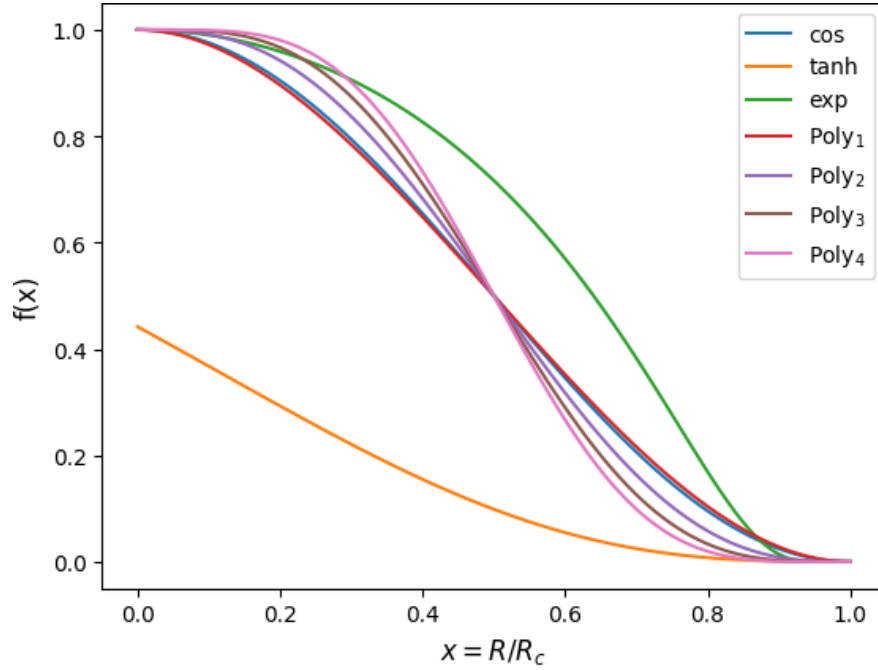


Figure 3.3: Plots showing the functional form of various cutoff functions in Table 3.1

### 3.3.1.1 Radial symmetry functions

Radial symmetry functions are constructed as a sum of Gaussians with the parameters  $\eta$  and  $\mu$ :

$$G^{rad} = G_i^1 = \sum_{j \neq i}^{\text{all}} e^{-\eta(R_{ij} - \mu)^2} f_c(R_{ij}) \quad (3.5)$$



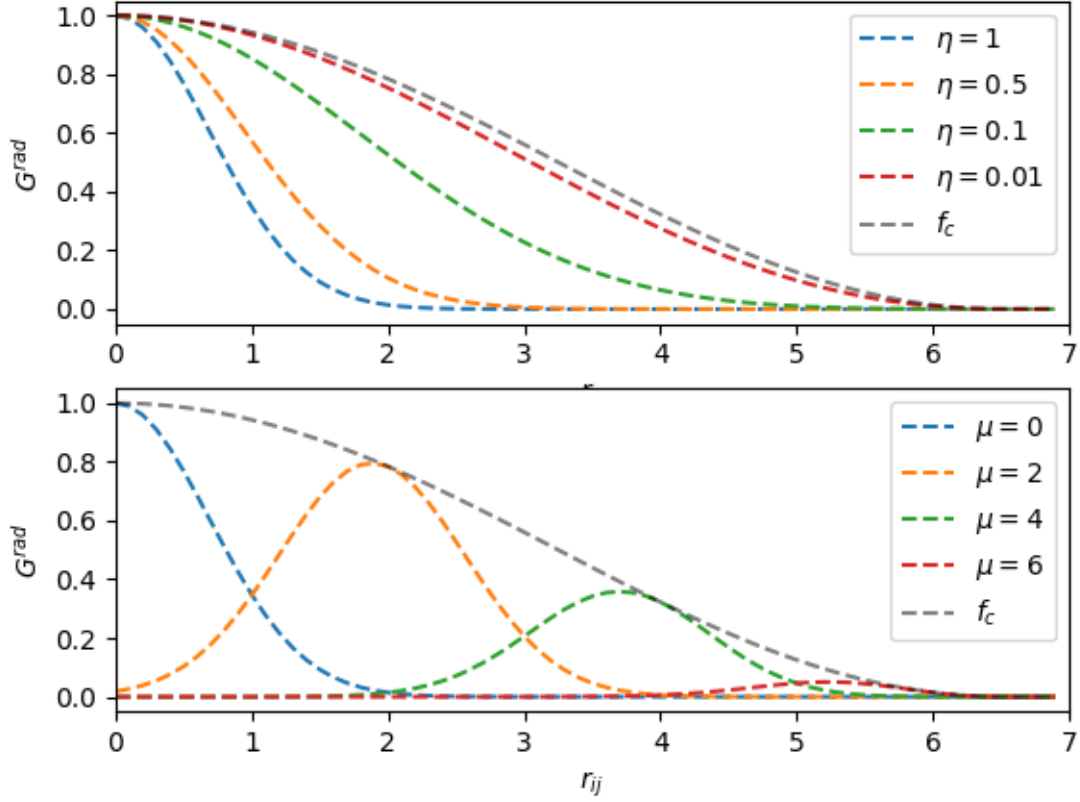


Figure 3.4: Effect of  $\eta$  and  $\mu$  on the radial symmetry function value  $G^{rad}$ .

The summation over all neighbors  $j$  ensures the independence of the coordination number. The effect of the two parameters  $\eta$  and  $\mu$  can be seen in Fig. 3.4

### 3.3.1.2 Angular symmetry functions

Angular terms are constructed for all triplets of atoms by summing the cosine values of the angles  $\theta_{ijk} = \frac{\mathbf{R}_{ij} \cdot \mathbf{R}_{ik}}{R_{ij} \cdot R_{ik}}$  centered at atom  $i$ , with  $\mathbf{R}_{ij} = \mathbf{R}_i - \mathbf{R}_j$ . two types of symmetry functions are proposed in the literature:

$$G_i^4 = 2^{1-\zeta} \sum_{j,k \neq i}^{\text{all}} (1 + \lambda \cos \theta_{ijk})^\zeta \cdot e^{-\eta(R_{ij}^2 + R_{ik}^2 + R_{jk}^2)} \cdot f_c(R_{ij}) \cdot f_c(R_{ik}) \cdot f_c(R_{jk}) \quad (3.6)$$

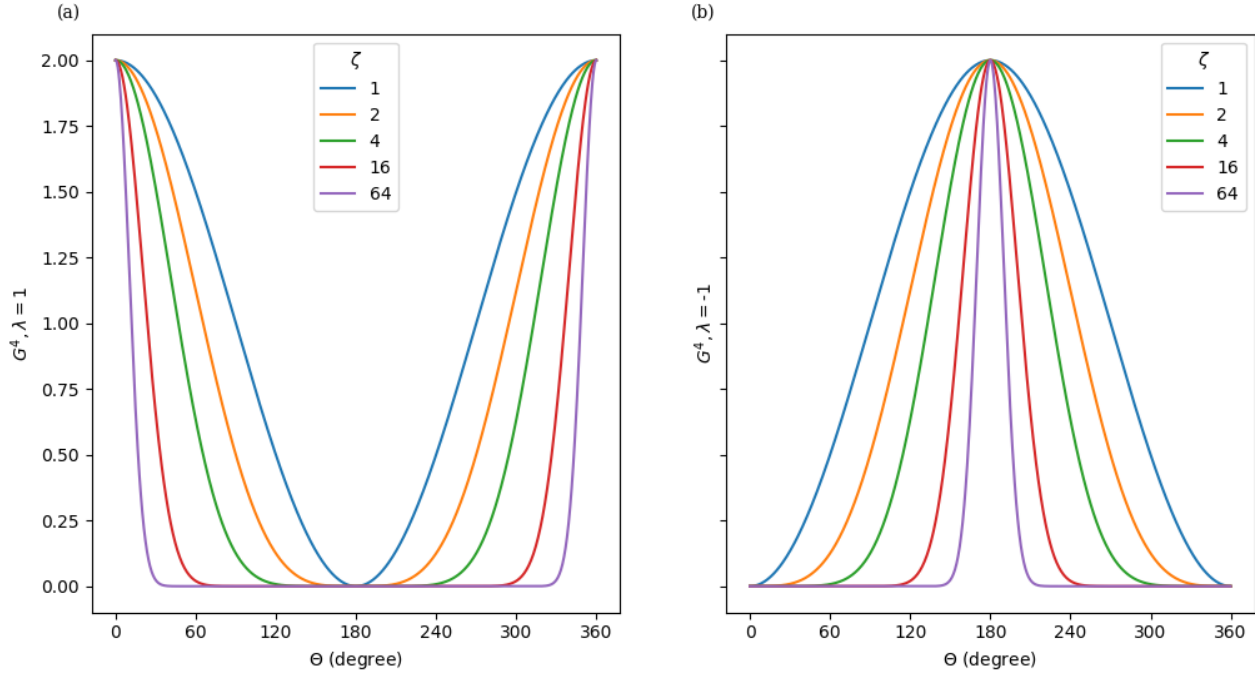


Figure 3.5: Angular contributions of the angular symmetry function  $G^4$  (similar effect on  $G^5$ . The plot corresponds to a example triatomic system, for a many-atoms system, a summation over the angular terms is used.

$$G_i^5 = 2^{1-\zeta} \sum_{j,k \neq i}^{\text{all}} (1 + \lambda \cos \theta_{ijk})^\zeta \cdot e^{-\eta(R_{ij}^2 + R_{ik}^2)} f_c(R_{ij}) \cdot f_c(R_{ik}) \quad (3.7)$$

with the parameters  $\lambda = (+1, -1)$ ,  $\eta$  and  $\zeta$ . The parameter  $\lambda$  shifts the maxima of the cosine function to  $\Theta_{ijk} = 0^\circ$  at  $\lambda = +1$  and  $\Theta_{ijk} = 180^\circ$  at  $\lambda = -1$ . The angular resolution is provided by the parameter  $\zeta$ . The effect of  $\zeta$  for a triatomic system is shown in Fig. 3.5. High  $\zeta$  values yield a narrower range of nonzero symmetry function values. Hence a distribution of *zeta* values are generally chosen to obtain a distribution of angles centered at the reference atom  $i$ .

In Fig. 3.6, to understand the effect of radial part on the angular symmetry functions, we take an example of  $R_{ij} = R_{jk} = R_{ik}$  and show the effect of  $\eta$ , the parameter that controls the radial resolution.

Since the  $G4$  symmetry function has the product of three Gaussians, it ensures that there

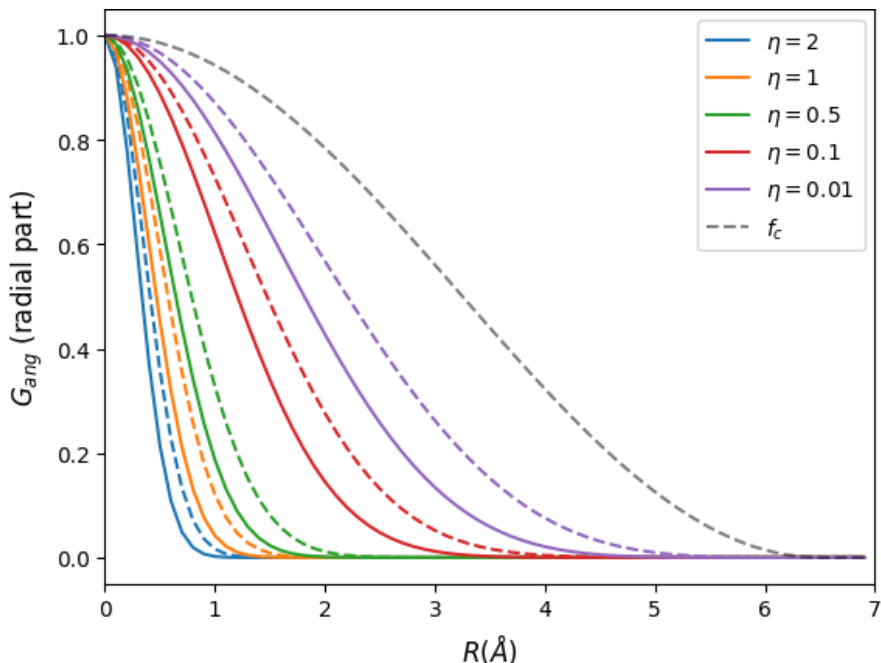


Figure 3.6: Radial part of the angular symmetry functions shown for the case  $\mathbf{R} = \mathbf{R}_{ij} = \mathbf{R}_{ik} = \mathbf{R}_{jk}$  and  $R_c = 7\text{\AA}$ . The solid curves represent the radial part of angular functions of type  $G^4$  and dashed curves correspond to the radial parts of type  $G^5$ .

are only triplets of atoms included in the summation, such that  $R_{ij}, R_{ik}, R_{jk} < R_c$ . On the other hand, for  $G^5$  symmetry function, there is no constraint on  $R_{jk}$  which results in a larger number of terms in the summation. This can be visualized in Fig. 3.7 where assuming  $R_{ij} = R_{ik} = 0.8 \times R_c$  (with  $\eta = 0.005 \text{ \AA}^{-2}$ ,  $\zeta = 1$ ,  $R_c = 6.5 \text{ \AA}$  and  $\lambda = 1$ ),  $G^5$  symmetry function has nonzero values for a large range of angles, while  $G^4$  symmetry function yields approximately zero for  $70 < \Theta_{ijk} < 290$ .

### 3.3.1.3 Weighted Atomic Centered Symmetry Functions

While the symmetry functions described in the previous sections show an excellent performance for a wide range of systems, serious problems arise for molecules composed of several different chemical species. Number of elements ( $N_{elem}$ ) directly governs the number of functions necessary to describe the system. To account for every possible combination,  $N_{elem}$  radial and  $N_{elem}(N_{elem} + 1)$  angular symmetry functions with  $\lambda = \pm 1$ . As the chemical

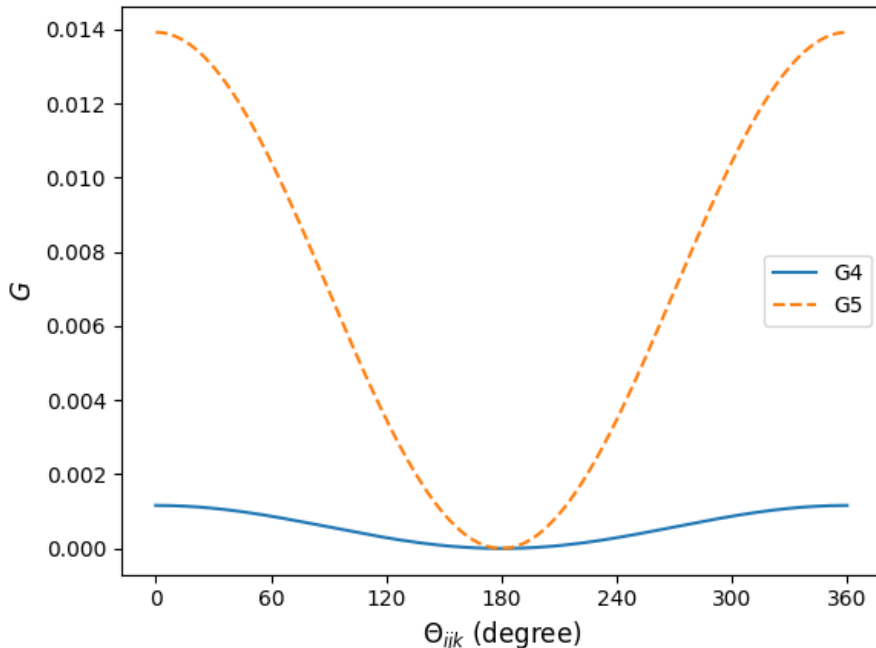


Figure 3.7: Comparison of the total angular functions  $G^4$  and  $G^5$  for atom  $i$  in a triatomic molecule. The interatomic distances  $\mathbf{R}_{ij}$  and  $\mathbf{R}_{ik}$  are fixed at  $0.8R_c$  and the symmetry function values are plotted as a function of the angle  $\Theta_{ijk}$  centered at  $i$ . Function  $G^4 \approx 0$  for angles  $70^\circ < \Theta_{ijk} < 290^\circ$  because of the resulting large distance  $\mathbf{R}_{jk}$  in the additional cutoff function  $f_c(R_{jk})$ .

composition of the molecules to be modeled increases, this number grows quickly. While 2 element systems can be described by  $2+2*3 = 8$  unique combinations of symmetry functions, for 4 and 5 elements system, 24 and 35 combinations are necessary. For a reasonable spacial resolution, a several symmetry functions are required for each of these combinations, which significantly increases the input size of the HDNNP. This not only increases the computational cost associated with training and evaluation of the HDNNP due to generation of a bulky architecture, but also the cost associated with the transformation of the Cartesian coordinates.

In order to overcome the above mentioned limitations of traditional symmetry functions, Gastegger et al. proposed introducing element-dependent weighting functions to define weighted atom centered symmetry functions (wACSFs).<sup>206</sup> So, instead of using separate functions to describe the system, the effect of composition is accounted for implicitly. The

resulting radial descriptors take the form

$$W_i^{\text{rad}} = \sum_{j \neq i}^N g(Z_j) e^{-\eta(r_{ij}-\mu)^2} f_{ij} \quad (3.8)$$

and angular descriptors:

$$W_i^{\text{ang}} = 2^{1-\zeta} \sum_{j \neq i}^N \sum_{k \neq i, j}^N h(Z_j, Z_k) (1 + \lambda \cos \theta_{ijk})^\zeta \times e^{-\eta(r_{ij}-\mu)^2} e^{-\eta(r_{ik}-\mu)^2} e^{-\eta(r_{jk}-\mu)^2} f_{ij} f_{ik} f_{jk} \quad (3.9)$$

$Z_j$  and  $Z_k$  are the atomic numbers of the elements  $j$  and  $k$  respectively and functions  $g(Z_j)$  and  $h(Z_i, Z_k)$  are the weighting functions which modify the contribution based on the chemical elements of the atoms involved of each radial and angular term respectively. While these functions can be designed in a wide variety of manner, Gastegger et al. suggested simple functions such that  $g(Z_j) = Z_j$  and  $h(Z_i, Z_k) = Z_j Z_k$ , which give satisfactory results.<sup>206</sup> The main advantage of wACSFs over the traditional SF is that by directly incorporation the information of elemental composition into the SF, it eliminates the need for separate set of functions for each combination of elements. Hence the number of wACSFs required to described

### 3.3.1.4 Parametrization of symmetry functions

The hyperparameters of the SF or wACSF i.e.  $\eta$ ,  $\mu$ ,  $\lambda$ , and  $\zeta$ , need to be determined to train and model HDNNPs. This search of parameters is largely done heuristically by trial and error which involves some knowledge of the system investigated and some chemical intuition. This process can make using and training HDNNPs a difficult task without prior experience. Few of these parameters can be chosen in a straightforward manner irrespective of the system in question. In general, it is beneficial to use two sets of angular functions with  $\lambda = \pm 1$  while keep all other parameters the same. This allows resolving all possible ranges of angles

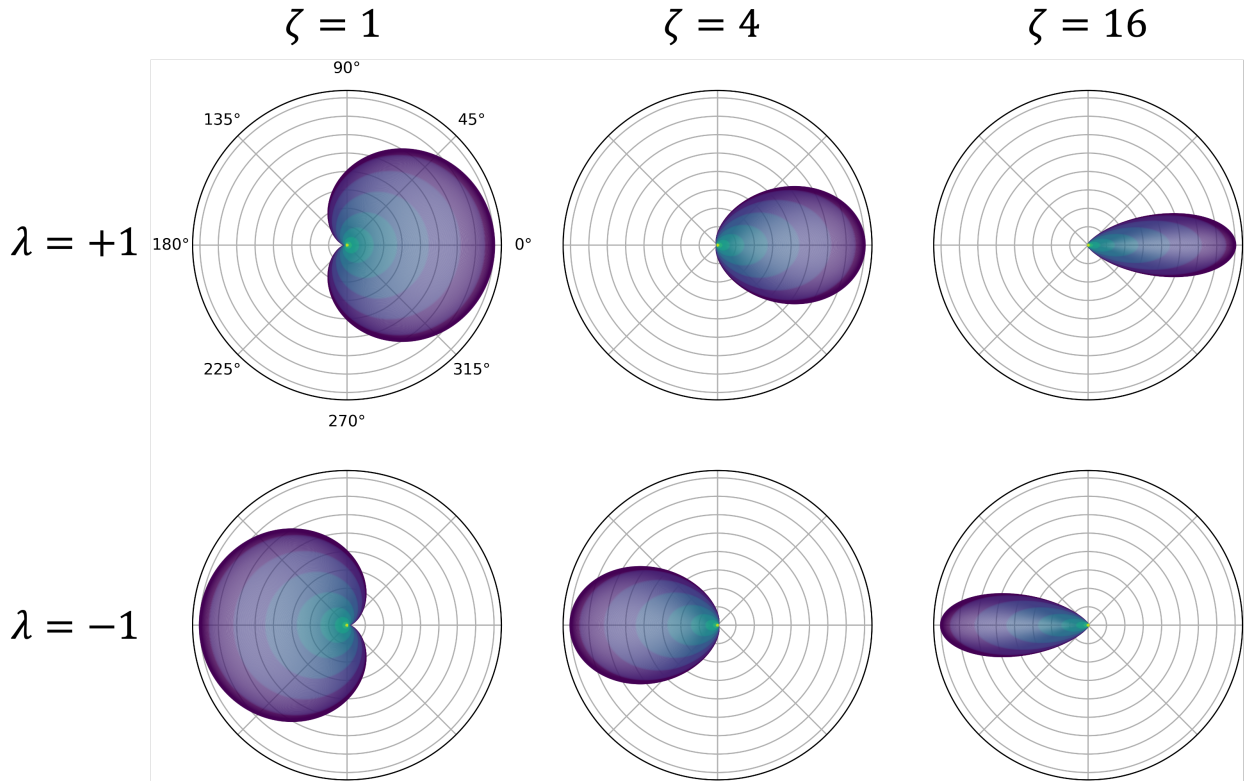


Figure 3.8: Polar plots depicting the influence of the parameters  $\lambda$  and  $\zeta$  on a single term of the sum in Eq. 3.7. All Gaussian functions are set to  $\eta = 0.01$ . Changing the sign of the phase  $\lambda$  moves the maximum of the angular density between  $0^\circ$  and  $180^\circ$ . Increasing the parameter  $\zeta$  focuses the function on a smaller range of angles close to the respective maxima.

present in the environment (Fig. 3.8). Similarly,  $\zeta = 1$  provides a reasonable coverage of the angular space. For larger  $\zeta$  values, descriptors focus increasingly on the regions close to  $0^\circ$  and  $180^\circ$  and information close to  $90^\circ$  is lost as seen in Fig. 3.8. In cases where number of required angular functions far out weights the radial, few wACSFs with higher value of  $\zeta$  can be advantageous.

The largest influence on the descriptor performance comes from the width ( $\eta$ ) and position ( $\mu$ ) parameters within the Gaussian functions defining the radial parts of both the radial and angular symmetry functions. These parameters modulate the spacial sensitivity of the corresponding descriptor. Gastegger et al. discuss two schemes for selecting appropriate sets of  $\eta_i$  and  $\mu_i$ : (1) Gaussian of different widths centered at the origin, (2) Gaussians of

the same width shifted from the origin. To generate parameters using the first scheme, the following steps can be followed<sup>206</sup> :

- Choose the number of symmetry functions  $N$
- Create a radial grid consists of  $N$  equally spaced points  $r_i$  ranging from  $r_0$  to  $r_N$ . The distance  $\Delta r$  between individual points in this grid can be expressed as:

$$\Delta r = \frac{r_N - r_0}{N - 1} \quad (3.10)$$

- For the centered Gaussian functions,  $r_0$  and  $r_N$  are set to 1 Å and  $(r_c - 0.5)$  Å respectively. For these, the shifts  $\mu_i$  are set to zero and the width of each Gaussian can be calculated as:

$$\eta_i = \frac{1}{2r_i^2} \quad (3.11)$$

For the alternative scheme consisting of the same with Gaussians shifted from the origin, the following steps:

- Set lower limit of  $r_0$  as 0.5 Å.
- Center of each individual Gaussian to one of the grid points ( $\mu_i = r_i$ )
- Widths  $\eta$  of the functions are chosen according to:

$$\eta = \frac{1}{2(\Delta r)^2} \quad (3.12)$$

### 3.3.2 Forces from HDDNP: Energy Gradients

The forces are negative gradients of the total energy with respect to the atomic positions. In order to calculate the force component  $F_{k,\alpha}$  acting on atom  $k$  with respect to the coordinate  $\mathbf{R}_{k,\alpha}$ , chain rule can be applied such that:

$$\begin{aligned}
F_{k,\alpha} &= -\frac{\partial E}{\partial R_{i,\alpha}} = -\sum_{i=1}^N \frac{\partial E_i}{\partial R_{i,\beta}} \\
&= -\sum_{i=1}^N \sum_{j=1}^{M_i} \frac{\partial E_i}{\partial G_{i,j}} \frac{\partial G_{i,j}}{\partial R_{k,\alpha}}
\end{aligned}
\tag{3.13}$$

where,  $N$  is the number of atoms, and  $M_i$  is the number of symmetry functions describing atom  $i$ . The first term  $\frac{\partial E_i}{\partial G_{i,j}}$  is defined by the NN architecture and the second term,  $\frac{\partial G_{i,j}}{\partial R_{k,\alpha}}$  is calculated from the definition of the chosen symmetry function.

Force acting on an atom depends on the positions of the atoms being as far as  $2 \cdot R_c$  away. As the force with respect to a coordinate  $\alpha$  of an atom  $i$  is the derivative of the energies  $E_j$  of all atoms  $j$  inside the cutoff sphere of  $i$ . In turn, the  $E_j$  depend on the positions of all atoms in their respective environments, and these atoms can be up to  $2 \cdot R_c$  away from atom  $i$ . As the positions of all atoms in the environment of  $j$  determine  $E_j$ , even an atom  $k$  being outside the cutoff sphere of atom  $i$  affects the contribution of atom  $i$  to  $E_j$ . Still, in practice this large effective range of the forces is not very important, since the effective physical range of the atomic interactions is usually much shorter than twice  $R_c \approx 12 - 20 \text{ \AA}$ .

### 3.3.3 Training Neural Networks based Potentials

#### 3.3.3.1 Reference Data generation

Neural Networks based potentials (NNPs) are very flexible in comparison to conventional physical potentials which is why they have higher accuracy in fitting reference dataset used for training. But at the same time NNPs if used to predict energies for structures which have considerably different configurations than the ones included in the training can lead to significant errors and poor performance since NNs have very limited extrapolation capabilities. Another common problem in training NNPs is the ‘‘overfitting’’ issue, which essentially means that the NN model tries to learn too many details in the training data along with the noise from the training data. As a result, the model performance is very poor on unseen or



test data sets. To solve these two issues, while training NNPs, we employ two methods:

1. Uniqueness of configuration can be checked before adding structures to the training dataset. This is done by two methods:
  - (a) Convert structures into a graph representation where atoms act as nodes and bonds between them act as the graph edges. By comparing the graphs, we can find if new structure added to the dataset is unique.<sup>207</sup>
  - (b) Use a kernel-based method where symmetry functions of two structures can be used to find the uniqueness of structures.<sup>208</sup>
2. To avoid overfitting, we use the well-known “early stopping” method. In this technique, the total dataset generated is split into a training set which is used to optimize the weight parameters of the Neural Network, and a validation or test set whose error is monitored while the iterative training (explained later in the chapter) of NNP is done. If the errors on both datasets are similar, the NNP is good at generalization but if the errors on the test set are high, overfitting has occurred. In that case, a part of the test set data is added back to training to improve the generalization of the potential. Therefore, the best set of weight parameters corresponds to the epoch with the smallest test set error. This method is explained using a schematic in Fig. 3.9

### 3.3.3.2 Training Procedure

**3.3.3.2.1 Self-consistent iterative training:** To improve the NNP, generally, an iterative process of data generation is used as shown in Fig. 3.10. From an initial reference data which contains some basic information about the system like the sensitivity of energy with respect to small bond distance perturbations, different adsorbate sites, optimization data etc., we can generate a first generation NNP. Using that NNP, we can generate new data quickly by using techniques like Basin Hopping, Monte Carlo Simulations, Genetic Algorithm, Ran-

## Splitting Data

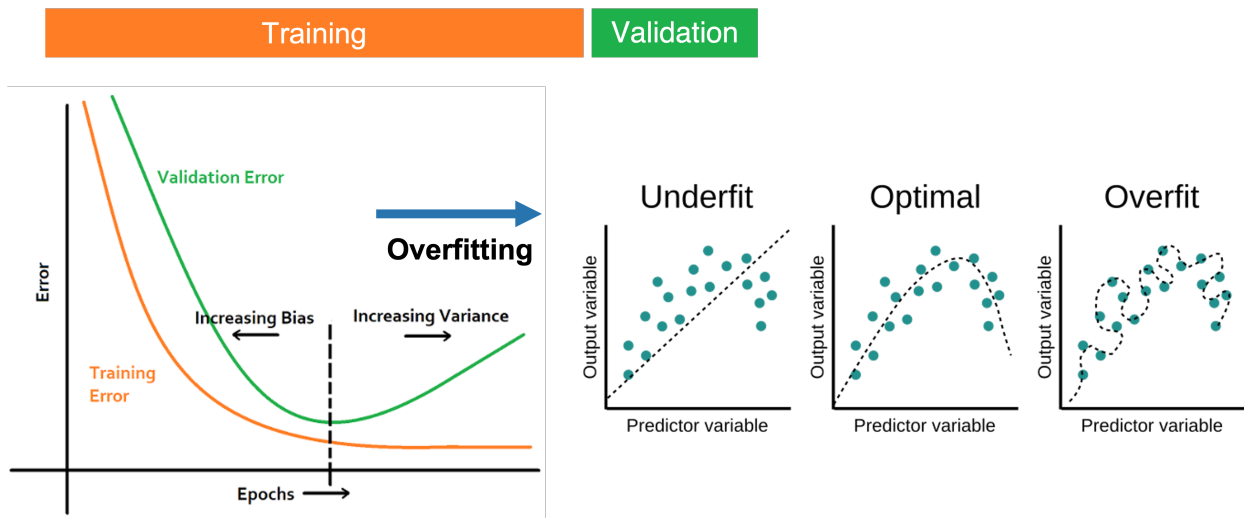


Figure 3.9: Schematic explain how early stop method if implemented to avoid the overfitting problem while training NNPs

dom perturbations, MD Simulations etc. From this generated data, we can choose relevant structures that can be recomputed using DFT and we can check the generality of the fit NNP. If the error on the new generated structures is high, it is added to the training and this cycle continues until desired accuracy of the NNP is achieved. In this manner, we can systematically and self-consistently improve the accuracy of the NNP. Generally the aim is to reach a RMSE of 1 meV/atom.

**3.3.3.2.2 Multiple-fit Procedure:** Early stop method can fail if there are parts of the configuration space in which no reference data are present at all, since in this case failures of the NNP would not be detected by a high error of the test set. In order to avoid doing computationally expensive first principles calculations to identify these missing configuration space in the training data, a “Multiple-fit” procedure can be used. In this method, for the same training set multiple NNPs are fit with different functional forms (e.g. using different architecture, different number of symmetry functions, different activation functions etc). From the multiple fits, the NNPs which have comparable quality (accuracy) are selected.

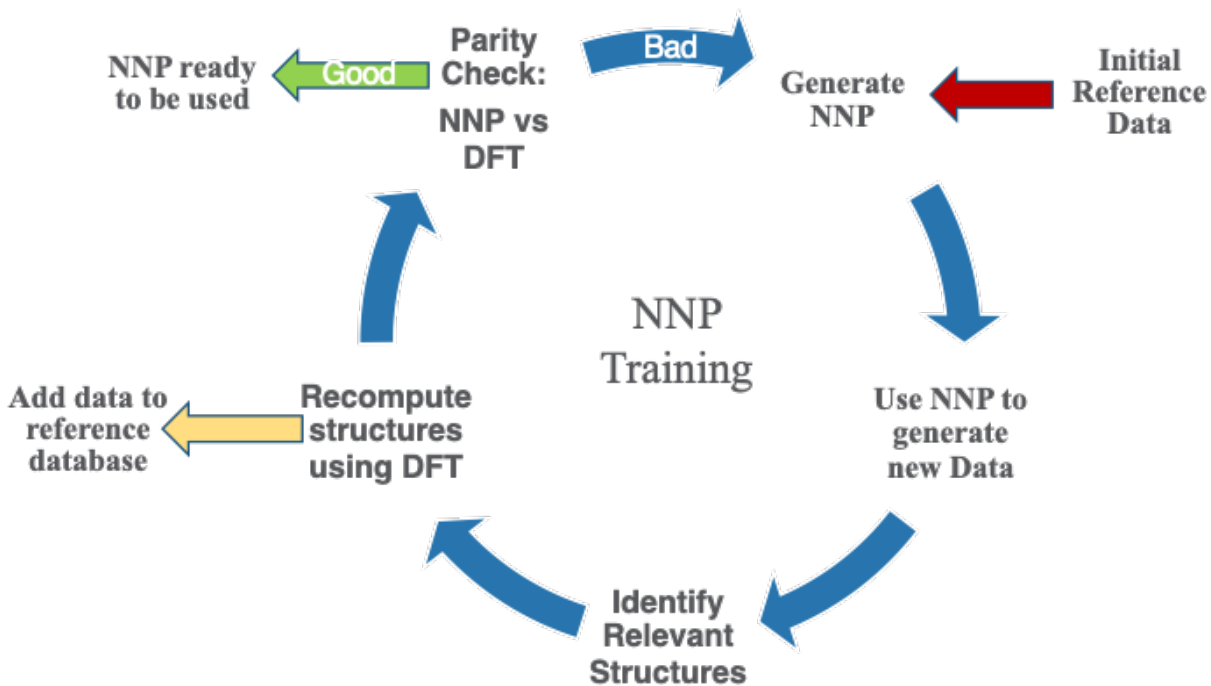


Figure 3.10: Schematic of the iterative training process used to improve the accuracy and generality of the Neural Network Potentials.

Using of these selected NNPs, a large number of structures are generated using the previously mentioned techniques. These generated structures can be recomputed using the remaining NNPs and the energy predictions for the various NNPs can be compared. The structures for which multiple NNPs disagree in terms of the predicted energy are either extrapolating or missing in the configurations space in training data. These structures can be added back to the training set and this procedure can be followed iteratively to improve the potential.

### 3.3.3.3 Optimization of the HDNNP Weight Parameters

Once a set of reference dataset is generated, we can use “supervised learning” to train a HDNNP. In this method, the output of NNP for each structure to the known (“true”) result from the reference calculation. In general, this corresponds to a minimization of an error function  $\Gamma$ , which is given as the sum of squared errors of the  $N_{struc}$  (number of structures)

individual members of the training set:

$$\Gamma = \frac{1}{N_{\text{stuct}}} \sum_{j=1}^{N_{\text{usct}}} \left[ (E_{\text{NN}}^j - E_{\text{Ref}}^j)^2 + \frac{\beta}{3N_{\text{atom}}^i} \sum_{j=1}^{3N_{\text{axp}}^i} (F_{\text{jNN}}^i - F_{\text{jRef}}^i)^2 \right] \quad (3.14)$$

where  $E_{\text{NN}}^j$  and  $E_{\text{Ref}}^j$  are the NN predicted and the reference DFT energies of the structure  $j$  respectively;  $N_{\text{atoms}}^j$  is number of atoms in structure  $j$ ;  $F_{\text{jNN}}^i$  and  $F_{\text{jRef}}^i$  are the force on atom  $i$  of the structure  $j$  with respect to the NN and DFT calculation respectively. The second term in the error function calculated the force error which is looped over the  $X$ ,  $Y$ , and  $Z$  directions hence the  $3N_{\text{atom}}^i$  term.  $\beta$  acts as a tunable parameter that adjusts the relative influence of the energies and force errors to the function since the force component is much larger than the number of energies. The optimization of the weights of the NN is done iteratively to minimize the error function. Each iteration of the optimization is called “epoch” in the context of NNs. The optimization can be performed using a wide range of optimization algorithms most of which use gradient-based methods. The most basic method for training used in the NN community is called the “backpropogation” method. It involves recursive calculation of the derivatives of the error function with respect to the weights starting from the output layer and proceeding to the input layer in the inverse order of the calculation of the NN output. It boils down to steepest descent optimization of each weight  $w$ , which can be a connecting weight  $a$  or a bias weight  $b$ . For an iteration  $t + 1$ , the updated weights are obtained according to:

$$w(t + 1) = w(t) - \eta \cdot \frac{\partial \Gamma}{\partial w[t]} \quad (3.15)$$

Here  $\eta$  is the learning rate can be a variable quantity that can be adapted as the learning progresses. More frequently used algorithms used in respect to training NNs are the Levenberg-Marquardt, Stochastic Gradient Descent (SGD), Nesterov Accelerated Gradient, Adaptive Gradient (AdaGrad), AdaDelta, Adam algorithm and in particular for HDNNPs the global extended Kalman filter which is implemented within the *n2p2* code used for train-

ing in the later chapters.<sup>209</sup>

### 3.4 Conclusion

In this chapter, we discussed the construction of a Machine Learning based interatomic potential for a fast and accurate exploration of potential energy surface. We review the traditional Feed Forward Neural Network architecture which mainly fails due to its inability to create an invariant input to the network and its inability to create a generalized NN model that works for any size of the system. We also discuss how introduction of symmetry functions (SF) and High Dimensional Neural Network Potentials (HDNNP) solves both these issues. Since the SF defines the input to the HDNNP, we discussed how an automatic parameterization scheme can be used to define the hyperparameters of the function. Finally we showed how the reference data for training is generated iteratively and using multiple-fit procedure; techniques like data splitting are used to avoid over-fitting; and different weight optimization algorithms utilized to reduce the loss function (prediction error) of the HDNNP. These techniques for developing a robust NN-based potential are utilized in the work discussed in the coming chapters of the dissertation.

## CHAPTER 4

# CO organization at ambient pressure on stepped Pt surfaces

### 4.1 Introduction

The active phase of transition metal heterogeneous catalysts presents atoms in different coordinations and environments. Surface science experiments over the last two decades have systematically studied the relationship between surface structure and catalytic activity by using single-crystal surfaces as model catalysts. Open surface structures or surfaces with high Miller index often show enhanced activity.<sup>210-214</sup> The high-index planes, denoted by a set of Miller indices ( $hkl$ ) with at least one index being larger than one have a high density of atomic steps and kinks. The low coordination atoms which define the atomic step/kink sites on the catalyst surface often enable enhanced binding of reactant molecules and exhibit higher activity for bond breaking.<sup>215-222</sup> At the same time, steps also play an important role in other surface processes like adsorbate induced reconstructions. The surface atoms at the step/kink site act as a natural locations for crystal growth and erosion; and as a source for mobile surface ad-atoms during the process of surface reconstruction.<sup>23,55,166,218,223,224</sup> This makes it important to study the assembly structure of adsorbate molecules on such stepped surfaces in realistic temperature and pressure conditions (which defines the adsorbate chemical potential) to understand the adsorption site distribution and the adsorbate coverage. Such a high coverage adsorbate structure is the initial configuration for adsorbate induced surface reconstruction processes at such stepped and kink surface sites. In this work, we

focus our attention on the Pt/CO system to understand the CO organization on Pt(553), Pt(557) and Pt(643) surfaces at room temperature and ambient pressure. All these surfaces show (111) terraces, separated by (111) and (100) mono-atomic steps for Pt(553) and Pt(557) respectively. Pt(643) is a case where the step includes kinks, hence presenting Pt atoms with a metallic coordination of 6.

Since the considered step surfaces all present (111) terraces, the behavior and organization of CO on the extended Pt(111) surface is a key reference. CO adopts on Pt(111) multiple ordered structures depending on the coverage. At 300 K and 1 atm pressure of CO, experiments (as scanning tunneling microscopy) and first principle modelling show that CO molecules adopt a so called “Moiré pattern” structure, in which CO, binding vertically through the C atom, is organized in a pseudo-hexagonal layer with a rotated supercell with respect to the underlying 1x1 hexagonal Pt layer. More specifically a  $(\sqrt{19} \times \sqrt{19})$ - $R23.4^\circ$ -13 CO unit cell is found where 13 CO molecules occupy a cell containing 19 Pt atoms, corresponding to a coverage of  $13/19 = 0.68$  ML.<sup>141,225-227</sup> Since the CO quasi-hexagonal layer has a slightly larger parameter than that of the Pt(111) layer, CO molecules span a variety of binding sites, from (quasi) top to bridge and hollow. Although the classification between these various sites relies on chosen thresholds and hence is somewhat ambiguous, one can determine that, among the 13 CO molecules, 7 are in a top or quasi top site, while 4 in bridge/ quasi-bridge and 2 in hollow sites. So about one half CO molecules are on the top site, while the other half is in a multiply bonded site. Many experiments are performed in UHV conditions with a small CO pressure and low temperature to reach a high CO coverage. In these conditions, the CO coverage is typically somewhat lower ( 0.5 ML) and a simple  $c(4 \times 2)$ -2CO superstructure is seen, with one top and one bridge CO. Hence, a very similar ratio (0.5) is seen between top and multiply bonded CO, compared to the high pressure Moiré pattern arrangement.

If we now move to stepped and kinked surfaces, the experimental characterization of adsorbate layers surfaces is challenging. These surfaces are heterogeneous, with different types of sites (step, kink, terrace), and adsorption is usually less ordered. For example, Tränkenschuh

et al. did not find any LEED pattern for CO adsorption on Pt(553), showing an absence of long range order, in contrast to Pt(111).<sup>228</sup> This absence of long range order was also seen on many other high index surfaces (Pt(533),<sup>229</sup> Pt(332),<sup>120</sup> Pt(210)<sup>230</sup> and Pt(321).<sup>231</sup> Spectroscopic characterization methods necessarily give space average information. For CO on stepped Pt surfaces, high resolution X-ray photoelectron spectroscopy (XPS) and electron energy loss spectroscopy (EELS) can distinguish between CO adsorbed at step sites and terrace sites, and between top and bridge bonded CO at each site.<sup>55,120,228,232–234</sup> On Pt(553), XPS at low pressure (less than  $3 \times 10^{-9}$  mbar) and low temperature (130K) shows that the terrace is only occupied when the edge sites are almost saturated with CO, while on the terrace the population of the top site is about twice that of the bridge site at saturation coverage of  $\sim 0.5$  ML.<sup>228</sup> This contrasts with the case of Pt(111) where at a similar coverage the population of top sites equals that of bridge sites. On Pt(335) at 0.5 ML coverage, EELS also shows that all edge sites are occupied with top CO, while on the terrace half of the sites are occupied with a 2:1 top-to-bridge ratio.<sup>120</sup>

In situ FTIR studies in solution and electrochemical conditions indicates that the preferred binding mode of CO on the terrace of stepped surfaces with short terraces depends on the type of step: surfaces with (100) steps (Pt(322) and Pt(311)) show a large amount of bridge site CO on their terraces, while those with (111) steps (Pt(332) and Pt(331)) mostly provide top site CO.<sup>235</sup> This suggests an interesting mechanism, of unknown origin to our knowledge, by which the type of step can control the binding site of CO on the terraces. Near-Field microscopies, such as scanning tunneling microscopy, provide images with molecular resolution, but the detailed interpretation of the images can be challenging, and time resolution is usually limited. STM images of 0.5 ML of CO on a Pt(111) surface presenting steps shows less order and higher mobility of CO molecules in the vicinity of the step.<sup>236</sup>

Computational studies that investigate high Miller index surfaces with high adsorbate coverage are very limited. The complexity of modeling such surfaces arises from two major



challenges: (1) the high computational cost of exploring such potential energy surface (PES) using accurate first principles calculations and (2) the myriad combinations of adsorption sites possible at high coverages. To tackle the first challenge, we use the approach developed by Behler and Parrinello to generate a High Dimensional Neural Network Potential (HDNNP)<sup>203</sup> that is trained on higher-level first principles calculations and can accurately describe the adsorbate–adsorbate and adsorbate–surface interactions on various high Miller surfaces. This approach is ideal for studying these systems because it scales favorably with respect to the dimensionality of the system and guarantees the permutation invariance of the PES due to the conversion of unique local environments into unique fingerprints. In the past few years, NN based methods have been increasingly used to construct such accurate PES successfully.<sup>237–245</sup> To tackle the second challenge of exploring the large combination of adsorption sites possible, we use a Basin-hopping algorithm.<sup>246</sup> This method transforms the PES into local minima basins and the transition between these basins is accomplished by performing a Monte-Carlo displacement trial move, followed by geometry optimization. Such a method is not very often applied while using DFT to compute the free energy of the system to evaluate the MC criteria due to the high cost of DFT calculations and due to the fact that a significantly high number of MC steps can be required to reach a global minimum. Having an accurate and quick energy calculator in terms of the HDNNP, we can efficiently generate a large number of configurations of CO on different Pt surfaces for a given coverage and chemical potential of CO.

In most theoretical studies, the PES is not thoroughly sampled and only a few local minima are found, the most stable one being supposed to represent the structure of the adsorbates on the substrate. This is due to the unaffordable cost of modeling and exploring the PES as we discussed before. However, it is now known that the pressure of the adsorbates can generate dynamic interfaces which can play a nontrivial role in understanding the actual distribution of the adsorbates on the surface. The majority of the discussion of such dynamic states in the literature has been focused on understanding the fluxionality of small nanoparticles

and nanostructured surfaces..<sup>247–252</sup> Sun et al., discussed the case of a  $\text{Pt}_{13}$  cluster under a pressure of hydrogen, found a large ensemble of low energy structures, and showed that these structures change with hydrogen coverage. Metastable structures are shown to dominate the catalytic activity. One observation made in the case of  $\text{Pt}_{13}\text{H}_{26}$  structures was that all the structures in the metastable ensemble exhibited a cuboctahedral  $\text{Pt}_{13}$  core, and the only variation in the structures was produced by the hydrogen atoms occupying different positions on the cluster. This indicates that metastable structures can be generated by just rearrangement of adsorbate atoms and hence that the concept of metastable ensembles can also be applied to a gas-surface interaction. In this work, using basin hopping simulations, we not only search for the global minima for CO adsorption structures on various stepped surfaces, but also find the coverage dependent ensemble of possible CO configurations. We show that the CO organization on the terrace are strongly affected by the geometry of the step ((100) or (111) facets), which controls the ratio between top and multiply-bonded CO molecules, that quasi-hexagonal CO lattices are formed on these terraces similarly to the case of  $\text{Pt}(111)$ <sup>23,141</sup> and that step edges are in most cases fully covered with one top site CO molecule on each step Pt atom.

## 4.2 Methods

### 4.2.1 First Principle Calculation Details

Calculations were performed using the Vienna Ab-initio Simulation Package<sup>253–256</sup> using the general gradient approximation (GGA) Perdew-Burke-Erzenhof (PBE) functional.<sup>257</sup> Core electrons were described using the projector augmented wave potentials.<sup>258,259</sup> A k-spacing of 0.25 is used for all the calculations and the generated k-point grid is centered at the  $\Gamma$  point. Periodic slabs of Pt surface with CO are separated by 12 Å vacuum in the z direction. A fermi smearing width of 0.2 eV was applied using the Methfessel-Paxton method (order 2). A cutoff energy of 400 eV is used. The known issue of overbinding of CO on Pt surfaces

(“Pt(111)/CO Puzzle”) has been corrected using the CO bond distance-based correction developed by us.<sup>225</sup> The generalized correction is given as  $\Delta = 4.77 * d_{CO} - 5.37$ , where  $\Delta$  is the correction applied in (eV) and  $d_{CO}$  is the bond length of adsorbed CO in (Å).

#### 4.2.2 Training a High Dimensional Neural Network Potential

We exploit the use of HDNNP to define the atomic potential for Pt/CO system to reduce the computational cost and explore the potential energy surface (PES) efficiently. The assumption in developing the HDNNP is that there exists a unique functional relation between the atomic coordinates and the potential energy. Using HDNNP, the total energy of the system is defined as a the sum of individual atomic contributions,  $E_s = \sum E_i$ , where the atomic energy  $E_i$  is found by training atomic Neural Networks using the structural and chemical environments ( $E_s = \sum NN(X_i^{env})$ ). These environments are defined using various feature transformations (descriptors) that convert Cartesian coordinates, which are not invariant with respect to translation and rotation of the system to invariant representations implemented using Atom-centered Symmetry Functions (ACSF),<sup>205</sup> smooth overlap of atomic positions (SOAP),<sup>260</sup> Many-body Tensor Representation (MBTR),<sup>261</sup> etc.

In this work, we use the high-dimensional neural network potential where the  $R_i^\alpha$  (Cartesian coordinates  $\alpha$  of atom  $i$ ) are transformed into a set of symmetry function values  $G_i^\mu$  for each atom  $i$ .<sup>203</sup> The developed NN utilises 2 hidden layers with 30 nodes each and a hyperbolic tangent activation function. A total of 46 symmetry functions were used for each element - Pt, C, and O. We use the weighted atom-centered symmetry function (wACSF) proposed by Gastegger et. al which can be repressed as:<sup>206</sup>

$$G_i^2 = \sum_{j \neq i} Z_j e^{-\eta(r_{ij}-r_s)^2} f_c(r_{ij}) \quad (4.1)$$

$$G_i^3 = 2^{1-\zeta} \sum_{\substack{j,k \neq i \\ j < k}} Z_j Z_k (1 + \lambda \cos \theta_{ijk})^\zeta e^{-\eta[(r_{ij}-r_s)^2 + (r_{ik}-r_s)^2 + (r_{jk}-r_s)^2]} f_c(r_{ij}) f_c(r_{ik}) f_c(r_{jk}) \quad (4.2)$$

$$f_c(r_{ij}) = ((15 - 6r_{ij})r_{ij} - 10)r_{ij}^3 + 1 \quad (4.3)$$

where,  $G_i^2$  represents the radial symmetry function and  $G_i^3$  represents the angular symmetry function.  $f_c$  represents a polynomial cutoff function.  $r_{ij} = |\mathbf{r}_i - \mathbf{r}_j|$  represents the interatomic distance between atom  $i$  and  $j$  and  $\theta_{ijk} = (\mathbf{r}_{ij} \cdot \mathbf{r}_{ik}) / (|\mathbf{r}_{ij}||\mathbf{r}_{ik}|)$  represents the angle spanned by the atoms  $i$ ,  $j$ , and  $k$ .  $Z_{i/j/k}$  represents the atomic numbers which are used as weights for the symmetry functions. The parameters  $\eta$  and  $r_s$  have been determined using the automatic selection algorithm developed by Imbalzano et. al based on equally dividing the cutoff radius ( $r_c = 6 \text{ \AA}$ ) in  $n$  intervals which is chosen here to be 5. Two sets of radial symmetry functions ( $G^2$ ) are used: (i) the first group centered on the reference atom ( $r_s = 0$ ) with  $\eta = 0.0278, 0.0529, 0.1007, 0.1916, 0.3648, 0.6944$  (6 symmetry functions) and (ii) second group is centered along the path between the central atom and its neighbour with  $r_s = 1.5, 2.1213, 3, 4$  and  $\eta = 2.5904, 1.2952, 0.6476, 0.3238$  respectively (4 symmetry functions). 36 angular symmetry functions ( $G^3$ ) have been defined with  $r_s = 0$ ;  $\eta = 0.0278, 0.0529, 0.1007, 0.1916, 0.3648, 0.6944$ ;  $\lambda = -1, 1$  and  $\zeta = 1, 4, 16$ . This creates atomic NN architectures that can be represented as 46-30-30-1.

The reference database is built iteratively. Starting from an initial reference data set (consisting of Pt(111) surface with different unit cell sizes and CO coverages), a first preliminary HDNNP is obtained. This HDNNP is used with BHMC simulations to generate more relevant data, which is used to validate the potential to check for extrapolations and missing Potential Energy Surface (PES) data. If the accuracy of the developed potential is insufficient, problematic structures are identified and added to the training set until a converged potential is obtained. In every iteration of the training, 10% of the total reference data generated is used as a validation fraction and over fitting is avoided by using the early stop algorithm. The final reference database consisted of 4289 structures. We used the n2p2 package for training.<sup>209</sup> This package provides an efficient approach for optimizing the weight parameters of the neural network via multi-stream Kalman filtering, using potential energies and atomic forces as reference data. A loss function for the training is defined as the sum of

energy and force RMSE (root mean square error), i.e., force coefficient  $\gamma = 1$ . For re-usability of the developed potential, we include the output weight parameter and other files in the Supporting Information. The “input.nn” file includes all variables needed to reproduce the NN as well, including symmetry functions, cutoff radius, and hidden layers and nodes and the “weights.\*.data” contains the weights of the atomic NNs.

### 4.2.3 Basin Hopping Monte Carlo (BHMC) Simulation

Basin Hopping method is a frequently used global optimization method for finding low energy structures. For our purposes, we use the method to generate new structures by taking advantage of the efficient HDNNP to quickly sample the configuration space that can be then recalculated by DFT to add to the reference database. This algorithm take advantage of basin hopping method and Monte Carlo method with local minimization to convert the potential energy surface (PES) from a curved surface to stepped shape basins..<sup>246</sup> The exploration of these basins is achieved by Monte Carlo sampling through atomic displacements and the Metropolis criterion. The free energy is calculated by subtracting the reference chemical potential (which is a function of temperature and pressure) of the adsorbate from the energy of the system as shown by the following equations:

$$\Delta G = E(nCO + slab) - E(slab) - n_{CO} \times \mu_{CO} \tag{4.4}$$

where  $E(nCO + slab)$  is the electronic energy of the optimized structure,  $E(slab)$  is the energy of the optimized bare Pt slab and  $\mu_{CO}$  is the chemical potential of CO in the gas phase. Translational and rotational terms are taken into account to calculate the CO gas phase chemical potential, but vibrational terms are not included, since they are neglected in the CO adsorbed state as well.

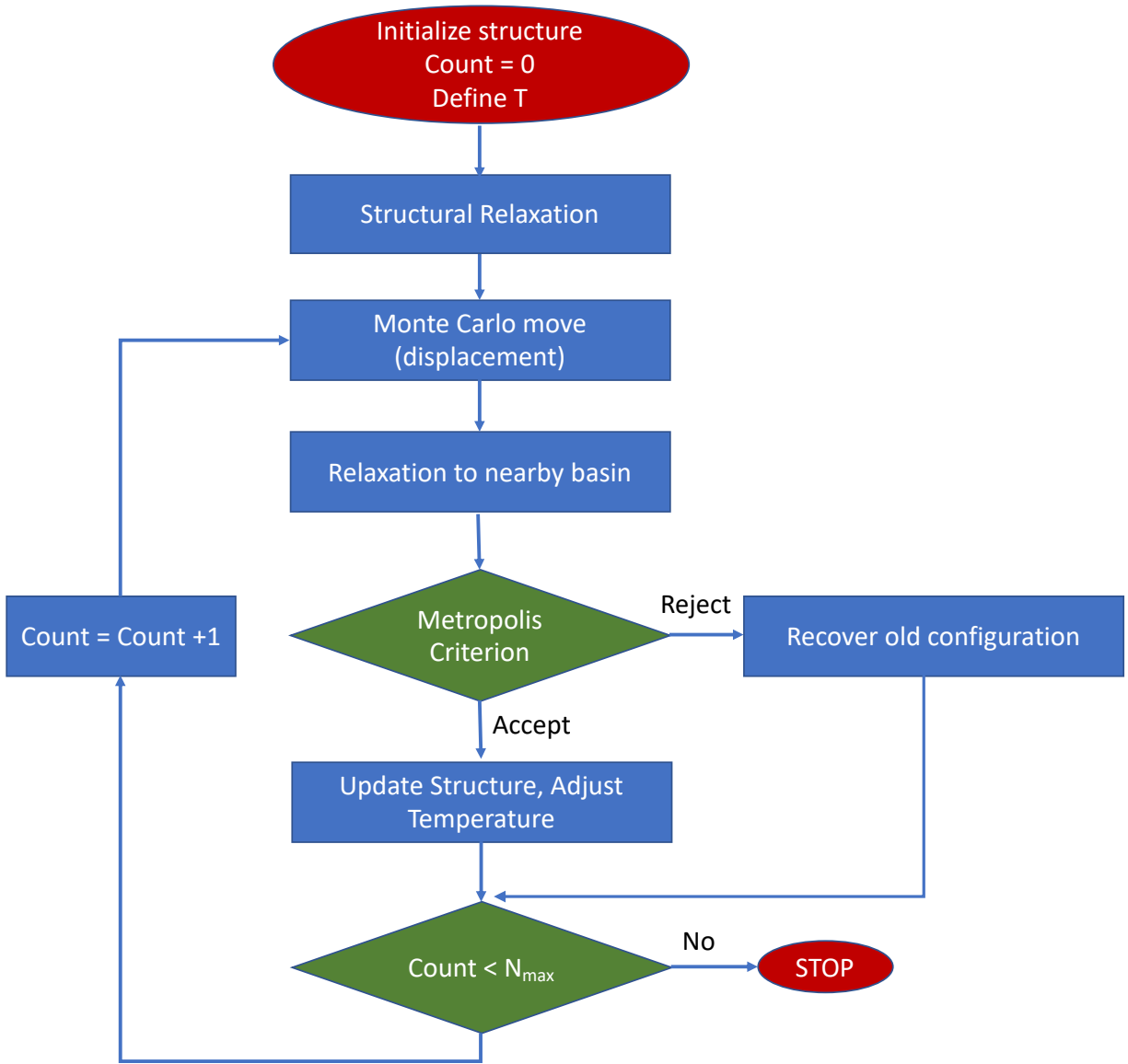


Figure 4.1: Basin Hopping Algorithm flowchart.

The Metropolis criterion implies that a MC move is always accepted if the free energy of the new structure  $\Delta G_{new}$  is lower than the previous structure,  $\Delta G_{old}$ , otherwise it is accepted with a probability  $\exp[(\Delta G_{old} - \Delta G_{new})/k_B T_{MC}]$ , which is determined by a random number drawn from the interval  $[0,1]$ . Here, the “temperature” for BH simulation ( $T_{MC}$ ) is an adjustable parameter. Based on the acceptance and rejection of the structures while running the BH simulation, this parameter can be adjusted. The flowchart shown in Fig.

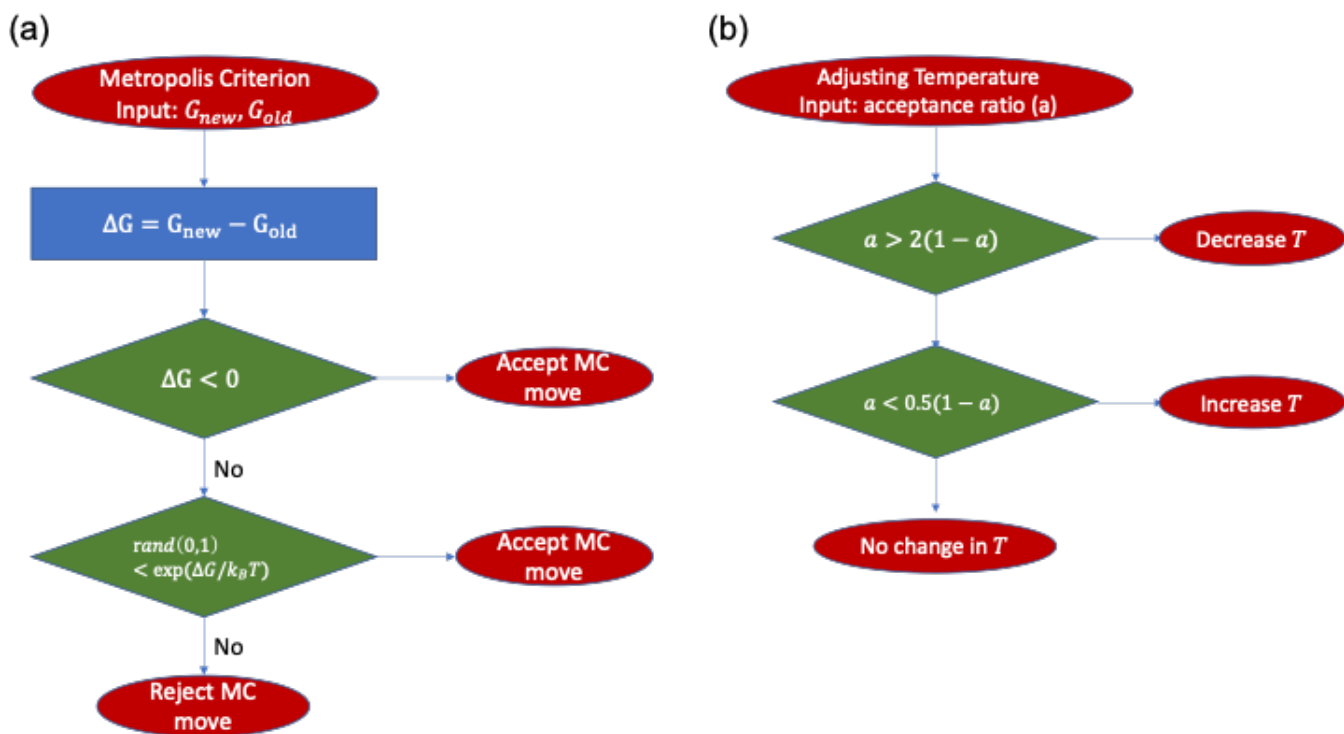


Figure 4.2: Flow-chart showing the algorithm for (a) Metropolis criterion - which decides the acceptance/ rejection of MC move and (b) adjusting temperature during the BH simulation where (a) is the acceptance ratio for the BH simulation.

4.1 and 4.2 explain the BHMC algorithm used in this work. BHMC algorithm differs from the standard MC algorithm in one step namely the local optimization that is performed at each point of the PES and since the BHMC exploration is performed by hopping among different basins, a larger atomic displacement ( $\Delta r_i$ ) can be used compared to standard MC. Both these features of BHMC simulations help increase the success rate in obtaining the global minima. Most BHMC implementations utilize random atomic displacements.<sup>262–264</sup> For high coverage of CO on Pt surfaces, random perturbation of adsorbate atoms leads to a low acceptance ratio ( $\sim 20\%$ ) since the motion of one CO molecule on the surface is only allowed if the neighboring adsorbed molecules move in a concerted manner. As a result, we introduced a new kind of move, “Clustering mutation algorithm”, where we cluster a few adsorbed molecules randomly and move all in the same random motion together. This was

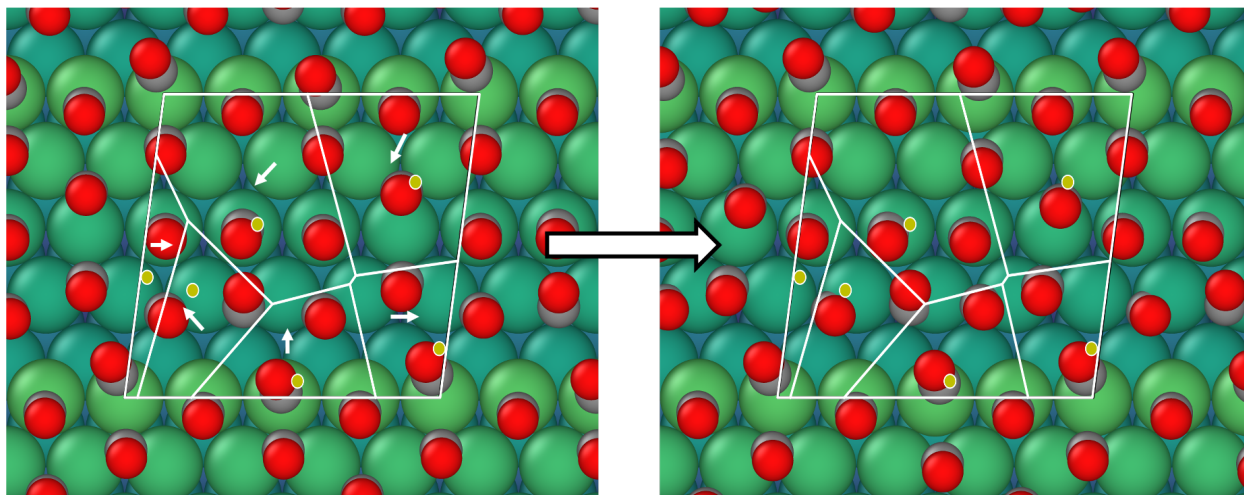


Figure 4.3: Clustering mutation algorithm implemented with the Basin Hopping algorithm. The dark gray balls represent carbon atoms and red balls represent oxygen atoms. The light gray balls are the substrate platinum atoms. The blue lines define the Voronoi tessellation and the yellow dots represent the centers for the Voronoi clusters. Atoms within one cluster are moved randomly in the same direction as seen in the model implementation.

done by dividing the surface into Voronoi tessellations using random center points within the unit cell. Such a move in conjunction with random atomic displacements significantly improved the exploration of the potential energy surface and increased the acceptance ratio (~50%).

The following steps are used in implementing this modified version of random atomic displacement.

1. Create a polygon (parallelogram) that maps the surface of the unit cell
2. Randomly generate  $n$  points within the polygon which act as the centroids of the Voronoi tessellation (like a power diagram). Using the polygon boundary and centroids, we can define the edges of the Voronoi tessellation (intersections of half-spaces).
3. Within the each obtained cell (“cluster”), we identify the adsorbate positions and all CO molecules within the cell are displaced in same direction randomly generated.

HDNNP is efficiently used with BHMC to explore the PES and find the low energy minima



ensemble of structures. Since the HDNNP is not fully accurate, the ordering of structures based on energies is not the same as predicted by the HDDNP when compared with DFT calculations. As a result, we recalculate with DFT all structures that have free energy  $G \leq G_{min} + 0.05eV/\text{\AA}^2$  which is a significantly higher error margin than the error expected from the HDNNP. This ensures that we have recalculated all the low energy minima ensemble of structures, which is then used to report the relative adsorption free energies and the minima structures. The (i) BHMC code, (ii) training, validation and test dataset and (iii) HDNNP files are made available on Github.<sup>265</sup>

### 4.3 Results and Discussions

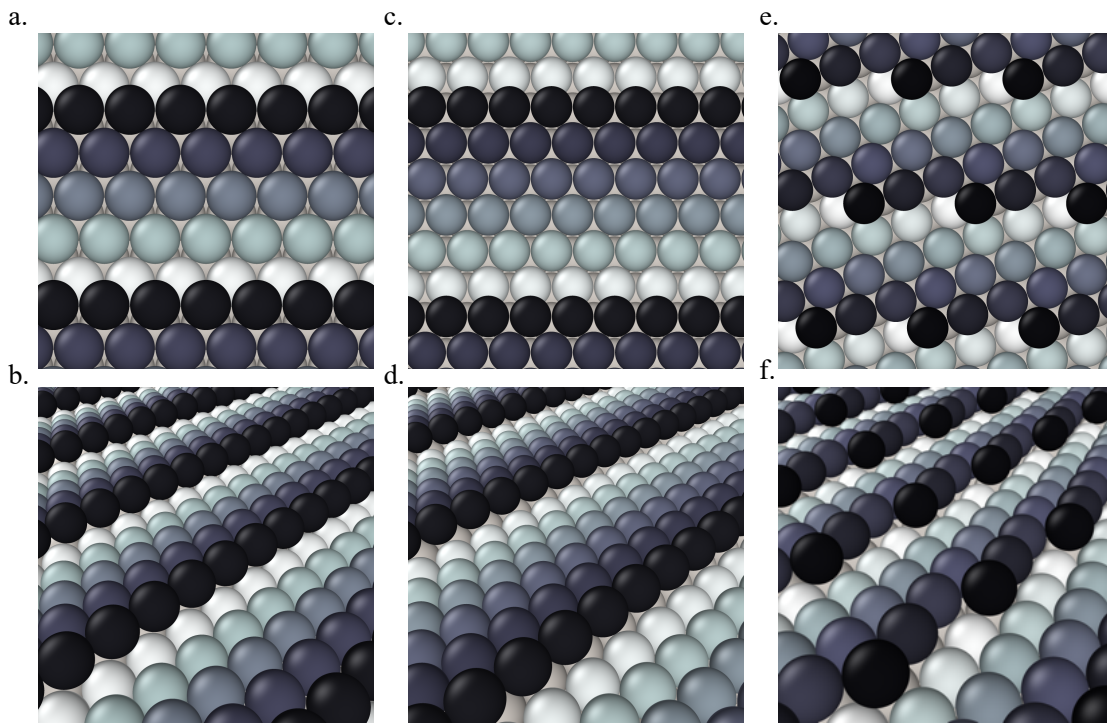


Figure 4.4: Ball Models of various clean surfaces considered. (a) Pt(553) top view, (b) Pt(553) side view, (c) Pt(557) top view, (d) Pt(557) side view, (e) Pt(643) top view, Pt(643) side view. Colors represent the z-position of the atoms. Black balls represent the step edge and others represent the terrace.

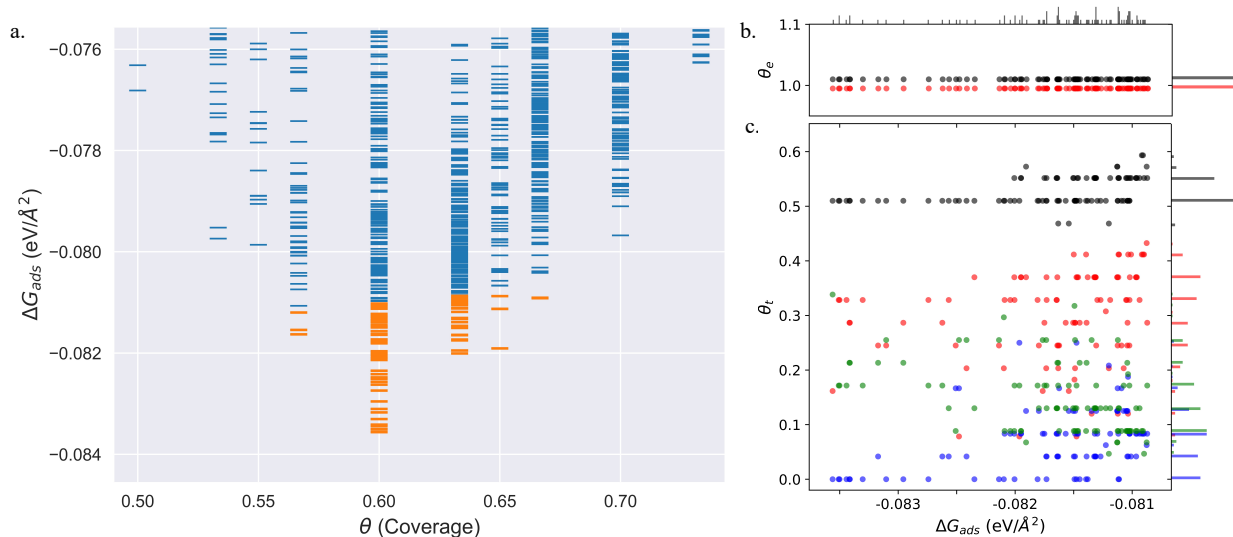


Figure 4.5: (a) Adsorption free energy per unit surface area  $\Delta G_{ads}$  (at  $T=300\text{K}$ ,  $P=1\text{ atm}$ ) plotted against CO coverage ( $\theta$ ) on Pt(553). Yellow markers represents the structures defining the Low energy minima ensemble. (b) and (c) represent the coverage of CO on the Pt step-edge and terrace as a function of the  $\Delta G_{ads}$  respectively.  $\bullet$  represents top site,  $\bullet$  represents bridge site,  $\bullet$  represents hollow sites and  $\bullet$  represents the total coverage. The density of different sites at various coverages is represented by the histogram attached to the right ordinate axis. The density of structures as a function of  $\Delta G_{ads}$  is represented by the histogram on the top abscissas axis. In plots (b) and (c), to distinguish the points, we move the red points (top sites) on the y-axis by  $-0.005$ , green points (hollow sites) have been moved by  $+0.005$  and black points (total coverage) have been moved by  $+0.01$ .

### 4.3.1 Pt(553)

Pt(553) can be represented as Pt(S)-[5(111)  $\times$  (111)] in step notation since it is formed by a 5 atom wide Pt(111) terrace followed by a mono-atomic 111-type step as shown in Fig. 4.4(a) and (b). One challenge is that no long-range order for CO is found experimentally on such stepped surfaces, while a unit cell is required to model the surface. We tackle this by considering several unit cells, that describe a rather large area of the step and terrace. This is possible only because we obtain a fast and accurate neural network potential enabling to sample a very large number of configurations for CO molecules, at variable coverage, on these unit cells. Such a sampling would be extremely computationally costly using DFT calculations. For Pt(553) we use 3x1, 4x1, 6x1 unit cells, with the first periodic direction

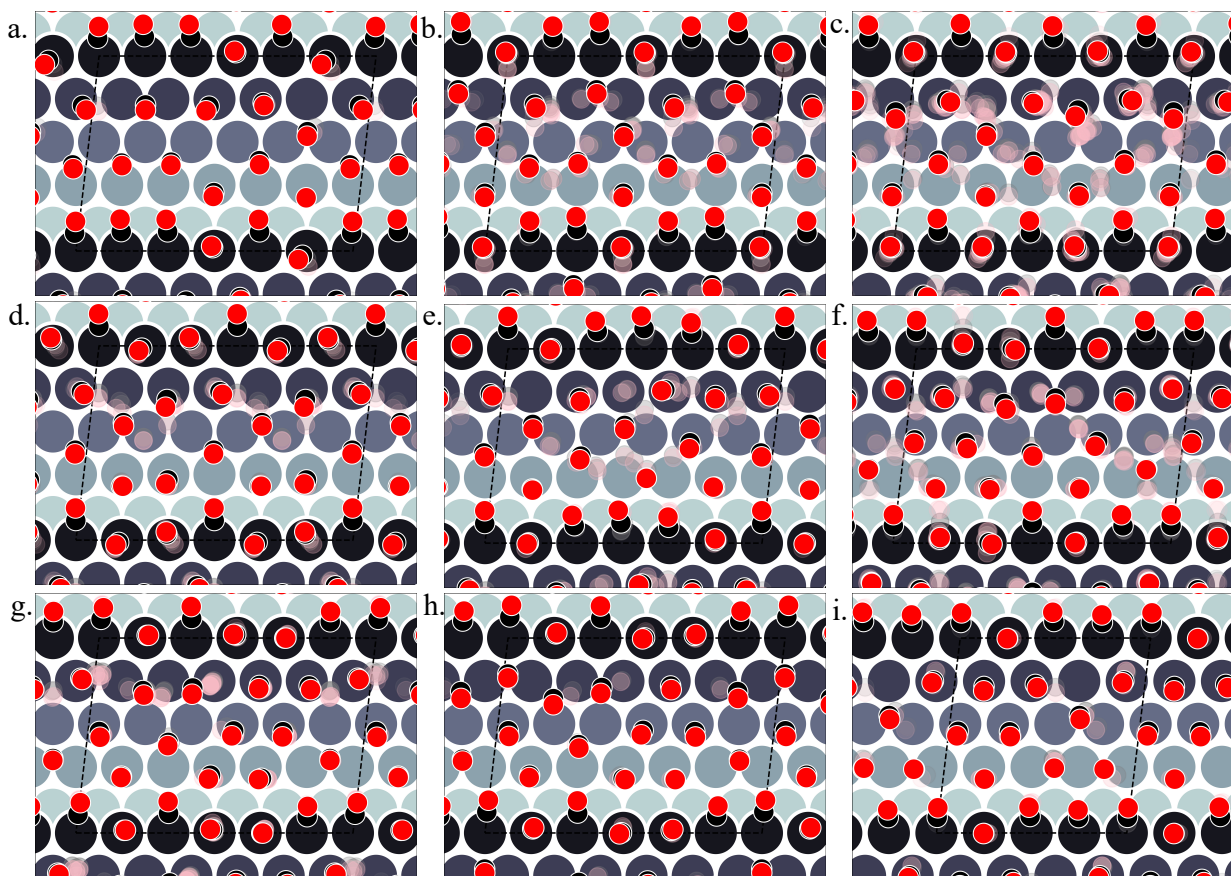


Figure 4.6: Various structures of CO orientations patterns observed in the LEME for Pt(553). (a) represents structures with  $\theta = 0.56$ ; (b)-(e) represent structures with  $\theta = 0.6$ ; (f)-(h) with  $\theta = 0.63$ ; (i) with  $\theta = 0.65$ . The Pt atoms are shown using a colormap (color-bar representing z-position of the Pt atom). For a given pattern, the lowest energy orientation of CO is shown using the solid black and red balls representing the positions of C and O respectively and the ensemble of structures are represented by the “cloud” of pink and grey balls.

being along the step edge while the second one ( $x_1$ ) corresponds to the (long) periodicity between one step and the next one. With these unit cells, we can explore the various organisation periodicities of molecules along the step edge using basin hopping simulations.

We calculate the total Gibbs free energy of adsorption for all CO molecules, including entropy terms for the gas phase molecules but neglecting the vibrational entropy for adsorbed molecules. This adsorption energy is then normalized to a  $1 \text{ \AA}^2$  surface area, to be able to compare different unit cells. Fig. 4.5(a) shows the Gibbs adsorption free energy of CO

per unit surface area on Pt(553) as a function of CO coverage. A total number of 1501 local minima configurations have been explored, and their free energy is shown by dashed lines in fig 2a, the orange lines (97 structures) representing the low energy accessible region, called here the low energy metastable ensemble (LEME). The energy interval for the LEME is chosen to 1 kT per CO adsorbate. The LEME found on the Pt(553) surface consists of structures with a coverage between  $\theta = 0.55$  and  $\theta = 0.67$ . So the first clear comment is that we do not find a single stable structure, and CO coverage for the considered T,P conditions, but in contrast, a large number of competing low energy structures are seen corresponding to a range of coverage. This simply explains the absence of long range order in the experiment. Common points and differences between these 97 structures in the LEME can be seen from Fig. 4.5, where the coverage for various CO binding modes (top, bridge, hollow) is indicated on the step edge (Fig 4.5 (b)) and on the terrace (Fig 4.5 (c)), as a function of the adsorption free energy per unit surface area. The data used to create this plot has been included on the Appendix (see Table B.1). All structures in the LEME have the step edge completely populated by on-top CO molecules, with one CO per Pt atom. The coverage of the terrace ranges between 0.5 and 0.6 ML, where in average on the LEME structures, top site occupation is dominating (average coverage 0.3 ML), followed by hollow sites (average coverage 0.14) and bridge sites (average coverage 0.07). Therefore, the amount of top CO molecules is in average about twice that of the multiply bound CO on the terrace of Pt(553).

Fig. 4.6(a-i) shows the structural arrangement of CO at various coverages between 0.55 and 0.67 found in LEME. For a given most stable structural arrangement of CO on the Pt(553) surface at a given coverage, small variations in the CO positions generate structures that have adsorption free energy within the energy window. From the LEME configurations obtained using Basin Hopping Monte Carlo (BHMC) simulations, unique configurations are identified by converting the chemical environment into graph representations using SurfGraph code developed by Deshpande et al.<sup>207</sup> The most energetically favourable structure (lowest Gibbs free energy) is shown by the red and black balls in Fig. 4.6(a-i) and the small variations are

shown using the “clouds” of pink and grey balls (representing the oxygen and carbon atoms respectively).

As proposed by the experiments, the step edge is totally covered by on-top CO molecules.<sup>120,228,235</sup> CO adsorption results from the competition between stabilizing CO-surface interactions and destabilizing CO-CO lateral interactions that increase with CO coverage. Hence, the CO equilibrium coverage depends on the strength of the molecule-surface interaction and on the CO chemical potential (governed by T and P). Step sites correspond to a lower Pt coordination and hence a stronger CO-Pt interaction than the (111) terraces (see Appendix section B.2). At the step, a coverage of 1 CO per Pt can be reached, but CO molecules present a different angular orientation to limit the CO-CO interactions. Such CO orientation leads to tilt angles from  $-25^\circ$  to  $46^\circ$ , where negative angles represent tilt towards the upper terrace and positive angles representing tilt towards the lower terrace. Different tilt motifs are seen along the step edge with x2, x3, or x6 periodicities providing quasi-degenerate energies. At a chemical potential of  $-15.29$  eV (corresponding to  $T=300\text{K}$  and  $P=1$  atm), the most favorable coverage of CO is found to be 0.6 ML (as seen from Fig. 4.5(a)), with 54 structures in the LEME with this coverage. Fig. 4.6(b-e) represent the four CO arrangement patterns observed at this coverage (in decreasing stability order). In these structures, we find that CO molecules on the terrace arrange in distorted hexagonal patterns, the denser atomic directions being tilted  $\sim 25\text{-}36^\circ$  with respect to the Pt step edge. These arrangements are limited by the short width of the terraces, but mimic the Moiré-like patterns seen on Pt(111). CO on the step Pt atoms interestingly arranges in a manner such that the quasi-hexagonal pattern on the lower terrace can be maintained. In a way the modulation of CO tilt angle along the step initiates the organisation of molecules on the lower terrace. Descending from the step to the lower terrace, the highly coordinated Pt atoms at the bottom of the step are not populated. The lack of CO at the bottom of the step is also observed at other coverages throughout the LEME structures for Pt(553) and can be attributed to reducing the repulsion between the on-top step CO and the CO on the lower terrace. In contrast, the

Pt row beyond the step edge on the upper terrace shows a high occupation of CO (0.5 - 0.83 ML). The coverage of 1 ML at the step edge implies a smaller coverage on the terrace of 0.5ML. The C-C distance at the densely populated step is between 2.8 and 3.0 Å (compared to 2.818 Å for the Pt-Pt distance), whereas the first C-C neighbor distance on the terrace varies between 3.2 and 3.4 Å, underlining the lower CO density on the terrace coming from a weaker adsorbate-surface interaction.

Three structures in the LEME are found at  $\theta = 0.56$  which are shown in 4.6(a). At this low coverage, we don't see any systematic arrangement of CO on the terrace, but the step edge still has a 1 ML CO coverage. At  $\theta = 0.63$ , we see 3 different patterns (33 structures) of CO arrangement on Pt(553) shown in Fig.4.6(f-h) with increasing adsorption free energy order. All the structures at this coverage have a 6x1 periodicity with a tilt angle of  $-17^\circ$  to  $44^\circ$  along the fully populated step edge. The CO coverage on the terrace is 0.54 (13 CO atoms on 24 Pt atoms). The CO arrangement on the terrace is less ordered compared to the arrangement found at  $\theta = 0.6$ , making the quasi-hexagonal pattern less visible. At  $\theta = 0.65$ , we observe only a 4x1 unit cell periodicity along the step edge and 4 structures manifest in the LEME structures (Fig.4.5(i)). Similar to the structures found at  $\theta = 0.6$ , we find that CO molecules on the terrace arrange in distorted hexagonal patterns with the denser atomic directions being tilted  $\sim 55^\circ$  with respect to the Pt step edge. A higher mobility of CO molecules is observed near the upper terrace, while the CO positions near the lower terrace and step edge remain approximately constant among the 4 structures. The C-C distance on the step with all CO molecules on the top site is between 2.8-3.0 Å and the first C-C neighbor distance on the terrace varies between 3.0-3.2 Å. At  $\theta = 0.67$ , we find one structures in the LEME with a 6x1 periodicity and CO arranging along parallel lines that are angled  $55^\circ$  (anti-clock wise) with respect to the step edge (see Appendix Fig. B.1).

Overall, for Pt(553), the low energy metastable ensemble of structures has a coverage between 0.56 and 0.65. The short terrace length in combination with the (111)-type step only allows clear quasi-hexagonal arrangements of CO. The low coordination Pt atoms at the step site

and the possibility of varying tilt angles of CO around the step edge enables a higher local coverage with CO adsorbing on the top site. On the terrace, C-C first neighbor distance decreases as the coverage increases to incorporate more CO on the surface. Comparing the site distribution on the terrace, we see that the majority of the structures have a higher top site coverage followed by hollow site occupation and the least occupied sites are the bridge sites.

### 4.3.2 Pt(557)

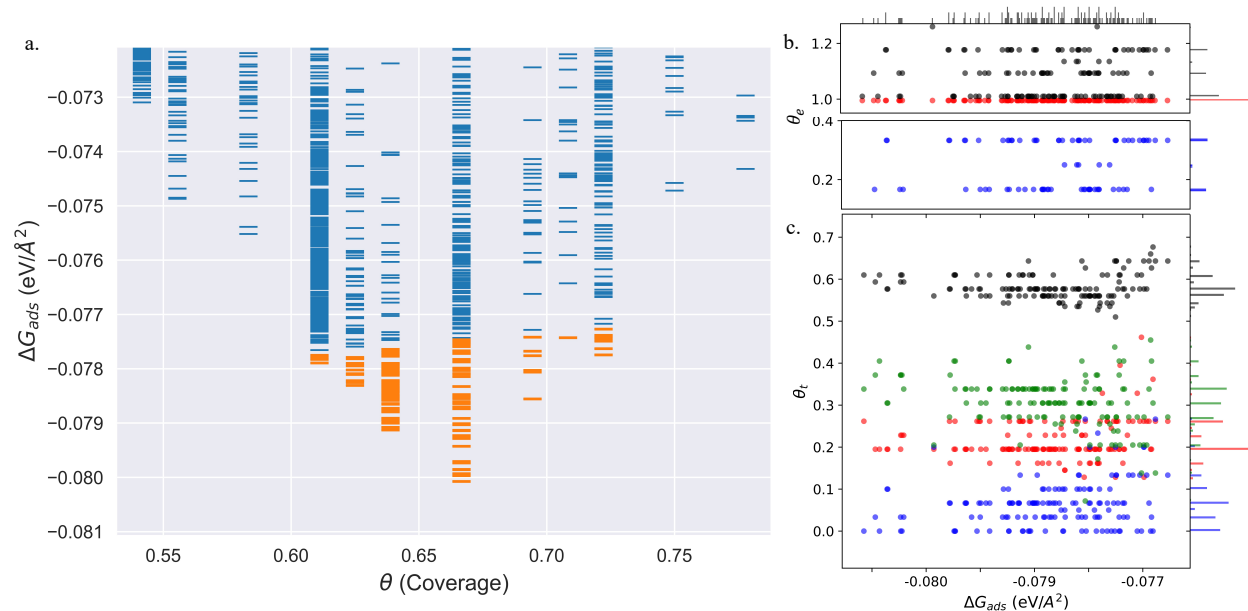


Figure 4.7: (a) Adsorption Free energy per unit area ( $\Delta G_{ads}$ ) plotted against CO coverage ( $\theta$ ) on Pt(557). Yellow markers represents the structures defining the LEME.(b) and (c) represent the coverage of CO on the Pt step-edge and terrace as a function of the  $\Delta G_{ads}$  respectively. ● represents top site, ● represents bridge site, ● represents hollow sites and ● represents the total coverage. The points in (b) and (c) have been moved in a similar fashion as Fig. 4.5 to distinguish the points better.



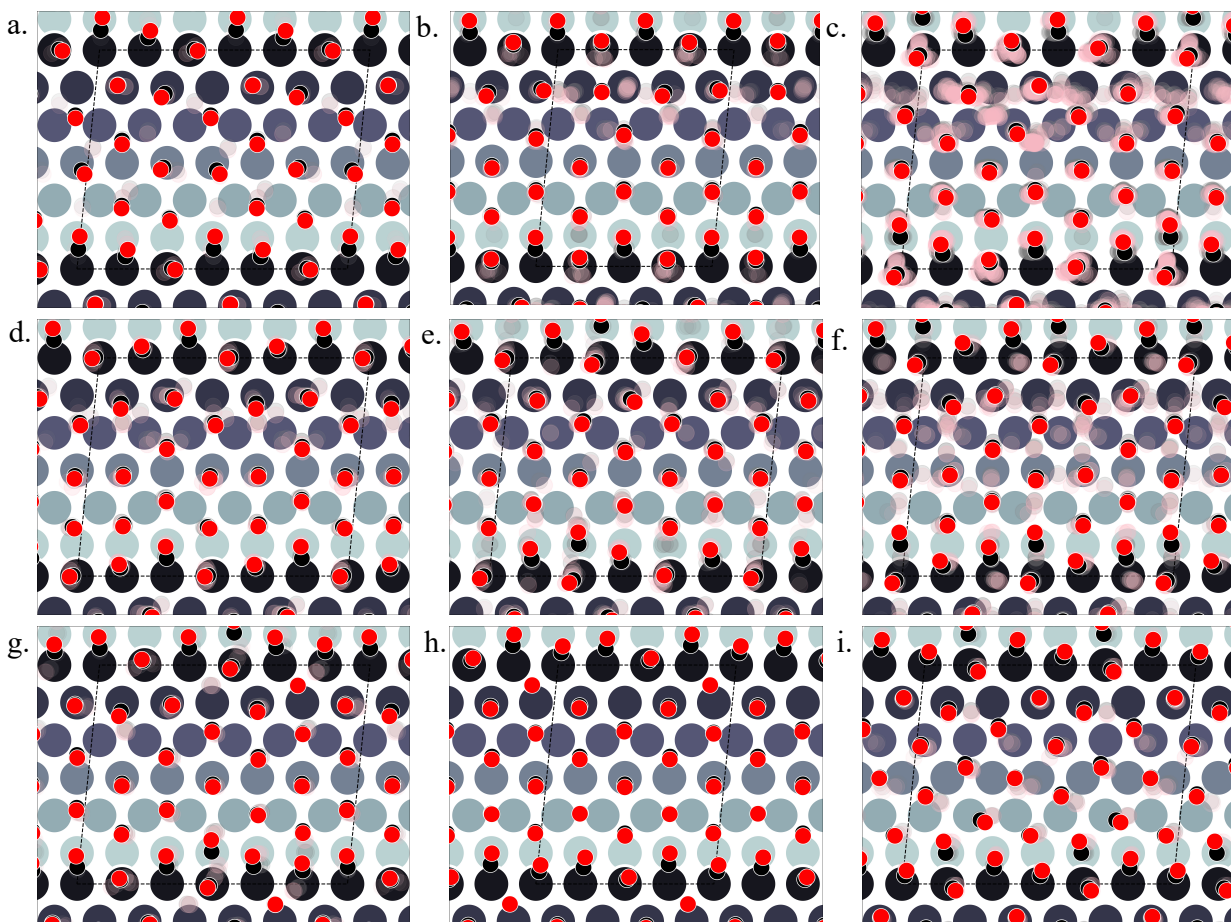


Figure 4.8: Various structures of CO orientations patterns observed in the LEME for Pt(557). (a) represents structures with  $\theta = 0.61$ ; (b) with  $\theta = 0.625$ ; (c) with  $\theta = 0.64$ ; (d-f) with  $\theta = 0.66$ , (g) with  $\theta = 0.69$ , (h) with  $\theta = 0.71$ , and (i) with  $\theta = 0.72$ . The Pt atoms are shown using a colormap (color-bar representing z-position of the Pt atom). For a given pattern, the lowest energy orientation of CO is shown using the solid black and red balls representing the positions of C and O respectively and the ensemble of structures are represented by the “cloud” of pink and grey balls.

Pt(557) can be represented as Pt[6(111)  $\times$  (100)] in step notation since it is formed by a 6 atom wide Pt(111) terrace followed by a mono-atomic 100-type step as shown in Fig. 4.4(c) and (d). We use 3x1, 4x1, and 6x1 unit cells to explore the CO organization on the surface. The low energy CO configurations on Pt(557) at RT and 1 atm CO pressure found by our HDNNP and basin hopping approach correspond to coverages between 0.61 ML and 0.72 ML with 142 structures in the LEME (Fig.4.7(a)). Similar to the Pt(553), the step site is



completely occupied by on-top CO molecules. However, the more open character of the (100) steps permits to have in addition CO molecules bridging between a step edge atom and one Pt immediately below in the lower terrace. The step edge atom can hence be bound to two CO molecules, one top and one bridge. In that case (as seen in figure 4.8(c,e-g and i), the top molecule is not leaning towards the lower terrace, but towards the upper terrace. With that mechanism, the coverage at the step can reach up to 1.25 ML (the bridging CO molecule is shared between the two Pt atoms (Fig. 4.7(b))). The uneven tilt of the CO molecules at the step edge initiates the organisation on the terrace, with quasi-hexagonal ordering throughout the LEME and helps incorporate higher coverage on the square step. The tilt angles range between  $-20^\circ$  and  $50^\circ$  with x2 and x3 periodic motifs that provide quasi-degenerate energies. For the structures in the LEME, on terrace, the coverage ranges from 0.50 to 0.67 ML, with on average, hollow sites dominating with a coverage of 0.3 ML, top sites with 0.22 ML and bridge sites at 0.06 ML (Fig. 4.7(c)). Hence, on average, on the terrace, multiply bounded CO on the terrace is in average almost twice that of the top site. This strongly contrasts with the previous case of Pt(553) where on the on-top CO was dominating on the terrace, indicating that the type of step has a strong influence on the configuration of CO molecules. At 300K and 1 atm condition, the most stable structure is found at  $\theta = 0.67$ . At this coverage, we find three types of CO arrangements as shown in Fig. 4.8(d),(e) and (f) (in the stability order). For the most stable structure at  $\theta = 0.67$ , CO arranges along parallel lines that are tilted  $\sim 30^\circ$  with respect to the Pt step edge (Fig. 4.8(d) - arrangement shown using black and red balls). Such a positioning of CO molecules on the terrace, which is accompanied by the CO molecules creating a x3 motif on the step with varying tilts towards the lower terrace, helps create a quasi-hexagonal pattern. Change of CO positions at the lower terrace (mainly between hollow and bridge site) results in quasi-degenerate LEME structures that have been represented by the pink and gray “clouds” in Fig. 4.8. At the same coverage, we find another orientation of CO at the step edge (with a x2 motif) with alternating CO molecules tilting towards and away from the lower terrace (Fig. 4.8(e)). At this coverage,

the C-C distance (first neighbor) varies between 2.7-3.18 Å on the terrace and 2.8-3.18 Å on the step edge.

Within the LEME, lower coverage structures are found with  $\theta = 0.61$  (4 structures),  $\theta = 0.625$  (12 structures), and  $\theta = 0.64$  (59 structures). At higher coverages, LEME includes structures with  $\theta = 0.69$  (6 structures),  $\theta = 0.71$  (1 structure),  $\theta = 0.72$  (8 structure). At these coverages, the quasi-hexagonal pattern is maintained on the terrace and the step coverage remains 1 ML as seen in Fig. 4.8. The CO quasi-hexagonal lattice rotation with respect to the step edge, is coverage dependent. At  $\theta = 0.61$ , CO arranges along parallel lines that are tilted  $\sim 23.5^\circ$ . At  $\theta = 0.625$  and  $\theta = 0.64$ , the angle increases to  $30^\circ$  and at  $\theta = 0.66$  the tilt angle further increases to  $\sim 40^\circ$ . Further increase in coverage leads to reduction in the tilt angle to  $30-35^\circ$  at  $\theta = 0.69$  and  $\theta = 0.71$  and to  $\sim 20^\circ$  at  $\theta = 0.72$ . The different rotation angles of the CO lattice allows maintaining approximately similar C-C first neighbor distances on the terrace ( $\sim 3.15-3.22$ ) while allowing more CO to be incorporated on the surface. Though out the LEME ensemble, the step manifests a x2 or x3 repeating motif. Except at  $\theta = 0.61$  and  $\theta = 0.71$ , all the other structures in the LEME show additional CO molecules bridging between the step edge and lower terrace allows for incorporating more CO on the surface. This increasing the step edge coverage to 1.17 ML.

Overall, for Pt(557), the low energy metastable ensemble of structures has a coverage between 0.61 and 0.72, slightly higher than the case of Pt(553). The formation of a more ordered hexagonal pattern for the CO adsorbates on the Pt substrate can be attributed to the longer terrace length and the square Pt(100) step. One striking difference concerns the binding sites of CO on the terrace, with the dominant multiply bonded CO on the (557) surface, while top sites were twice more numerous on the (553) termination. The more open Pt(100) step allows CO bridging between the terrace and the step edge which in turn allows the hexagonal pattern of CO lattice to continue across the stepped surface. These three factors have a significant impact on the CO arrangement on the surface.

### 4.3.3 Pt(643)

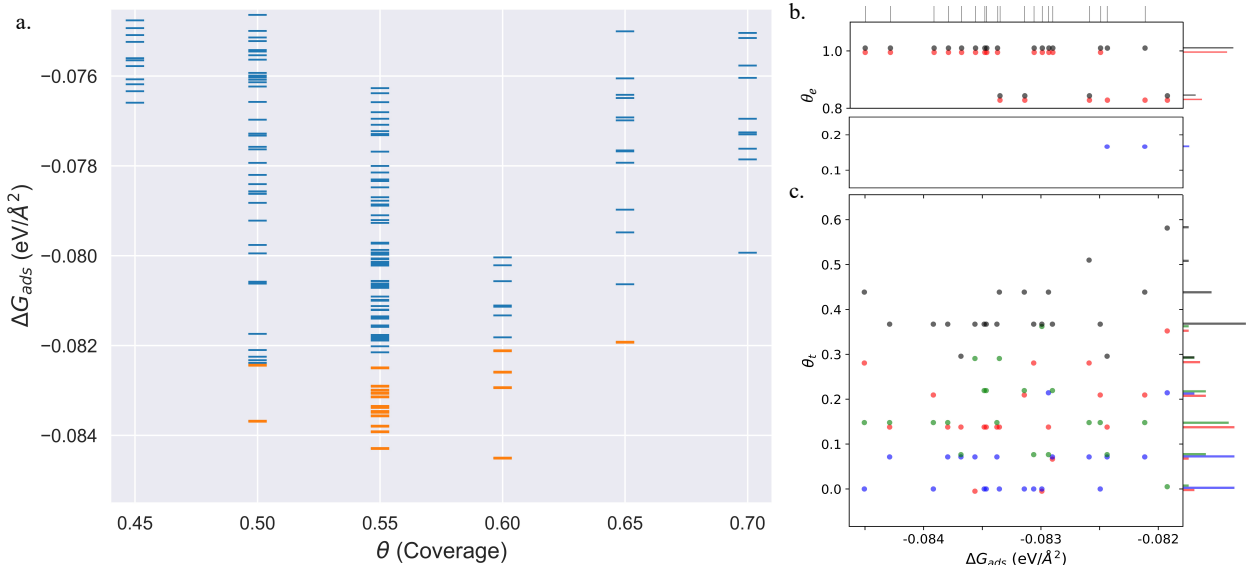


Figure 4.9: (a) Adsorption Free energy per unit area ( $\Delta G_{ads}$ ) plotted against CO coverage ( $\theta$ ) on Pt(643). Yellow markers represents the structures defining the LEME.(b) and (c) represent the coverage of CO on the Pt step-edge and terrace as a function of the  $\Delta G_{ads}$  respectively. ● represents top site, ● represents bridge site, ● represents hollow sites and ● represents the total coverage. The points in (b) and (c) have been moved in a similar fashion as Fig. 4.5 to distinguish the points better.

The Pt(643) surface consists of Pt(111) terraces separating Pt(100) steps that are broken by Pt(110) kink sites. The kink shows a convex site on a 6-coordinated Pt atom, next to a concave site on a 8-coordinated Pt atom (Fig. 4.4(e,f)). Basin hopping simulations using the neural network potential were run on a (2x1) unit cell (creating a 6 Pt atom step edge with the kink site) which showed a CO coverage from 0.5 to 0.65 ML (Fig. 4.9(a)) in the low energy minima ensemble of structures (20 structures) at 300 K and 1 atm conditions, the most stable structure having a coverage of 0.6 ML. The coverage of CO on the Pt step edge ( $\theta_e$ ), is shown in Fig. 4.9(b). In the ensemble, 4 structures show  $\theta_e = 0.83$  ML and 16 structures show  $\theta_e = 1.0$  ML. Two structures (with  $\theta_e = 1$  ML and  $\theta = 0.7$  ML) have CO on the bridge site at the concave site of the kink, which are shown using blue points on Fig.

4.9(b). For all the other structures, CO occupies the top site on the step edge and kink atoms. Compared to Pt(553) and Pt(557), Pt(643) has a smaller terrace length which does not allow a similar rotated hexagonal pattern arrangement of CO. On the contrary, the short terrace combined with the the kink site and the square step edge forces the CO organization parallel to the dense Pt atoms arrangement throughout the LEME structures. The short terrace also limits the number of structures in the LEME, the adsorbate layer being less fluxional.

At  $\theta = 0.5$ , 2 structures exist in the LEME (Fig. 4.10(a)). At this coverage, the step sites are fully covered with on-top CO and on the terrace top to bridge ratio is 1:1. The CO assembly at this coverage is less ordered, which results in more distributed positions. At  $\theta = 0.55$ , 13 structures ((Fig. 4.10(b))) are observed in the LEME which have all except two structures with low coordination step Pt atoms have a  $\theta_e = 1$  ML and the remaining two have a  $\theta_e = 0.83$  ML. At this coverage, on average over the LEME structures, the top to hollow site occupation ratio on the terrace is approximately 1:1 while bridge site occupation is negligible. The tilt of CO molecules at the kink atom can be large ( $\sim 40^\circ$ ). On the terrace, at  $\theta = 0.55$ , the parallel CO arrangement is broken near the kink site.

The most stable structure on Pt(643) is found at a  $\theta = 0.6$  and is shown in Fig. 4.10(c). Similar to the structures at  $\theta = 0.55$ , CO align along lines that are parallel to the step edge but the symmetry is maintained throughout. In the ensemble at this coverage,  $\theta_e$  varies from 0.83-1 ML and all CO adsorbed at the step occupy the top site. CO molecules on the terrace occupy the top (on average 0.23 ML) and hollow sites (on average 0.125 ML) with only minor (or no) occupation of bridge sites. The short terrace and parallel arrangement of CO with respect to the substrate Pt atoms possibly does not allow the bridge site occupation. At  $\theta = 0.65$ , we find only 1 structures in the LEME as shown in 4.10(d) where we observe similar arrangement of CO as for  $\theta = 0.55$ , where the CO alignment pattern is broken near the kink Pt atom site. At this coverage, once again top sites dominate the occupation on the terrace with 0.36 ML.

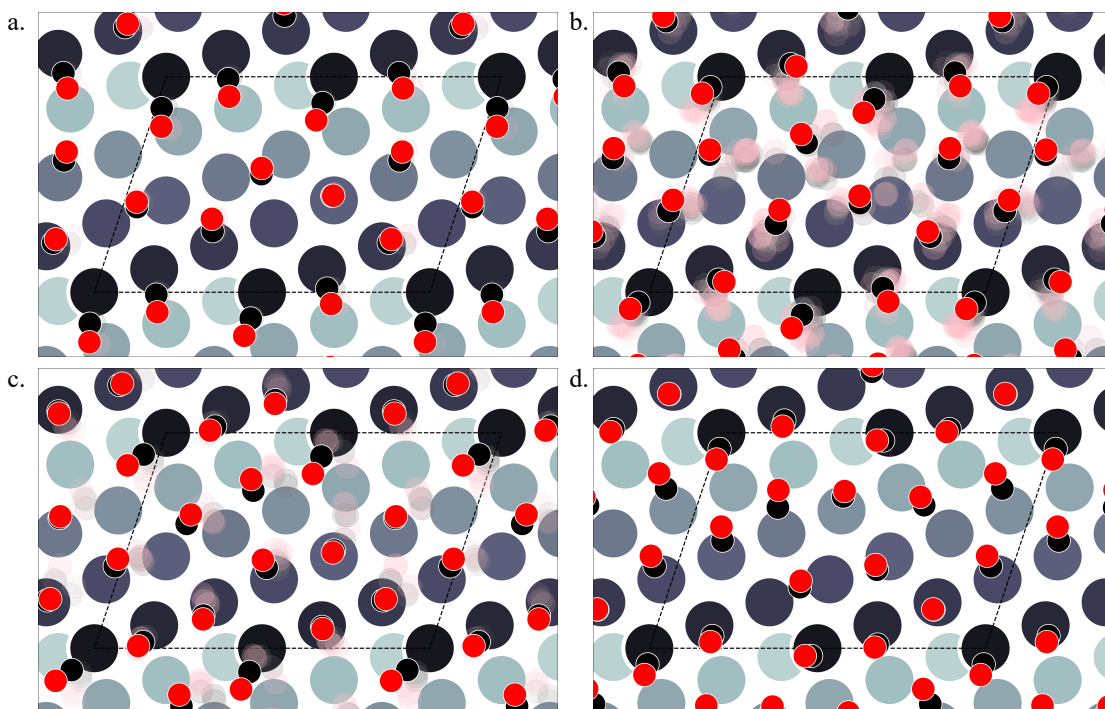


Figure 4.10: Various structures of CO orientations patterns observed in the LEME for Pt(643). (a) represent structures with  $\theta = 0.5$ ; (b) with  $\theta = 0.55$ ; (c) with  $\theta = 0.6$  and (d) with  $\theta = 0.65$ . The Pt atoms are shown using a colormap (color-bar representing z-position of the Pt atom). For a given pattern, the lowest energy orientation of CO is shown using the solid black and red balls representing the positions of C and O respectively and the ensemble of structures are represented by the “cloud” of pink and grey balls.

Overall, on Pt(643), we see a combined effect of a kink site, square step and a small terrace length which leads to an arrangement of CO that aligns parallel to the step edge. On average across the LEME structures we find an equal occupation of top and hollow sites while bridge occupation is limited. Such a behaviour is unique compared to Pt(553) and Pt(557) where we saw a development of hexagonal patterns of CO arrangement. Understanding the CO organization on such a surface with kinks and step can be important since the low coordination kink site appearing on this surface can show specific catalytic activity and also can be the starting point of restructuring event under CO pressure.

## 4.4 Conclusion

The organization of CO adsorbates on different surfaces including steps and kinks and presenting (111) terraces was modelled under an ambient pressure of CO at room temperature, by combining a neural network potential, trained using first principle structures, including energies and forces, and a basin hopping approach to efficiently explore the various configurations of the CO adsorbates, describing an extensive number of structures ( $\sim 4500$ ). The main conclusions are summarized below. In the considered conditions, the step edge (or kink) is totally occupied by on-top CO molecules, while terraces show a partial occupation close to 0.5 ML. One recurring feature is that the surface (Pt(553), Pt(557) or Pt(643)) does not show a single most stable CO adsorption structure at the considered CO chemical potential, but that a large number of adsorbate configurations on the terrace are close in energy. By considering a threshold of 1 kT per CO adsorbate, we defined the LEME, ensemble of structures thermally accessible, which contain 97, 142 and 20 distinct structures for the considered Pt(553), Pt(557) and Pt(643) unit cells respectively. These structures show imperfect quasi-hexagonal ordering on the terraces, while the arrangement along the step edge is more ordered, including different tilts with respect to the terrace normal to decrease CO-CO interactions. The large number of competing structures should result in a mixture of very small domains of different configurations, and hence an absence of long range order, as seen in the experiments. Some common results arise from this study. The first one concerns the distribution between top and multiply bonded CO on the (111) terraces. Stable adsorption configurations on the Pt(553) surface present more top site CO than multiply bonded ones on the (111) terrace, resulting in average in two top site CO for one multiply bonded CO. The situation is completely modified on the (111) terraces of the (557) surface, where in average two multiply bonded CO are seen for one top CO. On the kinked Pt(643) surface, the top CO molecules again dominate on the surface. These results should be compared with the extended Pt(111) surface where in the same conditions an equal number of top

and multiply bonded CO molecules are found. The three considered surfaces show different structures of the step edge: a (111) step for Pt(533), a (100) step for Pt(557) and a kink site with a short terrace for Pt(643). Since the binding energy of top CO is very close to that of multiply bonded CO on the (111) terrace, the structure of the step plays a key role in initiating the arrangement of CO on the lower terrace, since the CO at the step with their different amount of tilt towards the terrace act as a boundary condition to organize the adsorbates on the terrace. The (111) steps favor the construction of quasi-hexagonal layers where top site CO dominates, presenting alignments of CO at various possible angle with respect to the step edge, while in contrast the (100) steps pin configurations with a large fraction of multiply bonded sites.

Our calculated results agree well with the experimental data from Farias et al. in electrochemical conditions where Pt(322) and Pt(311) surfaces, that present a (100) step, show a large amount of bridge site CO on their terraces, while Pt(332) and Pt(331) surfaces, with a (111) step, show a very large majority of top site CO.<sup>235</sup> They also agree with the UHV experiments of Tränkenschuh et al. in the case of Pt(553)).<sup>228</sup> The kink surface (Pt(643)) shows a different type of arrangement where CO aligns parallel to the step edge. This demonstrates that the atomic arrangement at the steps controls the structure of the CO ad-layers at least in a zone close to the step edge.

Understanding CO adsorption at stepped surfaces is a prerequisite to study their catalytic reactivity in reactions involving CO. It is also of key importance as the initial structure leading to surface restructuring upon CO adsorption at ambient pressure. Indeed, extended Pt step edges are known to undergo reconstruction driven by CO adsorption at high coverage. Our study opens the way to realistic modelling of these restructuring events.

## CHAPTER 5

# Atomic scale mechanism of platinum catalyst restructuring under the pressure of CO gas

### 5.1 Introduction

Catalysis is central to chemical production, pollution abatement, and energy transformation. Supported metal catalysts are the workhorses of the largest current chemical processes. The notion of “active site” on the catalyst, i.e. the ensemble of surface atoms responsible for bond-breaking and forming steps on the reactants, and its structure and dynamics under reaction conditions are key for understanding the catalytic performance.<sup>266–268</sup> There are now clear evidences that surface sites of metal catalysts might not remain as prepared during a catalytic reaction; their structures and/or compositions evolve in the reaction conditions, under a pressure of reactants and/or products of the reaction.<sup>20,24,26,43–45,47,269,270</sup> For example, in reducing gas H<sub>2</sub> the surface region of an as-prepared Rh-Pd core-shell structured bimetallic catalyst restructured to a Pd-rich surface<sup>271,272</sup> while the surface of as-synthesized Pt-Cu alloy nanocubes restructured to a Pt skin layer.<sup>273</sup>

For a simpler case of a monometallic catalyst, tracking the surface structure of the stepped Pt(557) surface at room temperature in CO at different pressures revealed that the step edges start to restructure at a CO pressure as low as 10<sup>-8</sup> Torr and that a massive reconstruction occurs at a pressure of 0.5 Torr, the surface getting homogeneously covered by nanoclusters with a size of 2.2 nm.<sup>55</sup> This breakup of the surface creates more under-coordinated sites. When the CO pressure is decreased to 5×10<sup>-8</sup> Torr, these nanoclusters reunite back to a



stepped surface with curled step edges. The reversible formation of nanoclusters shows that this restructuring is driven and maintained by the high CO pressure.<sup>55</sup> Density Functional Theory (DFT) calculations showed that under a model CO coverage of 1 ML a surface restructured with triangular shape arrangements is more stable than the non-reconstructed surface. At the same time, restructuring of Pt(557), Pt(100), and Pt(110) was also observed in other gases such as O<sub>2</sub>.<sup>274</sup> A similar phenomenon occurs on Cu(111), Ni(557), Au(111), Au(110), Co(0001) in the presence of CO.<sup>19,23,24,99,275</sup> The early work by Tao et al. on Pt(557)<sup>55</sup> evidences the extensive reconstruction but did not explore at an atomic scale the elementary steps and mechanism of the surface transformation under a pressure of CO, which is the focus of the present work.

These earlier studies show that as-prepared surface sites could be readily transformed by the action of the adsorbates, rendering synthetic efforts to control the initial structure of the surface somewhat meaningless. Metal sites on the “surface clusters” can have lower coordination than those at the initial terrace or step sites, which can alter the activity and selectivity of the catalytic reactions.<sup>276–286</sup> Therefore, exploration of how the surface of a metal catalyst is restructured at an atomic scale in a gas phase of reactant(s) is key to identify catalytic active sites, fundamentally understand the catalytic mechanisms at a molecular level, and predictably develop novel, more active, more selective, or more durable catalysts.<sup>287,288</sup>

Other than the studies on metal single crystal surfaces, restructuring of the surface of metal nanoparticles in reactant gas, particularly Pt nanoparticles in CO or CO and O<sub>2</sub> mixture was studied through in-situ TEM,<sup>223,289</sup> in-situ IR,<sup>223</sup> EXAFS,<sup>25</sup> and AP-XPS.<sup>25</sup> For instance, the oscillatory change between faceted Pt nanoparticles and rounded Pt nanoparticles during catalysis of CO oxidation at 450°C was observed by Vendelbo et al.<sup>289</sup> Literature established the coupling of the increase and decrease of CO conversion with the proposed switch between the faceted nanoparticles with low-miller index surface and a rounded one with a mixture of low and high (i.e. stepped) Miller index surfaces.<sup>289</sup> The restructuring of the morphology

of metal nanoparticles in pure CO was reported.<sup>289</sup> The reconstruction of (100) terraces of Pt nanoparticles to high Miller index surface was suggested with in-situ STEM and in-situ IR.<sup>223</sup> This observation was supported by computation of adsorption energies which found the high miller-index surfaces such as (211) and (311) with adsorbed CO is thermodynamically favorable over CO on Pt(100).<sup>223</sup>

Although the surface restructuring phenomenon of metal catalysts under the pressure of a reactant gas is well documented experimentally, its origin and formation mechanism is not yet understood at the atomic scale, hindering rational catalyst design.<sup>19,24,55,99</sup> First principle atomistic modeling could be a major approach to explore the surface restructuring phenomenon under the pressure of a gas. Nevertheless, computational studies of metal catalyst surfaces and their restructurings under high adsorbate coverage are largely limited due to four major challenges: (1) the high computational expense of exploring surface reactivity using accurate first-principles calculations on surfaces described by large unit cells, (2) the numerous combinations of adsorption configurations possible at high coverages, (3) the large space of configuration for the metal surface restructuring under a pressure of a gas, and (4) the interdependence between the surface local structure/metallic coordination and the adsorbate coverage. Hence, to provide atomic-scale insights on adsorbate-induced restructuring on catalytic systems, computational modeling requires a fast but accurate energy and force calculator to enable the exploration of a large space of configurations.

To demonstrate how the atomic-scale restructuring mechanism of a metal surface under a pressure of a reactant gas could be uncovered, we integrate in-situ scanning tunneling microscopy (STM) experiments and large-scale simulations. Computationally, the determination of the CO overlayer coverage and arrangement for each Pt structure considered here requires sampling a large number of configurations, around 13000 single-point calculations. Considering the size of the unit cell required, this sampling cannot be performed directly with DFT and was critically enabled here by a fast neural network potential trained on first principle Density Functional Theory (DFT) calculations. Not only one but an ensemble

of low-energy configurations exists for the CO overlayer, and each configuration of the Pt atoms and this fluxionality of the adlayer will be important for the restructuring kinetics. The approach developed here enables an unbiased statistical sampling of the CO-Pt system at a given temperature and CO pressure, i.e. a grand canonical treatment at variable CO coverage. For optimal accuracy, the low-energy ensemble of structures was recalculated using DFT, so that all energies are of DFT accuracy.

Our combination of methods shows that the Pt surface restructuring is initiated by the formation of a few atoms large protrusions along the step edges and is driven by the high CO coverage, stabilizing low coordination sites. Small Pt islands, multiply coordinated with CO molecules, analogous to polymetallic carbonyl coordination complexes, can detach from the step edge to form subnano-size islands on the Pt terraces. Our calculations revealed that small islands (<12 Pt atoms), extracted from the step edge are metastable and only subnanometer-scale islands with a size of 12-19 atoms, are stable, which matches the experimentally observed 0.5-0.8 nm nanoclusters on the Pt(111) terraces with STM. We found that the stabilizing effect due to the formation of low coordination sites that strongly bind CO competes with the destabilization arising from the perturbation of the quasi-hexagonal pattern of CO molecules on the terraces. CO pressure-induced Pt atom detachment from the steps is additionally shown to be kinetically accessible. In the precursor state of the detachment, a leaving Pt atom protruding from a step edge adopts a configuration of a dicarbonyl surface complex ( $2\text{CO-Pt}_1$ ), facilitating its detachment.

## 5.2 Methods

Machine Learning atomistic potential of the class of High Dimensional Neural Network Potential (HDNNP) was trained on first principle Density Functional Theory (DFT) calculations. The structural and chemical environment information of each atom is used as the feature to train the potential energy surface, with both total energy and atomic forces. De-

ploying the Weighted Atom-centered Symmetry Functions, the Cartesian coordinates defining the atomic structure of the system are converted to translational and rotational invariant feature vectors.<sup>203,205,206</sup> The training was performed using the *n2p2* code which employs an efficient approach via multi-stream extended Kalman filtering to optimize the weights of the neural network minimizing the cost function defined by the sum of squared errors of energy and forces with a flexible parameter to adjust the importance of the two.<sup>209</sup> The machine learned iteratively by first constructing a preliminary HDNNP that was improved systematically and self-consistently by running NNP-based simulations to sample relevant configurations and evaluate their DFT energies to determine configurations that are not accurately described. These are then included in the training set until no further problematic structures can be identified. More details on the training of the NNP and its accuracy can be found in the appendix chapter C.

For effective reproducibility of the work, details of the hyperparameters of the symmetry function, the weight files of the neural network, and other details of the HDNNP are included in the appendix (Section C.8). The final training set consisted of 6153 structures and generated a HDNNP with a root mean square error compared to the reference DFT calculations of 1 meV/atom for energy and 0.06 eV/Å for the atomic forces. A larger set consisting of 13379 structures was used for validation with similar errors.

First-principles calculations were performed with the Vienna Ab-initio Simulation Package<sup>253,256</sup> using the general gradient approximation (GGA) Perdew-Burke-Erzenhof (PBE) functional.<sup>257</sup> Core electrons were described using the projector augmented wave method.<sup>258,259</sup> A k-spacing of 0.25 is used for all the calculations and the k-point grid is centered at the  $\Gamma$  point. A cutoff energy of 400 eV is used. A C-O bond distance-based correction developed by us has been applied to correct for the known over-binding of CO from Perdew-Burke-Erzenhof (PBE) functional,<sup>257</sup> the approach being previously validated for CO adsorption on Pt(111), Pt(100), and Pt stepped surfaces.<sup>225,290</sup>

Global optimization was performed using Basin Hopping Monte Carlo simulations (BHMC)

with an in-house open-source code. This algorithm takes advantage of local minimization to convert the potential energy surface (PES) from a curved surface to stepped shape basins.<sup>246</sup> The exploration of these basins is achieved by Monte Carlo sampling through atomic displacements and the Metropolis criterion. The free energy is calculated by subtracting the reference chemical potential (which is a function of temperature and pressure) of the adsorbate from the energy of the system as shown by the following equation:  $\Delta G = E(nCO + slab) - E(slab) - n_{CO} \times \mu_{CO}$ . Additional effects to the free energy of adsorption could arise from entropy effects, but this is not accessible in the current scope of the work. Due to the low temperature used here and to the high coverage of CO which hinders CO mobility, entropic contributions are expected to be low and should not change the qualitative picture presented. Apart from the random displacements generally used in the MC algorithm, we also utilize the “Clustering mutation algorithm” developed by us previously which has shown a better acceptance ratio in the BHMC simulations.<sup>290</sup>

To understand the kinetics of Pt restructuring under CO pressure, we cannot use the traditional nudged elastic band method since the coverage of CO keeps changing to stabilize the island formation and motion on the terrace.<sup>291,292</sup> Hence to simulate the extraction of one-Pt-atom protrusion at a Pt(553) step edge, we manually move the Pt atom towards the terrace perpendicular to the step edge. At each image of this extraction process, we perform grand canonical basin hopping using the fast HDNNP to find the lowest energy configuration of CO molecules. Here we make a Born-Oppenheimer-type approximation such that CO molecules are allowed to move more quickly compared to Pt (island) atoms to ensure the equilibrium of the CO molecules on the surface with the gas phase CO.

The structure of Pt surfaces in a CO environment (at different pressures) was studied using a high-pressure scanning tunneling microscope (HP-STM) system. The sample was placed inside the HP-STM cell (approximately 15mL in volume) with the cell door remained open for surface checking under the UHV environment. For the in-situ experiment, the HP-STM cell door was closed and CO gas was flown through the cell and over the sample during

STM image acquisition. The sample could be heated simultaneously by an IR laser (810 nm) irradiation on the back of the sample. The sample temperature was monitored using a K-type thermocouple spot-welded onto the back of the sample. More information about this system can be found in the literature.<sup>162</sup>

There are three limiting factors preventing us from obtaining STM images at atom scale or a resolution better than the images presented in this article: (i) Temperature: all STM images in Figure 5.1 were collected at room temperature under a pressure of CO instead of lower temperature or even cryogenic temperature which significantly helps to collect a high-resolution image. (ii) Scanning speed: as we were trying to catch the evolution of surface structure, we had to scan relatively fast, limiting the number of pixels per nm<sup>2</sup> and lowering the image resolution. (iii) feature of the surface morphology: the narrow terrace in terms of a relatively high density of step edge requires a faster feedback loop of scanning to compensate for the change of tunneling current. The faster response in the z-direction sacrificed the resolution. For the same reasons, no high-resolution images were obtained in the early work as well.<sup>55</sup>

## 5.3 Results

### 5.3.1 In situ imaging of restructuring at nanoscale

A sequence of STM images was acquired on the same stepped region of our Pt(111) sample in CO gas at a pressure of  $1.5 \times 10^{-6}$  Torr (Fig. 5.1). The terraces are ~5-10 nm wide. A low pressure is selected to slow down the surface restructuring events so that consecutive steps of the restructuring process can be tracked. Fig. 5.1(a) shows the image of the surface just after the introduction of CO. It features terraces with irregular step edges of Pt atoms. The blue arrow marks the area that evolves as a function of time. After 10 minutes (Fig. 5.1(b)), a subnanometer protrusion forms at the step, towards the lower terrace. This “peninsula” detaches from the step edge after 14 minutes (Fig. 5.1(c)), forming a subnanometer size

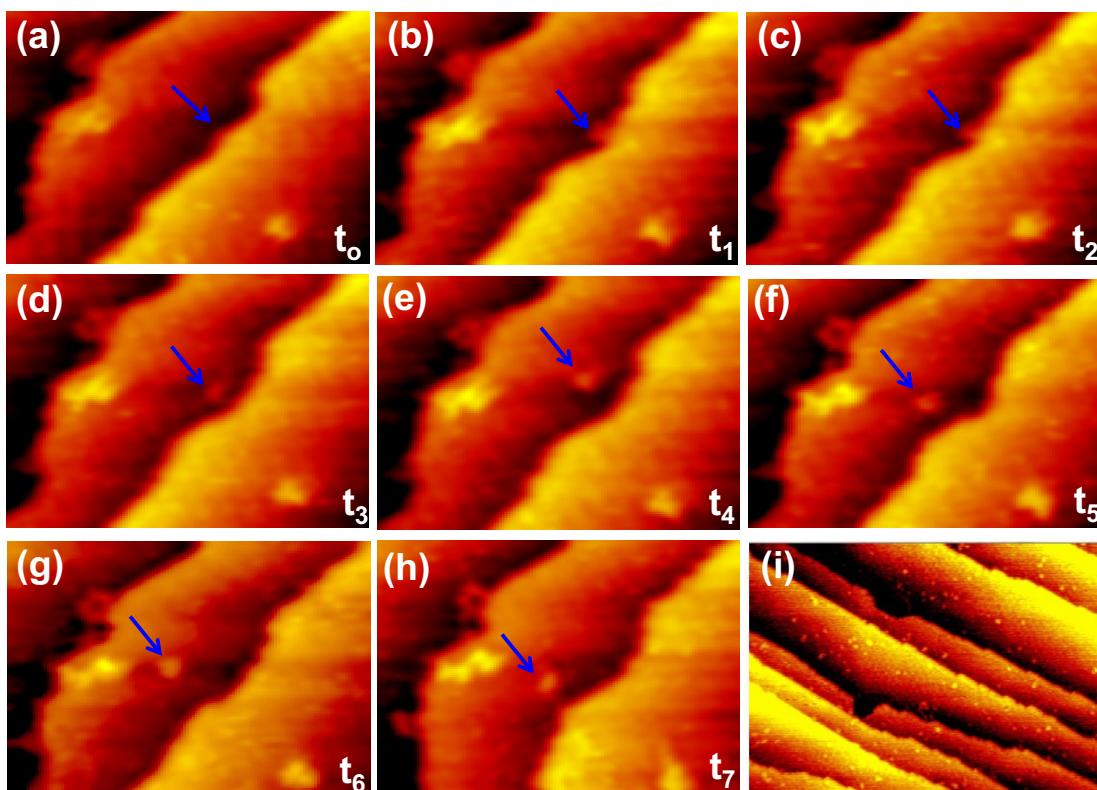


Figure 5.1: STM images of a Pt(111) surface at room temperature in gaseous CO. (a-h) STM images of the same region taken sequentially at different times: (a)  $t_0 = 0$ , (b)  $t_1 = 10$ , (c)  $t_2 = 12$ , (d)  $t_3 = 14$ , (e)  $t_4 = 16$ , (f)  $t_5 = 23$ , (g)  $t_6 = 25$ , (h)  $t_7 = 27$  min after the CO pressure was brought up to  $1.5 \times 10^{-6}$  Torr at room temperature; the size of each image (a-h) is  $15 \text{ nm} \times 20 \text{ nm}$ ; the acquisition time of each image is 1-2 minutes. In (a-h), the progressive detachment of a subnanometer cluster was observed experimentally. (i) STM image under a CO pressure of 0.1 Torr; size of the image is  $30 \text{ nm} \times 40 \text{ nm}$ ; nanoclusters with a size of 0.5-0.8 nm appeared as bright spots on terraces of Pt(111).

cluster on the terrace. The cluster then diffuses on the surface, with a slight apparent increase in size (Fig. 5.1(e)). The size of the Pt cluster does not increase further after 16 minutes while it continuously diffuses on the terrace. The pressure of CO has a major influence on the rate of these detachments of Pt clusters from the step. No such detachment was observed during the duration of the experiment for the same sample in UHV or under a CO pressure of  $5 \times 10^{-8}$  Torr (Fig. C.3). In contrast, at a higher pressure of 0.1 Torr, a great number of Pt nanoclusters with the size of 0.5-0.8 nm were formed on the terraces (Fig. 5.1(i)).

The images give important information on the surface transformation, but they do not provide an atomic scale mechanism of the restructuring. The time scale required to acquire the image is long (at least tens of seconds) preventing to record detailed time evolution. Hence, the specific atomistic structure of Pt atoms and CO molecules and the rearrangement kinetics on the surface is unknown. It is therefore mandatory to couple the experimental insight with atomistic simulations as we do here.

### 5.3.2 Grand canonical simulations of elementary restructuring processes

Various elementary steps for surface restructuring were explored using basing-hopping simulations and the trained neural network potential. A basin hopping algorithm is used to explore the potential energy surface and has shown application previously to understand CO arrangement on Pt stepped surfaces,<sup>290</sup> fluxionality of catalytic clusters<sup>251,252,293,294</sup> as well as for bio-molecules.<sup>295,296</sup> At the same time, HDNNP have been used to reduce the high computational cost of DFT simulations especially when used for global optimization problems..<sup>251,297-300</sup>

Two models of stepped surfaces have been considered, Pt(553) and Pt(557) (Fig S1 and S2 respectively). On Pt(553), the atoms of the step edge and their underneath atoms form triangular Pt arrangements in the counter-step (111 step) while Pt(557) gives square arrangements (100 step). The considered elementary restructuring processes are (i) step rearrangement, (ii) step atom extraction towards the lower terrace, and (iii) island formation on the terrace. One important feature is that the coverage and positions of the CO can dynamically change during each considered restructuring process. This feature has been considered by performing global optimization with basin hopping for the CO overlayer at variable CO coverage for each Pt surface structure (Section S3.3). To understand the effect of pressure, we perform the global optimization at different pressure conditions (0.0007, 0.5, and 450 Torr). Since the Gibbs free energy changes logarithmic with pressure ( $G \sim k_B T \ln(P/P^o)$ ), change in pressure from 0.0007 to 0.5 and 0.5 to 450 Torr results in a change in Gibbs free energy of  $\sim 7k_B T \approx$



0.15 eV (at RT). Hence with the limited accuracy of DFT calculations, these steps in pressure conditions give use a reasonable understanding of the overall effect. Since the CO diffusion barrier is low on the (111) surface of Pt and CO adsorption is not activated, we assumed that CO diffusion or addition/removal on the surface is very fast, so that the CO adlayer structure will remain in equilibrium with the gas phase upon Pt surface restructuring.

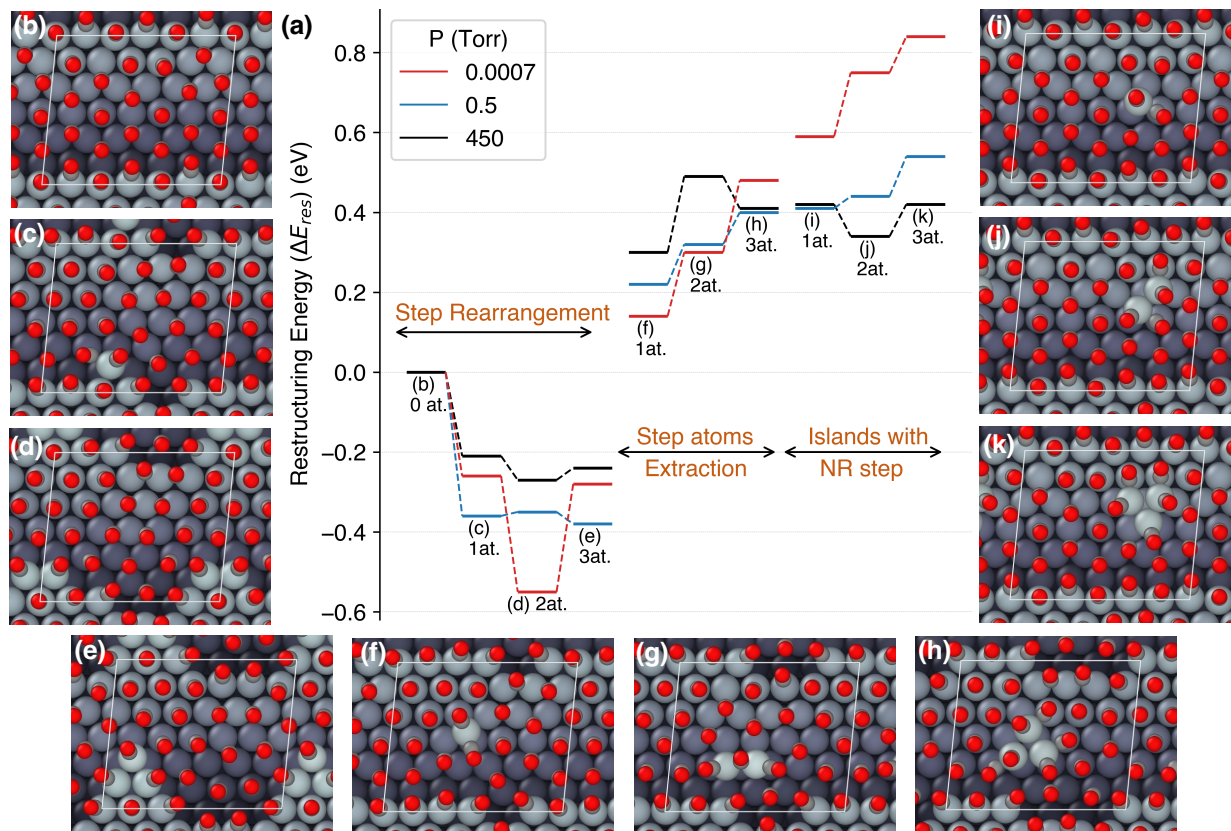


Figure 5.2: Simulation of elementary surface restructuring events at the Pt(557) step edge: (a) Restructuring energy under a CO pressure of 0.0007, 0.5 or 450 Torr for step rearrangement (structures b-e), step atom extraction (structures f-h) and island formation keeping the step unmodified (structures i-k). The parallelogram shown in white line marks a unit cell.

The step rearrangement process for the Pt(557) step edge is shown in Fig.5.2(b-d). 1, 2, or 3 atoms form a protrusion at the step edge. This process is markedly endothermic on the bare Pt(557) surface in the absence of CO adsorbates (by 0.54, 0.52, and 0.67 eV for 1, 2, and 3 atoms, respectively (Fig. C.13, Table C.4) since the coordination of Pt atoms is globally decreased. In contrast, under the pressure of CO, such a movement of step

atoms is stabilizing by 0.2 to 0.6 eV depending on the number of Pt atoms rearranged and the pressure. Clearly, the CO adsorbates promote the breaking of Pt-Pt bonds and the formation of low-coordinated Pt atoms along the step edge. CO coverage is high, even at 0.7 mTorr pressure, with full coverage at the step edge, and 0.67 to 0.83 ML on the terrace depending on the CO pressure (Table S5). Although the amount of CO is not systematically increased following the restructuring elementary step, the presence of CO adsorbates and their rearrangement is essential for the restructuring to occur. The formation of triangular apexes induced by CO adsorption on Pt (557) as in Fig.5.2(e) is in good agreement with STM experiments where such “triangular” restructuring has been evidenced.<sup>55</sup>

### 5.3.3 Mechanism of island formation on terraces

Moving ahead, we formed 1, 2, or 3 atom islands on the terrace of the stepped surface. Two approaches are considered. The first one just extracts atoms from the step edge, forming simultaneously a small island and a kinked step. In the second approach, the step is kept unmodified, hence assuming that the island atoms thermodynamically originate from the bulk of the Pt sample. The restructuring energy ( $\Delta E_{res}$ ) to form these small islands under the pressure of CO is found to be positive, i.e. destabilizing, by 0.14 to 0.84 eV depending on CO pressure and the type of islands. This destabilization is much smaller than that for the surface in the absence of CO adsorbate (between 1.37 and 3.0 eV depending on the configuration; see Fig. C.13), so that CO adsorption has a clear stabilizing effect on a Pt atom at low coordination, but the amplitude of the adsorption effect is not strong enough to compensate the intrinsic energy cost to form the low coordination islands. The CO coverage, here defined as the ratio of the number of CO molecules to the number of Pt atoms of an entity, such as an island or cluster, is high and depends on the size. For example, the CO coverage can be 2 for a dicarbonyl on Pt<sub>1</sub> (2CO-Pt<sub>1</sub>) and 1.5 for three CO molecules on Pt<sub>2</sub> (3CO-Pt<sub>2</sub>) compared to 1 for a Pt step atom of the initial surface. However, the energy stabilization contributed by the increased adsorption energy of CO is not large enough to

render the structures thermodynamically stable.

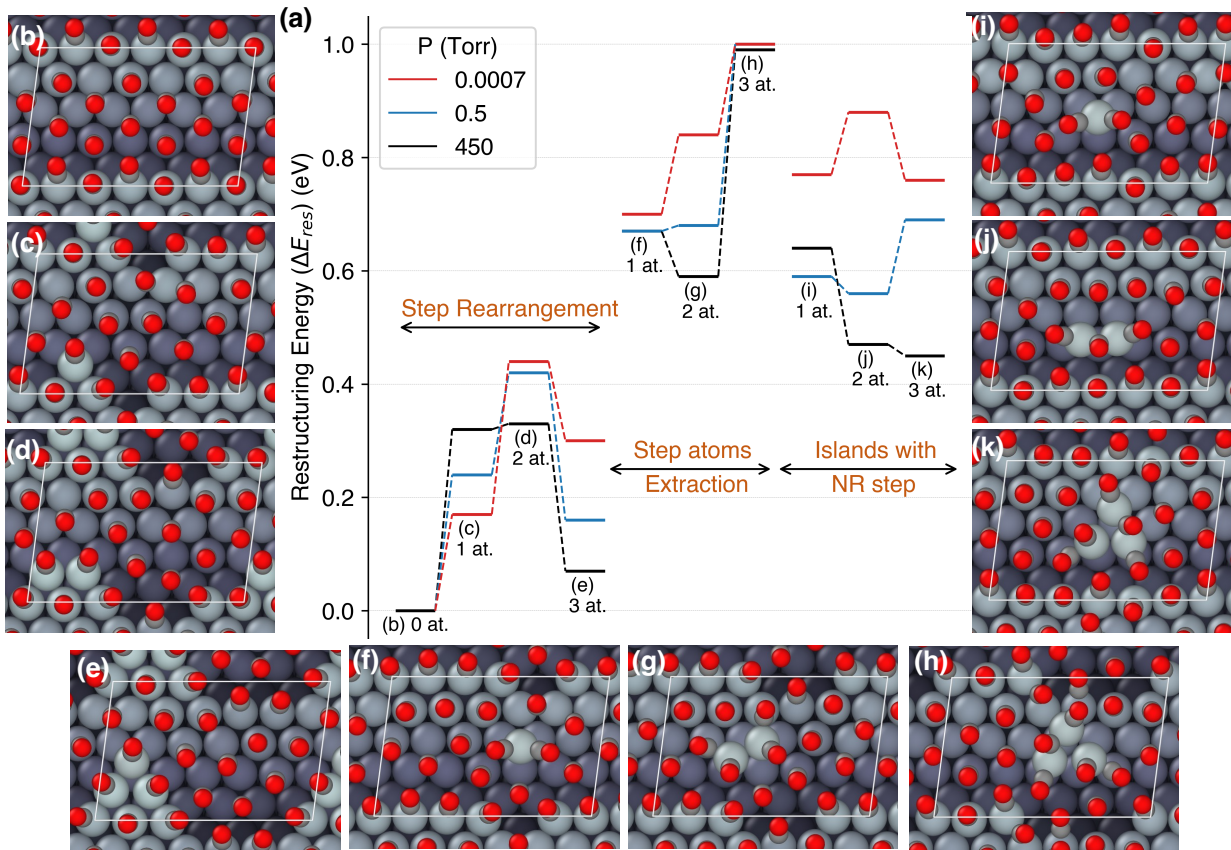


Figure 5.3: (a) Simulation of elementary surface restructuring events at the Pt(553) step edge: (a) Restructuring energy under a CO pressure of 0.0007, 0.5 or 450 Torr, for step rearrangement (structures b-e), step atom extraction (structures f-h) and island formation keeping the step unmodified (structures i-k).

Computational studies on Pt(553), another stepped surface (Fig. C.1), demonstrate how the restructuring process can depend on the specific geometry of the initial step. The main effect is similar, in that the stronger CO adsorption at low coordination Pt atoms. However, in contrast to Pt(557) (Fig. 5.2), step rearrangement events on Pt(553) are slightly endothermic by 0.1 to 0.4 eV (Fig. 5.3 (c, d, e)) and step atom extractions are also energetically less favored.

Since very small islands (1-3 atoms) are found to be metastable, we explored the formation of larger islands, featuring some more coordinated Pt atoms. If we suppose that an island

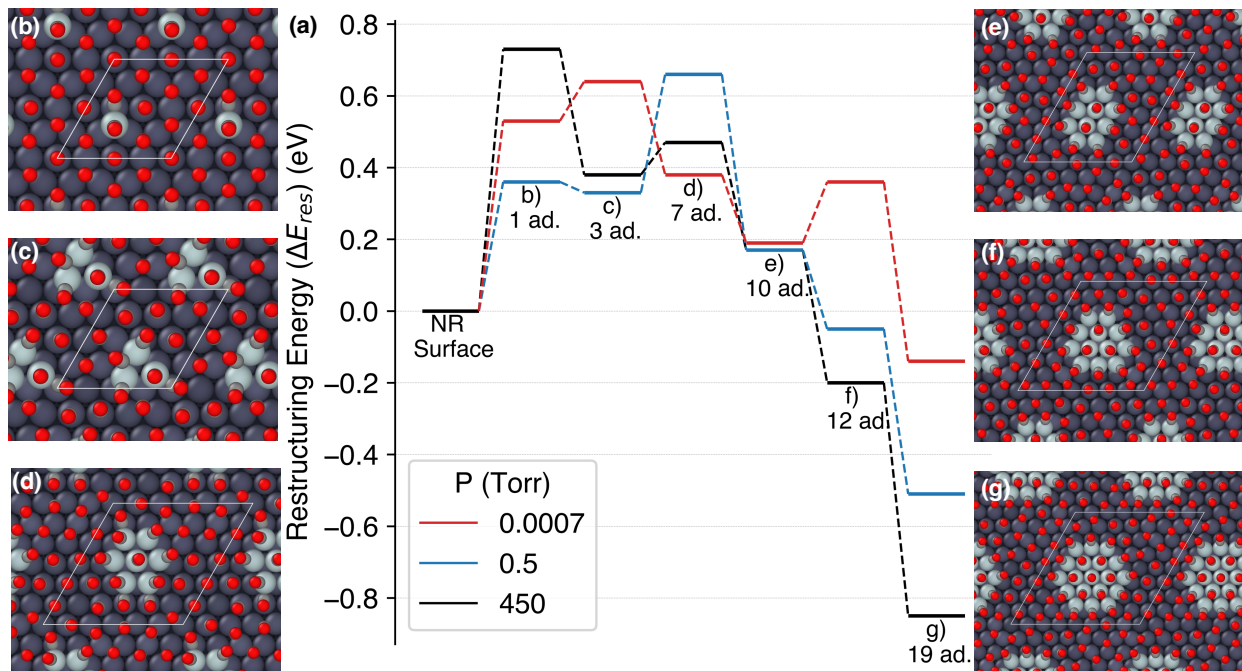


Figure 5.4: (a) Comparing the formation energies of Pt islands of increasing sizes from 1 to 19 atoms on a Pt(111) terrace under a CO pressure of 0.007, 0.5 or 450 Torr. (b-e) show the representative structures at a CO pressure of 450 Torr.

is moved away from the unmodified step, the system can be simplified as one consisting of a terrace and supported islands as shown in Fig. 5.4. Here we consider the formation of monolayer islands of sizes 1, 3, 7, 10, 12, and 19 atoms on Pt(111) (1 and 3 are repeated to show the consistency with the previous model including the step). The simulations recover the previous result that islands of sizes 1 and 3 are metastable by 0.4 to 0.7 eV in the range of the considered CO pressure.  $Pt_7$  shows similar stability. However, beyond that size, the restructuring energy ( $\Delta E_{res}$ ) starts to decrease. Notably, restructuring Pt(111) under the pressure of CO to form  $Pt_{12}$  or  $Pt_{19}$  islands is found to be exothermic. Such islands are far from being stable in the absence of CO. For example, the formation energy of  $Pt_{19}$  island on a Pt(111) surface is +7 eV (+0.4 eV per Pt atom) in the absence of CO. However, compared to CO on a terrace of Pt(111) of similar size, the net gain in CO adsorption energy in the presence of the  $Pt_{19}$  island is between 7.5 and 8 eV depending on the pressure, which can compensate the energy cost of forming such islands, making these reconstructions



thermodynamically favorable(see Fig. C.14, C.17).

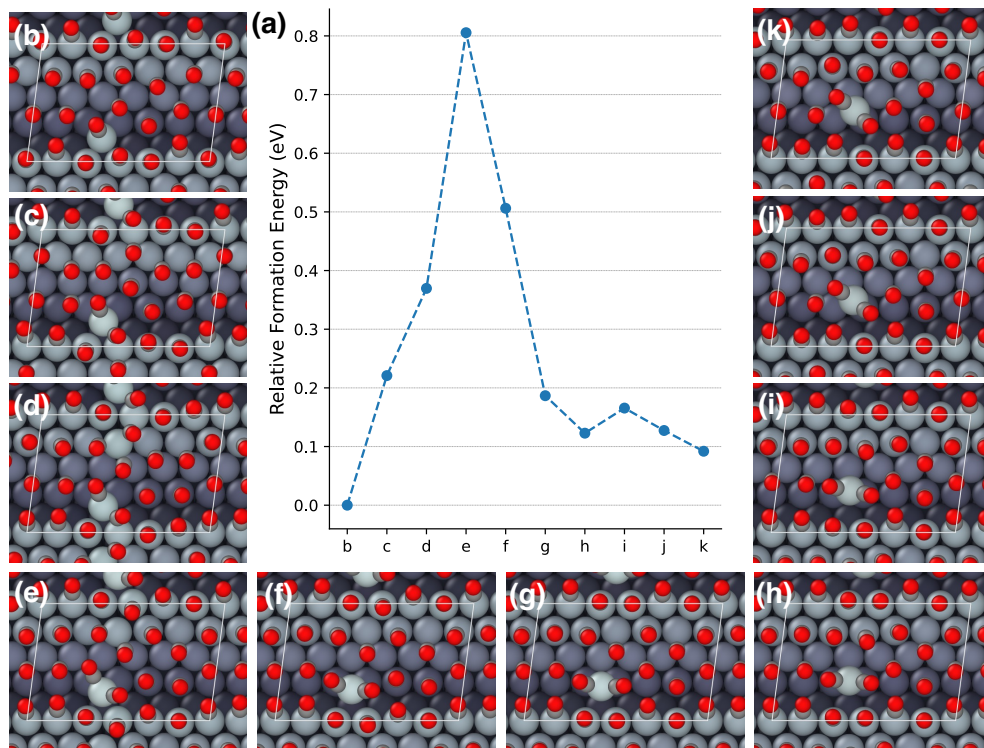


Figure 5.5: Kinetic reaction pathway for a restructuring event on Pt(553); (a) Reaction energy profile for the detachment of one Pt atom from the Pt(553) step edge (b-h) and its diffusion on the terrace (h-k) at a CO pressure of 450 Torr.

### 5.3.4 Kinetics of Pt restructuring under CO pressure

Beyond thermodynamics, kinetic aspects are also crucial for our understanding of restructuring processes. Exploring specific pathways for all these restructuring events whose thermodynamics were extensively studied here is highly challenging and beyond the scope of this report. Fig. 5.5 shows a representative example where CO-induced Pt mobility can occur with a moderate energy barrier when a one-Pt-atom protrusion at a Pt(553) step edge is extracted towards the terrace, while the other pathway (diffusion on the terrace) is shown in Fig. C.18(see section 2: Methods). In the initial configuration of the pathway (Fig. 5.5(b)), the Pt atom is attached to the step edge and, at the considered pressure condition (450

Torr) the total equilibrium CO coverage is 0.57 ML, one CO binding to the protruding Pt atom. In the final configuration (Fig. 5.5(k)), the Pt atom is on the terrace, stabilized by the formation of a dicarbonyl surface complex, and the equilibrium coverage of 0.6 ML (i.e. one more CO in the unit cell). The key point for a favorable energy pathway is to first rearrange the CO molecules on the initial configuration, by forming a metastable structure with one more CO adsorbate (Fig. 5.5(c)), less stable in free energy by 0.22 eV but with an additional CO coordination for the protruding atom, bridging with a step-edge Pt. This precursor state adopts a configuration that facilitates the detachment of the Pt atom by the formation of a dicarbonyl surface complex, with an overall energy barrier of 0.8 eV and a pathway shown from Fig.5.5(c) to Fig.5.5(h). The end of the process is simply an easy diffusion of the Pt-dicarbonyl moiety on the surface Fig.5.5(g-k). The fluxionality of the CO adlayer is of crucial importance, enabling the protruding Pt atom to reach, at a modest energy cost, a configuration of CO ligands optimal for the restructuring event (Fig. 5.5). The calculated barrier for CO-assisted atomic extraction from the step edge is accessible at 300 K and is compatible with the experimental time scales of restructuring.

## 5.4 Discussion

The main qualitative reason for the restructuring is the formation of lower-coordination Pt atom sites, where CO chemisorbs more strongly, thus compensating for the energy cost arising from the restructuring of the bare surface. Since breaking the Pt-Pt bond and adsorption of CO are the main contributors with opposing consequences to the catalyst rearrangement, the restructuring energy ( $\Delta E_{res}$ ) can be conveniently decomposed into the energy required for breaking Pt-Pt bonds ( $\Delta E_{metal}$ , positive) (on the bare surface) and the energy gained from the enhanced CO adsorption strength due to the modified coordination of Pt atoms upon restructuring, ( $\Delta E_{chem}$ , negative) such that  $\Delta E_{res} = \Delta E_{metal} + \Delta E_{chem}$ . If  $\Delta E_{chem} \geq \Delta E_{metal}$ , restructuring is thermodynamically favorable (Table S2, S4, S6).

When comparing the effect of the step structure, in the absence of CO adsorbates, the Pt(553) step is more difficult to restructure than Pt(557) (by 0.37-0.99 eV for Pt atoms step rearrangement and 0.19-0.71 eV for step extraction, Fig. C.12). On Pt (557), the restructuring results in the formation of (111) step edges, which are more stable than the initial (100) step edge, making the process energetically favorable. Unlike Pt (557), the restructuring in Pt(553) starts from a (111) step to form (100) microsteps, which are less stable (Fig. 5.3(d)). The restructuring energies to form small detached islands on Pt(553) (Fig. 5.3(i-k)) is similar to that on Pt(557). The relatively less energetically favorable restructuring on Pt(553) shows that the structure of the step is another significant descriptor for restructuring.

The investigated islands in Fig. 5.4 can be separated into two families. At small size (Pt<sub>1</sub> to Pt<sub>7</sub>) CO can bind to the cluster through several types of modes including atop or bridge on the island, atop or bridge between the island and support. Starting at a size of 10 Pt atoms a more regular pattern emerges: each Pt atom is covered by one CO on the island, such a high coverage being permitted because CO molecules can tilt outward to release the Pauli repulsion between them at a short distance (2.7-3 Å).<sup>55</sup> These subnanometer-size islands (Pt<sub>10</sub>-Pt<sub>19</sub>) combine a smaller destabilization to form the bare island (per Pt atom) and still a large fraction of low coordination atoms that provide stabilization from stronger CO binding. The stability of the subnano-island hence results from a subtle balance between low metal coordination and stabilization from CO adsorbates.

The correlation between restructuring energy and CO coverage is more complex than could be initially thought. Restructuring enhances CO adsorption because it creates sites with lower coordination at the step/edge. Therefore, the number of CO at step/edge sites is generally increased upon restructuring. On terraces, CO adsorbates adopt a quasi-hexagonal arrangement<sup>290</sup> that develops in extended Moiré patterns on large (111) areas.<sup>141,225</sup> By moving Pt atoms toward the terrace, restructuring perturbs this quasi-hexagonal arrangement and therefore destabilizes CO adsorption on the terrace. As a result, the number of CO

adsorbates on the terrace can decrease upon restructuring. This destabilization of CO on terraces is more important at high CO pressure since the CO coverage is higher. Overall, CO adsorption is stabilized upon restructuring, but this results from a combination of stabilization at the additional low-coordinated step sites and destabilization at terraces. Therefore, a higher CO pressure does not necessarily stabilize the restructuring, as can be seen in Figs. 5.2, 5.3, and 5.4. Nevertheless, the formation of nano-scale islands on Fig. 5.4 (islands with 12 and 19 Pt atoms) is more favorable at higher pressure since their more regular shapes and CO organization disturbs less the CO packing on the terrace.

At this point, we can compare the experimental and computational data obtained in the present paper. Upon CO adsorption at stepped Pt terraces, the first process evidenced by both experiment and theory is a rearrangement of the step edges by displacement of Pt atoms, but without detachment of Pt atoms or clusters on the terraces. Straight step edges are transformed into wandering or zigzag ones. Experiments and theory agree that the stability of these rearrangements depends on the type of steps. Steps with (100) counter-step facets (as on the Pt(557) surface) provide easy (exothermic) restructuring with the formation of extensive triangular nano-shapes on the terraces and “zig-zag” step edges.<sup>55</sup> In contrast steps with (111) counter-step facets (as on the Pt(533) surface) are much less prone to rearrangement because these steps are intrinsically more stable and the rearranged structure is metastable. Our stepped Pt(111) sample (Fig. 5.1) shows such (111) steps, and the step wandering remains very moderate. The second process concerns the true detachment of a small Pt island from the step towards the terrace. This process requires large enough terraces. This is not the case on the Pt(557) surface and the triangular nano-shapes do not detach from the step upper-terrace. In contrast on our Pt(111) surface, the step density is lower, and fully detached subnanometer-size islands are seen from the STM data and are calculated to be stable under the pressure of CO. Finally, the calculated barrier for detachment of a Pt atom assisted by high CO coverage is moderate (0.8 eV) which is fully compatible with the time scale of restructuring measured by the experiment. Our combined



theory-experiment approach hence provides a detailed view of the possible pathways and mechanisms of restructuring of stepped Pt surface under the pressure of CO.

Vibrational spectroscopy is a major method to characterize chemisorbed CO molecules. Indeed, the CO bond stretch frequency depends on the coordination of the surface Pt. For example, Avanesian et al. showed that the CO stretch frequency is lower when CO is bound to an undercoordinated Pt site representing the edges and corners of a Pt nanoparticle, compared to high coordination sites on the terraces.<sup>223</sup> This is explained by the fact that an undercoordinated Pt site results in a larger amount of charge transfer to the adsorbate leading to a larger shift in the vibrational frequency. In our case for the Pt<sub>12</sub> islands on Pt(111) surface (Fig. 5.4(f)), the CO stretch frequency is in the range 2025-2035 cm<sup>-1</sup> for the 12 CO molecules on the island, compared to 2060-2070 cm<sup>-1</sup> for CO adsorption on the terrace (top site).<sup>225</sup> Interestingly, CO molecules adsorbed in the center of the subnano-island show a very similar stretch frequency to those bound to the periphery Pt atoms. Therefore, Pt coordination is an important parameter, but not the only one, and CO local coverage or tilt with respect to the facet normal could also play a role.<sup>176</sup>

Our study shows that the restructuring of stepped areas of a Pt(111) surface occurs at room temperature with a minute time scale. It initiates at steps and propagates toward terraces at least for 5-10 nm. Such a restructuring by subnano-island formation can be viewed as an atomic scale roughening of the (111) terraces and affects a small fraction of the surface atoms. Although this could have a major influence on catalytic reactivity by creating low coordination sites, such restructuring might be difficult to follow by surface-sensitive spectroscopic methods, since the signal could be dominated by non-restructured surface sites. It is pertinent to compare the situation of model single crystal surfaces studied here to that of supported Pt nanoparticles considered in the literature. Avanesian et al. considered Pt nanoparticles in the range of 2 to 17 nm under the pressure of CO by TEM, IR, and DFT.<sup>223</sup> They suggest no restructuring at 298K and showed restructuring of the (100) facets at 363K but did not evidence a change of structure on the (111) facets. The restructuring by

island formation initiating at steps shown in the present paper would require large enough nanoparticles that can show steps on the (111) terraces ( $\geq 5$  nm in size). Already at 298 K under CO, (111) terraces of large nanoparticles should be restructured with subnano-islands, but this could be difficult to see with the TEM and IR. Indeed, these small islands would result in small contrast change for TEM and they would lead to only a small change in the fraction of under-coordinated sites, difficult to assess from the IR experiments. Therefore, the approaches on single crystal surfaces and nanoparticles are complementary. Different modes and scales of reconstruction can be present on different facets, and they can occur at different temperatures. Besides Pt(111), restructuring has been reported on numerous metal surfaces with low Miller-index including Cu(111),<sup>24</sup> Au(111),<sup>99</sup> Au(110),<sup>275</sup> Co(0001),<sup>19</sup> Pd(111), Pd(100), hence it is significant to explore the restructuring mechanisms in terms of kinetics at the atomic scale in the future.

## 5.5 Conclusion

We explored the atom-scale mechanism of the restructuring of stepped regions of Pt(111) under the pressure of CO and we show that restructuring initiates at step edge through the formation of Pt carbonyl subnano-islands on the lower terrace, based on both time-dependent HP-STM images and machine-learning enhancing computational studies. The generation of a fast machine learning potential allowed us to explore large surface unit cells with various surface models, a large number of adsorbate configurations, and complex surface restructuring processes. The integration of experimental in situ STM imaging and fast machine learning potential-based computational studies provides an atomic-scale understanding of the origin and mechanisms of the restructuring of platinum surfaces under the pressure of CO. Here, more generally, we demonstrated the importance of gaining atomic-scale comprehension of the dynamical transformation of metal catalyst surfaces, under a high coverage of adsorbates. The capture of such a dynamic atomic-scale picture of the ensemble of surface

structures of a catalyst in a reactant gas is a clear prerequisite for an accurate determination of catalytic reaction mechanisms at a molecular level. These atomic-scale understandings of the dynamics of metal catalyst surfaces under reactant gas pressure offer insights on how to design catalyst/reactant systems that would promote such metal surface restructuring to dynamically create catalytic sites under reaction conditions leading to maximizing the activity or selectivity for the desired reaction.

## CHAPTER 6

# Cu surface activation induced by CO adsorption-driven nanocluster decomposition

### 6.1 Introduction

Copper-base catalysts are employed in various reactions including the water gas shift (WGS), methanol oxidation, methanol synthesis reactions, etc.<sup>301-307</sup> In comparison to platinum, copper has a lower cohesive energy (3.50 versus 5.84 eV)<sup>308,309</sup> This significantly influences the effect of CO adsorption on Cu. As shown in previous chapters, Pt(111) surface is stable under CO pressures of 1 atm<sup>141,310</sup> but CO causes restructuring of stepped surfaces due to its stronger binding at step edges.<sup>55,290,311</sup> Even though the binding energy of CO on the Cu(111) surface is lower than that on Pt by 0.5 eV, the whole Cu(111) terraces are surprisingly reconstructed into Cu nanoclusters of size 0.5-1.5 nm at 0.2 Torr CO and 25°C.<sup>312</sup> These clusters are mobile and have a similar structure as the 3 (triangular) and 19 (hexagonal) atom islands seen at high temperatures on the Pt surface.<sup>311,312</sup>

As rearranging metal-metal (M-M) bonds at a terrace edge is the first step of restructuring for both these metals (Pt and Cu), the M-M bond (measured by cohesive energy) is an important factor. Compared to Pt, Cu cohesive energy is lower by 2.34 eV, which can qualitatively explain why the Cu surface can be readily restructured in 0.2 Torr CO at 25°C but Pt(111) cannot. Thus, the cohesive energy of a metal is another important factor contributing to the restructuring behavior of a metal surface. However, how M-M and M-CO bond strength interplay in the restructuring of transition metals is not clear.

Eren et al. using High pressure scanning tunneling microscopy showed that in UHV conditions, Cu(111) shows micrometer-scale terraces, atomic steps, and a few screw dislocations. At 0.1 Torr of CO, the step edges start to show restructuring while the terrace remains unchanged. With CO pressure increased to 0.2 Torr, the terraces became covered with nanoclusters. These nanoclusters increase in density as CO pressure increases until the surface is saturated.<sup>312</sup>

Similar to the reconstruction on Pt surface, the mechanism of the formation of these nanoclusters is still an unanswered question. The basic principle of CO molecules adsorbing strongly to edge/kink atoms on these nanoclusters is still valid, but the role of lower cohesive energy in the overall kinetics of the restructuring process is still in question. Understanding this can not only help in understanding the Cu/CO system but also reveal a more general trend of restructuring occurring in various transition metals with varying cohesive energies. In this chapter, we discuss ongoing work on the development of a similar neural network-based potential for the Cu/CO system to enable us to understand these large-scale restructuring systems with limited computational resources.

## 6.2 Methods

First-principles calculations were performed with the Vienna Ab-initio Simulation Package<sup>253,256</sup> using the general gradient approximation (GGA) Revised Perdew-Burke-Erzenhof (PRBE) functional.<sup>313</sup> Core electrons were described using the projector augmented wave method.<sup>258,259</sup> A k-spacing of 0.25 is used for all the calculations and the k-point grid is centered at the  $\Gamma$  point. A cutoff energy of 400 eV is used.

Data was generated for the HDNNP training using Grand Canonical Basin Hopping (GCBH) where the chemical potential of CO was calculated using the ideal gas thermodynamics. Translational and rotational terms are taken into account to calculate the CO gas phase chemical potential, but vibrational terms are not included, since they are neglected in the

CO adsorbed state as well. Cu atoms were also treated grand canonically by creating a reservoir of Cu using the bulk Cu energy. Apart from GCBH, we also use other techniques discussed earlier like NN-driven MD simulations, random perturbations, etc. to generate data efficiently for training and validation. Three different architectures of the NN were chosen (54-20-20-20-1, 54-30-30-1, and 54-30-30-30-1) of which 54-30-30-30-1 gave the best performance. The final potential has a training set consisting of 8981 structures which included various facets of Cu surface including (1) low index 111, 100 surfaces, (2) high indexed stepped surfaces like 1021, 410, 430, 533, 553, 557, 711 and 843 surfaces which consisted of both 100 and 111 type terraces with different step structures and (3) Stepped surfaces with ad atoms (generated automatically using GCBH simulations) and (4) 111 surface with nanoclusters of size ranging from 1 to 19 Cu atoms. The iterative training process as described previously in Chapter 3 was performed to achieve an RMSE of 1.74 eV/atom and 0.05 eV/Å for energy and forces respectively in both the training and the validation datasets.

Within the in-house GCBH code, we treat both CO molecules and Cu grand canonically by developing the following modifiers:

1. Randomize: Randomly perturb the system using a max.
2. Adsorb CO: Add a CO molecule on the surface.
3. Desorb CO: Remove a CO molecule from the surface.
4. Move CO: Desorb CO, followed by adsorbing CO on a different site.
5. Add Cu-CO: Add a Cu atom with CO adsorbed on top to the surface.
6. Remove Cu-CO: Remove a Cu atom with CO adsorbed on top from the surface.
7. Move Cu-CO

The code also identifies the surface of the surface automatically. This allows generating structures for training and exploring the potential energy surface in an efficient manner.

## 6.3 Results

### 6.3.1 HDNNP Accuracy

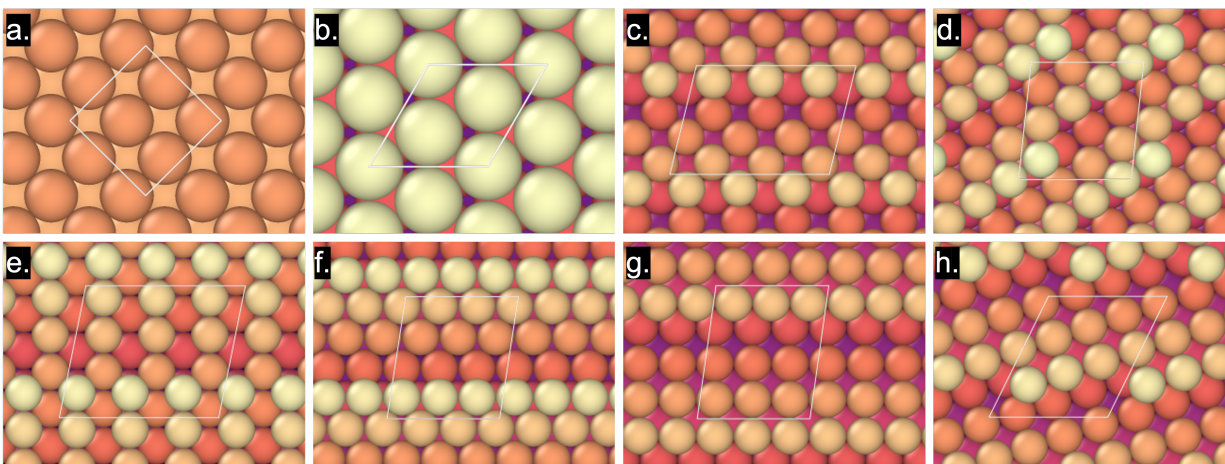


Figure 6.1: Various Cu facets used with GCBH to generate data for training the HDNNP: (a) 100, (b) 111, (c) 410, (d) 1021, (e) 430, (f) 533, (g) 711, (h) 843. All the balls represent Cu atom. The balls with lighter color (yellow) show the step edges and the darker colors represent the terrace. The color gradient shows the different height of the atoms in the unit cell.

The initial data for the HDNNP training was generated by performing Grand Canonical Basin Hopping (GCBH) simulation using DFT on various Cu facets shown in Fig. 6.1. The high miller index surfaces have either 111 or 100 terrace and different types of steps (square or triangular) and with kinks in case of Cu(843) and Cu(1021). These surfaces were chosen because they give a variety of Cu coordination that would be useful in describing the reconstruction process on low miller index Cu surfaces. This total dataset included 42734 structures of which only 4747 structures were used in training and 37987 were used in validation. Fig. 6.2 shows the parity plot comparing the HDNNP prediction with the reference DFT calculations with energy error of 1 meV/atom and 1.36 meV/atom for training

and force error of 0.05 eV/Å for both the training and validation set.

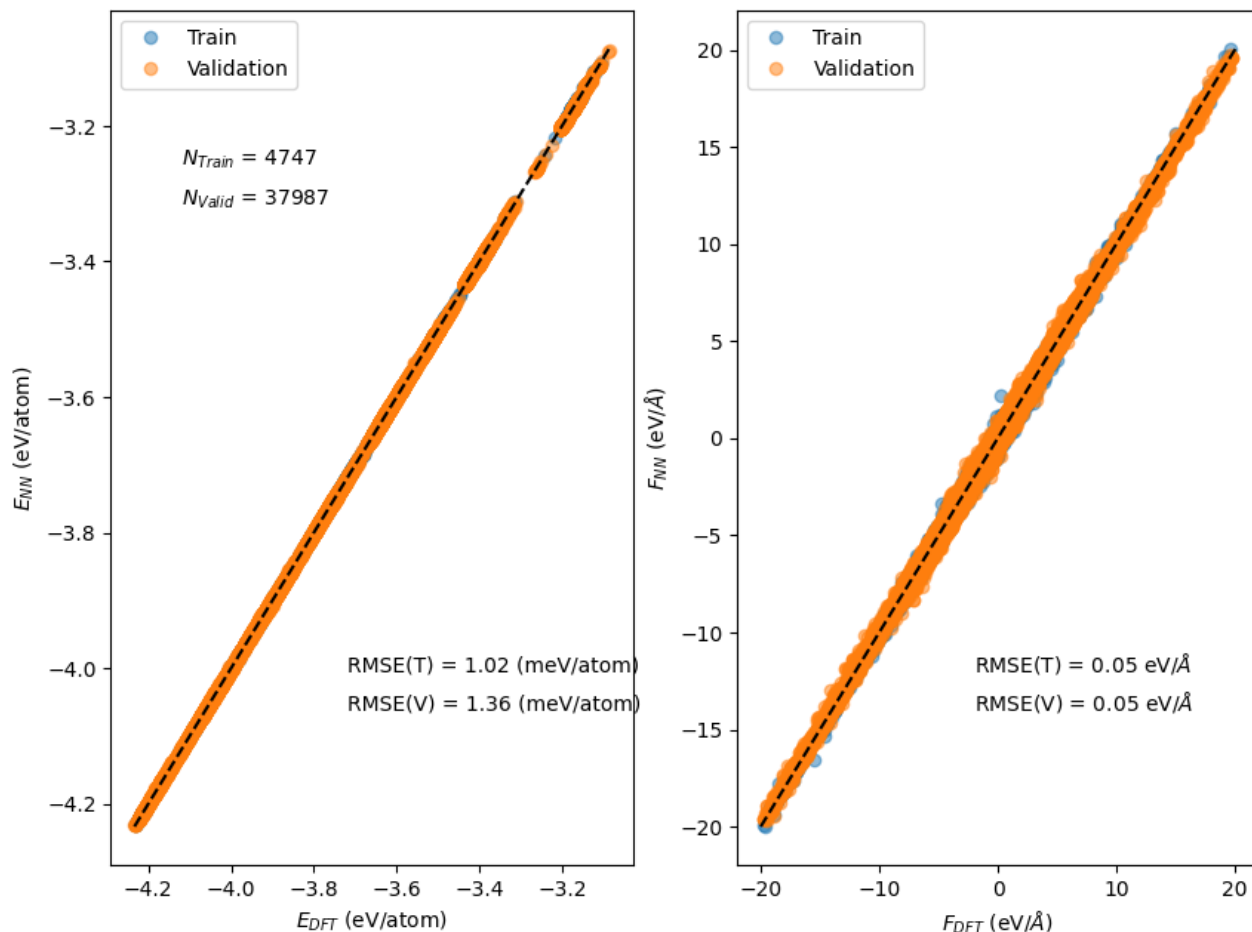


Figure 6.2: Parity plot comparing the Neural network predicted energy (per atom) and forces with the reference DFT calculations for the initial dataset generated.

With the HDNNP working well on the small stepped surface unit cells, we performed GCBH calculations on larger stepped unit cells. The parity plot in Fig. 6.3 shows the comparison of DFT and NN predictions for steps surfaces including Cu(553), Cu(557), Cu(711) and Cu(533) with 5-6 atoms along the step edge in a unit cell.

### 6.3.2 Restructuring events on different Cu surfaces

A few initial results from performing GCBH simulations on different Cu-stepped facets are discussed here. As mentioned in the methods section, we performed GCBH treating both CO



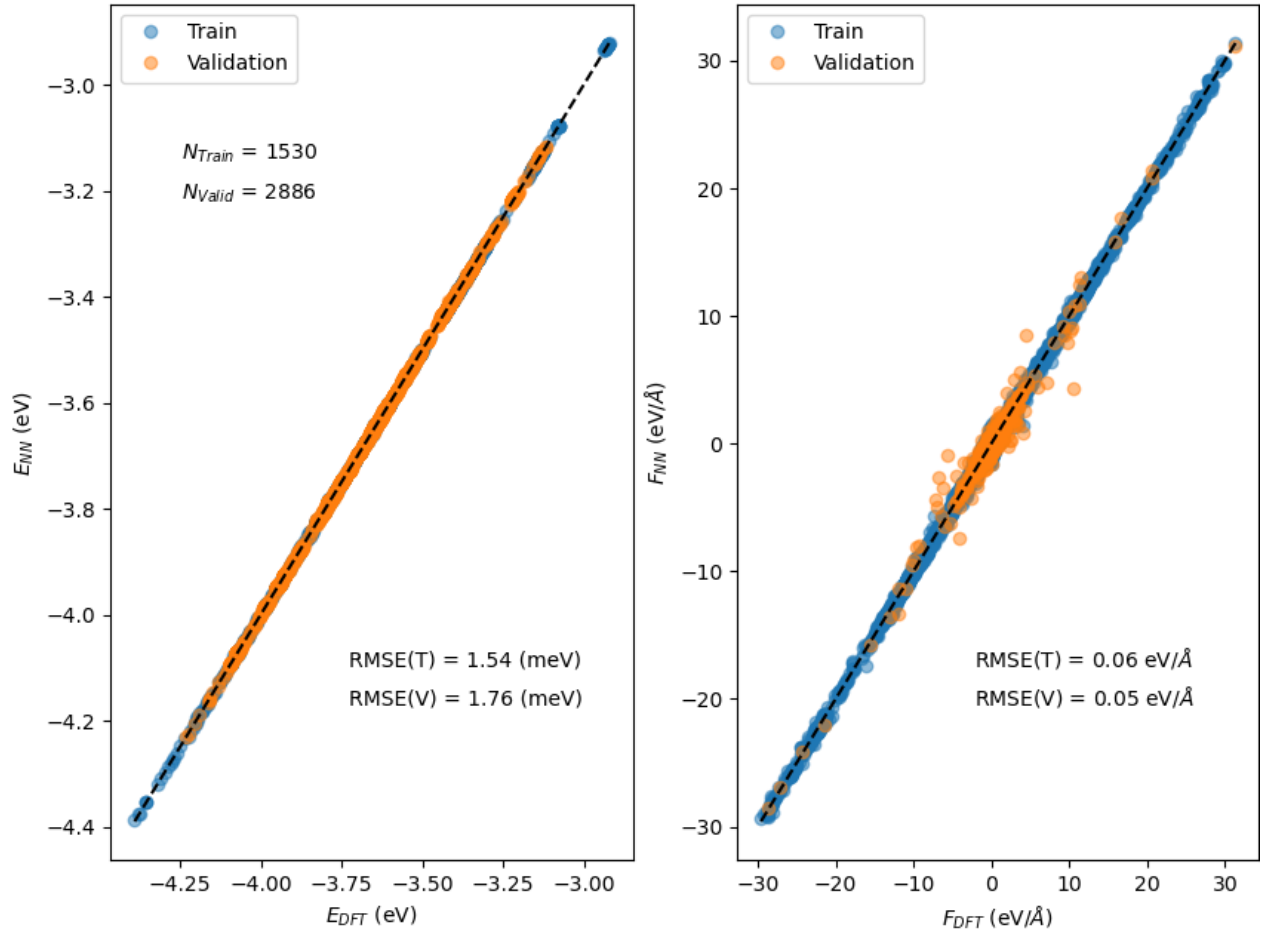


Figure 6.3: Parity plot comparing the Neural network predicted energy and forces with the reference DFT calculations for larger stepped surface unit cells dataset generated using GCBH simulations.

and Cu grand-canonically. In the process, the chemical potential of Cu is found by the energy increment associated with the formation of an extra layer of Cu on Cu(111) surface and CO chemical potential using the ideal gas phase treatment. As a result,  $\mu_{CO} = -14.9$  eV (for 760 Torr) and  $\mu_{Cu} = -3.21$  eV. We performed the calculations for Cu(553), Cu(533) and Cu(557). In the Fig. 6.4, 6.5, and 6.6 we show a heat-map of various surface configurations found using GCBH simulations for previously mentioned facets. Each square in the plot represents the structure with the lowest formation energy for the given number of Cu atoms and CO molecules in the system. The formation energy is calculated as  $g^{rel} = E - n_{CO} \times \mu_{CO} - n_{Cu} \times \mu_{Cu}$ .

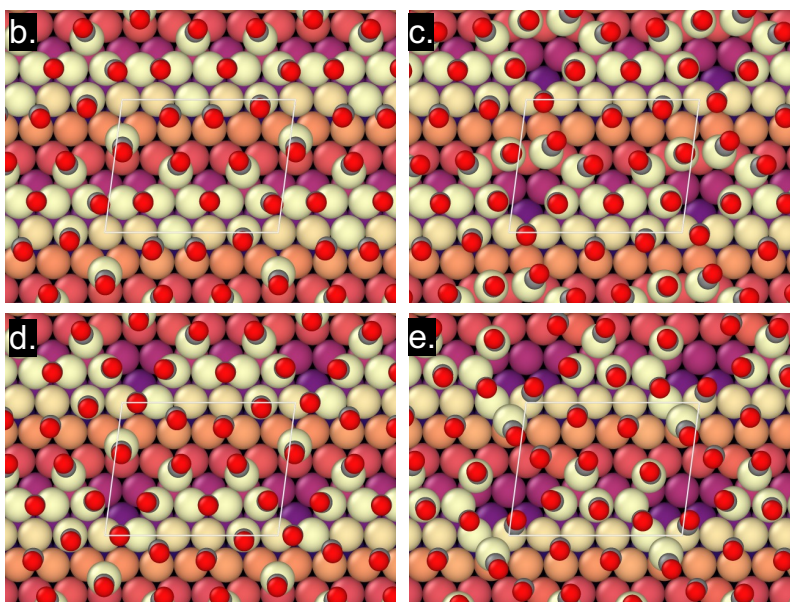
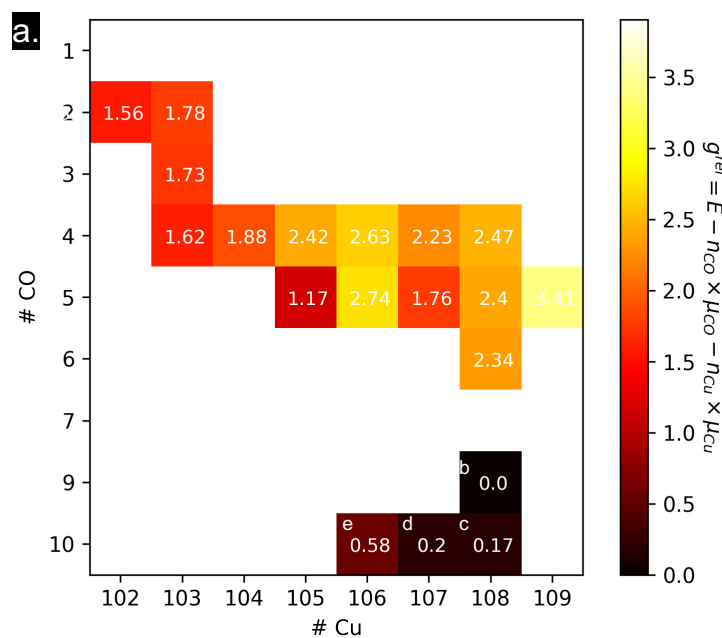


Figure 6.4: GCBH results for Cu(553) (a) Stability diagram that shows a heat map of the relative formation energy  $g^{rel} = E - n_{CO} \times \mu_{CO} - n_{Cu} \times \mu_{Cu}$  as a function number of Cu and CO in the system. The relative adsorption Gibbs free energy for a specific Cu/CO pair is labeled within the heat map. The four lowest energy structures (with  $g^{rel} = 0, 0.17, 0.2, 0.58$ ) found from the analysis are shown in increasing energy order from (b)-(e) respectively. The simulation is performed using 1 atm and 25°C conditions.

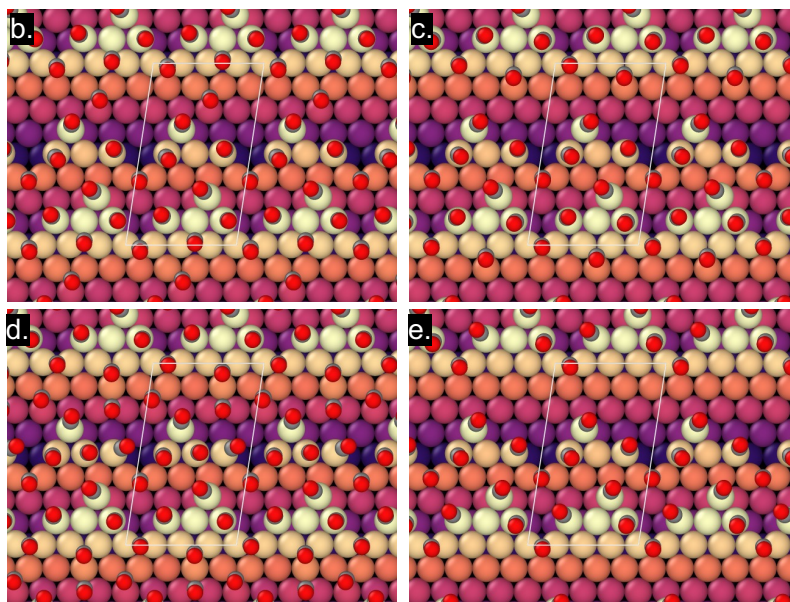
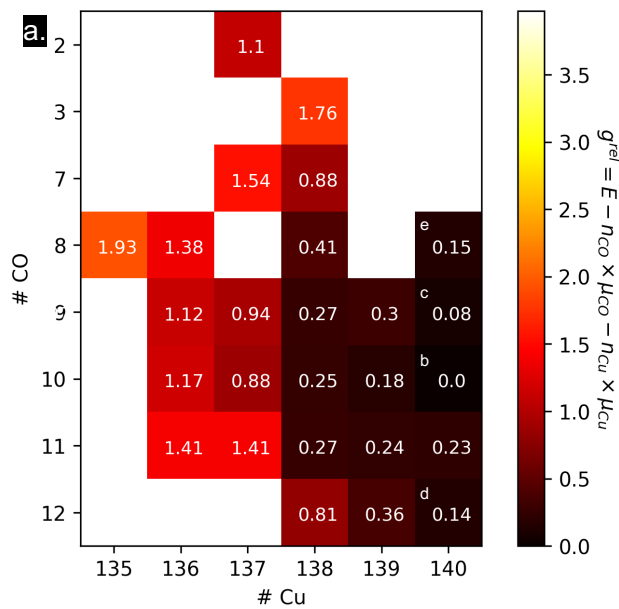


Figure 6.5: GCBH results for Cu(533) (a) Stability diagram that shows a heat map of the relative formation energy  $g^{rel} = E - n_{CO} \times \mu_{CO} - n_{Cu} \times \mu_{Cu}$  as a function number of Cu and CO in the system. The relative adsorption Gibbs free energy for a specific Cu/CO pair is labeled within the heat map. The four lowest energy structures (with  $g^{rel} = 0, 0.08, 0.14, 0.15$ ) found from the analysis are shown in increasing energy order from (b)-(e) respectively. The simulation is performed using 1 atm and 25°C conditions.

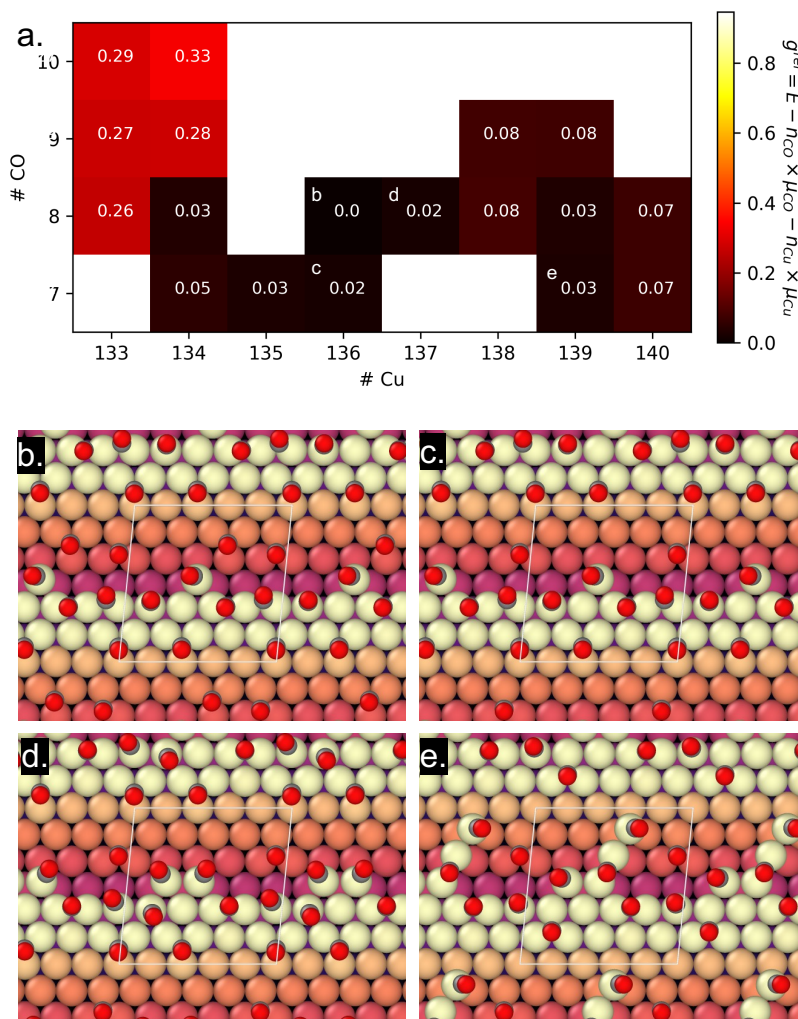


Figure 6.6: GCBH results for Cu(537) (a) Stability diagram that shows a heat map of the relative formation energy  $g^{rel} = E - n_{CO} \times \mu_{CO} - n_{Cu} \times \mu_{Cu}$  as a function number of Cu and CO in the system. The relative adsorption Gibbs free energy for a specific Cu/CO pair is labeled within the heat map. The four lowest energy structures (with  $g^{rel} = 0, 0.02, 0.03, 0.03$ ) found from the analysis are shown in increasing energy order from (b)-(e) respectively. The simulation is performed using 1 atm and 25°C conditions.

Cu(553) and Cu(533) structures have a triangular (111) step edge while Cu(557) have a square (100) step edge. Cu(553) surface has a longer terrace length as compared to Cu(533). From the GCBH analysis with CO at 1 atm (760 Torr), we find that all the surfaces show step rearrangement. Comparing Cu(553) with Cu(533), the longer terrace allows both the step rearrangement and 1-atom island formation. The lowest energy structures (within 0.2



eV of the minima) show various configurations of step rearrangement hinting to the fact that the fluxionality of the surface can be an important factor. For both the type of steps, we also observe higher density of CO on low coordination Cu sites than on the terraces.

### 6.3.2.1 CO induced nanoisland formation on Cu(111)

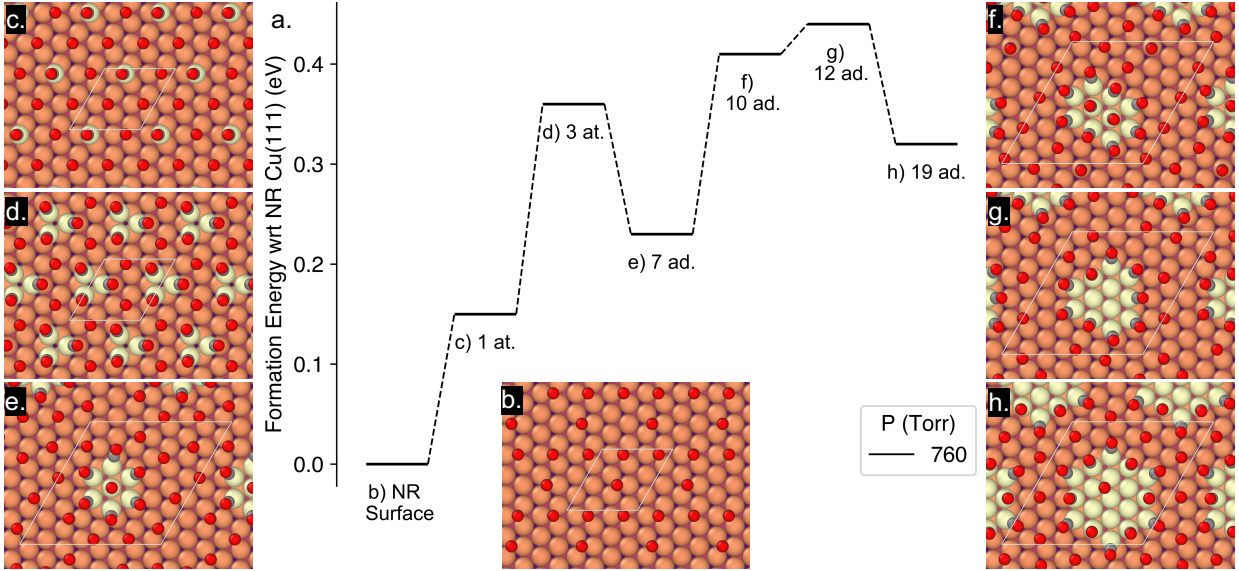


Figure 6.7: (a) Comparing the formation energies of Cu islands of increasing sizes from 1 to 19 atoms on Cu(111) terrace. (c-h) Showing the representative structures at 1 atm and 25°C are shown in the figure.

Similar to Pt(111), we consider the formation of monolayer islands of sizes 1, 3, 7, 10, 12, and 19 atoms on Cu(111). Results are not consistent with Pt(111). In the Fig. 6.7 we compare the formation of energy of various island sizes with the non-reconstructed (NR) Cu(111) surface. Here the relative formation energies are calculated as:

$$g^{rel} = X \times E_{111+island} - Y \times E_{111} - n_{island} \cdot \mu_{Cu} + (Y \cdot n_{CO,111} - X \cdot n_{CO,111+island}) \cdot \mu_{CO} \quad (6.1)$$

where X, Y defined such that the unit cell size of the reference (111) surface ( $\sqrt{12} \times \sqrt{12}$  unit cell as shown in Fig. 6.7(b)).  $E_{111}$  and  $E_{111+island}$  and the DFT energies for adsorbed CO

structure on the non-reconstructed 111 surface and the one with island respectively;  $n_i$  islands is the number Cu atoms making up the island;  $n_{CO,111}$  and  $n_{CO,111+island}$  are the number of CO molecules adsorbed on the reference NR structure and with islands respectively.

From our initial analysis, we find that formation of these islands is not thermodynamically favorable. In other words, the stabilizing effect of CO is not enough to compensate the energy cost of forming an island on the surface. We also observe that on the 111 terrace, CO adsorbs only on FCC site while on the islands, CO adsorbs on the top site. The preference of FCC site on Cu(111) is debatable with respect to the experimental results and could be a reason why our island formation energy analysis does not match the the STM studies.<sup>24</sup>

## 6.4 Conclusion

We discussed the (on-going) work on CO-induced restructuring of Cu surface using computational atomistic thermodynamics, global optimization techniques and NN-based interatomic potential. We obtain a HDNNP for the Cu/CO system trained on a number of stepped surfaces and island structures which gives an overall energy error of 1.74 meV/atom and force error of 0.05 eV/Å for both the training data (8981 structures) and validation data (42873 structures). Using GCBH algorithm treating CO molecules and Cu atoms grand-canonically, we show step rearrangement of Cu(553), Cu(533) and Cu(557) facets to thermodynamically stable at 1 atm pressure. On Cu(111), RPBE functional shows preference of CO on the FCC-site. While the step reconstruction is thermodynamically stable, formation of islands on Cu(111) surface is shown to be 0.1 to 0.4 eV destabilizing depending on the size of the islands. This contradicts the experimental findings and could be a functional issue of site preference which needs further investigation.

# CHAPTER 7

## Conclusion

Through this dissertation, we have shown the importance of understanding the substantial and important restructuring that is induced by the adsorbates. With a combined effort from experimental methods including high-pressure scanning tunneling microscopy and computational techniques involving training a Neural Network potential to deal with large systems and the scale of the problem, we are able to understand in detail the mechanism of Pt restructuring. The methods developed for the Pt/CO system are now also being adapted for the Cu/CO system to understand the difference in mechanisms for the two metals with different cohesive energies.

We demonstrate that the “Pt/CO Puzzle” can be implicitly solved by an adsorbed CO bond distance-based correction. Our computational methods successfully observe the formation of superimposed hexagonal/quasi-hexagonal lattice of CO on hexagonal Pt(111) in the correct pressure conditions at room temperature. Furthermore, with the help of observations from the STM images, we also observed that on Pt(100) CO molecules adopt a one-dimensional coincidence lattice creating  $(n \times 2)$  type unit cells ( $n=4,6,8$ ) with  $(2n-1)$  CO adsorbed. The resulting adsorption structure of CO creates a skewed hexagonal lattice which reduces CO-CO repulsion. The matching results between the computational method and experimental data meant that the developed scheme was successful at correcting the GGA-level predicted site and adsorption energy errors.

With the correction developed, we were able to develop a “fast calculator” in the form of a High-Dimensional Neural Network Potential (HDNNP) which was trained using DFT data

and could predict the energy and forces based on just structural and chemical information of a system. Using this potential with global optimization algorithms (Grand Canonical Basin Hopping), we were able to explore the PES efficiently. We started with understanding CO organization on stepped and kink surfaces assuming the surface is not reconstructed. The study helped us understand that the CO structure such surfaces depends on a number of factors including the step type (111 or 100), the terrace length, kink sites, etc.

The structures of CO organized on non-reconstructed stepped surface became the starting point to understand restructuring events driven by CO at high coverage and ambient pressure. With further improvement to the HDDNP, we were able to utilize the potential to simulate large scale step restructuring and island formation on the surface. From our computational study, we conclusively show that the main reason for the restructuring of the surface is the formation of lower-coordination Pt atom sites at the step edges where CO binds more strongly. This increased CO binding energy compensates the energy cost arising from the restructuring of the bare surface. We also show how small islands with size  $<12$  atoms are meta stable and only larger islands are thermodynamically stable. Finally using the NN-based potential, we show that rearrangement of CO molecules leads to increase in CO coverage and formation of dicarbonyl surface complex which is a key step to start detachment of Pt atoms from the step edge.

Broadly through this dissertation, we demonstrate the importance of understanding the atomic-scale dynamics of metal catalyst surfaces under high coverage of adsorbate. We establish that a comprehensive, atomic-scale understanding of the ensemble of surface structures of a catalyst in a reactant gas is crucial for determining catalytic reaction mechanisms at a molecular level. These atomic-scale insights into the dynamics of surface reconstruction induced by the adsorbate can be used to design catalyst/reactant systems that promote surface restructuring and create optimal catalytic sites under reaction conditions to ultimately maximize the activity or selectivity for the desired reaction.



## REFERENCES

- [1] National Research Council et al. *Catalysis for Energy: Fundamental Science and Long-Term Impacts of the US Department of Energy Basic Energy Sciences Catalysis Science Program*. National Academies Press, 2009.
- [2] Paul Sabatier and Nobel Lecture. “The method of direct hydrogenation by catalysis”. In: *Nobel Lecture* 11 (1912).
- [3] Gabor A Somorjai and Yimin Li. *Introduction to surface chemistry and catalysis*. John Wiley & Sons, 2010.
- [4] Iurô Horiuti and Michael Polanyi. “Exchange reactions of hydrogen on metallic catalysts”. In: *Transactions of the Faraday Society* 30 (1934), pp. 1164–1172.
- [5] Max Appl. “The Haber-Bosch process and the development of chemical engineering”. In: *A century of chemical engineering* (1982), pp. 29–54.
- [6] John Humphreys, Rong Lan, and Shanwen Tao. “Development and recent progress on ammonia synthesis catalysts for Haber–Bosch process”. In: *Advanced Energy and Sustainability Research* 2.1 (2021), p. 2000043.
- [7] Kathleen C Taylor. “Automobile catalytic converters”. In: *Catalysis*. Springer, 1984, pp. 119–170.
- [8] Jan Kašpar, Paolo Fornasiero, and Neal Hickey. “Automotive catalytic converters: current status and some perspectives”. In: *Catalysis today* 77.4 (2003), pp. 419–449.
- [9] R Horn et al. “Syngas by catalytic partial oxidation of methane on rhodium: Mechanistic conclusions from spatially resolved measurements and numerical simulations”. In: *Journal of Catalysis* 242.1 (2006), pp. 92–102.
- [10] Atsushi Ishihara et al. “Addition effect of ruthenium on nickel steam reforming catalysts”. In: *Fuel* 84.12-13 (2005), pp. 1462–1468.

- [11] Mariana MVM Souza, Octávio R Macedo Neto, and Martin Schmal. “Synthesis gas production from natural gas on supported Pt catalysts”. In: *Journal of Natural Gas Chemistry* 15.1 (2006), pp. 21–27.
- [12] Jae-Hong Ryu et al. “Promotion of palladium-based catalysts on metal monolith for partial oxidation of methane to syngas”. In: *Applied Catalysis B: Environmental* 80.3-4 (2008), pp. 306–312.
- [13] Juan Adanez et al. “Progress in chemical-looping combustion and reforming technologies”. In: *Progress in energy and combustion science* 38.2 (2012), pp. 215–282.
- [14] Jens Kehlet Nørskov et al. “Origin of the overpotential for oxygen reduction at a fuel-cell cathode”. In: *The Journal of Physical Chemistry B* 108.46 (2004), pp. 17886–17892.
- [15] Zhi Wei Seh et al. “Combining theory and experiment in electrocatalysis: Insights into materials design”. In: *Science* 355.6321 (2017), eaad4998.
- [16] Jens Kehlet Nørskov et al. “Trends in the exchange current for hydrogen evolution”. In: *Journal of The Electrochemical Society* 152.3 (2005), J23.
- [17] Stephanie Nitopi et al. “Progress and perspectives of electrochemical CO<sub>2</sub> reduction on copper in aqueous electrolyte”. In: *Chemical reviews* 119.12 (2019), pp. 7610–7672.
- [18] Wen Ju et al. “Understanding activity and selectivity of metal-nitrogen-doped carbon catalysts for electrochemical reduction of CO<sub>2</sub>”. In: *Nature communications* 8.1 (2017), pp. 1–9.
- [19] Jon Wilson and Cor De Groot. “Atomic-scale restructuring in high-pressure catalysis”. In: *Journal of Physical Chemistry* 99.20 (1995), pp. 7860–7866.
- [20] D. Loffreda, L. Piccolo, and P. Sautet. “Surface restructuring under gas pressure from first principles: A mechanism for CO-induced removal of the Au(110)-(1x2) reconstruction”. In: *Physical Review B - Condensed Matter and Materials Physics* 71.11 (2005), pp. 1–4.

- [21] L. Piccolo et al. “The adsorption of CO on Au(1 1 1) at elevated pressures studied by STM, RAIRS and DFT calculations”. In: *Surface Science* 566-568.1-3 PART 2 (2004), pp. 995–1000.
- [22] Franklin Feng Tao and Miquel Salmeron. “In situ studies of chemistry and structure of materials in reactive environments”. In: *Science* 331.6014 (2011), pp. 171–174.
- [23] Luan Nguyen et al. “Visualization of Surfaces of Pt and Ni Model Catalysts in Reactive Environments Using Ambient Pressure High Temperature Scanning Tunneling Microscopy and Understanding the Restructurings of Surfaces of Model Metal Catalysts under Reaction Conditions at Near Ambient Pressure”. In: *J Phys Chem C* 117.2 (2013), pp. 971–977.
- [24] Baran Eren et al. “Activation of Cu (111) surface by decomposition into nanoclusters driven by CO adsorption”. In: *Science* 351.6272 (2016), pp. 475–478.
- [25] Franklin Feng Tao et al. “Formation of second-generation nanoclusters on metal nanoparticles driven by reactant gases”. In: *Nano Letters* 16.8 (2016), pp. 5001–5009.
- [26] Núria J. Divins et al. “Influence of the support on surface rearrangements of bimetallic nanoparticles in real catalysts”. In: *Science* 346.6209 (2014), pp. 620–623.
- [27] Arghya Banerjee et al. “Origin of the formation of nanoislands on cobalt catalysts during Fischer–Tropsch synthesis”. In: *Acs Catalysis* 5.8 (2015), pp. 4756–4760.
- [28] Payam Kaghazchi and Timo Jacob. “Roughening of hcp metal surfaces induced by nitrogen adsorption”. In: *Physical Chemistry Chemical Physics* 14.40 (2012), pp. 13903–13906.
- [29] Matteo Cargnello et al. “Control of metal nanocrystal size reveals metal-support interface role for ceria catalysts”. In: *Science* 341.6147 (2013), pp. 771–773.
- [30] Y Li et al. “Complex structural dynamics of nanocatalysts revealed in Operando conditions by correlated imaging and spectroscopy probes”. In: *Nature Communications* 6 (2015), p. 7583.

- [31] Hemma Mistry et al. “Highly selective plasma-activated copper catalysts for carbon dioxide reduction to ethylene”. In: *Nature Communications* 7 (2016), p. 12123.
- [32] Rachel M Anderson et al. “An experimental and theoretical investigation of the inversion of Pd Pt core shell dendrimer-encapsulated nanoparticles”. In: *Acs Nano* 7.10 (2013), pp. 9345–9353.
- [33] Anatoly I Frenkel and Jeroen A Van Bokhoven. “X-ray spectroscopy for chemical and energy sciences: the case of heterogeneous catalysis”. In: *Journal of Synchrotron Radiation* 21.5 (2014), pp. 1084–1089.
- [34] a Patlolla et al. “Characterization of metal-oxide catalysts in operando conditions by combining X-ray absorption and raman spectroscopies in the same experiment”. In: *Topics in Catalysis* 56.11 (2013), pp. 896–904.
- [35] Audrey S. Duke et al. “In Situ Ambient Pressure X-ray Photoelectron Spectroscopy Studies of Methanol Oxidation on Pt(111) and Pt-Re Alloys”. In: *Journal of Physical Chemistry C* 119.40 (2015), pp. 23082–23093.
- [36] Audrey S. Duke et al. “In situ studies of carbon monoxide oxidation on platinum and platinum-rhenium alloy surfaces”. In: *Journal of Physical Chemistry C* 119.1 (2015), pp. 381–391.
- [37] J. B. Park et al. “In situ scanning tunneling microscopy studies of bimetallic cluster growth: Pt-Rh on TiO<sub>2</sub>(1 1 0)”. In: *Surface Science* 600.14 (2006), pp. 2913–2923.
- [38] Andrei Kolmakov et al. “Graphene oxide windows for in situ environmental cell photoelectron spectroscopy”. In: *Nature Nanotechnology* 6.10 (2011), p. 651.
- [39] Alexey Lipatov et al. “Highly selective gas sensor arrays based on thermally reduced graphene oxide”. In: *Nanoscale* 5.12 (2013), pp. 5426–5434.
- [40] Joshua D Stoll and Andrei Kolmakov. “Electron transparent graphene windows for environmental scanning electron microscopy in liquids and dense gases”. In: *Nanotechnology* 23.50 (2012), p. 505704.

- [41] Bas Lm Hendriksen et al. “The role of steps in surface catalysis and reaction oscillations”. In: *Nature Chemistry* 2.9 (2010), p. 730.
- [42] Beatriz Roldan Cuenya. “Metal nanoparticle catalysts beginning to shape-up”. In: *Accounts of Chemical Research* 46.8 (2013), pp. 1682–1691.
- [43] E. Lira et al. “Role and evolution of nanoparticle structure and chemical state during the oxidation of NO over size- and shape-controlled Pt/ $\gamma$ -Al<sub>2</sub>O<sub>3</sub> catalysts under operando conditions”. In: *Acs Catalysis* 4.6 (2014), pp. 1875–1884.
- [44] Hemma Mistry et al. “Pressure-Dependent Effect of Hydrogen Adsorption on Structural and Electronic Properties of Pt/ $\gamma$ -Al<sub>2</sub>O<sub>3</sub> Nanoparticles”. In: *Chemcatchem* 6.1 (2014), pp. 348–352.
- [45] Yu Lei et al. “Adsorbate-induced structural changes in 1-3 nm platinum nanoparticles”. In: *Journal of the American Chemical Society* 136.26 (2014), pp. 9320–9326.
- [46] Yu Lei et al. “Combining Electronic and Geometric Effects of ZnO-Promoted Pt Nanocatalysts for Aqueous Phase Reforming of 1-Propanol”. In: *Acs Catalysis* 6.6 (2016), pp. 3457–3460.
- [47] Simon R Bare et al. “Characterizing industrial catalysts using in situ XAFS under identical conditions”. In: *Physical Chemistry Chemical Physics* 12.27 (2010), pp. 7702–7711.
- [48] Ya Huei Cathy Chin, Mónica García-Diéguez, and Enrique Iglesia. “Dynamics and thermodynamics of Pd-PdO phase transitions: Effects of pd cluster size and kinetic implications for catalytic methane combustion”. In: *Journal of Physical Chemistry C* 120.3 (2016), pp. 1446–1460.
- [49] Chong Min Wang et al. “In situ TEM investigation of congruent phase transition and structural evolution of nanostructured silicon/carbon anode for lithium ion batteries”. In: *Nano Letters* 12.3 (2012), pp. 1624–1632.

- [50] Patricia Abellan et al. “Gaining Control over Radiolytic Synthesis of Uniform Sub-3-nanometer Palladium Nanoparticles: Use of Aromatic Liquids in the Electron Microscope”. In: *Langmuir* 32.6 (2016), pp. 1468–1477.
- [51] Ayman M. Karim et al. “Synthesis of 1 nm Pd Nanoparticles in a Microfluidic Reactor: Insights from in Situ X-ray Absorption Fine Structure Spectroscopy and Small-Angle X-ray Scattering”. In: *The Journal of Physical Chemistry C* 119.23 (2015), pp. 13257–13267.
- [52] Ayman M. Karim et al. “In situ X-ray absorption fine structure studies on the effect of pH on Pt electronic density during aqueous phase reforming of glycerol”. In: *Acs Catalysis* 2.11 (2012), pp. 2387–2394.
- [53] G Ertl et al. *Handbook of heterogeneous catalysis* Wiley. 2008.
- [54] Weifeng Tu and Ya Huei Chin. “Catalytic consequences of chemisorbed oxygen during methanol oxidative dehydrogenation on Pd clusters”. In: *Acs Catalysis* 5.6 (2015), pp. 3375–3386.
- [55] Feng Tao et al. “Break-up of stepped platinum catalyst surfaces by high CO coverage”. In: *Science* 327.5967 (2010), pp. 850–853.
- [56] Shen Zhao et al. “Operando Characterization of Catalysts through use of a Portable Microreactor”. In: *Chemcatchem* 7.22 (2015), pp. 3683–3691.
- [57] A. Patlolla et al. “Application of operando XAS, XRD, and Raman spectroscopy for phase speciation in water gas shift reaction catalysts”. In: *Acs Catalysis* 2.11 (2012), pp. 2216–2223.
- [58] Miaofang Chi et al. “Surface faceting and elemental diffusion behaviour at atomic scale for alloy nanoparticles during in situ annealing”. In: *Nature Communications* 6 (2015), pp. 1–9.
- [59] S Hagstrom, Hb Lyon, and G.A. Somorjai. “Surface structures on the clean platinum (100) surface”. In: *Physical Review Letters* 15.11 (1965), p. 491.

- [60] Minseok Kim, Wee Sun Sim, and David A King. “CO-induced removal of the Pt {100}-hex reconstruction studied by RAIRS”. In: *Journal of the Chemical Society, Faraday Transactions* 92.23 (1996), pp. 4781–4785.
- [61] Feng Tao et al. “Restructuring of hex-Pt (100) under CO gas environments: formation of 2-D nanoclusters”. In: *Nano Letters* 9.5 (2009), pp. 2167–2171.
- [62] Zhongwei Zhu et al. “In situ scanning tunneling microscopy and X-ray photoelectron spectroscopy studies of ethylene-induced structural changes on the Pt (100)-hex surface”. In: *The Journal of Physical Chemistry C* 117.6 (2013), pp. 2799–2804.
- [63] Michael S Pierce et al. “CO-induced lifting of Au (001) surface reconstruction”. In: *The Journal of Physical Chemistry C* 112.7 (2008), pp. 2231–2234.
- [64] M Salmeron et al. “A LEED-AES study of the reconstructed Pt (110) surface and the effect of oxygen treatment”. In: *Surface Science* 91.2-3 (1980), pp. 373–384.
- [65] T Gritsch et al. “Mechanism of the CO-induced  $1 \times 2 \rightarrow 1 \times 1$  structural transformation of Pt (110)”. In: *Physical Review Letters* 63.10 (1989), p. 1086.
- [66] P Thostrup et al. “CO-induced restructuring of Pt (110)-(1×2): bridging the pressure gap with high-pressure scanning tunneling microscopy”. In: *The Journal of Chemical Physics* 118.8 (2003), pp. 3724–3730.
- [67] Rickmer Kose and David A King. “Energetics and CO-induced lifting of a (1×2) surface reconstruction observed on Pt(311)”. In: *Chemical Physics Letters* 313.1-2 (1999), pp. 1–6.
- [68] J. Greeley et al. “CO vibrational frequencies on methanol synthesis catalysts: a DFT study”. In: *Journal of Catalysis* 213.1 (2003), pp. 63–72.
- [69] N. Schumacher et al. “Trends in low-temperature water-gas shift reactivity on transition metals”. In: *Journal of Catalysis* 229.2 (2005), pp. 265–275.
- [70] Amit A. Gokhale et al. “Effect of Sn on the reactivity of Cu surfaces”. In: *Journal of Physical Chemistry B* 108.37 (2004), pp. 14062–14073.

- [71] Amit A. Gokhale, James A. Dumesic, and Manos Mavrikakis. “On the mechanism of low-temperature water gas shift reaction on copper”. In: *Journal of the American Chemical Society* 130.4 (2008), pp. 1402–1414.
- [72] Meijiao Ren et al. “Influence of Microwave Irradiation on the Structural Properties of Carbon-Supported Hollow Copper Nanoparticles and Their Effect on the Synthesis of Dimethyl Carbonate”. In: *Chemcatchem* 8.4 (2016), pp. 861–871.
- [73] Shun Li Li et al. “Inorganic-organic hybrid materials with different dimensions constructed from copper-fluconazole metal-organic units and Keggin polyanion clusters”. In: *Dalton Transactions* 15 (2008), pp. 2015–2025.
- [74] Yu Chen et al. “Synthesis of 3-Methylindole from Glycerol Cyclization with Aniline over CuCr/Al<sub>2</sub>O<sub>3</sub> Catalysts Modified by Alkali Earth Oxides”. In: *Heteroatom Chemistry* 24.4 (2013), pp. 263–270.
- [75] Guangwen Zhou et al. “Step-edge-induced oxide growth during the oxidation of Cu surfaces”. In: *Physical Review Letters* 109.23 (2012), pp. 1–5.
- [76] Langli Luo et al. “Effect of oxygen gas pressure on orientations of Cu<sub>2</sub>O nuclei during the initial oxidation of Cu(100), (110) and (111)”. In: *Surface Science* 606.23-24 (2012), pp. 1790–1797.
- [77] Qing Zhu et al. “Early and transient stages of Cu oxidation: Atomistic insights from theoretical simulations and in situ experiments”. In: *Surface Science* 652 (2016), pp. 98–113.
- [78] Jess Wellendorff et al. “A benchmark database for adsorption bond energies to transition metal surfaces and comparison to selected DFT functionals”. In: *Surface Science* 640 (2015), pp. 36–44.
- [79] C. Klink et al. “Interaction of C with Ni(100): Atom-resolved studies of the “clock” reconstruction”. In: *Phys. Rev. Lett.* 71 (26 Dec. 1993), pp. 4350–4353.



- [80] R Raval et al. “CO induced reconstruction of Pd110 characterised by RAIRS”. In: *Journal of Electron Spectroscopy and Related Phenomena* 54 (1990), pp. 629–638.
- [81] P Hu et al. “A LEED structural study of the CO induced reconstruction of Pd {110} evidence for a missing row structure”. In: *Surface science* 249.1-3 (1991), pp. 1–7.
- [82] Marie Døvre Strømsheim et al. “CO-Induced Surface Reconstruction of the Co (11–20) Surface—A Combined Theoretical and Experimental Investigation”. In: *The Journal of Physical Chemistry C* 124.52 (2020), pp. 28488–28499.
- [83] Marie E Turano et al. “Oxygen-induced surface reconstructions on curved Ag (111)”. In: *Journal of Vacuum Science & Technology A: Vacuum, Surfaces, and Films* 39.5 (2021), p. 053201.
- [84] W Oed et al. “Adsorbate induced reconstruction phase p (2× 2) O/Ni (100)”. In: *Surface Science* 225.3 (1990), pp. 242–248.
- [85] A Grossmann, W Erley, and H Ibach. “Adsorbate-induced surface stress and surface reconstruction: oxygen, sulfur and carbon on Ni (111)”. In: *Surface science* 337.3 (1995), pp. 183–189.
- [86] MJ Harrison et al. “Adsorbate-induced surface reconstruction and surface-stress changes in Cu (100)/ O: Experiment and theory”. In: *Physical Review B* 74.16 (2006), p. 165402.
- [87] F Jensen et al. “Surface reconstruction of Cu (110) induced by oxygen chemisorption”. In: *Physical Review B* 41.14 (1990), p. 10233.
- [88] Ralf Terborg et al. “The coverage dependence of the local structure of C on Ni (100): a structural precursor to adsorbate-induced reconstruction”. In: *Surface science* 446.3 (2000), pp. 301–313.
- [89] C Klink et al. “An STM study of carbon-induced structures on Ni (111): evidence for a carbidic-phase clock reconstruction”. In: *Surface science* 342.1-3 (1995), pp. 250–260.

- [90] Ralf Terborg et al. “Structural precursor to adsorbate-induced reconstruction: C on Ni (100)”. In: *Physical Review B* 60.15 (1999), p. 10715.
- [91] B Voigtländer, S Lehwald, and H Ibach. “Hydrogen adsorption and the adsorbate-induced Ni (110) reconstruction-an EELS study”. In: *Surface Science* 208.1-2 (1989), pp. 113–135.
- [92] Andrew M Glines and A Brad Anton. “Effects of the hydrogen-induced (1× 2) surface reconstruction on the kinetics of ethylene hydrogenation on Ni (110)”. In: *Surface science* 286.1-2 (1993), pp. 122–138.
- [93] Y Kuk, PJ Silverman, and HQ Nguyen. “Adsorbate-induced reconstruction in the Ni (110)-H system”. In: *Physical review letters* 59.13 (1987), p. 1452.
- [94] L Hammer et al. “Hydrogen-induced restructuring of close-packed metal surfaces: H/Ni (111) and H/Fe (110)”. In: *Physical Review B* 47.23 (1993), p. 15969.
- [95] Kari Kankaala, Tapio Ala-Nissila, and See-Chen Ying. “Theory of adsorbate-induced surface reconstruction on W (100)”. In: *Physical Review B* 47.4 (1993), p. 2333.
- [96] B. Böller, M. Ehrensperger, and J. Wintterlin. “In Situ Scanning Tunneling Microscopy of the Dissociation of CO on Co(0001)”. In: *Acs Catalysis* 5.11 (2015), pp. 6802–6806.
- [97] Martin Ehrensperger and Joost Wintterlin. “In situ high-pressure high-temperature scanning tunneling microscopy of a Co(0 0 0 1) Fischer-Tropsch model catalyst”. In: *Journal of Catalysis* 319 (2014), pp. 274–282.
- [98] M. Ehrensperger and J. Wintterlin. “In situ scanning tunneling microscopy of the poisoning of a Co(0001) Fischer-Tropsch model catalyst by sulfur”. In: *Journal of Catalysis* 329 (2015), pp. 49–56.
- [99] L Piccolo et al. “The adsorption of CO on Au (1 1 1) at elevated pressures studied by STM, RAIRS and DFT calculations”. In: *Surf Sci* 566 (2004), pp. 995–1000.

- [100] AAB Padama et al. “CO-induced Pd segregation and the effect of subsurface Pd on CO adsorption on CuPd surfaces”. In: *Journal of Physics: Condensed Matter* 29.2 (2016), p. 025005.
- [101] Hyun You Kim and Graeme Henkelman. “CO adsorption-driven surface segregation of Pd on Au/Pd bimetallic surfaces: role of defects and effect on CO oxidation”. In: *ACS Catalysis* 3.11 (2013), pp. 2541–2546.
- [102] Joseph R. Michalka, Patrick W. McIntyre, and J. Daniel Gezelter. “Molecular dynamics simulations of the surface reconstructions of Pt(557) and Au(557) under Exposure to CO”. In: *Journal of Physical Chemistry C* 117.28 (2013), pp. 14579–14587.
- [103] Joseph R Michalka and J Daniel Gezelter. “Island Formation on Pt/Pd (557) Surface Alloys in the Presence of Adsorbed CO: A Molecular Dynamics Study”. In: *The Journal of Physical Chemistry C* 119.25 (2015), pp. 14239–14247.
- [104] P Van Beurden et al. “Mechanism and dynamics of the CO-induced lifting of the Pt (100) surface reconstruction”. In: *Physical review letters* 90.6 (2003), p. 066106.
- [105] Ib Chorkendorff and Johannes W Niemantsverdriet. *Concepts of modern catalysis and kinetics*. Vol. 138. Wiley Online Library, 2003.
- [106] Ayman D Allian et al. “Chemisorption of CO and mechanism of CO oxidation on supported platinum nanoclusters”. In: *Journal of the American Chemical Society* 133.12 (2011), pp. 4498–4517.
- [107] Yp Gavin Chua et al. “Controlling the CO oxidation rate over Pt/TiO<sub>2</sub> catalysts by defect engineering of the TiO<sub>2</sub> support”. In: *Journal of Catalysis* 311 (2014), pp. 306–313.
- [108] Andreas Eichler. “CO oxidation on transition metal surfaces: reaction rates from first principles”. In: *Surface Science* 498.3 (2002), pp. 314–320.

- [109] Qi Fu, Howard Saltsburg, and Maria Flytzani-Stephanopoulos. “Active nonmetallic Au and Pt species on ceria-based water-gas shift catalysts”. In: *Science* 301.5635 (2003), pp. 935–938.
- [110] Ja Rodriguez et al. “Activity of CeO<sub>x</sub> and TiO<sub>x</sub> nanoparticles grown on Au (111) in the water-gas shift reaction”. In: *Science* 318.5857 (2007), pp. 1757–1760.
- [111] Chia-Hao Lin, Chung-Liang Chen, and Jeng-Han Wang. “Mechanistic studies of water-gas-shift reaction on transition metals”. In: *The Journal of Physical Chemistry C* 115.38 (2011), pp. 18582–18588.
- [112] Lars C Grabow et al. “Mechanism of the water gas shift reaction on Pt: First principles, experiments, and microkinetic modeling”. In: *The Journal of Physical Chemistry C* 112.12 (2008), pp. 4608–4617.
- [113] Mark E Dry. “The fischer-tropsch process: 1950–2000”. In: *Catalysis Today* 71.3-4 (2002), pp. 227–241.
- [114] Andrei Y Khodakov, Wei Chu, and Pascal Fongarland. “Advances in the development of novel cobalt Fischer- Tropsch catalysts for synthesis of long-chain hydrocarbons and clean fuels”. In: *Chemical Reviews* 107.5 (2007), pp. 1692–1744.
- [115] Jp Den Breejen et al. “On the origin of the cobalt particle size effects in Fischer- Tropsch catalysis”. In: *Journal of the American Chemical Society* 131.20 (2009), pp. 7197–7203.
- [116] Neil R Avery. “Electron energy loss spectroscopic study of CO on Pt (111)”. In: *The Journal of Chemical Physics* 74.7 (1981), pp. 4202–4203.
- [117] Ra Shigeishi and David A King. “Chemisorption of carbon monoxide on platinum {111}: Reflection-absorption infrared spectroscopy”. In: *Surface Science* 58.2 (1976), pp. 379–396.

- [118] Alison Crossley and David A King. “Infrared spectra for co isotopes chemisorbed on Pt “111”: Evidence for strong adsorbate coupling interactions”. In: *Surface Science* 68 (1977), pp. 528–538.
- [119] G Ertl, M Neumann, and Km Streit. “Chemisorption of CO on the Pt (111) surface”. In: *Surface Science* 64.2 (1977), pp. 393–410.
- [120] H Hopster and H Ibach. “Adsorption of CO on Pt (111) and Pt 6 (111)×(111) studied by high resolution electron energy loss spectroscopy and thermal desorption spectroscopy”. In: *Surface Science* 77.1 (1978), pp. 109–117.
- [121] H Steininger, S Lehwald, and H Ibach. “On the adsorption of CO on Pt (111)”. In: *Surface Science* 123.2-3 (1982), pp. 264–282.
- [122] Be Hayden and Am Bradshaw. “The adsorption of CO on Pt (111) studied by infrared-reflection-adsorption spectroscopy”. In: *Studies in Surface Science and Catalysis*. Vol. 14. Elsevier, 1983, p. 51.
- [123] Jp Biberrian and Ma Van Hove. “A new model for CO ordering at high coverages on low index metal surfaces: A correlation between LEED, HREELS and IRS: II. CO adsorbed on fcc (111) and hep (0001) surfaces”. In: *Surface Science* 138.2-3 (1984), pp. 361–389.
- [124] M Tüshaus et al. “Yet another vibrational study of the adsorption system Pt {111}-CO”. In: *Journal of Electron Spectroscopy and Related Phenomena* 44.1 (1987), pp. 305–316.
- [125] M Kiskinova, a Szab, and Jt Yates Jr. “Compressed CO overlayers on Pt (111)–evidence for tilted CO species at high coverages by digital ESDIAD”. In: *Surface Science* 205.1-2 (1988), pp. 215–229.
- [126] E Schweizer et al. “The potential energy surface, vibrational phase relaxation and the order-disorder transition in the adsorption system Pt {111}-CO”. In: *Surface Science* 213.1 (1989), pp. 49–89.

- [127] Wa Brown, R Kose, and Da King. “Femtomole adsorption calorimetry on single-crystal surfaces”. In: *Chemical Reviews* 98.2 (1998), pp. 797–832.
- [128] Wt Lee et al. “Why do heats of adsorption of simple gases on platinum surfaces vary so little with surface structure?” In: *Surface Science* 416.1-2 (1998), pp. 141–151.
- [129] Hyun Jin Yang et al. “STM Investigation of CO ordering on Pt (111): From an isolated molecule to high-coverage superstructures”. In: *The Journal of Physical Chemistry C* 117.32 (2013), pp. 16429–16437.
- [130] Keith Mccrea et al. “Surface structure sensitivity of high-pressure CO dissociation on Pt (557), Pt (100) and Pt (111) using sum frequency generation surface vibrational spectroscopy”. In: *Surface Science* 494.3 (2001), pp. 238–250.
- [131] Pr Norton, Ja Davies, and Te Jackman. “Absolute coverages of CO and O on Pt (111); comparison of saturation CO coverages on Pt (100),(110) and (111) surfaces”. In: *Surface Science Letters* 122.1 (1982), pp. L593–L600.
- [132] Yy Yeo, L Vattuone, and Da King. “Energetics and kinetics of CO and NO adsorption on Pt {100}: Restructuring and lateral interactions”. In: *The Journal of Chemical Physics* 104.10 (1996), pp. 3810–3821.
- [133] Rj Behm et al. “The interaction of CO and Pt (100). I. Mechanism of adsorption and Pt phase transition”. In: *The Journal of Chemical Physics* 78.12 (1983), pp. 7437–7447.
- [134] Moon-Bong Song, Koichiro Yoshimi, and Masatoki Ito. “STM observations of bridge-bonded CO on Pt (111) and asymmetric on-top CO on Pt (100)”. In: *Chemical Physics Letters* 263.3-4 (1996), pp. 585–590.
- [135] R Martin, P Gardner, and Am Bradshaw. “The adsorbate-induced removal of the Pt {100} surface reconstruction. Part II: CO”. In: *Surface Science* 342.1-3 (1995), pp. 69–84.

- [136] Stephanie Maniguet, Rebecca J Mathew, and Andrea E Russell. “EXAFS of carbon monoxide oxidation on supported Pt fuel cell electrocatalysts”. In: *The Journal of Physical Chemistry B* 104.9 (2000), pp. 1998–2004.
- [137] Neng Guo et al. “Determination of CO, H<sub>2</sub>O and H<sub>2</sub> coverage by XANES and EXAFS on Pt and Au during water gas shift reaction”. In: *Physical Chemistry Chemical Physics* 12.21 (2010), pp. 5678–5693.
- [138] Am Lahee, Jp Toennies, and Ch Wöll. “Low energy adsorbate vibrational modes observed with inelastic helium atom scattering: CO on Pt (111)”. In: *Surface Science* 177.2 (1986), pp. 371–388.
- [139] O Björneholm et al. “Overlayer structure from adsorbate and substrate core level binding energy shifts: CO, CCH<sub>3</sub> and O on Pt (111)”. In: *Surface Science* 315.1-2 (1994), pp. L983–L989.
- [140] Bnj Persson, M Tüshaus, and Am Bradshaw. “On the nature of dense CO adlayers”. In: *The Journal of Chemical Physics* 92.8 (1990), pp. 5034–5046.
- [141] Sarah R Longwitz et al. “High-coverage structures of carbon monoxide adsorbed on Pt (111) studied by high-pressure scanning tunneling microscopy”. In: *J Phys Chem B* 108.38 (2004), pp. 14497–14502.
- [142] Gt Kasun Kalhara Gunasooriya and Mark Saeys. “CO Adsorption on Pt (111): From Isolated Molecules to Ordered High-Coverage Structures”. In: *Acs Catalysis* 8.11 (2018), pp. 10225–10233.
- [143] M-L Bocquet and Ph Sautet. “STM and chemistry: a qualitative molecular orbital understanding of the image of CO on a Pt surface”. In: *Surface Science* 360.1-3 (1996), pp. 128–136.
- [144] G Kresse, a Gil, and Ph Sautet. “Significance of single-electron energies for the description of CO on Pt (111)”. In: *Physical Review B* 68.7 (2003), p. 073401.

- [145] F Abild-Pedersen and M P Andersson. “CO adsorption energies on metals with correction for high coordination adsorption sites—A density functional study”. In: *Surface Science* 601.7 (2007), pp. 1747–1753.
- [146] Marek Gajdoš, Andreas Eichler, and Jürgen Hafner. “CO adsorption on close-packed transition and noble metal surfaces: trends from ab initio calculations”. In: *Journal of Physics: Condensed Matter* 16.8 (2004), p. 1141.
- [147] Peter J Feibelman et al. “The CO/Pt (111) puzzle”. In: *The Journal of Physical Chemistry B* 105.18 (2001), pp. 4018–4025.
- [148] Qing-Miao Hu, Karsten Reuter, and Matthias Scheffler. “Towards an exact treatment of exchange and correlation in materials: Application to the “CO adsorption puzzle” and other systems”. In: *Physical Review Letters* 98.17 (2007), p. 176103.
- [149] L Schimka et al. “Accurate surface and adsorption energies from many-body perturbation theory”. In: *Nature Materials* 9.9 (2010), p. 741.
- [150] Sarah Gautier et al. “Molecular adsorption at Pt (111). How accurate are DFT functionals?” In: *Physical Chemistry Chemical Physics* 17.43 (2015), pp. 28921–28930.
- [151] Kaining Duanmu and Donald G Truhlar. “Validation of density functionals for adsorption energies on transition metal surfaces”. In: *Journal of Chemical Theory and Computation* 13.2 (2017), pp. 835–842.
- [152] Yun Wang et al. “Successful a priori modeling of CO adsorption on pt (111) using periodic hybrid density functional theory”. In: *Journal of the American Chemical Society* 129.34 (2007), pp. 10402–10407.
- [153] K Doll. “CO adsorption on the Pt (1 1 1) surface: a comparison of a gradient corrected functional and a hybrid functional”. In: *Surface Science* 573.3 (2004), pp. 464–473.
- [154] George Blyholder. “Molecular orbital view of chemisorbed carbon monoxide”. In: *The Journal of Physical Chemistry* 68.10 (1964), pp. 2772–2777.



- [155] Bjørk Hammer, Y Morikawa, and Jens Kehlet Nørskov. “CO chemisorption at metal surfaces and overlayers”. In: *Physical Review Letters* 76.12 (1996), p. 2141.
- [156] Patanachai Janthon et al. “Adding pieces to the CO/Pt (111) puzzle: the role of dispersion”. In: *The Journal of Physical Chemistry C* 121.7 (2017), pp. 3970–3977.
- [157] Alfred Gil et al. “Site preference of CO chemisorbed on Pt (1 1 1) from density functional calculations”. In: *Surface Science* 530.1-2 (2003), pp. 71–87.
- [158] Sara E Mason, Ilya Grinberg, and Andrew M Rappe. “First-principles extrapolation method for accurate CO adsorption energies on metal surfaces”. In: *Physical Review B* 69.16 (2004), p. 161401.
- [159] Rutger a Van Santen and Matthew Neurock. *Molecular heterogeneous catalysis: a conceptual and computational approach*. John Wiley & Sons, 2009.
- [160] G Held et al. “Determination of adsorption sites of pure and coadsorbed CO on Ni (111) by high resolution X-ray photoelectron spectroscopy”. In: *Surface Science* 398.1-2 (1998), pp. 154–171.
- [161] D Talbi and Gs Chandler. “Extensive ab Initio Study of the C2O2, C2S2, and C2OS Systems: Stabilities and Singlet- Triplet Energy Gaps”. In: *The Journal of Physical Chemistry A* 104.24 (2000), pp. 5872–5881.
- [162] Feng Tao, Luan Nguyen, and Shiran Zhang. “Design of a new reactor-like high temperature near ambient pressure scanning tunneling microscope for catalysis studies”. In: *Review of Scientific Instruments* 84.3 (2013), p. 034101.
- [163] Marc Tm Koper et al. “Field-dependent chemisorption of carbon monoxide and nitric oxide on platinum-group (111) surfaces: Quantum chemical calculations compared with infrared spectroscopy at electrochemical and vacuum-based interfaces”. In: *The Journal of Chemical Physics* 113.10 (2000), pp. 4392–4407.
- [164] Francesc Illas et al. “Origin of the vibrational shift of CO chemisorbed on Pt (111)”. In: *Physical Review B* 52.16 (1995), p. 12372.

- [165] Yy Yeo, L Vattuone, and Da King. “Calorimetric heats for CO and oxygen adsorption and for the catalytic CO oxidation reaction on Pt {111}”. In: *The Journal of Chemical Physics* 106.1 (1997), pp. 392–401.
- [166] Franklin Tao and Peter A Crozier. “Atomic-scale observations of catalyst structures under reaction conditions and during catalysis”. In: *Chemical Reviews* 116.6 (2016), pp. 3487–3539.
- [167] Detre Teschner et al. “Understanding palladium hydrogenation catalysts: when the nature of the reactive molecule controls the nature of the catalyst active phase”. In: *Angewandte Chemie International Edition* 47.48 (2008), pp. 9274–9278.
- [168] Karsten Reuter and Matthias Scheffler. “Composition and structure of the RuO<sub>2</sub> (110) surface in an O<sub>2</sub> and CO environment: Implications for the catalytic formation of CO<sub>2</sub>”. In: *Physical Review B* 68.4 (2003), p. 045407.
- [169] a Michaelides et al. “Structures and thermodynamic phase transitions for oxygen and silver oxide phases on Ag {1 1 1}”. In: *Chemical Physics Letters* 367.3-4 (2003), pp. 344–350.
- [170] Matthijs a Van Spronsen et al. “Dynamics of Surface Alloys: Rearrangement of Pd/Ag (111) Induced by CO and O<sub>2</sub>”. In: *The Journal of Physical Chemistry C* 123.13 (2018), pp. 8312–8323.
- [171] D. F. Ogletree, M.A. Van Hove, and G.A. Somorjai. “LEED intensity analysis of the structures of clean Pt (111) and of CO adsorbed on Pt (111) in the c (4× 2) arrangement”. In: *Surface Science* 173.2-3 (1986), pp. 351–365.
- [172] G.S. Blackman et al. “Mix of molecular adsorption sites detected for disordered CO on Pt (111) by diffuse low-energy electron diffraction”. In: *Physical Review Letters* 61.20 (1988), p. 2352.

- [173] M Ø Pedersen et al. “CO on Pt (111): binding site assignment from the interplay between measured and calculated STM images”. In: *Chemical Physics Letters* 299.5 (1999), pp. 403–409.
- [174] Nv Petrova and In Yakovkin. “Lateral interaction and CO adlayer structures on the Pt (111) surface”. In: *Surface Science* 519.1-2 (2002), pp. 90–100.
- [175] Ignacio Villegas and Michael J Weaver. “Carbon monoxide adlayer structures on platinum (111) electrodes: A synergy between in-situ scanning tunneling microscopy and infrared spectroscopy”. In: *The Journal of Chemical Physics* 101.2 (1994), pp. 1648–1660.
- [176] D Loffreda, D Simon, and P Sautet. “Dependence of stretching frequency on surface coverage and adsorbate–adsorbate interactions: a density-functional theory approach of CO on Pd (111)”. In: *Surface Science* 425.1 (1999), pp. 68–80.
- [177] G Brodén, G Pirug, and Hp Bonzel. “Chemisorption of CO on the unreconstructed Pt (100) surface”. In: *Surface Science* 72.1 (1978), pp. 45–52.
- [178] William T Vetterling et al. *Numerical recipes: example book C*. Cambridge University Press, 1992.
- [179] Josef Ischtwan and Michael A Collins. “Molecular potential energy surfaces by interpolation”. In: *The Journal of Chemical Physics* 100.11 (1994), pp. 8080–8088.
- [180] Meredith Jt Jordan, Keiran C Thompson, and Michael A Collins. “Convergence of molecular potential energy surfaces by interpolation: Application to the  $\text{OH} + \text{H}_2 \rightarrow \text{H}_2\text{O} + \text{H}$  reaction”. In: *The Journal of Chemical Physics* 102.14 (1995), pp. 5647–5657.
- [181] Michael A Collins. “Molecular potential-energy surfaces for chemical reaction dynamics”. In: *Theoretical Chemistry Accounts* 108.6 (2002), pp. 313–324.

- [182] Albert P Bartók et al. “Gaussian approximation potentials: The accuracy of quantum mechanics, without the electrons”. In: *Physical Review Letters* 104.13 (2010), p. 136403.
- [183] George Cybenko. “Approximation by superpositions of a sigmoidal function”. In: *Mathematics of Control, Signals and Systems* 2.4 (1989), pp. 303–314.
- [184] Kurt Hornik, Maxwell Stinchcombe, and Halbert White. “Multilayer feedforward networks are universal approximators”. In: *Neural Networks* 2.5 (1989), pp. 359–366.
- [185] Fv Prudente and Jjs Neto. “The fitting of potential energy surfaces using neural networks. Application to the study of the photodissociation processes”. In: *Chemical Physics Letters* 287.5-6 (May 1998), pp. 585–589.
- [186] Fv Prudente, Ph Acioli, and Jjs Neto. “The fitting of potential energy surfaces using neural networks: Application to the study of vibrational levels of H-3(+).” In: *Journal of Chemical Physics* 109.20 (Nov. 1998), pp. 8801–8808.
- [187] Acp Bittencourt, Fv Prudente, and Jdm Vianna. “The fitting of potential energy and transition moment functions using neural networks: transition probabilities in OH (A(2)Sigma(+)-> X-2 Pi)”. In: *Chemical Physics* 297.1-3 (Feb. 2004), pp. 153–161.
- [188] Tm Rocha et al. “The use of neural networks for fitting potential energy surfaces: A comparative case study for the H-3(+) molecule”. In: *International Journal of Quantum Chemistry* 95.3 (Nov. 2003). 11th Brazilian Symposium on Theoretical Chemistry, Caxambu Minas Gerais, Brazil, Nov. 18-21, 2001, pp. 281–288.
- [189] S Manzhos et al. “A nested molecule-independent neural network approach for high-quality potential fits”. In: *Journal of Physical Chemistry A* 110.16 (Apr. 2006), pp. 5295–5304.
- [190] Sergei Manzhos and Tucker Carrington Jr. “Using neural networks, optimized coordinates, and high-dimensional model representations to obtain a vinyl bromide potential surface”. In: *Journal of Chemical Physics* 129.22 (Dec. 2008).

- [191] Sergei Manzhos and Tucker Carrington Jr. “Using redundant coordinates to represent potential energy surfaces with lower-dimensional functions”. In: *Journal of Chemical Physics* 127.1 (July 2007).
- [192] Sergei Manzhos and Tucker Carrington Jr. “A random-sampling high dimensional model representation neural network for building potential energy surfaces”. In: *Journal of Chemical Physics* 125.8 (Aug. 2006).
- [193] M. Malshe et al. “Development of generalized potential-energy surfaces using many-body expansions, neural networks, and moiety energy approximations”. In: *Journal of Chemical Physics* 130.18 (May 2009).
- [194] M. Malshe et al. “Parametrization of analytic interatomic potential functions using neural networks”. In: *Journal of Chemical Physics* 129.4 (July 2008).
- [195] Tb Blank et al. “NEURAL-NETWORK MODELS OF POTENTIAL-ENERGY SURFACES”. In: *Journal of Chemical Physics* 103.10 (Sept. 1995), pp. 4129–4137.
- [196] S Lorenz, a Gross, and M Scheffler. “Representing high-dimensional potential-energy surfaces for reactions at surfaces by neural networks”. In: *Chemical Physics Letters* 395.4-6 (Sept. 2004), pp. 210–215.
- [197] S Lorenz, M Scheffler, and A Gross. “Descriptions of surface chemical reactions using a neural network representation of the potential-energy surface”. In: *Physical Review B* 73.11 (Mar. 2006).
- [198] Jorg Behler, Sonke Lorenz, and Karsten Reuter. “Representing molecule-surface interactions with symmetry-adapted neural networks”. In: *Journal of Chemical Physics* 127.1 (July 2007).
- [199] Joerg Behler, Karsten Reuter, and Matthias Scheffler. “Nonadiabatic effects in the dissociation of oxygen molecules at the Al(111) surface”. In: *Physical Review B* 77.11 (Mar. 2008).

- [200] Jeffery Ludwig and Dionisios G. Vlachos. “Ab initio molecular dynamics of hydrogen dissociation on metal surfaces using neural networks and novelty sampling”. In: *Journal of Chemical Physics* 127.15 (Oct. 2007).
- [201] Diogo A. R. S. Latino et al. “Mapping Potential Energy Surfaces by Neural Networks: The ethanol/Au(111) interface”. In: *Journal of Electroanalytical Chemistry* 624.1-2 (Dec. 2008), pp. 109–120.
- [202] Christian Carbogno et al. “Signatures of nonadiabatic O-2 dissociation at Al(111): First-principles fewest-switches study”. In: *Physical Review B* 81.3 (Jan. 2010).
- [203] Jörg Behler and Michele Parrinello. “Generalized Neural-Network Representation of High-Dimensional Potential-Energy Surfaces”. In: *Phys. Rev. Lett.* 98.14 (14 Apr. 2007), p. 146401.
- [204] Jörg Behler et al. “Pressure-induced phase transitions in silicon studied by neural network-based metadynamics simulations”. In: *Physica Status Solidi (b)* 245.12 (2008), pp. 2618–2629.
- [205] Jörg Behler. “Atom-centered symmetry functions for constructing high-dimensional neural network potentials”. In: *The Journal of Chemical Physics* 134.7 (2011), p. 074106.
- [206] Michael Gastegger et al. “wACSF–Weighted atom-centered symmetry functions as descriptors in machine learning potentials”. In: *The Journal of Chemical Physics* 148.24 (2018), p. 241709.
- [207] Siddharth Deshpande, Tristan Maxson, and Jeffrey Greeley. “Graph theory approach to determine configurations of multidentate and high coverage adsorbates for heterogeneous catalysis”. In: *Npj Computational Materials* 6.1 (2020), pp. 1–6.
- [208] Lauri Himanen et al. “DScribe: Library of descriptors for machine learning in materials science”. In: *Computer Physics Communications* 247 (2020), p. 106949.

- [209] Andreas Singraber et al. “Parallel multistream training of high-dimensional neural network potentials”. In: *Journal of Chemical Theory and Computation* 15.5 (2019), pp. 3075–3092.
- [210] G. A. Somorjai and D.W. Blakely. “Mechanism of catalysis of hydrocarbon reactions by platinum surfaces”. In: *Nature* 258.5536 (1975), pp. 580–583.
- [211] Gabor A Somorjai. “Surface science and catalysis”. In: *Science* 227.4689 (1985), pp. 902–908.
- [212] Shi-Gang Sun et al. “Electrocatalytic properties of Pt(111), Pt(332), Pt(331) and Pt(110) single crystal electrodes towards ethylene glycol oxidation in sulphuric acid solutions”. In: *Journal of Electroanalytical Chemistry* 340.1-2 (1992), pp. 213–226.
- [213] Helmut Baltruschat et al. “From Stepped Single Crystal Surfaces to Ordered Bimetallic Electrodes: Adsorption and Electrocatalysis as Studied by DEMS and STM”. In: *In-Situ Spectroscopic Studies of Adsorption at the Electrode and Electrocatalysis*. Elsevier, 2007, pp. 471–537.
- [214] Na Tian, Zhi-You Zhou, and Shi-Gang Sun. “Platinum metal catalysts of high-index surfaces: from single-crystal planes to electrochemically shape-controlled nanoparticles”. In: *The Journal of Physical Chemistry C* 112.50 (2008), pp. 19801–19817.
- [215] J T Yates. “Surface chemistry at metallic defect sites”. In: *J. Vac. Sci. Technol. A* 13 (1995).
- [216] H S Taylor. “A theory of the catalytic surface”. In: *Proc. R. Soc. Lond. A* 108 (1925).
- [217] B Hammer, O H Nielsen, and J K Nørskov. “Structure sensitivity in adsorption: CO interaction with stepped and reconstructed Pt surfaces”. In: *Catal. Lett.* 46 (1997).
- [218] G.A. Somorjai. “Surface reconstruction and catalysis”. In: *Annual Review of Physical Chemistry* 45.1 (1994), pp. 721–751.
- [219] T Zambelli et al. “Identification of the ‘active sites’ of a surface-catalyzed reaction”. In: *Science* 273 (1996).

- [220] S Dahl. “Role of steps in N<sub>2</sub> activation on Ru(0001)”. In: *Phys. Rev. Lett.* 83 (1999).
- [221] J J C Geerlings. “Fischer–Tropsch technology—from active site to commercial process”. In: *Appl. Catal. A* 186 (1999).
- [222] R T Vang. “Controlling the catalytic bond-breaking selectivity of Ni surfaces by step blocking”. In: *Nature Mater.* 4 (2005).
- [223] Talin Avanesian et al. “Quantitative and atomic-scale view of CO-induced Pt nanoparticle surface reconstruction at saturation coverage via DFT calculations coupled with in situ TEM and IR”. In: *Journal of the American Chemical Society* 139.12 (2017), pp. 4551–4558.
- [224] Xueying Zhao et al. “Adsorbate induced kink formation in straight step edges on Cu(533) and Cu(221)”. In: *Surface Science* 563.1-3 (2004), pp. 217–224.
- [225] Vaidish Sumaria et al. “Optimal Packing of CO at a High Coverage on Pt(100) and Pt(111) Surfaces”. In: *Acs Catalysis* 10.16 (2020), pp. 9533–9544.
- [226] E Kruse Vestergaard et al. “Comment on “High pressure adsorbate structures studied by scanning tunneling microscopy: CO on Pt (111) in equilibrium with the gas phase””. In: *Physical Review Letters* 88.25 (2002), p. 259601.
- [227] John a Jensen et al. “High pressure adsorbate structures studied by scanning tunneling microscopy: CO on Pt(111) in equilibrium with the gas phase”. In: *Physical Review Letters* 80.6 (1998), p. 1228.
- [228] B Tränkenschuh et al. “A site-selective in situ study of CO adsorption and desorption on Pt(355)”. In: *The Journal of Chemical Physics* 124.7 (2006), p. 074712.
- [229] Ma Henderson, a Szabo, and Jt Yates Jr. “Direct observation of adsorbate dynamics from low-frequency vibration on a step defect—CO on Pt (112)”. In: *The Journal of Chemical Physics* 91.11 (1989), pp. 7255–7264.
- [230] Jf Lang and Ri Masel. “An XPS study of nitric oxide, carbon monoxide and oxygen adsorption on Pt(210)”. In: *Surface Science* 167.2-3 (1986), pp. 261–270.



- [231] John L Gland, Michael R McClellan, and F Read Mcfeely. “Carbon monoxide oxidation on the kinked Pt(321) surface”. In: *The Journal of Chemical Physics* 79.12 (1983), pp. 6349–6356.
- [232] Js Luo et al. “CO adsorption site occupation on Pt(335): a quantitative investigation using TPD and EELS”. In: *Surface Science* 274.1 (1992), pp. 53–62.
- [233] Am Baro and H Ibach. “New study of CO adsorption at low temperature (90 K) on Pt(111) by EELS”. In: *The Journal of Chemical Physics* 71.12 (1979), pp. 4812–4816.
- [234] H Ibach and D Bruchmann. “Surface Phonons on Stepped Pt(111) Surfaces”. In: *Physical Review Letters* 41.14 (1978), p. 958.
- [235] Manuel Js Farias et al. “Monitoring of CO Binding Sites on Stepped Pt Single Crystal Electrodes in Alkaline Solutions by in Situ FTIR Spectroscopy”. In: *Langmuir* 36.3 (2019), pp. 704–714.
- [236] Kedong Wang et al. “Study of CO diffusion on stepped Pt (1 1 1) surface by scanning tunneling microscopy”. In: *Surface Science* 604.3-4 (2010), pp. 322–326.
- [237] Jacob R Boes and John R Kitchin. “Neural network predictions of oxygen interactions on a dynamic Pd surface”. In: *Molecular Simulation* 43.5-6 (2017), pp. 346–354.
- [238] Lingjun Zhu et al. “Unified and Transferable Description of Dynamics for H<sub>2</sub> Dissociative Adsorption on Multiple Copper Surfaces via Machine Learning”. In: *Physical Chemistry Chemical Physics* (2020).
- [239] Nick Gerrits et al. “Accurate probabilities for highly activated reaction of polyatomic molecules on surfaces using a high-dimensional neural network potential: CHD<sub>3</sub>+Cu(111)”. In: *The Journal of Physical Chemistry Letters* 10.8 (2019), pp. 1763–1768.
- [240] Marcos Del Cueto et al. “New Perspectives on CO<sub>2</sub>-Pt (111) Interaction with a High-Dimensional Neural Network Potential Energy Surface”. In: *The Journal of Physical Chemistry C* 124.9 (2020), pp. 5174–5181.

- [241] Brian Kolb et al. “High-dimensional atomistic neural network potentials for molecule–surface interactions: HCl scattering from Au(111)”. In: *The Journal of Physical Chemistry Letters* 8.3 (2017), pp. 666–672.
- [242] Khosrow Shakouri et al. “Accurate neural network description of surface phonons in reactive gas–surface dynamics: N<sub>2</sub>+ Ru(0001)”. In: *The Journal of Physical Chemistry Letters* 8.10 (2017), pp. 2131–2136.
- [243] Qinghua Liu et al. “Constructing high-dimensional neural network potential energy surfaces for gas–surface scattering and reactions”. In: *The Journal of Physical Chemistry C* 122.3 (2018), pp. 1761–1769.
- [244] Yaolong Zhang, Xueyao Zhou, and Bin Jiang. “Bridging the gap between direct dynamics and globally accurate reactive potential energy surfaces using neural networks”. In: *The Journal of Physical Chemistry Letters* 10.6 (2019), pp. 1185–1191.
- [245] Meng Huang et al. “Adiabatic and nonadiabatic energy dissipation during scattering of vibrationally excited CO from Au (111)”. In: *Physical Review B* 100.20 (2019), p. 201407.
- [246] David J Wales and Jonathan Pk Doye. “Global optimization by basin-hopping and the lowest energy structures of Lennard-Jones clusters containing up to 110 atoms”. In: *The Journal of Physical Chemistry A* 101.28 (1997), pp. 5111–5116.
- [247] Elisa Jimenez-Izal and Anastassia N Alexandrova. “Computational design of clusters for catalysis”. In: *Annual Review of Physical Chemistry* 69 (2018), pp. 377–400.
- [248] Huanchen Zhai and Anastassia N. Alexandrova. “Fluxionality of Catalytic Clusters: When It Matters and How to Address It”. In: *Acs Catalysis* 7.3 (2017), pp. 1905–1911. eprint: <https://doi.org/10.1021/acscatal.6b03243>.
- [249] Prasenjit Ghosh, Matteo Farnesi Camellone, and Stefano Fabris. “Fluxionality of Au clusters at ceria surfaces during CO oxidation: Relationships among reactivity, size,

- cohesion, and surface defects from DFT simulations”. In: *The Journal of Physical Chemistry Letters* 4.14 (2013), pp. 2256–2263.
- [250] Huanchen Zhai and Anastassia N Alexandrova. “Ensemble-average representation of Pt clusters in conditions of catalysis accessed through GPU accelerated deep neural network fitting global optimization”. In: *Journal of Chemical Theory and Computation* 12.12 (2016), pp. 6213–6226.
- [251] Geng Sun and Philippe Sautet. “Metastable structures in cluster catalysis from first-principles: Structural ensemble in reaction conditions and metastability triggered reactivity”. In: *Journal of the American Chemical Society* 140.8 (2018), pp. 2812–2820.
- [252] Geng Sun, Anastassia N Alexandrova, and Philippe Sautet. “Structural rearrangements of subnanometer Cu oxide clusters govern catalytic oxidation”. In: *Acs Catalysis* 10.9 (2020), pp. 5309–5317.
- [253] Georg Kresse and Jürgen Hafner. “Ab initio molecular dynamics for liquid metals”. In: *Physical Review B* 47.1 (1993), p. 558.
- [254] Georg Kresse and Jürgen Hafner. “Ab initio molecular-dynamics simulation of the liquid-metal–amorphous-semiconductor transition in germanium”. In: *Physical Review B* 49.20 (1994), p. 14251.
- [255] Georg Kresse and Jürgen Furthmüller. “Efficient iterative schemes for ab initio total-energy calculations using a plane-wave basis set”. In: *Physical Review B* 54.16 (1996), p. 11169.
- [256] Georg Kresse and Jürgen Furthmüller. “Efficiency of ab-initio total energy calculations for metals and semiconductors using a plane-wave basis set”. In: *Computational Materials Science* 6.1 (1996), pp. 15–50.
- [257] John P Perdew, Kieron Burke, and Matthias Ernzerhof. “Generalized gradient approximation made simple”. In: *Physical Review Letters* 77.18 (1996), p. 3865.

- [258] Peter E Blöchl. “Projector augmented-wave method”. In: *Physical Review B* 50.24 (1994), p. 17953.
- [259] Georg Kresse and Daniel Joubert. “From ultrasoft pseudopotentials to the projector augmented-wave method”. In: *Physical Review B* 59.3 (1999), p. 1758.
- [260] Albert P. Bartók, Risi Kondor, and Gábor Csányi. “On representing chemical environments”. In: *Phys. Rev. B* 87 (18 May 2013), p. 184115.
- [261] Haoyan Huo and Matthias Rupp. “Unified representation for machine learning of molecules and crystals”. In: *Arxiv Preprint Arxiv:1704.06439* 13754 (2017).
- [262] Ralf Gehrke and Karsten Reuter. “Assessing the efficiency of first-principles basin-hopping sampling”. In: *Physical Review B* 79.8 (2009), p. 085412.
- [263] Ronald P White and Howard R Mayne. “An investigation of two approaches to basin hopping minimization for atomic and molecular clusters”. In: *Chemical Physics Letters* 289.5-6 (1998), pp. 463–468.
- [264] Hyoung Gyu Kim, Si Kyung Choi, and Hyuck Mo Lee. “New algorithm in the basin hopping Monte Carlo to find the global minimum structure of unary and binary metallic nanoclusters”. In: *The Journal of Chemical Physics* 128.14 (2008), p. 144702.
- [265] [https://github.com/vsumaria/Pt\\_CO\\_steps\\_NNP](https://github.com/vsumaria/Pt_CO_steps_NNP).
- [266] Yuanyuan Li et al. “Dynamic structure of active sites in ceria-supported Pt catalysts for the water gas shift reaction”. In: *Nat Commun* 12.1 (2021), p. 914.
- [267] Jacques C Vedrène. “Revisiting active sites in heterogeneous catalysis: Their structure and their dynamic behaviour”. In: *Appl. Catal., A* 474 (2014), pp. 40–50.
- [268] Charlotte Vogt and Bert M Weckhuysen. “The concept of active site in heterogeneous catalysis”. In: *Nat. Rev. Chem.* 6 (2022), pp. 89–111.
- [269] George Yan et al. “Reaction product-driven restructuring and assisted stabilization of a highly dispersed Rh-on-ceria catalyst”. In: *Nat. Catal.* 5.2 (2022), pp. 119–127.

- [270] Philipp Grosse et al. “Dynamic transformation of cubic copper catalysts during CO<sub>2</sub> electroreduction and its impact on catalytic selectivity”. In: *Nat Commun* 12.1 (2021), p. 6736.
- [271] Feng Tao et al. “Evolution of structure and chemistry of bimetallic nanoparticle catalysts under reaction conditions”. In: *Journal of the American Chemical Society* 132.25 (2010), pp. 8697–8703.
- [272] Feng Tao et al. “Reaction-driven restructuring of Rh-Pd and Pt-Pd core-shell nanoparticles”. In: *Science* 322.5903 (2008), pp. 932–934.
- [273] Junjun Shan et al. “Tuning catalytic performance through a single or sequential post-synthesis reaction (s) in a gas phase”. In: *Acs Catalysis* 7.1 (2017), pp. 191–204.
- [274] Zhongwei Zhu et al. “Formation of nanometer-sized surface platinum oxide clusters on a stepped Pt (557) single crystal surface induced by oxygen: a high-pressure STM and ambient-pressure XPS study”. In: *Nano Letters* 12.3 (2012), pp. 1491–1497.
- [275] Y Jugnet et al. “CO chemisorption on Au (1 1 0) investigated under elevated pressures by polarized reflection absorption infrared spectroscopy and scanning tunneling microscopy”. In: *Surf Sci* 521.1-2 (2002), pp. L639–L644.
- [276] G Hoogers and Da King. “Adsorbate-induced step-doubling reconstruction of a vicinal metal surface: Oxygen on Rh {332}”. In: *Surf Sci* 286.3 (1993), pp. 306–316.
- [277] Elmar Hahn et al. “Orientational instability of vicinal Pt surfaces close to (111)”. In: *Phys Rev Lett* 72.21 (1994), p. 3378.
- [278] B Lang, Rw Joyner, and G. A. Somorjai. “Low energy electron diffraction studies of chemisorbed gases on stepped surfaces of platinum”. In: *Surf Sci* 30.2 (1972), pp. 454–474.
- [279] A-M Lanzilotto and Sl Bernasek. “The sulfur induced reconstruction of the Pt (S)-[6 (111)×(100)] surface”. In: *J. Chem. Phys.* 84.6 (1986), pp. 3553–3558.

- [280] O Haase et al. “Role of regular steps on the formation of missing-row reconstructions: oxygen chemisorption on Ni (771)”. In: *Phys Rev Lett* 66.13 (1991), p. 1725.
- [281] R Koch et al. “Can oxygen modify step arrangements? STM and LEED investigations on Ni (771)”. In: *Surf Sci* 272.1-3 (1992), pp. 17–26.
- [282] He Dorsett et al. “Oxygen-induced step ordering on Ni (119)”. In: *Surf Sci* 342.1-3 (1995), pp. 261–271.
- [283] Dg Castner and G.A. Somorjai. “LEED and thermal desorption studies of small molecules (H<sub>2</sub>, O<sub>2</sub>, CO, CO<sub>2</sub>, NO, C<sub>2</sub>H<sub>4</sub>, C<sub>2</sub>H<sub>2</sub> and C) chemisorbed on the stepped rhodium (755) and (331) surfaces”. In: *Surf Sci* 83.1 (1979), pp. 60–82.
- [284] Da Walko and Ik Robinson. “Structure of Cu (115): Clean surface and its oxygen-induced facets”. In: *Phys Rev B* 59.23 (1999), p. 15446.
- [285] Tl Einstein et al. “Step doubling and related transitions on vicinal surfaces”. In: *J. Vac. Sci. Technol. A* 10.4 (1992), pp. 2600–2605.
- [286] Tp Pearl et al. “Influence of oxygen dissolution history on reconstruction behavior of a stepped metal surface”. In: *Chem Phys Lett* 364.3-4 (2002), pp. 284–289.
- [287] Zisheng Zhang, Borna Zandkarimi, and Anastassia N Alexandrova. “Ensembles of metastable states govern heterogeneous catalysis on dynamic interfaces”. In: *Accounts Chem Res* 53.2 (2020), pp. 447–458.
- [288] Geng Sun and Philippe Sautet. “Active Site Fluxional Restructuring as a New Paradigm in Triggering Reaction Activity for Nanocluster Catalysis”. In: *Accounts Chem Res* 54.20 (2021), pp. 3841–3849.
- [289] Sb Al Vendelbo et al. “Visualization of oscillatory behaviour of Pt nanoparticles catalysing CO oxidation”. In: *Nature Materials* 13.9 (2014), pp. 884–890.
- [290] Vaidish Sumaria and Philippe Sautet. “CO organization at ambient pressure on stepped Pt surfaces: first principles modeling accelerated by neural networks”. In: *Chemical Science* 12.47 (2021), pp. 15543–15555.

- [291] Graeme Henkelman and Hannes Jónsson. “Improved tangent estimate in the nudged elastic band method for finding minimum energy paths and saddle points”. In: *The Journal of Chemical Physics* 113.22 (2000), pp. 9978–9985.
- [292] Graeme Henkelman, Blas P Uberuaga, and Hannes Jónsson. “A climbing image nudged elastic band method for finding saddle points and minimum energy paths”. In: *The Journal of Chemical Physics* 113.22 (2000), pp. 9901–9904.
- [293] Runhai Ouyang, Yu Xie, and De-En Jiang. “Global minimization of gold clusters by combining neural network potentials and the basin-hopping method”. In: *Nanoscale* 7.36 (2015), pp. 14817–14821.
- [294] Victor Fung and De-En Jiang. “Exploring structural diversity and fluxionality of Pt<sub>n</sub> (n= 10–13) clusters from first-principles”. In: *The Journal of Physical Chemistry C* 121.20 (2017), pp. 10796–10802.
- [295] David J Wales and Harold A Scheraga. “Global optimization of clusters, crystals, and biomolecules”. In: *Science* 285.5432 (1999), pp. 1368–1372.
- [296] Konstantin Klenin et al. “Modelling proteins: Conformational sampling and reconstruction of folding kinetics”. In: *Biochimica Et Biophysica Acta (bba)-Proteins and Proteomics* 1814.8 (2011), pp. 977–1000.
- [297] Martín Leandro Paleico and Jörg Behler. “Global optimization of copper clusters at the ZnO (10 1 0) surface using a DFT-based neural network potential and genetic algorithms”. In: *The Journal of Chemical Physics* 153.5 (2020), p. 054704.
- [298] Si-Da Huang et al. “Material discovery by combining stochastic surface walking global optimization with a neural network”. In: *Chemical Science* 8.9 (2017), pp. 6327–6337.
- [299] Qidong Lin et al. “Searching configurations in uncertainty space: Active learning of high-dimensional neural network reactive potentials”. In: *Journal of Chemical Theory and Computation* 17.5 (2021), pp. 2691–2701.

- [300] Geng Sun, Anastassia N Alexandrova, and Philippe Sautet. “Pt8 cluster on alumina under a pressure of hydrogen: Support-dependent reconstruction from first-principles global optimization”. In: *The Journal of Chemical Physics* 151.19 (2019), p. 194703.
- [301] K. Klier. “Methanol Synthesis”. In: *Advances in Catalysis*. Vol. NA. 1982, pp. 243–313.
- [302] David S. Newsome. “The Water-Gas Shift Reaction”. In: *Catalysis Reviews* 21.2 (1980), pp. 275–318.
- [303] János; Goodman Szanyi D. Wayne. “Methanol synthesis on a Cu(100) catalyst”. In: *Catalysis Letters* 10.5 (1991), pp. 383–390.
- [304] J.; Campbell Yoshihara Charles T. “Methanol Synthesis and Reverse Water–Gas Shift Kinetics over Cu(110) Model Catalysts: Structural Sensitivity”. In: *Journal of Catalysis* 161.2 (1996), pp. 776–782.
- [305] Malte Behrens et al. “The active site of methanol synthesis over Cu/ZnO/Al<sub>2</sub>O<sub>3</sub> industrial catalysts”. In: *Science* 336.6083 (2012), pp. 893–897.
- [306] George A. Olah. “Towards Oil Independence Through Renewable Methanol Chemistry”. In: *Angewandte Chemie (International ed. in English)* 52.1 (2012), pp. 104–107.
- [307] Malte Behrens. “Heterogeneous Catalysis of CO<sub>2</sub> Conversion to Methanol on Copper Surfaces”. In: *Angewandte Chemie (International ed. in English)* 53.45 (2014), pp. 12022–12024.
- [308] K. Kambe. “Cohesive Energy of Noble Metals”. In: *Physical Review* 99.2 (1955), pp. 419–422.
- [309] Charles Kittel et al. *Introduction to solid state physics*. Vol. 8. Wiley New York, 1953.
- [310] David C Tang et al. “High pressure scanning tunneling microscopy study of CO poisoning of ethylene hydrogenation on Pt (111) and Rh (111) single crystals”. In: *The Journal of Physical Chemistry B* 108.35 (2004), pp. 13300–13306.



- [311] Vaidish Sumaria et al. “Atomic-Scale Mechanism of Platinum Catalyst Restructuring under a Pressure of Reactant Gas”. In: *Journal of the American Chemical Society* (2022).
- [312] M C Wahl et al. “Activation of Cu(111) surface by decomposition into nonoclusters driven by CO adsorption”. In: 351.6272 (2016).
- [313] BHLB Hammer, Lars Bruno Hansen, and Jens Kehlet Nørskov. “Improved adsorption energetics within density-functional theory using revised Perdew-Burke-Ernzerhof functionals”. In: *Physical review B* 59.11 (1999), p. 7413.
- [314] Yan Zhao and Donald G Truhlar. “Computational characterization and modeling of buckyball tweezers: density functional study of concave–convex  $\pi\pi$  interactions”. In: *Physical Chemistry Chemical Physics* 10.19 (2008), pp. 2813–2818.
- [315] Raphael F Ribeiro et al. “Use of solution-phase vibrational frequencies in continuum models for the free energy of solvation”. In: *The Journal of Physical Chemistry B* 115.49 (2011), pp. 14556–14562.
- [316] Stefan Grimme. “Supramolecular Binding Thermodynamics by Dispersion-Corrected Density Functional Theory”. In: *Chemistry – a European Journal* 18.32 (2012), pp. 9955–9964. eprint: <https://chemistry-europe.onlinelibrary.wiley.com/doi/pdf/10.1002/chem.201200497>.

# APPENDIX A

## Supplementary Information for Chapter 2

### A.1 Coverage effect on CO bond distance based adsorption energy correction

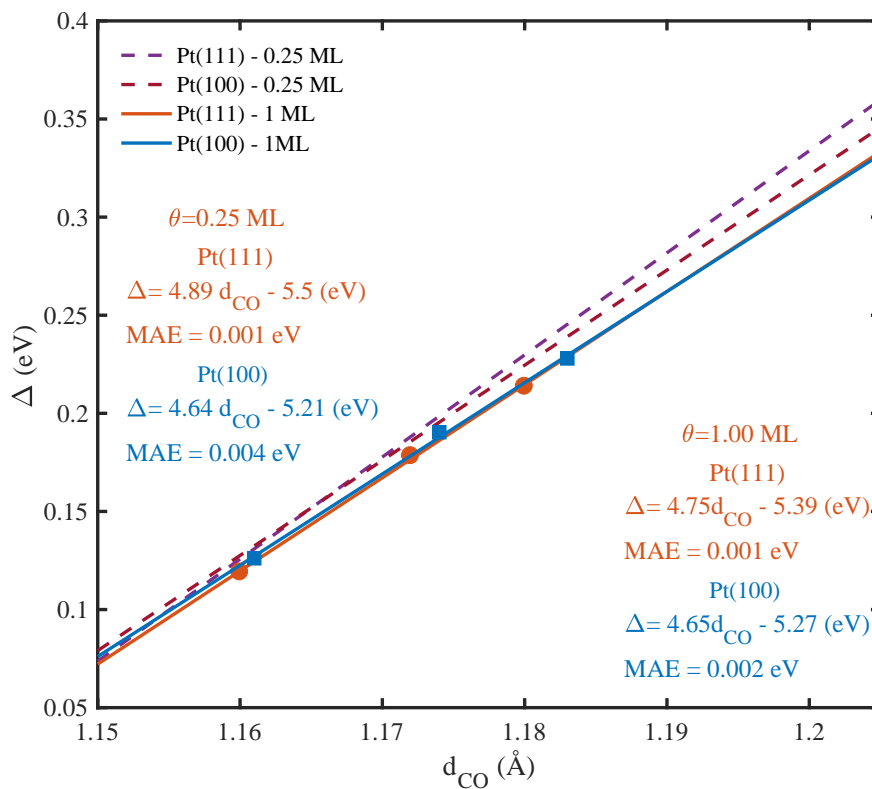


Figure A.1: The suggested correction in adsorption energy ( $\Delta$ ) plotted against the adsorbed CO bond distance ( $d_{CO}$ ) for various sites (top, bridge and hollow/hcp) for Pt(100) and Pt(111). The corrections developed using adsorption energy data for coverage of 0.25 ML and 1.00 ML have been compared.

## A.2 Atomistic Thermodynamics Approach

According to thermodynamics, the most stable surface should have the lowest adsorption energy at a given temperature and pressure, so we need to measure the stability of different surface structures. To do so, we use first-principles atomistic thermodynamics approach which provides a general framework for studying structures under the influence of reactive gas phase. We consider a surface in contact with an CO atmosphere described by an CO pressure  $P$  and temperature  $T$ . This means that the environment acts as a reservoir, because it can give or take any amount of CO to or from the sample without changing the temperature or pressure. The Gibbs free energy of adsorption for CO per unit area of the unit cell ( $\Delta G_{ads}^{CO}(T, P)$ ) on a given slab can be mathematically expressed as:

$$\Delta G_{ads}^{CO}(T, P) = \frac{G_{CO_n@slab} - G_{slab} - n_{CO} \mu_{CO(g)}(T, P)}{A} \quad (\text{A.1})$$

$$G = H - TS$$

Where  $G_{ads}^{CO}$  is the Gibbs free energy (eV) of the complete system with the clean slab and  $n_{CO}$  number of CO adsorbed on the surface area of  $A$  ( $\text{\AA}^2$ ).  $\mu_{CO(g)}$  is the chemical potential of CO(g) and  $G_{slab}$  is the Gibbs free energy of the clean slab. Each Gibbs free energy term can be calculated by separately calculating the enthalpy ( $H$ ) and entropy ( $S$ ) terms.

### A.2.1 Ideal Gas

Treating CO as an ideal gas, we express the enthalpy of gas phase CO in the following manner:

$$H(T) = E_{\text{elec}} + E_{\text{ZPE}} + \int_0^T C_P dT \quad (\text{A.2})$$

Where,  $E_{elec}$  = Electronic energy,  $E_{ZPE}$  = zero point energy and last term is the integral over the constant-pressure heat capacity ( $C_p$ ).

$$E_{ZPE} = \frac{1}{2} \sum_i^{\text{vib DOF}} \epsilon_i \quad (\text{A.3})$$

Where  $\epsilon_i = h\omega_i$  are the energies associated with vibrational frequencies  $\omega_i$ .

The constant volume heat capacity can be measured separately for translational ( $C_{V,tran}$ ), vibrations ( $C_{V,vib}$ ), rotational ( $C_{V,rot}$ ) and electronic part ( $C_{V,elec}$ ), and a  $k_B$  (in eV) term is added to get  $C_p$  value as follows:

$$C_P = k_B + C_{V,trans} + C_{V,rot} + C_{V,vib} + C_{V,elec} \quad (\text{A.4})$$

For 3-D gas, translational heat capacity can be calculated as:

$$C_{V,trans} = \frac{3}{2} k_B \quad (\text{A.5})$$

Rotational heat capacity can be shown to be:

$$C_{V,rot} = \begin{cases} 0, & \text{Monoatomic species} \\ k_B, & \text{Linear Molecule} \\ 3/2k_B & \text{Nonlinear Molecule} \end{cases} \quad (\text{A.6})$$

CO being a linear molecule, we use  $C_{V,rot} = k_B$ . Vibrational heat capacity contains  $3N-6$  DOF for nonlinear molecules and  $3N-5$  DOF for linear molecules, where N is the number of atoms. The integral form of vibrational heat capacity can be shown as:

$$\int_0^T C_{V,vib}dT = \sum_i^{\text{vib DOF}} \frac{\epsilon_i}{e^{\epsilon_i/k_B T} - 1} \quad (\text{A.7})$$

For ideal gas, the electronic contribution to the heat capacity can be assumed to be zero.

Ideal gas entropy as a function of T and P can be expressed as a sum of translational ( $S_{\text{trans}}$ ), rotational ( $S_{\text{rot}}$ ), electronic ( $S_{\text{elec}}$ ) and vibrational ( $S_{\text{vib}}$ ) contributions with a pressure correction as:

$$\begin{aligned} S(T, P) &= S(T, P^\circ) - k_B \ln \frac{P}{P^\circ} \\ &= S_{\text{trans}} + S_{\text{rot}} + S_{\text{elec}} + S_{\text{vib}} - k_B \ln \frac{P}{P^\circ} \end{aligned} \quad (\text{A.8})$$

$$S_{\text{trans}} = k_B \left\{ \ln \left[ \left( \frac{2\pi M k_B T}{h^2} \right)^{3/2} \frac{k_B T}{P^\circ} \right] + \frac{5}{2} \right\} \quad (\text{A.9})$$

$$S_{\text{rot}} = \begin{cases} 0 & , \text{ if Monoatomic} \\ k_B \left[ \ln \left( \frac{8\pi^2 I k_B T}{\sigma h^2} \right) + 1 \right] & , \text{ if Linear} \\ k_B \left\{ \ln \left[ \frac{\sqrt{\pi I_A I_B I_C}}{\sigma} \left( \frac{8\pi^2 k_B T}{h^2} \right)^{3/2} \right] + \frac{3}{2} \right\} & , \text{ if Nonlinear} \end{cases} \quad (\text{A.10})$$

$$S_{\text{vib}} = k_B \sum_i^{\text{vib DOF}} \left[ \frac{\epsilon_i}{k_B T (e^{\epsilon_i/k_B T} - 1)} - \ln (1 - e^{-\epsilon_i/k_B T}) \right] \quad (\text{A.11})$$

$$S_{\text{elec}} = k_B \ln [2 \times (\text{total spin}) + 1] \quad (\text{A.12})$$

Finally using the enthalpy and entropy, we find the chemical potential of CO ( $\mu_{\text{CO}(g)}$ ) as:

$$\mu_{\text{CO}(g)} = G(T, P) = H(T) - TS(T, P) \quad (\text{A.13})$$

### A.3 Harmonic Oscillator (HO) approximation

Assuming that the adsorbate has no real translational and rotational degree of freedom, we can treat all the 3N DOF of the adsorbates harmonically. Using this approximation, we can calculate the internal energy (U) and entropy of the adsorbate as follows:

$$U(T) = E_{\text{elec}} + E_{\text{ZPE}} + \sum_i^{\text{harm DOF}} \frac{\epsilon_i}{e^{\epsilon_i/k_{\text{B}}T} - 1} \quad (\text{A.14})$$

$$S = k_{\text{B}} \sum_i^{\text{harm DOF}} \left[ \frac{\epsilon_i}{k_{\text{B}}T (e^{\epsilon_i/k_{\text{B}}T} - 1)} - \ln(1 - e^{-\epsilon_i/k_{\text{B}}T}) \right] \quad (\text{A.15})$$

Where,  $\epsilon_i$  are the harmonic energies for the adsorbate atoms.

The Helmholtz free energy (F) can hence be calculated as:

$$F(T) = U(T) - T S(T) \quad (\text{A.16})$$

Assuming that the  $pV$  term in  $H = U + pV$  is negligible, the Helmholtz Free energy can be used as an approximate for the Gibbs Free energy since  $G \approx F$ .

### A.4 Vibrational Frequency

The vibrational modes are calculated from a finite difference approximation of the Hessian matrix which is generated by calculating the forces for 6 displacements per adsorbate atom in the +/- x,y and z directions while keeping the clean Pt slab fixed (since there is a very small effect on the energies when Pt allowed to move). These calculations were performed using the Atomic Simulation Environment Vibrations Class.

Frequencies below  $100 \text{ cm}^{-1}$  have a large effect on the calculated adsorption entropy. Changing such a frequency from  $50$  to  $40 \text{ cm}^{-1}$  results in a  $2 \text{ J}/(\text{mol K})$  change in the entropy at  $300$

K. In order to deal with this error, we use a cut-off frequency method as previously suggested by Cramer and Truhlar<sup>314,315</sup> or Grimme.<sup>316</sup> Basically, all frequencies below the cut-off (we used  $100\text{ cm}^{-1}$ ) are uniformly shifted up to the cut-off value before entropy calculation in the HO approximation.

## A.5 Relationship between correction and vibrational frequency

Since the vibrational frequency of the adsorbed CO scales with the CO bond distance, the suggested correction also scales well with the vibrational frequencies. These scaling relations have been shown in the figure A.2 for Pt(111) and A.3 for Pt(100) surface.

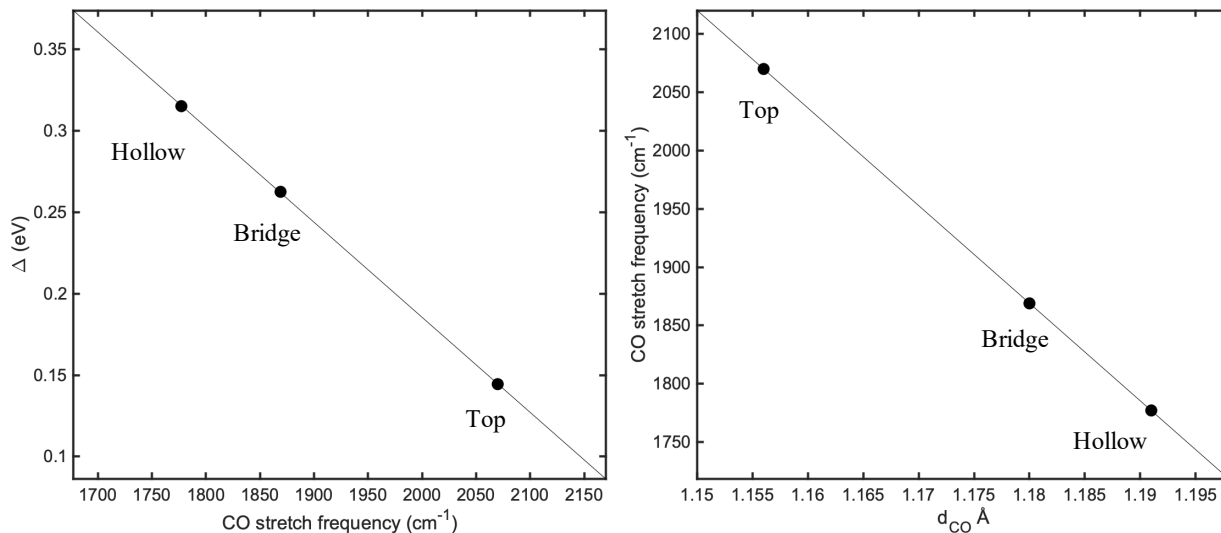


Figure A.2: CO bond length based correction as a function of vibrational frequency and the vibrational frequency as a function of CO bond length for Pt(111).

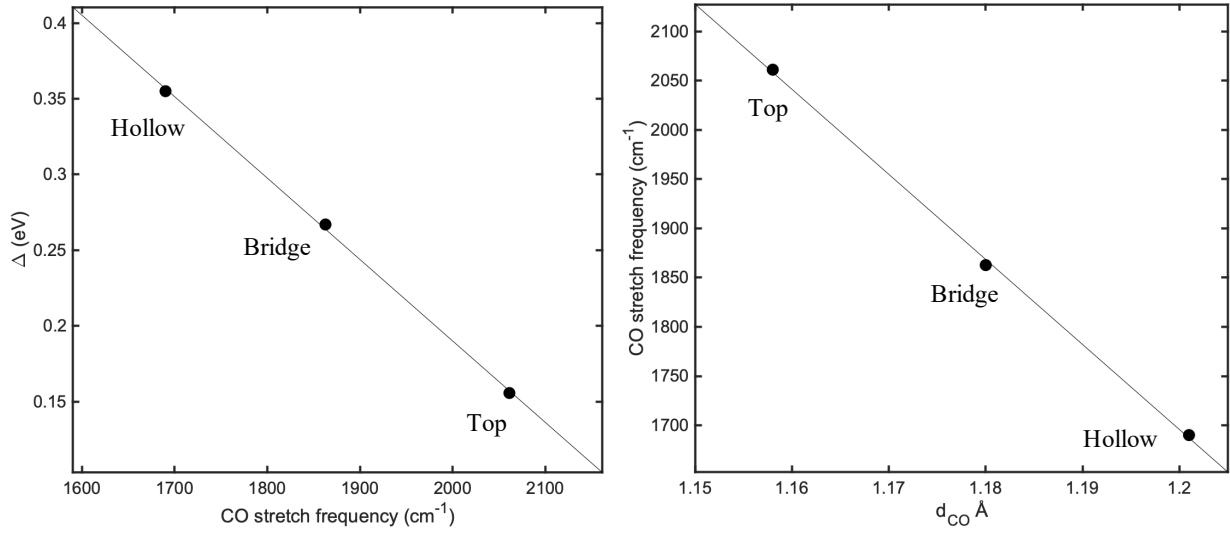
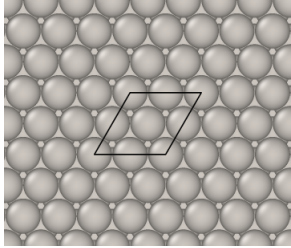


Figure A.3: CO bond length based correction as a function of vibrational frequency and the vibrational frequency as a function of CO bond length for Pt(100).

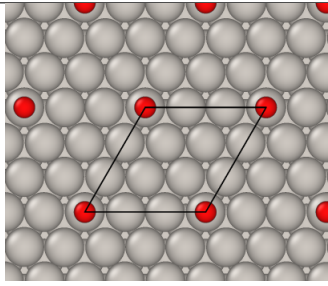
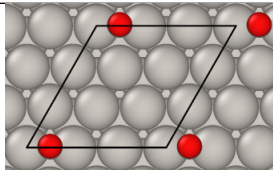
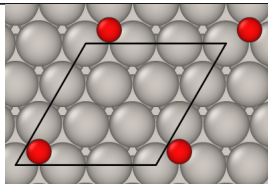
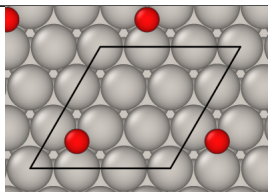
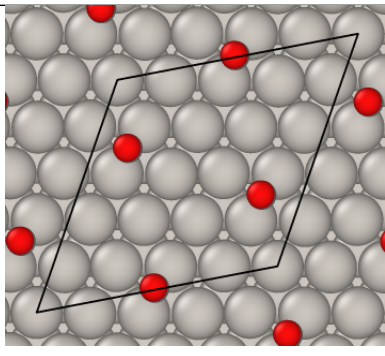
## A.6 Various surface terminations considered

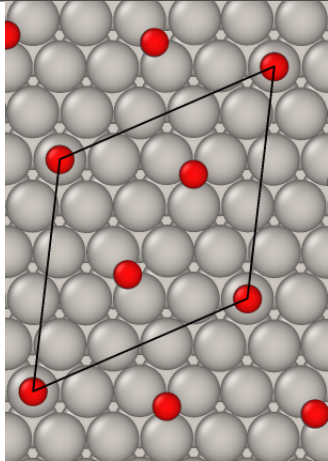
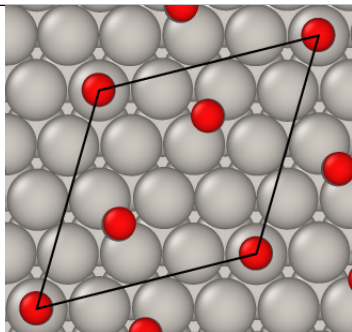
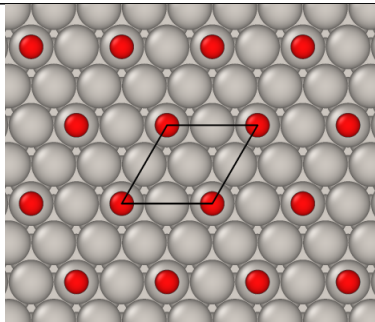
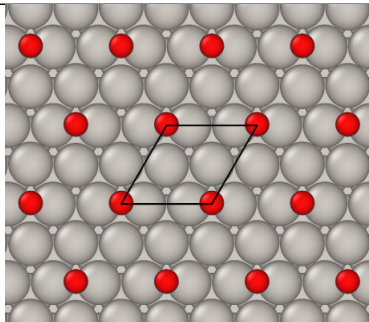
### A.6.1 Pt(111)

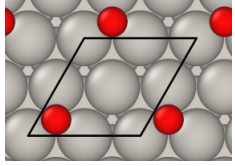
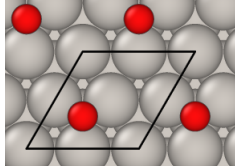
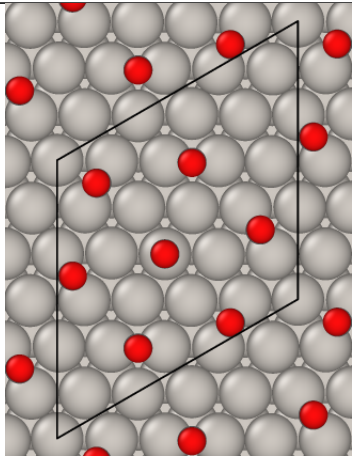
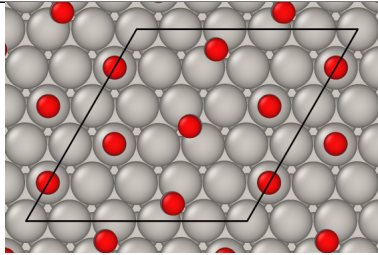
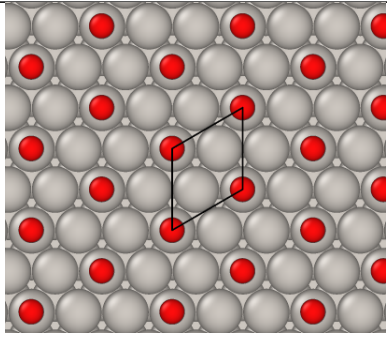
Table A.1: Average CO adsorption energies ( $\Delta E_{\text{CO}} = E_{\text{CO}_n@slab} - E_{slab} - n_{\text{CO}} \times E_{\text{CO}} + \Delta ZPE$ ) calculated for the various structures considered for Pt(111). The structures, unit cell, CO coverage and average adsorption energies have been listed in the table.

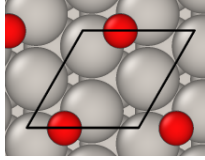
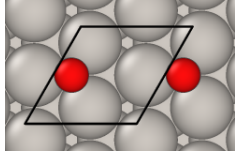
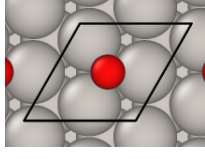
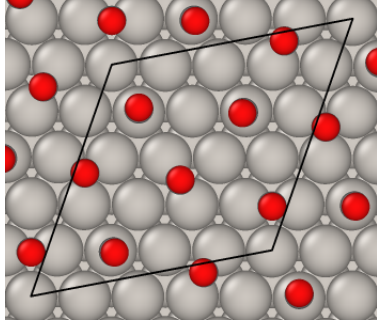
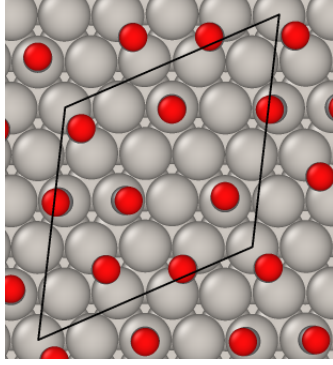
ID	Structure	Unit Cell	$\theta$	$\Delta E_{\text{CO}}^{\text{avg}}$ (eV)	$\Delta E_{\text{CO}}/\text{A}$ (eV/Å <sup>2</sup> )
1		p(2 × 2)	0.00	0.00	-

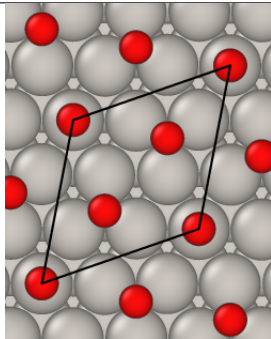
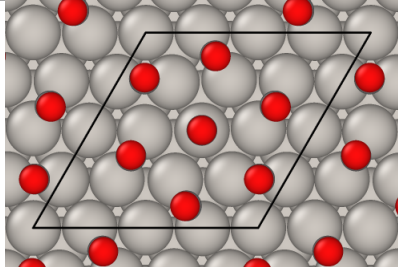
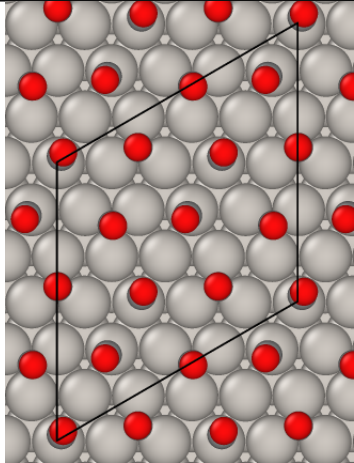
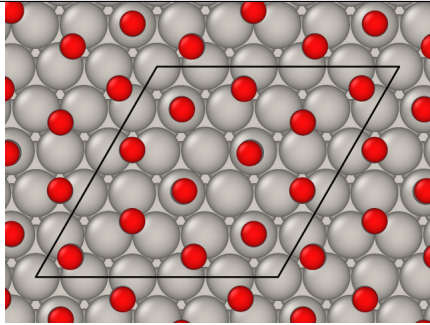


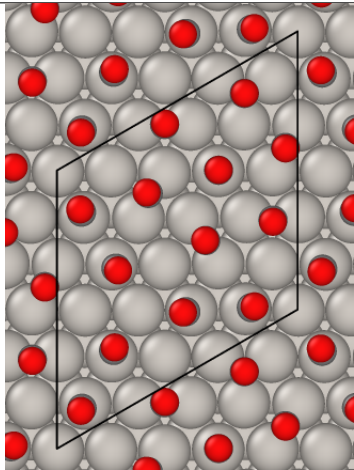
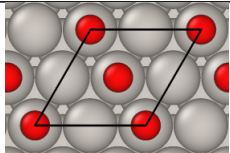
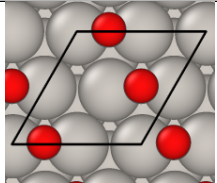
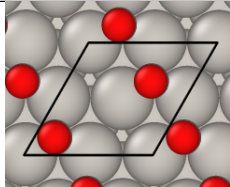
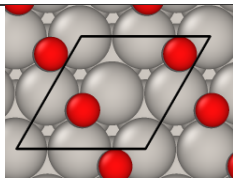
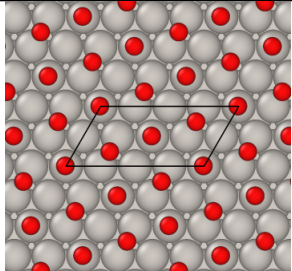
2		$p(3 \times 3)\text{-1CO (T)}$	0.11	-1.47	-0.0238
3		$p(3 \times 3)\text{-1CO (B)}$	0.11	-1.48	-0.0239
4		$p(3 \times 3)\text{-1CO (F)}$	0.11	-1.49	-0.0240
5		$p(3 \times 3)\text{-1CO (H)}$	0.11	-1.46	-0.0236
6		$(\sqrt{21} \times \sqrt{21})R10.8^\circ\text{-3CO}$	0.14	-1.49	-0.0310

7		$(\sqrt{19} \times \sqrt{19})R23.4^\circ-3CO$	0.16	-1.49	-0.0341
8		$(\sqrt{13} \times \sqrt{13})R14^\circ-3CO$	0.23	-1.47	-0.0493
9		$p(2 \times 2)-1CO (T)$	0.25	-1.42	-0.0518
10		$p(2 \times 2)-1CO (B)$	0.25	-1.46	-0.0532

11		$p(2 \times 2)$ -1CO (F)	0.25	-1.44	-0.0525
12		$p(2 \times 2)$ -1CO (H)	0.25	-1.44	-0.0523
13		$(\sqrt{27} \times \sqrt{27})$ -7CO	0.26	-1.45	-0.0545
14		$p(5 \times 5)$ -7CO	0.28	-1.38	-0.0562
15		$(\sqrt{3} \times \sqrt{3})R30^\circ$ -1CO (T)	0.33	-1.50	-0.0727

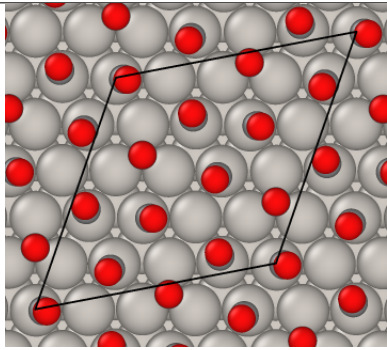
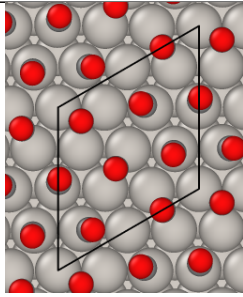
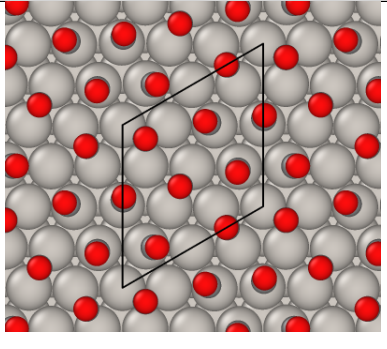
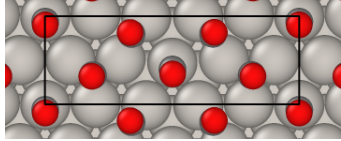
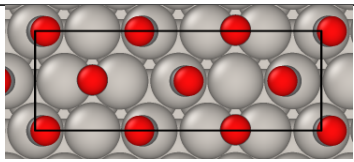
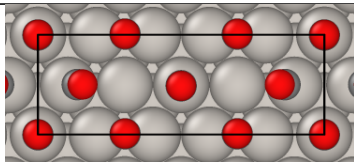
16		$(\sqrt{3} \times \sqrt{3})R30^\circ$ -1CO (B)	0.33	-1.51	-0.0730
17		$(\sqrt{3} \times \sqrt{3})R30^\circ$ -1CO (F)	0.33	-1.40	-0.0679
18		$(\sqrt{3} \times \sqrt{3})R30^\circ$ -1CO (H)	0.33	-1.39	-0.0672
19		$(\sqrt{21} \times \sqrt{21})R10.8^\circ$ - 7CO	0.33	-1.43	-0.0691
20		$(\sqrt{19} \times \sqrt{19})R23.4^\circ$ - 7CO	0.37	-1.41	-0.0728

21		$(\sqrt{7} \times \sqrt{7})R19.1^\circ-3CO$	0.43	-1.40	-0.0874
22		$p(4 \times 4)-7CO$	0.44	-1.40	-0.0890
23		$(\sqrt{27} \times \sqrt{27})-12CO$	0.44	-1.39	-0.0895
24		$p(5 \times 5)-12CO$	0.48	-1.30	-0.0910

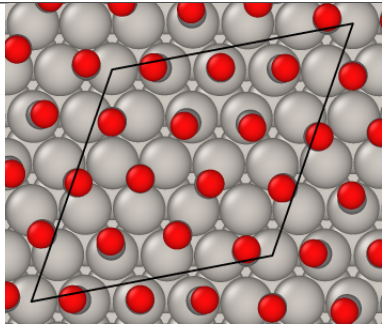
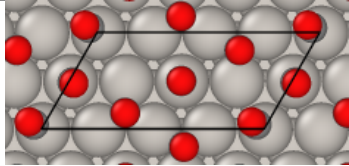
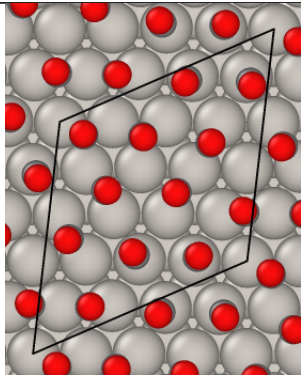
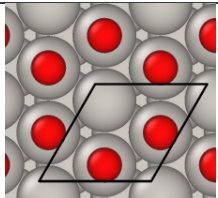
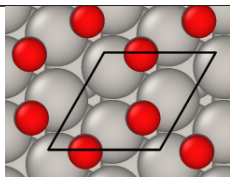
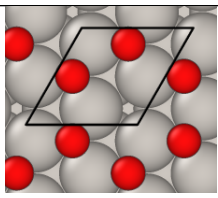
25		$(\sqrt{27} \times \sqrt{27})\text{-}13\text{CO}$	0.48	-1.38	-0.0967
26		$p(2 \times 2)\text{-}2\text{CO (T)}$	0.50	-1.14	-0.0830
27		$p(2 \times 2)\text{-}2\text{CO (B)}$	0.50	-1.17	-0.0854
28		$p(2 \times 2)\text{-}2\text{CO (F)}$	0.50	-1.16	-0.0844
29		$p(2 \times 2)\text{-}2\text{CO (H)}$	0.50	-1.12	0.0811
30		$c(4 \times 2)\text{-}2\text{CO (2T-2B)}$	0.50	-1.39	-0.1008

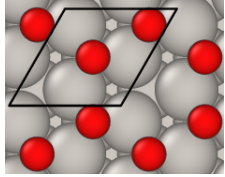
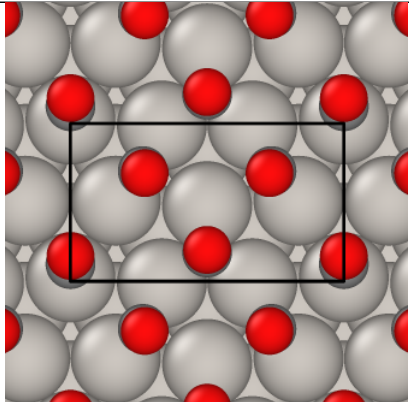
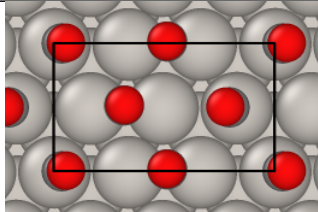
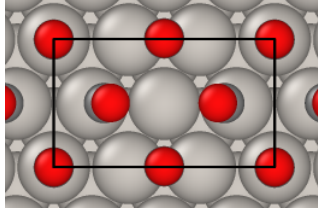
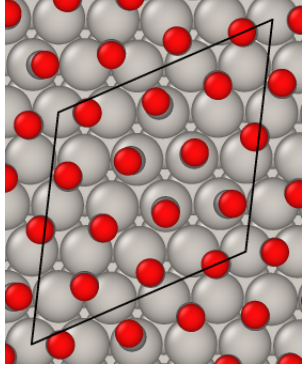


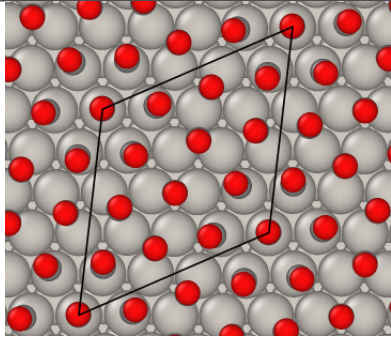
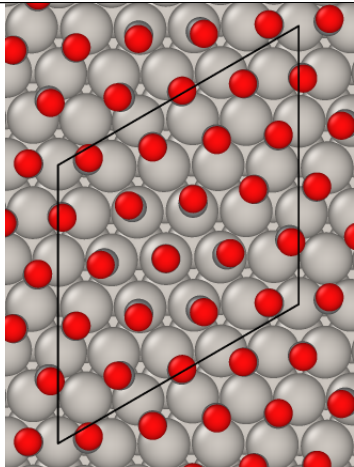
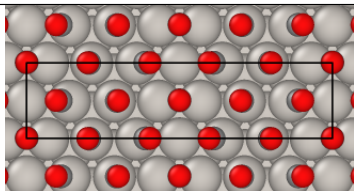
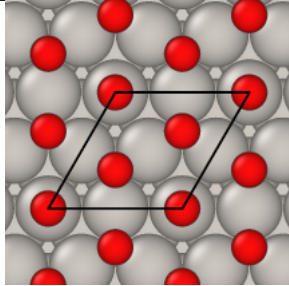
31		$c(4 \times 2)$ -2CO (3T-1B)	0.50	-1.34	-0.0971
32		$p(5 \times 5)$ -13CO	0.52	-1.30	-0.0983
33		$(\sqrt{13} \times \sqrt{13})R14^\circ$ -7CO	0.54	-1.36	-0.1067
34		$(\sqrt{7} \times \sqrt{7})R19.1^\circ$ -4CO	0.57	-1.34	-0.1115

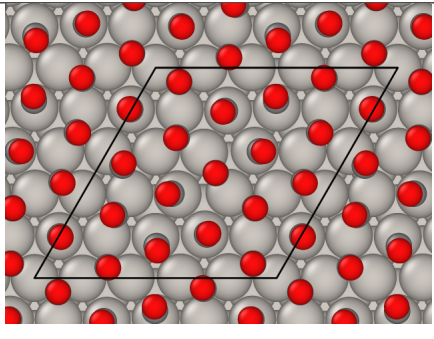
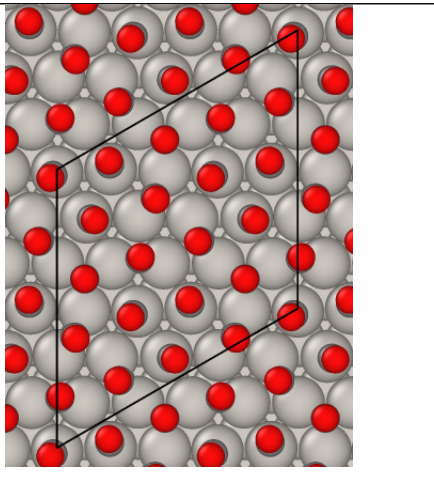
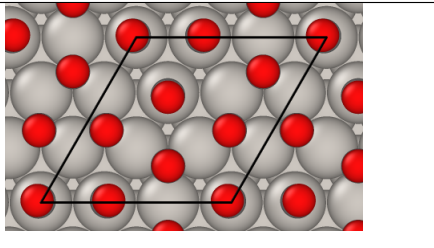
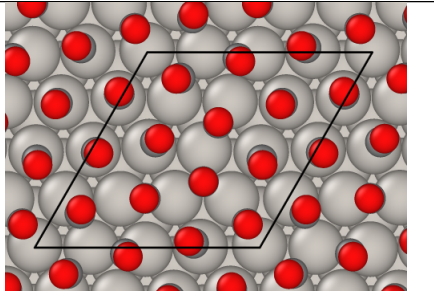
35		$(\sqrt{21} \times \sqrt{21})R10.8^\circ$ - 12CO	0.57	-1.30	-0.1076
36		$(2\sqrt{3} \times 2\sqrt{3})$ -7CO (3T- 3B-1H)	0.58	-1.21	-0.1114
37		$(2\sqrt{3} \times 2\sqrt{3})$ -7CO (4T- 2B-1H)	0.58	-1.34	-0.1139
38		$c(\sqrt{3} \times 5)$ rect-3CO (2T-4B)	0.60	-1.23	-0.1075
39		$c(\sqrt{3} \times 5)$ rect-3CO (4T-2B) (1)	0.60	-1.30	-0.1132
40		$c(\sqrt{3} \times 5)$ rect-3CO (4T-2B) (2)	0.60	-1.28	-0.1120

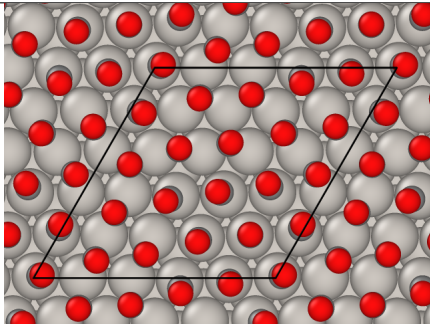
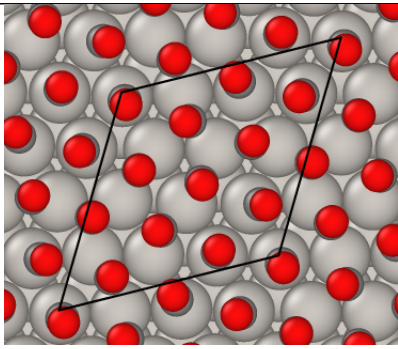


41		$(\sqrt{21} \times \sqrt{21})R10.8^\circ$ - 13CO	0.62	-1.28	-0.1156
42		$(4 \times 2)$ -5CO	0.625	-1.21	-0.1107
43		$(\sqrt{19} \times \sqrt{19})R23.4^\circ$ - 12CO	0.63	-1.27	-0.1164
44		$(\sqrt{3} \times \sqrt{3})R30^\circ$ -2CO (T)	0.66	-1.02	-0.0993
45		$(\sqrt{3} \times \sqrt{3})R30^\circ$ -2CO (B)	0.66	-0.98	-0.0953
46		$(\sqrt{3} \times \sqrt{3})R30^\circ$ -2CO (F)	0.66	-1.00	-0.0967

47		$(\sqrt{3} \times \sqrt{3})R30^\circ$ -2CO (H)	0.66	-0.95	-0.0921
48		$(\sqrt{3} \times 3)$ rect-4CO (1T-3B)	0.67	-1.19	-0.1150
49		$(\sqrt{3} \times 3)$ rect-4CO (2T-2B)	0.67	-1.20	-0.1167
50		$(\sqrt{3} \times 3)$ rect-4CO (3T-1B)	0.67	-1.23	-0.1194
51		$(\sqrt{19} \times \sqrt{19})R23.4^\circ$ -3CO-13CO (2)	0.68	-1.21	-0.1208

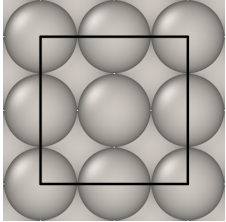
52		$(\sqrt{19} \times \sqrt{19})R23.4^\circ-$ $13CO (1)$	0.68	-1.23	-0.1220
53		$(\sqrt{27} \times \sqrt{27})-19CO$	0.7	-1.19	-0.1219
54		$c(\sqrt{3} \times 7)rect-5CO$	0.714	-1.17	-0.1218
55		$p(2 \times 2)-3CO$	0.75	-1.16	-0.1265

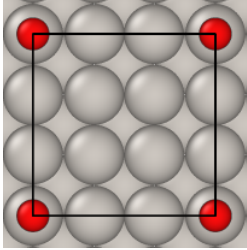
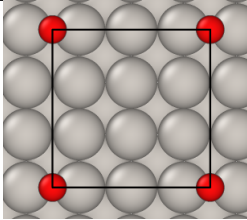
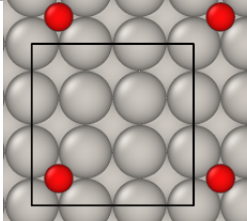
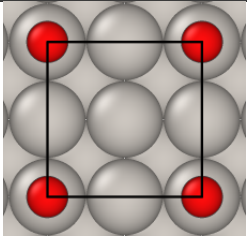
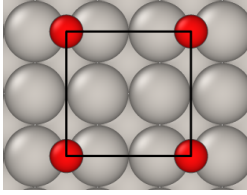
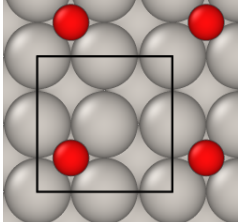
56		p(5×5)-19CO	0.76	-1.07	-0.1177
57		$(\sqrt{27} \times \sqrt{27})$ -21CO	0.78	-1.10	-0.1243
58		p(3×3)-7CO	0.78	-1.09	-0.1232
59		p(4×4)-13CO	0.81	-1.03	-0.1213

60		p(5x5)-21CO	0.84	-0.93	-0.1132
61		$(\sqrt{13} \times \sqrt{13})R14^\circ$ - 12CO	0.92	-0.78	-0.1041

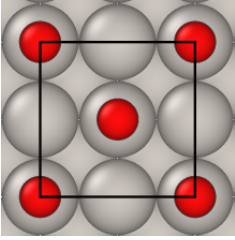
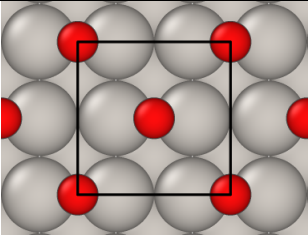
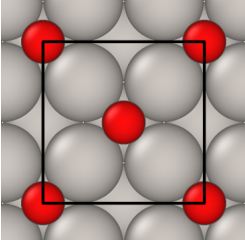
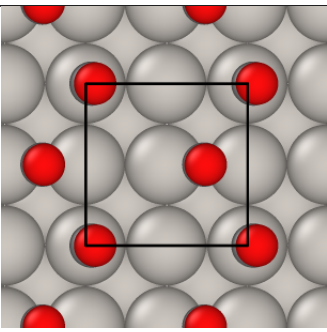
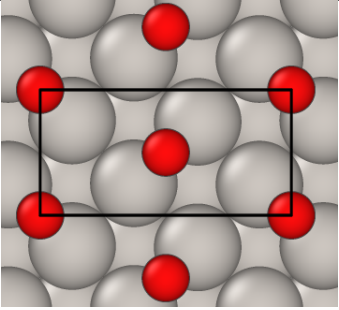
### A.6.2 Pt(100)

Table A.2: Average CO adsorption energies ( $\Delta E_{CO} = E_{CO_n@slab} - E_{slab} - n_{CO} \times E_{CO} + \Delta ZPE$ ) calculated for the various structures considered for Pt(100). The structures, unit cell, CO coverage and average adsorption energies have been listed in the table.

ID	Structure	Unit Cell	$\theta$	$\Delta E_{CO}^{avg}$ (eV)	$\Delta E_{CO}/A$ (eV/Å <sup>2</sup> )
1		c(2x2)	0.00	-	-

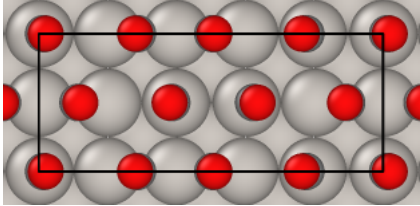
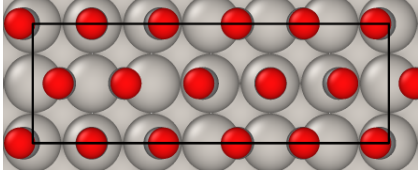
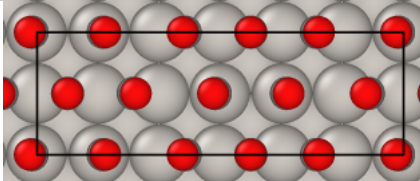
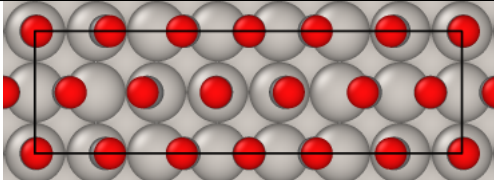
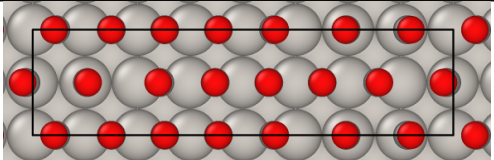
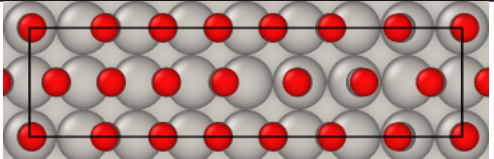
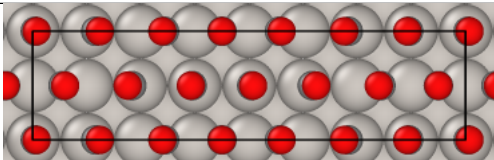
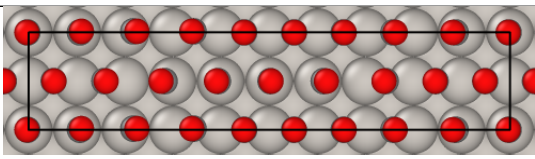
2		$p(3 \times 3)\text{-1CO (T)}$	0.11	-1.71	-0.024
3		$p(3 \times 3)\text{-1CO (B)}$	0.11	-1.82	-0.025
4		$p(3 \times 3)\text{-1CO (H)}$	0.11	-1.15	-0.016
5		$p(2 \times 2)\text{-1CO (T)}$	0.25	-1.70	-0.053
6		$p(2 \times 2)\text{-1CO (B)}$	0.25	-1.80	-0.057
7		$p(2 \times 2)\text{-1CO (H)}$	0.25	-1.23	-0.039

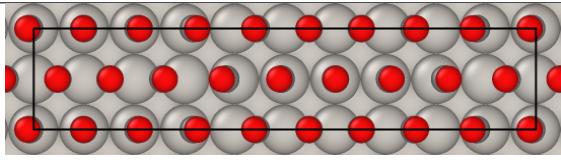
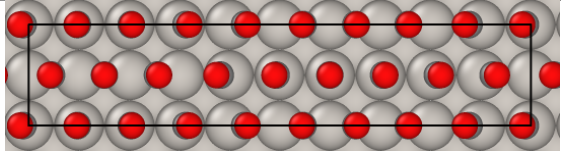


8		$c(2 \times 2)$ -1CO (T)	0.50	-1.71	-0.108
9		$c(2 \times 2)$ -1CO (B)	0.50	-1.76	-0.111
10		$c(2 \times 2)$ -1CO (H)	0.50	-1.13	-0.071
11		$p(2 \times 2)$ -2CO (T-B)	0.50	-1.70	-0.107
12		$(2\sqrt{2} \times \sqrt{2})R45^\circ$ - 2CO	0.50	-1.75	-0.111

13		$c(5\sqrt{2} \times \sqrt{2})R45^\circ$ - 3CO (T)	0.60	-1.61	-0.121
14		$c(5\sqrt{2} \times \sqrt{2})R45^\circ$ - 3CO	0.60	-1.68	-0.127
15		$(3\sqrt{2} \times \sqrt{2})R45^\circ$ - 4CO	0.67	-1.64	-0.138
16		$(4 \times 2)$ -6CO (2T- 4B)	0.75	-1.58	-0.149
17		$(4 \times 2)$ -6CO (4T- 2B)	0.75	-1.57	-0.148
18		$(5 \times 2)$ -8CO (2T- 6B)	0.80	-1.50	-0.151
19		$(5 \times 2)$ -8CO (4T- 4B)	0.80	-1.51	-0.153



20		$(5 \times 2)$ -8CO (6T-2B)	0.80	-1.52	-0.153
21		$(6 \times 2)$ -10CO (6T-4B)	0.83	-1.48	-0.156
22		$(6 \times 2)$ -10CO (4T-6B)	0.83	-1.49	-0.156
23		$(7 \times 2)$ -12CO	0.86	-1.44	-0.156
24		$(8 \times 2)$ -14CO (4T-10B)	0.875	-1.42	-0.157
25		$(8 \times 2)$ -14CO (6T-8B)	0.875	-1.44	-0.159
26		$(8 \times 2)$ -14CO (8T-6B)	0.875	-1.44	-0.159
27		$(10 \times 2)$ -18CO (8T-10B)	0.90	-1.40	-0.159

28		(10 × 2)-18CO (10T-8B)	0.90	-1.40	-0.159
29		(10 × 2)-18CO (12T-6B)	0.90	-1.38	-0.156

### A.6.3 Generalized Correction

We wanted to emphasize the fact that by using the generalized correction correlation, the stability diagram does not change. We still see the same phases for both Pt(111) and Pt(100).

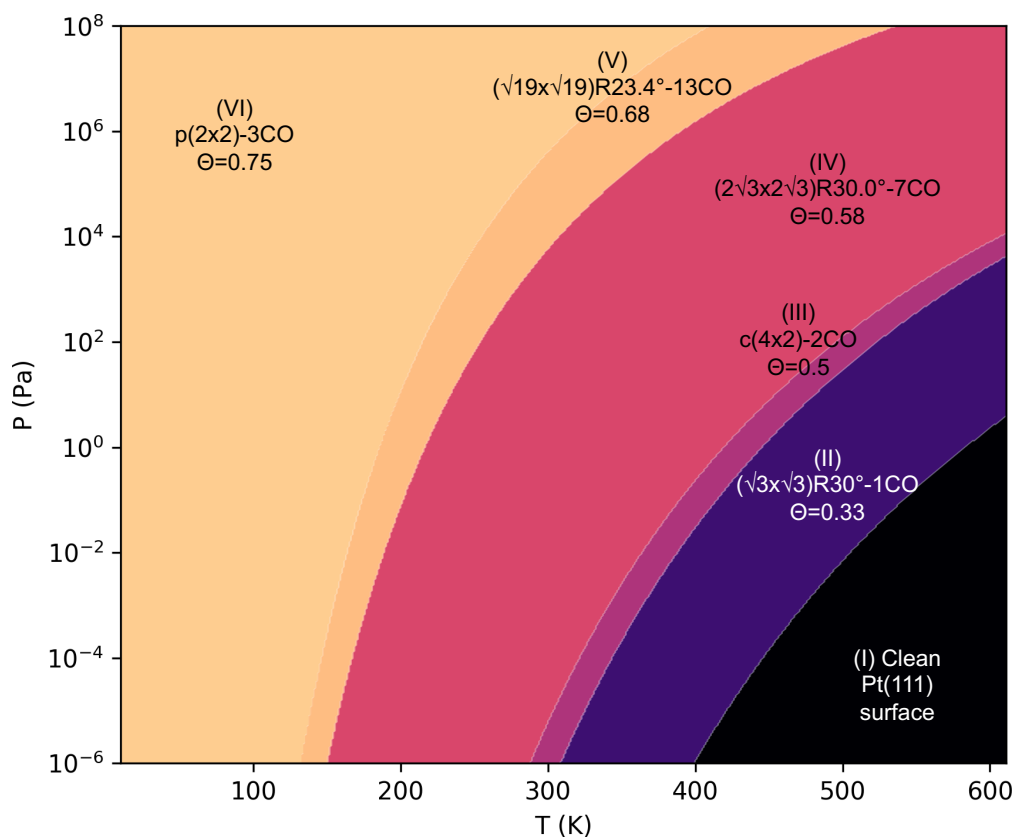


Figure A.4: Pt(111) surface stability diagram using the generalized correction for both the surfaces.

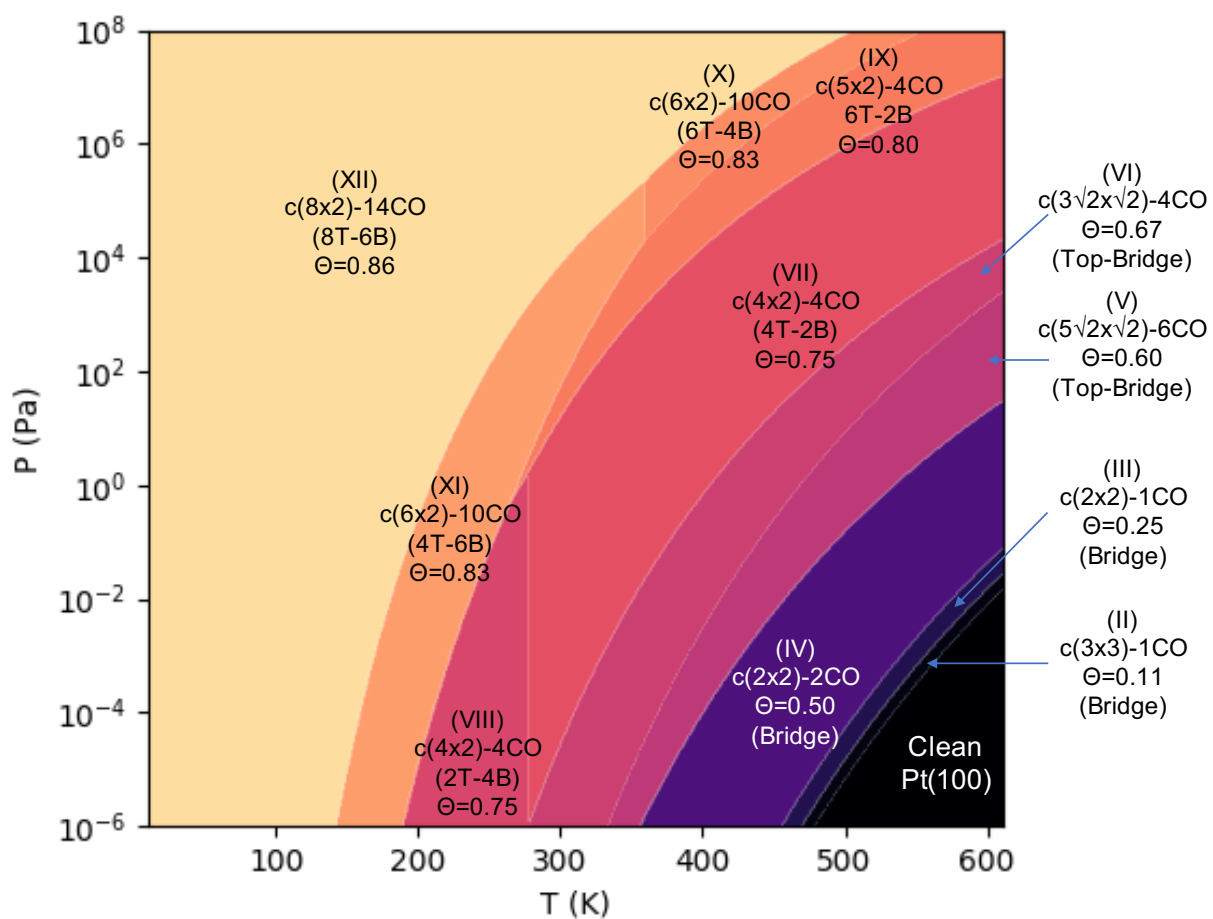


Figure A.5: Pt(100) surface stability diagram using the generalized correction for both the surfaces.

#### A.6.4 Simulated STM imaging

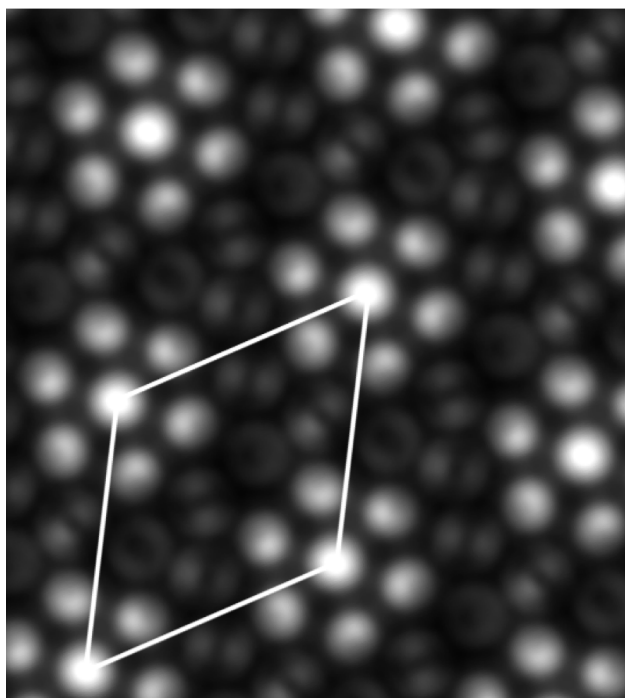


Figure A.6: Simulated STM image of  $(\sqrt{19} \times \sqrt{19})R23.4^\circ$ -13CO structure containing. The STM is generated using the partial charge densities and p4vasp software. The bright features in the image are attributed to CO adsorbed on the top (or quasi-top) site. The faded, less bright spot represents the bridge site.

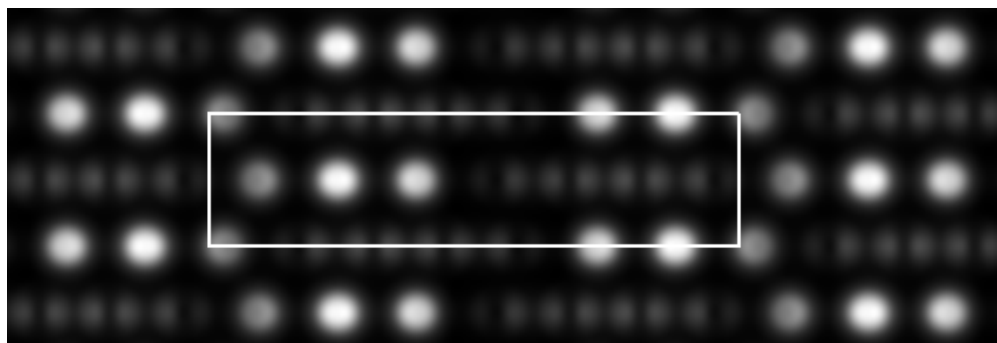


Figure A.7: Simulated STM image of  $c(8 \times 2)$  structure containing 6 top/quasi-top and 8 bridge/quasi-bridge CO molecules per unit cell. The STM is generated using the partial charge densities and p4vasp software.

## A.6.5 Surface Stability Diagram without Energy Correction

### A.6.5.1 Pt(111)

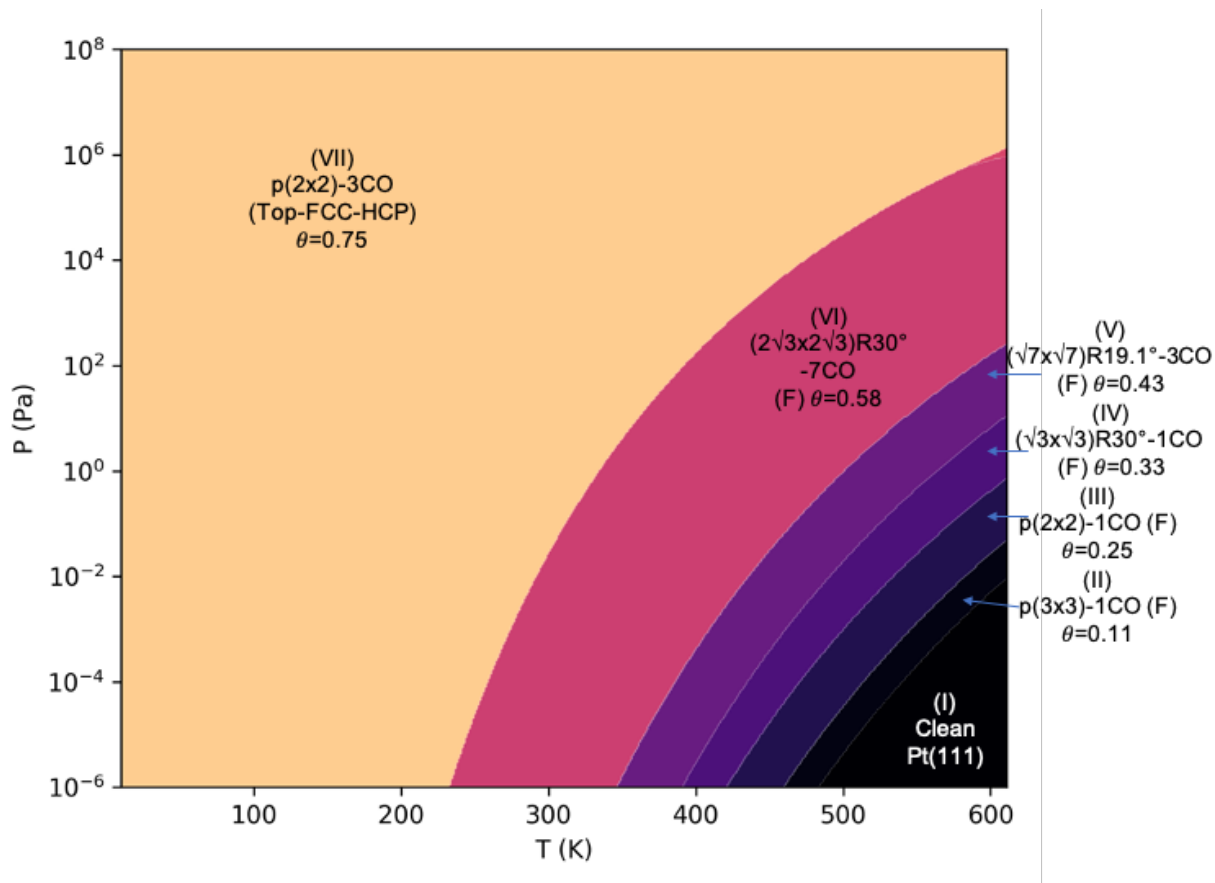


Figure A.8: Surface stability diagram for Pt(111) representing the stable surface terminations as a function of pressure and temperature without applying the energy corrections. This figure can be compared with figure 2 of the main text.

### A.6.5.2 Pt(100)

For Pt(100), the surface terminations that are stable remain the same before and after energy correction but the chemical potential of CO over which the surfaces are stable changes. Hence we see small differences in between the surface stability diagram constructed without the incorporation of energy corrections (A.9) and the stability diagram constructed with the

incorporation of energy corrections.

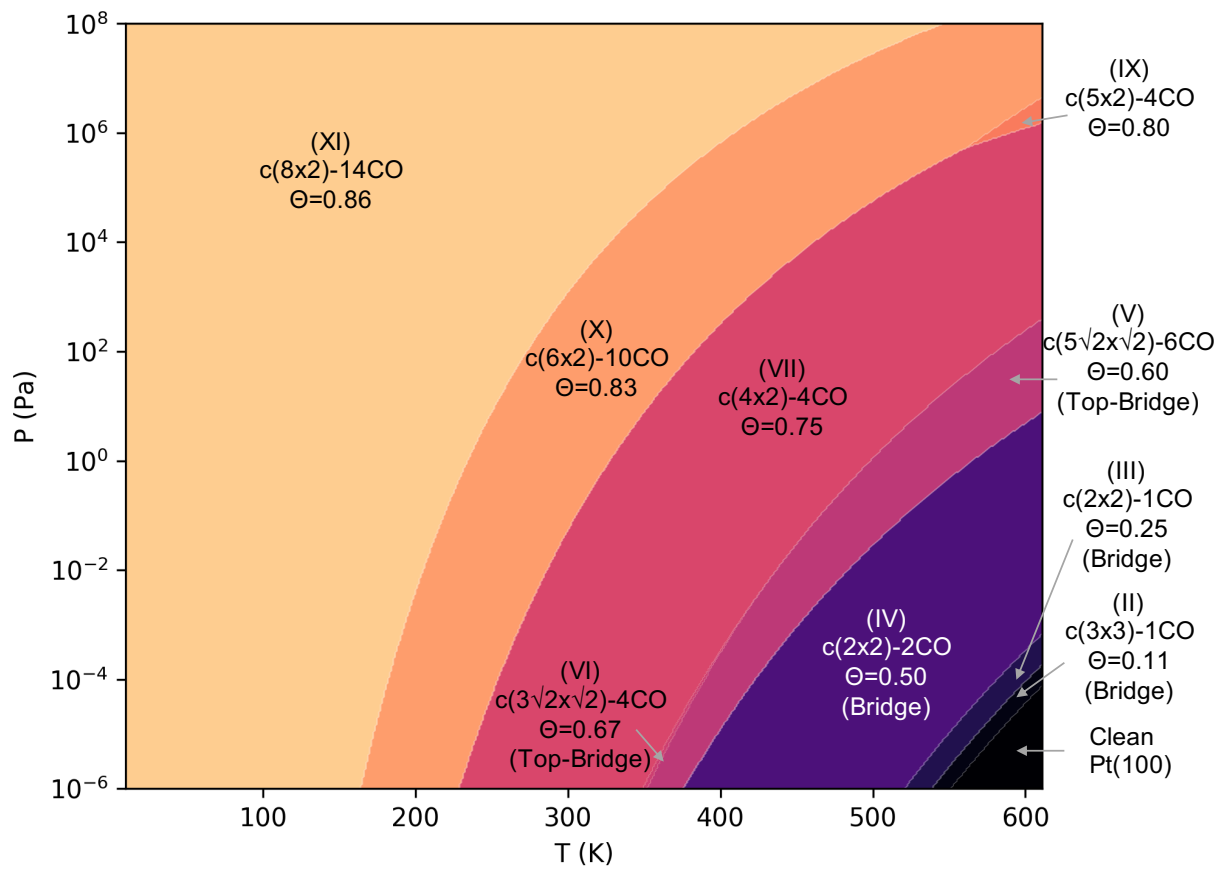


Figure A.9: Surface stability diagram for Pt(100) represents the stable surface terminations as a function of pressure and temperature without applying the energy corrections. This figure can be compared with figure 3 of the main text.

## A.7 Vibrational Frequencies Pt(111)

Pt(111)

p(3x3)-1C0 (T)	2062.52	481.47	395.36	394.05	91.01	89.86
p(3x3)-1C0 (B)	1849.71	394.58	378.30	360.02	198.36	54.16
p(3x3)-1C0 (F)	1751.01	337.95	311.13	310.37	157.94	156.01
p(3x3)-1C0 (H)	1759.09	344.76	319.10	318.17	162.79	160.70
( $\sqrt{21}\times\sqrt{21}$ )-3C0	1850.62	1842.16	1841.86	395.87	395.44	394.37
381.76	381.18	380.68	354.57	352.96	352.68	208.16
201.74	64.29	50.10	47.38			204.31
( $\sqrt{19}\times\sqrt{19}$ )-3C0	2063.87	1850.56	1747.96	483.61	397.52	392.05
390.61	383.47	367.89	352.65	329.62	324.86	207.20
164.14	77.82	77.34	62.88			171.40
( $\sqrt{13}\times\sqrt{13}$ )-3C0	2067.33	1852.82	1840.37	476.57	397.10	393.55
389.06	387.69	383.91	378.64	358.58	356.07	209.09
70.43	58.45	57.73	56.07			200.07
p(2x2)-1C0 (T)	2069.94	481.38	388.22	387.43	86.50	83.39
p(2x2)-1C0 (B)	1868.99	384.95	381.14	365.94	195.00	66.31
p(2x2)-1C0 (F)	1777.17	344.25	286.15	285.89	154.60	153.79
p(2x2)-1C0 (H)	1786.56	359.12	319.92	319.74	162.73	161.72
( $\sqrt{27}\times\sqrt{27}$ )-7C0	2073.60	1886.50	1860.20	1860.00	1853.40	1853.10
1849.70	465.50	408.80	408.60	396.90	396.40	395.80
392.70	392.40	381.50	379.50	379.10	375.30	373.20
364.90	364.00	363.30	359.10	358.50	356.20	192.40
190.80	190.50	189.90	189.60	71.30	66.10	63.90
60.20	57.80	56.70	46.90			62.40
p(5x5)-7C0	2066.40	2051.20	2049.80	2049.60	1847.70	1838.10
1836.90	467.50	466.90	466.70	465.60	393.30	391.00
384.50	384.00	383.50	383.20	382.60	382.10	381.30
381.30	380.30	378.30	361.70	356.80	353.30	201.30
195.30	67.40	61.60	60.00	59.70	58.70	57.20
54.00	51.70	51.30	42.30			54.90

( $\sqrt{3 \times \sqrt{3}}$ )-1C0 (T)	2073.29	479.66	382.00	380.88	55.84	43.70
( $\sqrt{3 \times \sqrt{3}}$ )-1C0 (B)	1882.67	380.14	376.00	362.48	202.66	67.24
( $\sqrt{3 \times \sqrt{3}}$ )-1C0 (F)	1787.80	337.80	295.40	294.50	145.00	141.30
( $\sqrt{3 \times \sqrt{3}}$ )-1C0 (H)	1797.36	342.54	308.69	307.00	162.94	160.63
( $\sqrt{21 \times \sqrt{21}}$ )-7C0	2073.20	2062.00	2061.90	1856.50	1846.10	1846.00
1750.10	475.70	474.20	473.40	395.00	394.70	394.20
391.90	391.30	385.10	384.80	383.90	383.10	382.20
362.60	362.40	362.00	342.40	309.00	306.60	200.10
193.30	154.40	149.90	68.80	64.60	63.50	54.10
53.70	53.20	51.60	39.10			
( $\sqrt{19 \times \sqrt{19}}$ )-7C0	2074.40	2059.20	2056.60	2047.00	1851.50	1839.70
1836.40	477.10	475.90	474.80	473.10	410.50	401.40
398.10	394.40	393.00	390.90	390.20	389.50	388.40
386.90	382.70	379.00	369.20	367.50	365.70	205.80
194.00	73.90	66.70	60.40	51.60	50.40	49.70
46.30	44.70	39.90	26.00			47.80
( $\sqrt{7 \times \sqrt{7}}$ )-3C0	2081.01	1776.38	1750.95	467.14	385.69	383.42
353.07	350.55	322.25	320.82	315.80	314.04	162.47
160.09	156.43	73.63	57.67			161.89
p(4x4)-7C0	2073.60	1886.50	1860.20	1860.00	1853.40	1853.10
1849.70	465.50	408.80	408.60	396.90	396.40	395.80
392.70	392.40	381.50	379.50	379.10	375.30	373.20
364.90	364.00	363.30	359.10	358.50	356.20	192.40
190.80	190.50	189.90	189.60	71.30	66.10	63.90
60.20	57.80	56.70	46.90			62.40
( $\sqrt{27 \times \sqrt{27}}$ )-12C0	2078.60	2066.20	2066.10	2056.10	2055.90	2052.50
1765.40	1757.60	1757.30	1750.80	1750.70	1747.40	471.90
471.10	467.90	467.60	467.40	398.70	398.10	471.30
389.10	388.70	388.60	388.20	388.10	381.60	397.80
349.90	349.20	349.00	348.50	347.80	345.70	389.30
324.60	322.10	321.20	320.80	319.80	317.80	381.50
308.90	308.70	158.60	158.30	158.10	154.30	381.10
152.10	151.70	151.40	151.20	150.80	149.60	325.80
58.60	49.60	48.80	48.40	44.50	44.20	324.80
28.50	27.60					309.10
						152.90
						58.70
						32.80



p(5x5)-12C0	2074.60	2062.10	2059.50	2057.40	1865.60	1854.00
1848.30	1843.50	1842.40	1838.90	1765.60	1756.20	462.90
460.30	459.50	406.00	403.70	402.20	400.60	396.80
393.70	391.50	391.00	389.80	389.10	387.60	385.00
379.20	376.90	376.00	373.00	371.10	369.70	360.40
355.30	354.90	352.40	351.70	351.40	344.00	330.10
315.60	310.50	200.00	199.60	196.10	193.60	193.20
161.20	160.70	156.80	151.60	75.30	72.80	69.20
65.00	63.80	62.60	58.10	57.90	55.00	51.30
46.70	45.20					47.10

(√27x√27)-13C0	2078.10	2067.60	2055.50	2054.70	2054.30	2043.40
2042.50	1858.30	1851.10	1848.80	1836.20	1833.30	1742.10
474.30	472.00	471.00	469.90	467.40	466.40	415.60
411.80	411.20	409.00	400.80	399.80	398.70	398.10
394.90	394.30	394.00	392.70	392.10	390.20	386.30
385.30	384.10	383.30	382.40	381.10	379.20	372.20
363.70	356.70	356.00	354.90	348.00	327.80	201.20
193.90	193.10	192.40	165.20	159.30	84.80	77.60
72.10	70.90	67.60	66.10	63.50	60.80	59.00
54.80	51.80	51.10	49.00	45.60	45.00	41.60
						24.20

p(2x2)-2C0 (T)	2087.72	2010.31	471.31	458.70	458.21	407.05
380.41	368.91	246.57	76.18	67.56	21.70	

p(2x2)-2C0 (B)	1914.05	1840.87	466.98	386.19	375.12	369.41
356.31	338.61	253.56	195.65	150.38	64.20	

p(2x2)-2C0 (F)	1846.15	1774.22	463.02	360.60	358.03	339.04
299.66	281.06	269.01	172.67	138.32	125.59	

p(2x2)-2C0 (H)	1850.92	1778.84	473.69	359.56	351.05	346.63
304.05	283.29	272.32	169.16	135.68	134.92	

c(4x2)-2C0 (2T-2B)		2080.27	2061.17	1842.20	1830.90	471.60
470.90	417.56	411.70	402.02	395.65	395.47	394.15
384.89	374.77	373.88	201.83	200.48	69.59	68.25
62.57	57.72	51.15				66.87

c(4x2)-2C0 (3T-1B)		2077.77	2047.19	2024.63	1831.54	476.44
473.47	468.39	424.27	407.79	403.35	393.59	392.38
384.77	376.27	353.20	205.01	103.57	91.86	87.36
72.97	66.44	60.01				76.23

p(5x5)-13C0	2077.80	2064.50	2064.00	2054.20	2046.30	2045.60
1862.90	1844.80	1844.10	1818.70	1814.70	1758.90	1740.00
464.80	463.50	461.70	460.30	458.70	414.40	412.50
408.50	406.90	403.20	401.40	400.10	395.80	393.20
391.80	390.80	389.60	384.30	382.40	381.40	378.10
376.40	372.50	371.40	367.70	364.50	361.90	351.50
337.70	328.40	324.30	321.10	306.20	299.40	196.10
191.60	190.00	188.40	165.00	157.90	157.00	156.60
89.00	83.70	79.50	78.50	77.40	75.20	72.30
68.60	58.80	56.00	55.60	50.60	48.10	14.90

(√13x√13)-7C0	2078.90	2050.40	2050.00	1866.20	1847.50	1847.40
1756.30	472.10	467.20	466.40	405.00	404.30	403.30
396.30	395.70	387.60	382.90	382.80	382.20	381.90
373.10	369.50	368.30	347.00	334.60	332.40	196.00
192.10	162.20	157.00	77.40	71.60	69.70	64.90
57.00	53.90	53.60	49.10			59.40

(√7x√7)-4C0	2078.94	1885.43	1843.92	1843.58	468.20	417.44
416.36	414.96	395.86	393.93	383.21	378.17	374.24
350.23	348.91	208.52	205.17	197.97	92.67	86.21
70.35	67.21					80.47

(√21x√21)-12C0	2081.60	2052.20	2052.00	2046.80	2046.30	2036.30
2035.70	2034.40	2034.10	1731.10	1729.10	1728.40	467.90
466.00	462.80	462.00	461.40	461.30	460.70	460.40
404.40	404.00	401.00	400.70	397.60	397.30	397.00
380.50	380.10	379.00	378.80	378.10	376.40	376.10
374.70	355.30	354.60	353.80	353.50	352.90	352.10
349.90	349.10	174.00	172.20	169.90	168.20	165.10
84.50	82.20	79.50	78.60	77.30	76.60	72.40
68.30	67.10	65.80	61.70	60.40	58.70	56.90
44.70	43.20					51.60

(√12x√12)-7C0 (3T-3B-1H)	2079.79	2042.79	2042.50	2040.41	1855.67
1839.95	1744.52	472.30	467.20	464.68	460.96
411.64	409.17	405.93	402.55	391.08	390.28
378.66	374.83	371.07	367.91	360.70	346.58
192.02	168.51	153.52	98.76	93.91	89.92
79.85	72.56	71.94	66.31	60.73	87.88

(√12x√12)-7C0 (4T-2B-1H)	2078.15	2041.54	2040.87	2039.06	1853.17
1837.61	1742.53	472.91	467.49	467.00	464.23
411.07	408.77	405.56	403.02	390.20	389.79
378.40	376.46	371.71	368.33	360.49	345.62
					327.99
					201.34

195.69	162.53	152.34	107.39	100.60	97.59	94.86	92.49
84.09	76.35	68.47	60.43	38.75			
c( $\sqrt{3 \times 5}$ )rect-3C0	(2T-4B)	2080.46	2070.61	1875.14	1868.09	1776.95	
1772.59	456.49	452.89	444.94	442.48	401.14	398.08	387.03
380.43	379.15	376.66	366.83	364.49	355.40	353.73	341.00
340.28	311.19	308.57	208.14	202.23	172.86	170.06	159.85
147.71	118.20	113.76	79.01	70.22	69.18	64.57	
c( $\sqrt{3 \times 5}$ )rect-3C0	(4T-2B) (1)	2081.59	2061.60	2037.16	2031.98		
1833.10	1830.97	473.79	473.31	465.83	465.53	418.82	418.04
417.85	415.77	408.81	403.51	400.51	397.29	396.61	391.13
387.41	385.76	375.91	374.15	199.00	198.46	119.45	109.79
106.35	103.00	98.38	92.93	89.76	76.76	76.35	63.40
c( $\sqrt{3 \times 5}$ )rect-3C0	(4T-2B) (2)	2082.87	2064.70	2040.77	2016.83		
1838.30	1833.33	476.86	470.62	463.82	462.87	434.33	424.93
420.87	414.92	409.66	404.31	401.41	399.96	392.59	388.42
384.77	383.22	374.47	371.06	203.67	200.19	133.56	114.72
103.91	101.47	87.39	83.63	80.95	70.21	67.97	60.76
( $\sqrt{21 \times 21}$ )-13C0	2080.00	2056.70	2051.20	2044.60	2037.60	2027.00	
1886.70	1861.90	1859.80	1850.20	1842.60	1829.50	1764.50	476.80
473.60	469.10	468.30	466.20	464.00	460.70	430.50	429.20
418.00	415.90	413.50	409.70	408.10	402.70	401.10	399.50
398.20	396.00	393.20	391.20	390.10	385.90	384.60	382.80
381.70	380.90	378.40	376.70	373.80	371.60	362.90	360.90
357.70	352.50	343.80	335.20	331.90	320.20	214.10	205.70
195.10	193.40	191.50	188.20	172.10	159.90	101.40	98.00
95.20	92.90	89.10	85.00	83.20	80.10	75.80	71.60
69.10	66.20	64.70	63.70	59.20	57.80	55.10	51.20
(4x2)-5C0	2088.10	2068.60	2025.40	1758.30	1734.60	458.10	
454.60	448.60	447.90	424.80	406.70	399.80	394.00	367.20
365.70	365.50	355.60	343.70	334.30	306.10	180.40	177.50
175.80	173.70	147.70	89.60	83.90	61.20	43.90	15.00
( $\sqrt{19 \times 19}$ )-12C0	2078.30	2055.50	2044.90	2042.80	1900.10	1880.70	
1868.00	1866.00	1862.60	1847.10	1788.70	1770.20	472.70	472.20
469.50	468.30	465.80	462.90	453.00	429.60	428.20	425.70
417.90	415.00	414.30	410.40	407.60	406.60	399.30	396.40
393.90	390.00	387.00	382.10	379.90	378.30	375.00	367.80
362.90	360.50	357.30	347.90	339.60	334.40	329.50	324.90
310.20	300.60	213.20	211.60	207.80	195.80	192.40	190.30
189.50	170.40	146.70	124.10	100.50	96.80	88.70	84.30

79.40	76.80	73.30	69.30	68.50	65.10	63.40	60.90
57.50	49.50						
( $\sqrt{3 \times \sqrt{3}}$ )-2C0 (T)	2096.16	1996.90	474.39	456.39	427.19	426.10	
400.25	399.11	212.30	209.15	78.66	71.96		
( $\sqrt{3 \times \sqrt{3}}$ )-2C0 (B)	1947.77	1848.29	482.14	438.87	394.92	388.47	
374.85	357.77	248.72	226.89	199.24	36.29		
( $\sqrt{3 \times \sqrt{3}}$ )-2C0 (F)	1876.44	1777.45	426.52	423.52	360.87	336.20	
332.96	326.18	250.02	248.31	148.84	143.35		
( $\sqrt{3 \times \sqrt{3}}$ )-2C0 (H)	1885.71	1785.63	424.41	423.79	360.27	334.18	
333.28	320.21	250.31	246.39	144.77	140.84		
( $\sqrt{3 \times 3}$ )rect-4C0 (1T-3B)	2074.30	1892.18	1863.51	1792.07	466.54		
453.91	446.38	415.70	403.56	390.32	376.93	361.63	357.27
353.08	327.01	326.12	215.27	208.10	178.02	166.96	118.62
113.28	70.13	64.12					
( $\sqrt{3 \times 3}$ )rect-4C0 (2T-2B)	2081.45	2036.87	1881.59	1830.20	471.96		
464.36	438.51	433.41	428.14	418.03	411.48	403.29	393.27
367.23	336.61	320.36	214.26	197.94	171.30	109.78	91.27
86.51	62.24	59.57					
( $\sqrt{3 \times 3}$ )rect-4C0 (3T-1B)	2085.13	2035.75	2017.28	1832.90	475.13		
459.44	458.51	436.76	426.83	416.14	409.97	407.19	394.91
387.70	383.87	373.41	206.75	135.28	108.60	104.48	99.80
82.86	63.97	55.60					
( $\sqrt{19 \times \sqrt{19}}$ )-13C0 (2)	2081.00	2057.10	2050.20	2041.30	2036.50		
1898.60	1877.60	1875.30	1863.20	1857.60	1792.20	1781.60	1771.60
472.20	471.40	466.40	464.70	462.80	458.50	455.40	454.70
444.90	433.20	427.70	427.10	422.50	417.80	412.30	409.90
409.20	405.80	403.70	401.40	398.60	393.40	389.10	382.30
380.80	377.80	377.00	373.30	372.00	363.90	355.30	353.10
346.50	343.90	330.30	324.60	316.20	305.20	300.40	214.40
213.70	210.40	205.60	194.10	191.20	177.50	171.20	164.20
141.80	128.60	112.80	110.20	104.00	97.40	94.00	90.30
88.50	84.70	82.90	80.90	74.70	70.30	65.20	59.20
56.80							

( $\sqrt{19 \times \sqrt{19}}$ )-13C0 (1)	2083.20	2053.60	2053.20	2040.80	2040.50	
2034.10	2020.70	1873.90	1860.90	1852.90	1836.20	1780.90
476.90	468.30	465.80	465.10	461.70	461.10	459.30
443.10	431.50	430.50	425.30	424.30	419.10	416.70
409.80	406.10	404.70	402.30	399.20	396.90	394.60
390.40	388.20	385.10	384.00	381.60	380.90	379.90
375.20	368.10	364.50	361.80	333.50	300.10	291.60
206.60	204.60	199.60	186.10	178.40	142.60	116.40
110.70	108.70	102.50	94.20	94.10	90.80	85.90
78.80	77.50	76.00	74.40	67.50	65.80	58.20
45.50						
( $\sqrt{27 \times \sqrt{27}}$ )-19C0	2080.70	2055.80	2055.70	2041.40	2041.30	2034.90
2020.80	1911.00	1889.50	1889.40	1873.10	1868.30	1868.10
1859.80	1859.50	1821.90	1802.60	1801.50	476.00	475.20
472.70	471.20	470.30	467.70	467.40	465.90	462.00
461.20	459.50	432.20	432.10	431.00	430.90	430.40
426.00	425.30	421.20	417.60	417.20	410.00	408.50
407.00	403.20	403.10	399.60	398.40	398.20	389.10
388.40	379.70	379.70	379.00	373.90	367.10	366.90
364.60	363.60	358.80	358.40	358.00	338.10	333.50
331.90	329.10	328.90	315.60	281.00	280.30	219.10
217.00	215.30	213.60	210.80	192.00	191.10	189.90
186.50	185.70	146.90	114.60	114.40	112.30	109.60
102.10	96.40	93.90	92.80	90.20	89.40	84.20
81.30	77.00	74.50	74.00	71.30	67.10	65.30
57.70	54.70	42.90	39.10			
c( $\sqrt{3 \times 5}$ )rect-5C0	2088.30	2072.10	2055.40	2041.90	2025.10	2020.30
2006.90	2006.20	1837.60	1837.00	475.90	475.80	466.70
459.90	459.20	458.60	457.90	445.20	445.00	430.80
428.10	427.70	418.80	416.90	413.60	412.10	411.60
406.80	404.00	394.20	394.10	381.70	381.50	378.00
375.30	372.40	208.30	208.20	150.50	149.10	136.50
127.40	123.50	123.50	122.20	120.70	106.10	103.20
101.40	81.40	76.80	74.80	70.20	60.50	
p(2x2)-3C0	2091.13	1823.31	1757.62	440.22	425.65	425.40
399.80	399.30	363.29	341.44	340.81	333.86	197.11
159.05	155.80	100.82	97.94			194.83
p(5x5)-19C0	2086.00	2076.10	2073.80	2067.70	2049.50	2047.20
2046.20	2035.40	1885.80	1862.50	1857.50	1849.10	1802.00
1777.50	1768.90	1765.00	1760.80	1755.90	511.50	489.40
451.70	450.80	446.40	444.90	443.10	442.30	441.80
437.20	435.80	433.40	427.80	425.20	423.50	422.40
417.90	416.00	414.70	412.40	411.70	407.10	404.50
397.30	394.80	393.80	391.00	389.20	386.10	384.60
380.40	378.60	377.20	374.90	373.60	365.20	363.40

356.00	355.10	350.10	348.20	346.30	342.80	339.50	334.80
326.30	323.60	311.90	308.80	307.70	303.50	235.20	225.10
222.10	206.70	203.80	202.20	200.90	198.50	189.40	180.60
171.40	165.50	163.00	162.00	156.60	152.70	149.40	144.30
143.80	136.00	132.20	122.70	117.80	114.80	109.40	103.70
103.10	98.70	96.30	94.00	92.20	87.40	83.00	82.20
80.60	77.70	66.80	60.60				
( $\sqrt{27 \times 27}$ )-21C0	2084.00	2070.60	2070.60	2049.10	2049.00	2046.80	
2046.70	2045.80	2045.30	1880.70	1873.70	1873.20	1850.00	1849.80
1845.80	1845.30	1845.10	1844.50	1768.60	1767.90	1767.90	473.60
473.50	466.50	466.50	465.60	464.20	463.10	453.30	453.20
451.50	450.00	450.00	444.10	443.80	443.70	443.20	442.90
442.80	432.10	432.10	428.80	420.40	419.90	417.60	417.50
415.70	415.70	402.60	402.60	401.50	401.40	399.80	399.50
398.50	396.70	396.60	391.40	390.70	390.30	390.30	389.10
389.10	383.30	375.60	375.50	374.50	374.50	363.00	362.90
361.50	360.90	353.60	353.10	353.00	343.50	343.50	341.30
340.10	339.90	339.10	337.10	337.10	337.00	223.50	223.40
219.70	218.90	218.80	218.50	216.80	210.80	210.80	183.30
183.30	182.10	181.80	181.80	180.60	142.90	140.60	140.50
134.70	134.50	129.10	128.90	128.10	126.90	118.30	112.00
111.60	111.40	108.10	105.40	105.30	98.10	97.80	87.80
87.60	77.30	77.20	73.00	71.10	63.30	63.10	59.00
p(3x3)-7C0	2091.50	2054.30	2054.10	1822.50	1777.60	1768.30	
1768.00	467.60	455.50	447.00	446.30	439.20	438.40	436.90
419.10	418.50	413.10	412.40	405.90	370.90	368.50	360.80
359.10	356.70	337.40	330.10	330.00	325.10	221.40	211.80
206.70	183.70	177.10	162.60	157.30	156.70	144.20	122.20
116.80	77.90	75.00	55.00				
p(4x4)-13C0	2086.50	2055.00	2054.80	2038.70	2031.10	2031.00	
1905.60	1872.80	1872.50	1854.40	1852.40	1852.30	1771.00	497.00
492.50	491.20	472.20	468.30	460.40	459.20	453.00	451.40
448.30	448.10	446.80	438.30	437.20	431.10	426.80	420.40
419.50	415.80	412.60	411.90	411.10	406.50	405.40	395.90
394.90	390.60	389.80	388.70	375.50	375.10	374.90	366.00
360.30	359.80	350.40	348.80	329.70	325.60	231.00	229.50
228.20	219.80	212.10	204.80	195.40	188.00	168.40	166.00
163.60	149.50	148.70	141.40	132.00	129.60	127.20	120.40
109.50	108.40	95.70	92.30	91.30	81.20	71.10	68.20
p(5x5)-21C0	2085.00	2059.90	2056.80	2051.90	2040.50	2034.00	
2025.60	2023.50	2014.00	2006.80	1912.90	1899.90	1883.20	1880.40
1868.60	1861.70	1858.30	1829.30	1801.00	1794.10	1786.50	540.30
517.50	515.10	483.10	477.10	472.20	460.70	458.80	453.80
452.60	451.90	449.70	448.60	447.60	446.80	445.50	442.50
441.90	440.70	439.50	438.40	436.40	434.60	431.60	427.90

426.70	425.20	422.10	420.90	418.50	412.70	412.00	411.40
410.30	409.80	408.40	406.80	405.00	404.20	400.20	398.80
397.10	395.40	393.00	389.10	385.50	380.90	376.90	375.60
372.90	370.30	367.60	366.50	358.00	353.10	347.80	343.80
338.50	335.30	324.60	319.00	305.70	302.10	248.70	241.30
238.30	226.50	221.60	219.30	213.10	207.30	205.20	192.70
187.30	185.80	182.30	180.90	176.90	173.60	171.90	169.70
167.20	164.50	162.20	154.60	150.30	147.00	136.60	133.10
130.80	128.40	123.00	120.70	118.70	111.50	108.20	106.00
100.40	96.70	94.80	89.50	86.20	76.90	69.10	67.90

( $\sqrt{13 \times \sqrt{13}}$ )-12C0	2088.20	2051.50	2043.80	2035.60	2027.70	1920.30	
1882.30	1877.60	1867.90	1866.60	1848.30	1782.70	603.60	553.90
527.00	505.70	496.10	481.90	468.40	455.30	453.90	451.50
449.50	444.70	441.60	436.00	432.40	428.30	426.30	425.60
423.60	417.20	413.50	412.60	409.50	403.70	400.80	393.30
389.50	384.80	381.30	372.80	362.10	361.20	353.30	345.10
340.40	319.40	291.10	266.30	261.00	254.50	247.50	230.90
224.80	214.00	207.30	199.30	194.50	184.90	181.50	176.60
171.10	156.70	143.30	138.60	129.20	120.10	117.30	111.70
85.20	78.10						

## A.8 Vibrational Frequencies Pt(100)

Pt(100)

p(3x3)-1C0 (H)	48.10	48.10	380.40	380.40	491.20	2048.40
p(3x3)-1C0 (B)	55.60	202.20	378.30	398.40	407.00	1844.50
p(3x3)-1C0 (F)	55.60	202.20	378.30	398.40	407.00	1844.50
p(2x2)-1C0 (T)	44.80	44.80	379.10	379.10	491.60	2061.10
p(2x2)-1C0 (B)	61.00	203.80	381.90	389.90	393.40	1862.70
p(2x2)-1C0 (H)	64.32	63.32	223.03	224.76	268.72	1690.12
c(2x2)-1C0 (T)	29.40	32.20	39.40	42.50	379.60	380.10
	386.40	387.00	491.10	494.20	2019.10	2076.10
c(2x2)-1C0 (B)	66.40	72.10	201.30	202.70	373.10	374.50
	376.20	383.80	408.80	408.90	1847.60	1893.10
c(2x2)-1C0 (H)	59.87	59.07	160.09	159.23	215.33	216.57
	224.41	225.72	249.44	254.00	1713.69	1754.45
p(2x2)-2C0 (T-B)	56.30	65.50	110.40	201.90	357.00	372.10
	383.30	419.40	425.70	480.90	1844.70	2070.30
c(2√2x√2)-1C0	78.90	80.30	205.90	206.80	378.70	378.90
	381.30	381.70	388.90	401.90	1861.70	1896.20
c(5√2x√2)-3C0 (T)		48.60	45.70	43.00	43.30	46.90
	56.10	59.10	59.40	68.70	70.70	71.10
	79.50	370.70	374.90	375.30	376.00	377.00
	379.70	380.00	380.90	386.20	392.80	395.60
	480.10	480.40	487.10	488.50	489.30	490.50
	2014.00	2019.60	2030.60	2052.40	2054.20	2079.60
c(5√2x√2)-3C0 (T)		62.60	60.40	46.40	46.70	54.50
	63.00	65.60	66.00	74.10	76.50	76.90
	84.40	371.20	374.80	375.00	375.70	377.50
	379.80	380.30	380.50	385.60	393.30	395.80
	480.20	480.60	487.20	488.70	489.40	490.70
	2013.90	2019.60	2030.50	2052.30	2054.10	2079.50



(3√2x√2)-4C0	67.00	78.20	85.70	86.60	107.40	112.50
209.80	211.80	371.90	373.30	374.20	375.90	380.60
402.20	414.00	423.50	429.10	473.60	476.50	1852.90
2056.20	2072.60					1856.80

(4x2)-6C0 (2T-4B)		52.50	53.00	57.10	63.80	88.80
94.90	119.50	121.10	203.40	205.10	217.20	217.30
337.80	351.40	357.10	373.60	375.70	389.00	392.10
423.90	424.80	437.70	439.00	447.70	464.50	465.30
487.40	1844.40	1859.10	1865.20	1886.40	2059.90	2073.00

(4x2)-6C0 (4T-2B)		52.90	58.80	63.60	66.10	73.60
74.90	76.60	93.30	116.50	120.30	203.10	203.20
366.50	375.80	376.80	380.50	384.80	386.40	387.70
391.90	431.20	434.50	435.20	436.30	469.10	469.70
474.00	1835.10	1836.50	2023.60	2035.40	2047.50	2079.80

(5x2)-8C0 (2T-6B)		67.40	69.10	71.80	72.10	73.60
99.50	103.50	131.30	132.60	205.80	206.30	214.80
218.90	244.00	244.90	324.30	325.70	329.80	333.70
377.80	380.50	381.00	392.00	394.60	411.70	412.30
431.30	437.00	438.00	439.90	463.30	466.50	466.70
470.20	517.10	521.80	1847.60	1849.40	1861.80	1880.20
1917.40	2063.30	2072.40				1880.50

(5x2)-8C0 (4T-4B)		67.20	78.60	82.00	82.40	90.40
95.20	114.20	115.90	118.70	122.20	135.70	137.90
209.90	230.20	231.80	336.80	342.50	362.50	366.70
368.10	380.70	381.70	384.80	388.70	390.80	394.40
429.50	437.70	442.30	443.00	446.20	463.90	464.60
472.80	492.80	496.10	1842.40	1847.00	1858.70	1878.50
2049.70	2056.00	2078.20				2028.30

(5x2)-8C0 (6T-2B)		26.70	60.00	66.00	68.30	74.20
76.80	77.50	99.90	100.80	102.20	105.50	125.60
134.60	212.80	213.40	293.00	301.00	361.90	364.80
379.90	384.80	387.80	388.60	391.20	391.50	393.20
415.40	437.00	438.90	448.90	449.50	459.80	467.90
469.70	474.00	475.10	1836.10	1837.10	1997.60	2013.20
2044.60	2050.90	2080.50				2024.40

(6x2)-8C0 (6T-4B)		33.20	52.80	59.10	60.30	68.90
71.30	75.90	85.70	87.40	89.80	95.40	110.30
125.30	132.60	135.20	209.20	209.40	229.50	229.50
350.60	353.10	354.70	356.90	359.90	367.40	368.60
379.60	383.30	386.10	389.70	391.20	391.30	391.80
433.00	442.70	444.60	446.90	447.50	459.30	460.20
467.00	468.50	470.60	504.60	504.70	1839.50	1839.50
						1856.90

1858.20 2022.40 2026.50 2036.20 2053.10 2059.60 2080.90

(6x2)-8C0 (4T-6B) 66.80 72.00 73.00 73.60 78.00  
83.10 89.10 89.90 106.90 109.60 131.10 133.50 138.40  
140.00 207.30 209.00 217.60 218.60 248.30 248.40 328.00  
331.10 334.90 337.40 371.60 373.00 378.30 379.80 385.30  
386.20 391.50 393.00 393.50 396.30 415.50 421.40 427.90  
435.30 440.80 444.60 447.80 450.80 462.10 462.30 467.40  
467.50 476.70 483.70 521.70 523.70 1843.00 1850.40 1854.00  
1871.80 1873.50 1886.20 2045.10 2050.30 2064.40 2076.50

(7x2)-12C0 55.50 56.00 62.30 65.70 71.60 73.10  
73.80 81.30 86.20 88.70 94.90 107.90 116.40 125.40  
133.30 137.00 142.30 143.70 201.00 202.00 221.70 222.00  
244.30 244.30 335.10 342.10 349.70 353.00 357.90 359.30  
371.70 373.50 379.30 380.10 382.00 387.60 389.90 391.70  
392.60 394.80 395.60 396.00 419.80 431.80 434.20 438.10  
443.70 445.70 452.90 454.60 459.20 459.50 464.60 465.00  
468.30 470.60 482.90 486.30 530.70 532.00 1841.90 1843.20  
1850.90 1863.10 1873.50 1884.40 2025.80 2038.30 2043.70 2062.20  
2064.60 2081.30

(8x2)-14C0 (4T-10B) 55.70 57.30 58.50 62.60 64.40  
66.60 72.50 84.20 89.50 91.80 96.60 118.40 125.20  
138.80 139.40 196.50 202.90 210.90 213.40 228.50 229.70  
230.40 230.90 243.90 245.50 247.90 273.20 275.50 317.80  
319.00 351.60 353.50 357.90 364.20 365.50 366.60 370.70  
375.30 382.80 384.20 385.40 386.90 387.80 388.00 395.80  
396.50 419.20 420.60 429.10 429.20 429.80 429.90 430.30  
444.80 445.10 457.40 459.10 462.30 463.20 463.30 470.70  
472.70 473.10 483.40 487.70 490.10 515.20 525.30 559.60  
565.40 1848.00 1848.50 1857.10 1862.50 1876.10 1877.00 1878.50  
1901.70 1923.40 1956.10 2029.80 2049.20 2060.70 2077.00

(8x2)-14C0 (6T-8B) 46.30 52.00 58.40 64.60 72.00  
77.60 78.30 80.50 84.80 86.90 94.80 102.50 106.80  
114.20 126.80 136.00 139.40 143.20 146.80 204.60 208.10  
211.70 221.20 221.90 239.50 240.90 250.80 251.80 326.90  
330.10 350.00 354.10 357.40 359.40 371.00 371.30 377.50  
378.50 382.60 382.80 384.80 389.90 392.40 393.80 395.80  
396.80 398.40 398.60 415.30 430.90 432.10 439.40 440.70  
443.00 445.90 453.80 455.80 459.10 459.90 464.60 465.50  
467.50 468.60 470.40 473.40 475.40 510.80 516.10 554.50  
556.60 1840.40 1842.90 1853.20 1859.80 1862.50 1877.10 1886.00  
1920.40 2024.60 2037.50 2043.80 2060.30 2067.10 2079.60

(8x2)-14C0 (8T-6B) 41.20 42.40 57.20 60.50 69.70

70.70	77.70	78.50	82.00	87.70	97.10	106.70	107.70
112.40	114.90	115.30	117.40	125.90	133.00	138.70	138.80
141.60	219.00	219.20	231.90	232.10	252.70	252.90	348.40
350.50	352.30	353.80	357.70	358.60	359.50	360.20	380.10
380.50	383.10	383.40	386.20	386.70	387.90	388.70	390.00
393.40	393.70	395.80	402.00	402.40	432.30	434.10	438.90
440.60	444.70	444.80	454.60	455.20	455.30	455.40	461.60
461.80	467.50	468.70	470.10	470.30	488.10	489.60	537.50
537.90	1839.30	1839.50	1847.70	1848.10	1869.80	1870.70	2022.10
2024.30	2030.90	2040.00	2045.90	2062.70	2067.60	2082.10	

(10x2)-18C0 (8T-10B)			54.90	60.40	63.80	66.40	72.00
73.70	78.10	81.90	84.80	86.10	105.90	107.00	109.90
115.50	123.40	127.90	132.80	134.20	138.40	147.00	147.10
154.20	154.90	155.20	155.80	204.60	208.20	208.70	223.90
225.00	236.00	237.80	248.50	250.20	263.40	263.90	333.50
336.70	351.60	355.30	359.60	361.80	369.70	369.90	373.80
374.10	376.00	376.30	381.30	386.30	386.50	387.90	390.60
390.90	391.10	392.90	393.50	394.40	394.80	396.20	405.70
408.90	415.10	432.70	433.20	437.00	438.90	444.90	447.40
448.30	450.20	454.90	455.40	458.30	459.30	459.90	461.80
462.90	464.50	465.70	467.60	468.70	469.50	470.40	498.20
502.20	535.90	539.50	571.90	572.90	1842.00	1842.10	1853.50
1853.60	1855.00	1868.20	1872.10	1881.50	1888.90	1921.00	2020.50
2027.90	2034.60	2045.00	2051.20	2065.80	2069.90	2079.30	

(10x2)-18C0 (10T-8B)			64.20	66.60	68.30	71.50	72.50
77.30	81.40	87.40	90.60	92.00	95.00	100.90	115.30
118.20	119.00	124.80	126.00	129.70	136.70	140.30	140.60
142.70	145.20	148.00	149.70	151.20	159.90	160.30	223.10
223.60	235.00	235.30	250.80	251.10	258.10	258.40	345.40
347.90	350.90	354.10	357.10	358.40	359.30	361.20	371.40
371.90	382.30	382.90	383.10	383.30	383.80	384.50	386.90
387.80	388.10	389.70	390.30	392.10	394.30	395.90	396.70
396.90	407.00	407.50	433.50	435.00	437.20	439.20	447.60
448.00	448.50	449.40	454.30	454.90	459.90	460.30	460.70
460.90	462.90	463.90	466.20	467.50	469.00	469.10	479.80
481.50	518.50	519.90	561.80	562.00	1840.00	1840.20	1845.60
1845.80	1859.90	1860.20	1877.10	1877.80	2021.70	2022.90	2028.50
2033.70	2038.90	2050.40	2053.90	2069.10	2072.30	2083.00	

(10x2)-18C0 (12T-6B)			57.50	57.50	60.90	64.70	68.00
75.50	76.40	76.90	81.20	87.00	89.10	96.20	98.10
100.90	105.60	115.80	120.60	121.40	127.40	128.40	131.30
137.90	140.20	142.20	145.60	146.50	148.70	150.30	161.60
164.20	218.80	224.10	230.90	238.80	249.50	258.00	261.70
305.10	326.40	345.30	362.70	365.00	365.70	369.60	370.50
374.30	380.60	380.90	381.40	382.40	383.10	383.30	384.60
385.90	386.60	388.60	390.30	391.70	392.40	394.70	398.00

400.10	407.90	408.60	419.00	422.80	437.50	439.00	444.20
445.70	451.80	452.40	454.20	455.00	459.10	459.80	460.90
461.00	461.30	462.50	466.10	466.60	470.00	471.10	472.70
474.50	498.40	503.50	549.60	554.80	1832.00	1833.30	1842.90
1846.90	1862.70	1865.30	1968.80	1990.80	2006.20	2010.90	2026.00
2030.90	2034.60	2049.00	2051.10	2068.00	2072.00	2083.00	

## APPENDIX B

### Supplementary Information for Chapter 4

#### B.1 LEME structures data

##### B.1.1 Pt(553)

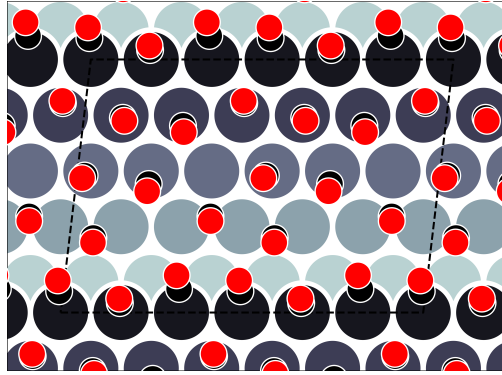


Figure B.1: CO orientation on Pt(553) at  $\theta = 0.65$  in the LEME structure

Data used to generate Fig. 4.5.

Table B.1: Pt(553) LEME structures data: Free energy per unit area ( $G/A$ ), Coverage of CO on the terrace top site ( $\theta_t(T)$ ), bridge site ( $\theta_t(B)$ ), hollow site ( $\theta_t(H)$ ) and on the step edge top site ( $\theta_e(T)$ ), bridge site ( $\theta_e(B)$ ), hollow site ( $\theta_e(H)$ ), total coverage of CO on the terrace ( $\theta_t$ ) and on the step edge ( $\theta_e$ ) and the surface area of the unit cell ( $A$ )

$G/A$ (eV/ $\text{\AA}^2$ )	$\theta_t(T)$	$\theta_t(B)$	$\theta_t(H)$	$\theta_e(T)$	$\theta_e(B)$	$\theta_e(H)$	$\theta_t$	$\theta_e$	$A(\text{\AA}^2)$
-0.0836	0.17	0	0.33	1	0	0	0.5	1	182.97
-0.0835	0.33	0	0.17	1	0	0	0.5	1	182.97

-0.0835	0.33	0	0.17	1	0	0	0.5	1	182.97
-0.0834	0.33	0	0.17	1	0	0	0.5	1	182.97
-0.0834	0.29	0	0.21	1	0	0	0.5	1	182.97
-0.0834	0.29	0	0.21	1	0	0	0.5	1	182.97
-0.0833	0.33	0	0.17	1	0	0	0.5	1	182.97
-0.0832	0.25	0.04	0.21	1	0	0	0.5	1	182.97
-0.0831	0.25	0	0.25	1	0	0	0.5	1	182.97
-0.083	0.29	0	0.21	1	0	0	0.5	1	182.97
-0.0827	0.33	0	0.17	1	0	0	0.5	1	182.97
-0.0826	0.29	0.04	0.17	1	0	0	0.5	1	182.97
-0.0826	0.33	0.04	0.13	1	0	0	0.5	1	182.97
-0.0825	0.25	0.17	0.08	1	0	0	0.5	1	182.97
-0.0825	0.08	0.17	0.25	1	0	0	0.5	1	182.97
-0.0824	0.21	0.04	0.25	1	0	0	0.5	1	182.97
-0.0823	0.38	0	0.13	1	0	0	0.5	1	182.97
-0.0821	0.25	0	0.25	1	0	0	0.5	1	182.97
-0.0821	0.21	0	0.29	1	0	0	0.5	1	182.97
-0.0821	0.33	0.08	0.08	1	0	0	0.5	1	182.97
-0.082	0.33	0.08	0.08	1	0	0	0.5	1	182.97
-0.082	0.38	0.08	0.08	1	0	0	0.54	1	182.97
-0.082	0.33	0	0.17	1	0	0	0.5	1	182.97
-0.082	0.08	0.25	0.17	1	0	0	0.5	1	182.97
-0.082	0.38	0.08	0.08	1	0	0	0.54	1	182.97
-0.0819	0.38	0.08	0.08	1	0	0	0.54	1	182.97
-0.0819	0.38	0.13	0.06	1	0	0	0.56	1	121.98
-0.0818	0.33	0	0.17	1	0	0	0.5	1	182.97

-0.0818	0.25	0.13	0.13	1	0	0	0.5	1	182.97
-0.0818	0.17	0.08	0.25	1	0	0	0.5	1	182.97
-0.0818	0.29	0.08	0.17	1	0	0	0.54	1	182.97
-0.0817	0.21	0.04	0.25	1	0	0	0.5	1	182.97
-0.0817	0.38	0	0.17	1	0	0	0.54	1	182.97
-0.0817	0.33	0.04	0.13	1	0	0	0.5	1	182.97
-0.0816	0.33	0.08	0.13	1	0	0	0.54	1	182.97
-0.0816	0.33	0.08	0.13	1	0	0	0.54	1	182.97
-0.0816	0.25	0.04	0.21	1	0	0	0.5	1	182.97
-0.0816	0.38	0.04	0.13	1	0	0	0.54	1	182.97
-0.0816	0.25	0.08	0.17	1	0	0	0.5	1	182.97
-0.0816	0.21	0.04	0.21	1	0	0	0.46	1	182.97
-0.0816	0.25	0.17	0.08	1	0	0	0.5	1	182.97
-0.0816	0.29	0.08	0.13	1	0	0	0.5	1	182.97
-0.0815	0.17	0.13	0.17	1	0	0	0.46	1	182.97
-0.0815	0.29	0.13	0.13	1	0	0	0.54	1	182.97
-0.0815	0.42	0.04	0.08	1	0	0	0.54	1	182.97
-0.0815	0.19	0	0.31	1	0	0	0.5	1	121.98
-0.0815	0.21	0.04	0.25	1	0	0	0.5	1	182.97
-0.0815	0.29	0.13	0.08	1	0	0	0.5	1	182.97
-0.0815	0.29	0.08	0.13	1	0	0	0.5	1	182.97
-0.0815	0.38	0	0.13	1	0	0	0.5	1	121.98
-0.0815	0.08	0.25	0.17	1	0	0	0.5	1	182.97
-0.0815	0.38	0.08	0.08	1	0	0	0.54	1	182.97
-0.0815	0.38	0.08	0.08	1	0	0	0.54	1	182.97
-0.0814	0.29	0	0.21	1	0	0	0.5	1	182.97

-0.0814	0.42	0	0.08	1	0	0	0.5	1	182.97
-0.0814	0.29	0.04	0.21	1	0	0	0.54	1	182.97
-0.0814	0.38	0	0.13	1	0	0	0.5	1	182.97
-0.0813	0.13	0.13	0.25	1	0	0	0.5	1	121.98
-0.0813	0.38	0.04	0.13	1	0	0	0.54	1	182.97
-0.0813	0.38	0.08	0.08	1	0	0	0.54	1	182.97
-0.0813	0.38	0.04	0.13	1	0	0	0.54	1	182.97
-0.0813	0.38	0.04	0.13	1	0	0	0.54	1	182.97
-0.0813	0.38	0.04	0.13	1	0	0	0.54	1	182.97
-0.0813	0.38	0.04	0.13	1	0	0	0.54	1	182.97
-0.0813	0.25	0.13	0.17	1	0	0	0.54	1	182.97
-0.0813	0.33	0.08	0.08	1	0	0	0.5	1	182.97
-0.0813	0.33	0.04	0.13	1	0	0	0.5	1	182.97
-0.0812	0.31	0.06	0.13	1	0	0	0.5	1	121.98
-0.0812	0.21	0.21	0.04	1	0	0	0.46	1	182.97
-0.0812	0.33	0.08	0.13	1	0	0	0.54	1	182.97
-0.0811	0.38	0.13	0.06	1	0	0	0.56	1	121.98
-0.0811	0.38	0.13	0.06	1	0	0	0.56	1	121.98
-0.0811	0.25	0.17	0.08	1	0	0	0.5	1	182.97
-0.0811	0.13	0.13	0.25	1	0	0	0.5	1	121.98
-0.0811	0.38	0.08	0.08	1	0	0	0.54	1	182.97
-0.0811	0.42	0	0.13	1	0	0	0.54	1	182.97
-0.0811	0.42	0	0.13	1	0	0	0.54	1	182.97
-0.0811	0.25	0.17	0.08	1	0	0	0.5	1	182.97
-0.0811	0.21	0.13	0.17	1	0	0	0.5	1	182.97
-0.0811	0.33	0.13	0.08	1	0	0	0.54	1	182.97
-0.081	0.33	0.13	0.08	1	0	0	0.54	1	182.97



-0.081	0.25	0.04	0.21	1	0	0	0.5	1	182.97
-0.081	0.29	0.13	0.08	1	0	0	0.5	1	182.97
-0.081	0.13	0.19	0.19	1	0	0	0.5	1	121.98
-0.081	0.42	0.04	0.08	1	0	0	0.54	1	182.97
-0.081	0.25	0.08	0.17	1	0	0	0.5	1	182.97
-0.081	0.33	0.08	0.08	1	0	0	0.5	1	182.97
-0.081	0.38	0.08	0.08	1	0	0	0.54	1	182.97
-0.081	0.42	0.04	0.08	1	0	0	0.54	1	182.97
-0.081	0.38	0.08	0.08	1	0	0	0.54	1	182.97
-0.081	0.38	0.04	0.13	1	0	0	0.54	1	182.97
-0.081	0.38	0.08	0.08	1	0	0	0.54	1	182.97
-0.0809	0.33	0.08	0.13	1	0	0	0.54	1	182.97
-0.0809	0.42	0.08	0.08	1	0	0	0.58	1	182.97
-0.0809	0.42	0.08	0.08	1	0	0	0.58	1	182.97
-0.0809	0.42	0.08	0.04	1	0	0	0.54	1	182.97
-0.0809	0.44	0.06	0.06	1	0	0	0.56	1	121.98
-0.0809	0.29	0.08	0.17	1	0	0	0.54	1	182.97

### B.1.2 Pt(557)

Data used to generate Fig. Fig. 4.7.

Table B.2: Pt(557) LEME structures data: Free energy per unit area (G/A), Coverage of CO on the terrace top site ( $\theta_t(\text{T})$ ), bridge site ( $\theta_t(\text{B})$ ), hollow site ( $\theta_t(\text{H})$ ) and on the step edge top site ( $\theta_e(\text{T})$ ), bridge site ( $\theta_e(\text{B})$ ), hollow site ( $\theta_e(\text{H})$ ), total coverage of CO on the terrace ( $\theta_t$ ) and on the step edge ( $\theta_e$ ) and the surface area of the unit cell (A)

G/A (eV/Å <sup>2</sup> )	$\theta_t(\text{T})$	$\theta_t(\text{B})$	$\theta_t(\text{H})$	$\theta_e(\text{T})$	$\theta_e(\text{B})$	$\theta_e(\text{H})$	$\theta_t$	$\theta_e$	A(Å <sup>2</sup> )
-0.0801	0.27	0	0.33	1	0	0	0.6	1	118.5

-0.08	0.2	0.03	0.37	1	0.17	0	0.58	1.08	237.01
-0.0799	0.2	0	0.4	1	0	0	0.6	1	237.01
-0.0799	0.2	0.1	0.3	1	0.33	0	0.57	1.17	237.01
-0.0799	0.2	0.1	0.3	1	0.33	0	0.57	1.17	237.01
-0.0797	0.2	0.03	0.37	1	0.17	0	0.58	1.08	237.01
-0.0797	0.23	0	0.37	1	0	0	0.6	1	237.01
-0.0797	0.23	0	0.37	1	0	0	0.6	1	237.01
-0.0797	0.23	0.03	0.33	1	0.17	0	0.58	1.08	237.01
-0.0794	0.2	0.2	0.2	1	0.5	0	0.55	1.25	237.01
-0.0793	0.27	0.07	0.27	1	0.33	0	0.57	1.17	118.5
-0.0793	0.17	0.07	0.37	1	0.33	0	0.57	1.17	237.01
-0.0792	0.2	0	0.4	1	0	0	0.6	1	118.5
-0.0792	0.27	0	0.33	1	0	0	0.6	1	237.01
-0.0792	0.2	0	0.4	1	0	0	0.6	1	118.5
-0.0791	0.2	0.07	0.33	1	0.33	0	0.57	1.17	118.5
-0.0791	0.2	0.07	0.33	1	0.33	0	0.57	1.17	118.5
-0.0791	0.2	0.07	0.3	1	0.17	0	0.55	1.08	237.01
-0.0791	0.2	0.03	0.33	1	0	0	0.57	1	237.01
-0.079	0.27	0	0.33	1	0	0	0.6	1	118.5
-0.079	0.27	0.07	0.27	1	0.33	0	0.57	1.17	118.5
-0.079	0.27	0.03	0.27	1	0	0	0.57	1	237.01
-0.079	0.2	0.07	0.3	1	0.17	0	0.55	1.08	237.01
-0.0789	0.2	0.07	0.3	1	0.17	0	0.55	1.08	237.01
-0.0789	0.27	0	0.33	1	0	0	0.6	1	118.5
-0.0789	0.17	0.07	0.33	1	0.17	0	0.55	1.08	237.01
-0.0788	0.2	0.03	0.33	1	0	0	0.57	1	237.01

-0.0788	0.2	0.1	0.27	1	0.33	0	0.53	1.17	237.01
-0.0788	0.2	0.03	0.33	1	0	0	0.57	1	237.01
-0.0787	0.23	0.03	0.3	1	0.17	0	0.55	1.08	237.01
-0.0787	0.2	0.1	0.27	1	0.33	0	0.53	1.17	237.01
-0.0787	0.2	0	0.4	1	0	0	0.6	1	118.5
-0.0787	0.2	0	0.4	1	0	0	0.6	1	118.5
-0.0787	0.27	0.07	0.27	1	0.33	0	0.57	1.17	118.5
-0.0787	0.2	0.07	0.3	1	0.17	0	0.55	1.08	237.01
-0.0787	0.2	0.07	0.33	1	0.33	0	0.57	1.17	118.5
-0.0787	0.2	0.07	0.33	1	0.33	0	0.57	1.17	118.5
-0.0787	0.2	0.03	0.33	1	0	0	0.57	1	237.01
-0.0787	0.17	0.07	0.33	1	0	0	0.57	1	237.01
-0.0786	0.2	0.07	0.3	1	0.17	0	0.55	1.08	237.01
-0.0786	0.27	0.07	0.27	1	0	0	0.6	1	118.5
-0.0786	0.27	0.13	0.2	1	0.33	0	0.57	1.17	118.5
-0.0786	0.27	0	0.33	1	0	0	0.6	1	118.5
-0.0786	0.27	0	0.33	1	0	0	0.6	1	118.5
-0.0786	0.2	0.03	0.33	1	0.17	0	0.55	1.08	237.01
-0.0786	0.2	0	0.43	1	0	0	0.63	1	237.01
-0.0785	0.27	0.07	0.27	1	0	0	0.6	1	118.5
-0.0785	0.23	0	0.33	1	0	0	0.57	1	237.01
-0.0785	0.27	0	0.3	1	0	0	0.57	1	237.01
-0.0785	0.2	0.07	0.33	1	0	0	0.6	1	118.5
-0.0785	0.2	0.07	0.33	1	0	0	0.6	1	118.5
-0.0785	0.2	0.07	0.3	1	0.17	0	0.55	1.08	237.01
-0.0785	0.2	0.07	0.33	1	0.33	0	0.57	1.17	118.5

-0.0785	0.2	0.03	0.33	1	0	0	0.57	1	237.01
-0.0785	0.2	0.07	0.33	1	0.33	0	0.57	1.17	118.5
-0.0785	0.2	0.13	0.27	1	0.33	0	0.57	1.17	118.5
-0.0785	0.17	0.07	0.33	1	0	0	0.57	1	237.01
-0.0784	0.17	0.1	0.3	1	0.17	0	0.55	1.08	237.01
-0.0784	0.2	0.07	0.3	1	0.17	0	0.55	1.08	237.01
-0.0784	0.2	0.1	0.27	1	0.17	0	0.55	1.08	237.01
-0.0784	0.2	0.03	0.33	1	0	0	0.57	1	237.01
-0.0784	0.27	0.03	0.27	1	0.17	0	0.55	1.08	237.01
-0.0784	0.23	0	0.33	1	0	0	0.57	1	237.01
-0.0784	0.2	0.07	0.3	1	0.17	0	0.55	1.08	237.01
-0.0784	0.17	0.1	0.3	1	0.17	0	0.55	1.08	237.01
-0.0784	0.2	0.03	0.33	1	0	0	0.57	1	237.01
-0.0784	0.2	0.07	0.3	1	0	0	0.57	1	237.01
-0.0783	0.2	0.03	0.33	1	0.17	0	0.55	1.08	237.01
-0.0783	0.2	0.07	0.33	1	0	0	0.6	1	118.5
-0.0783	0.23	0.03	0.3	1	0	0	0.57	1	237.01
-0.0783	0.2	0.1	0.25	1	0	0	0.55	1	158.01
-0.0783	0.2	0.07	0.3	1	0	0	0.57	1	237.01
-0.0783	0.17	0.1	0.3	1	0.33	0	0.53	1.17	237.01
-0.0783	0.2	0.07	0.3	1	0.33	0	0.53	1.17	237.01
-0.0783	0.25	0.05	0.25	1	0	0	0.55	1	158.01
-0.0782	0.2	0.1	0.27	1	0.33	0	0.53	1.17	237.01
-0.0782	0.27	0	0.3	1	0	0	0.57	1	237.01
-0.0782	0.23	0	0.33	1	0	0	0.57	1	237.01
-0.0782	0.15	0.05	0.35	1	0	0	0.55	1	158.01

-0.0782	0.15	0.1	0.3	1	0.25	0	0.53	1.13	158.01
-0.0782	0.2	0.03	0.33	1	0	0	0.57	1	237.01
-0.0781	0.27	0.07	0.27	1	0.33	0	0.57	1.17	118.5
-0.0781	0.27	0.07	0.23	1	0	0	0.57	1	237.01
-0.0781	0.2	0.1	0.25	1	0.25	0	0.53	1.13	158.01
-0.0781	0.27	0.03	0.27	1	0	0	0.57	1	237.01
-0.0781	0.2	0.13	0.27	1	0.33	0	0.57	1.17	118.5
-0.0781	0.2	0.05	0.3	1	0.25	0	0.53	1.13	158.01
-0.0781	0.2	0.13	0.27	1	0.33	0	0.57	1.17	118.5
-0.0781	0.17	0.1	0.3	1	0.33	0	0.53	1.17	237.01
-0.0781	0.23	0.03	0.3	1	0.17	0	0.55	1.08	237.01
-0.0781	0.23	0	0.4	1	0	0	0.63	1	237.01
-0.078	0.13	0.1	0.33	1	0.17	0	0.55	1.08	237.01
-0.078	0.27	0.27	0.07	1	0.33	0	0.57	1.17	118.5
-0.078	0.23	0.03	0.37	1	0.17	0	0.62	1.08	237.01
-0.078	0.2	0	0.35	1	0	0	0.55	1	158.01
-0.078	0.2	0.07	0.3	1	0.17	0	0.55	1.08	237.01
-0.078	0.17	0.1	0.3	1	0.17	0	0.55	1.08	237.01
-0.078	0.2	0.2	0.2	1	0.33	0	0.57	1.17	118.5
-0.078	0.2	0.07	0.3	1	0.17	0	0.55	1.08	237.01
-0.078	0.17	0.1	0.3	1	0.17	0	0.55	1.08	237.01
-0.0779	0.2	0.05	0.3	1	0	0	0.55	1	158.01
-0.0779	0.2	0.03	0.33	1	0.17	0	0.55	1.08	237.01
-0.0779	0.2	0	0.37	1	0	0	0.57	1	237.01
-0.0779	0.17	0.03	0.37	1	0.17	0	0.55	1.08	237.01
-0.0779	0.17	0.23	0.17	1	0.5	0	0.52	1.25	237.01

-0.0779	0.17	0.07	0.33	1	0.17	0	0.55	1.08	237.01
-0.0779	0.2	0.03	0.33	1	0.17	0	0.55	1.08	237.01
-0.0779	0.2	0.1	0.25	1	0.25	0	0.53	1.13	158.01
-0.0779	0.27	0.07	0.2	1	0	0	0.53	1	118.5
-0.0779	0.33	0	0.27	1	0	0	0.6	1	118.5
-0.0778	0.27	0	0.27	1	0	0	0.53	1	118.5
-0.0778	0.27	0.07	0.27	1	0	0	0.6	1	118.5
-0.0778	0.2	0.05	0.3	1	0	0	0.55	1	158.01
-0.0778	0.2	0.1	0.25	1	0.25	0	0.53	1.13	158.01
-0.0778	0.25	0	0.3	1	0	0	0.55	1	158.01
-0.0778	0.2	0.13	0.2	1	0	0	0.53	1	118.5
-0.0778	0.27	0.07	0.23	1	0.17	0	0.55	1.08	237.01
-0.0778	0.2	0	0.43	1	0	0	0.63	1	237.01
-0.0778	0.13	0.2	0.2	1	0.33	0	0.5	1.17	118.5
-0.0777	0.27	0.13	0.27	1	0.33	0	0.63	1.17	118.5
-0.0777	0.27	0.13	0.27	1	0.33	0	0.63	1.17	118.5
-0.0777	0.27	0.07	0.23	1	0	0	0.57	1	237.01
-0.0777	0.2	0.03	0.37	1	0.17	0	0.58	1.08	237.01
-0.0777	0.2	0	0.4	1	0	0	0.6	1	118.5
-0.0777	0.4	0	0.2	1	0	0	0.6	1	118.5
-0.0777	0.17	0.07	0.33	1	0	0	0.57	1	237.01
-0.0777	0.2	0.03	0.4	1	0.17	0	0.62	1.08	237.01
-0.0777	0.2	0.07	0.33	1	0.33	0	0.57	1.17	118.5
-0.0776	0.23	0.03	0.3	1	0.17	0	0.55	1.08	237.01
-0.0776	0.27	0.13	0.27	1	0.33	0	0.63	1.17	118.5
-0.0776	0.27	0.13	0.2	1	0.33	0	0.57	1.17	118.5

-0.0776	0.33	0	0.27	1	0	0	0.6	1	118.5
-0.0775	0.27	0.13	0.2	1	0.33	0	0.57	1.17	118.5
-0.0775	0.47	0	0.13	1	0	0	0.6	1	118.5
-0.0775	0.27	0.2	0.2	1	0.33	0	0.63	1.17	118.5
-0.0775	0.13	0.2	0.27	1	0.33	0	0.57	1.17	118.5
-0.0775	0.27	0.13	0.2	1	0.33	0	0.57	1.17	118.5
-0.0774	0.27	0.07	0.33	1	0.33	0	0.63	1.17	118.5
-0.0774	0.2	0	0.45	1	0	0	0.65	1	158.01
-0.0774	0.2	0.03	0.4	1	0.17	0	0.62	1.08	237.01
-0.0774	0.37	0	0.3	1	0	0	0.67	1	237.01
-0.0774	0.27	0.27	0.13	1	0.33	0	0.63	1.17	118.5
-0.0773	0.27	0.13	0.27	1	0.33	0	0.63	1.17	118.5

### B.1.3 Pt(643)

Data used to generate Fig. 4.9

Table B.3: Pt(643) LEME structures data: Free energy per unit area (G/A), Coverage of CO on the terrace top site ( $\theta_t(\text{T})$ ), bridge site ( $\theta_t(\text{B})$ ), hollow site ( $\theta_t(\text{H})$ ) and on the step edge top site ( $\theta_e(\text{T})$ ), bridge site ( $\theta_e(\text{B})$ ), hollow site ( $\theta_e(\text{H})$ ), total coverage of CO on the terrace ( $\theta_t$ ) and on the step edge ( $\theta_e$ ) and the surface area of the unit cell (A)

G/A (eV/Å <sup>2</sup> )	$\theta_t(\text{T})$	$\theta_t(\text{B})$	$\theta_t(\text{H})$	$\theta_e(\text{T})$	$\theta_e(\text{B})$	$\theta_e(\text{H})$	$\theta_t$	$\theta_e$
-0.0845	0.29	0.00	0.14	1.00	0.00	0.00	0.43	1.00
-0.0843	0.14	0.07	0.14	1.00	0.00	0.00	0.36	1.00
-0.0839	0.21	0.00	0.14	1.00	0.00	0.00	0.36	1.00
-0.0838	0.14	0.07	0.14	1.00	0.00	0.00	0.36	1.00
-0.0837	0.14	0.07	0.07	1.00	0.00	0.00	0.29	1.00
-0.0836	0.00	0.07	0.29	1.00	0.00	0.00	0.36	1.00

-0.0835	0.14	0.00	0.21	1.00	0.00	0.00	0.36	1.00
-0.0835	0.14	0.00	0.21	1.00	0.00	0.00	0.36	1.00
-0.0834	0.14	0.07	0.14	1.00	0.00	0.00	0.36	1.00
-0.0834	0.14	0.00	0.29	0.83	0.00	0.00	0.43	0.83
-0.0831	0.21	0.00	0.21	0.83	0.00	0.00	0.43	0.83
-0.0831	0.29	0.00	0.07	1.00	0.00	0.00	0.36	1.00
-0.0830	0.00	0.00	0.36	1.00	0.00	0.00	0.36	1.00
-0.0829	0.14	0.21	0.07	1.00	0.00	0.00	0.43	1.00
-0.0829	0.07	0.07	0.21	1.00	0.00	0.00	0.36	1.00
-0.0826	0.29	0.07	0.14	0.83	0.00	0.00	0.50	0.83
-0.0825	0.21	0.00	0.14	1.00	0.00	0.00	0.36	1.00
-0.0824	0.14	0.07	0.07	0.83	0.17	0.00	0.29	1.00
-0.0821	0.21	0.07	0.14	0.83	0.17	0.00	0.43	1.00
-0.0819	0.36	0.21	0.00	0.83	0.00	0.00	0.57	0.83



## B.2 CO-Surface vs CO-CO lateral interaction

### B.2.1 CO-Surface Interaction

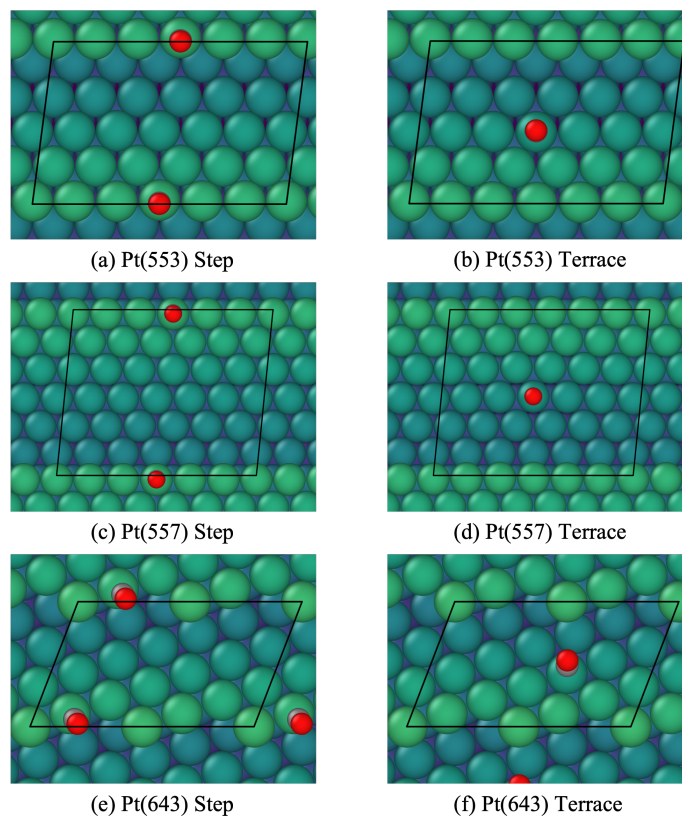


Figure B.2: Configurations used to compare adsorption energy of CO on step edge and the terrace.

Table B.4: Comparison the adsorption energy of CO on the step edge and the terrace.

	Step (eV)	Terrace (eV)
Pt(553)	-1.84	-1.21
Pt(557)	-1.85	-1.33
Pt(643)	-1.81	-1.25

## B.3 Neural Network Evaluation

### B.3.1 Pt(553)

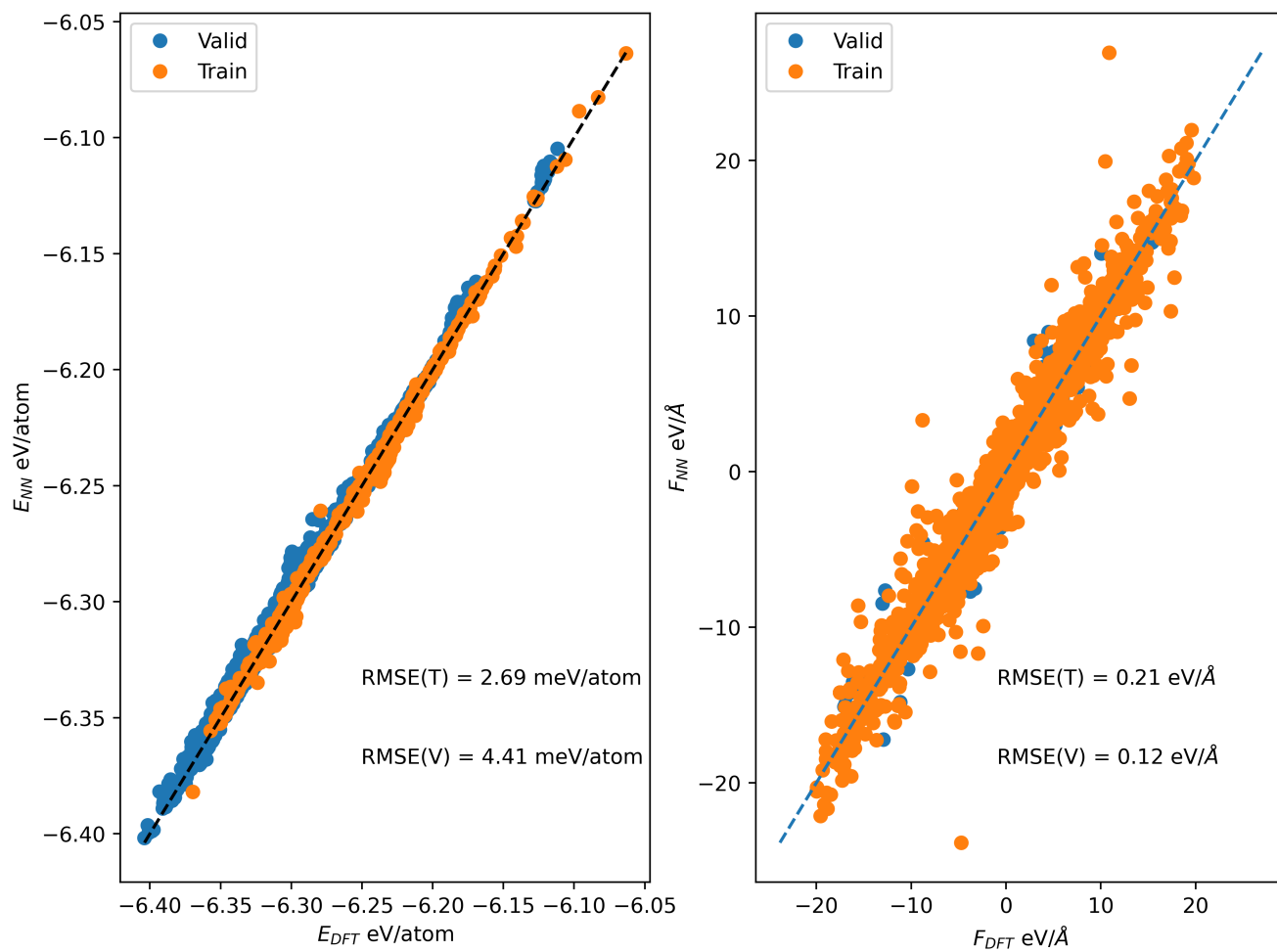


Figure B.3: Parity plot comparing the reference DFT energies and forces with the neural network estimates for Pt(553)

### B.3.2 Pt(557)

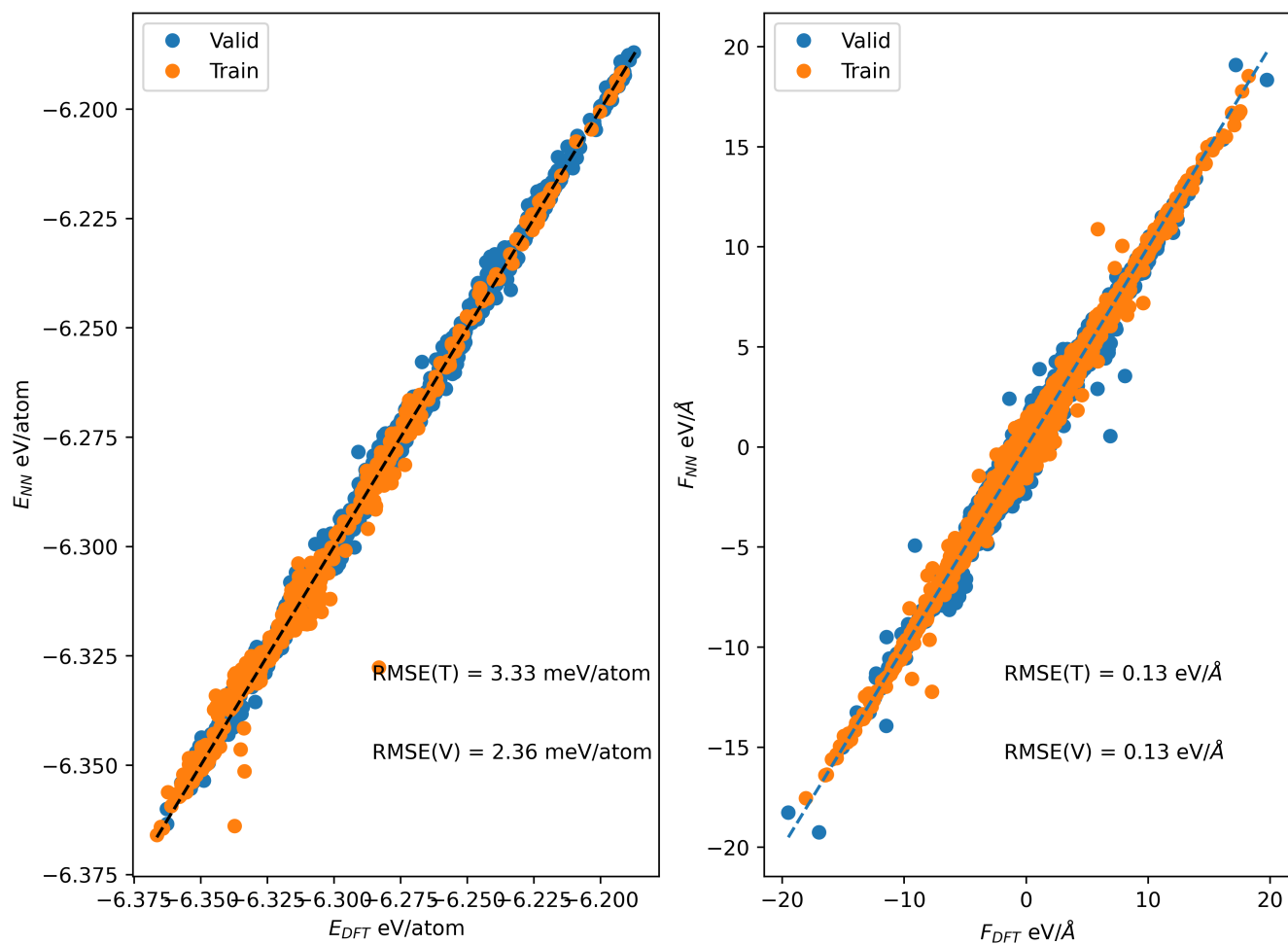


Figure B.4: Parity plot comparing the reference DFT energies and forces with the neural network estimates for Pt(557)

### B.3.3 Pt(643)

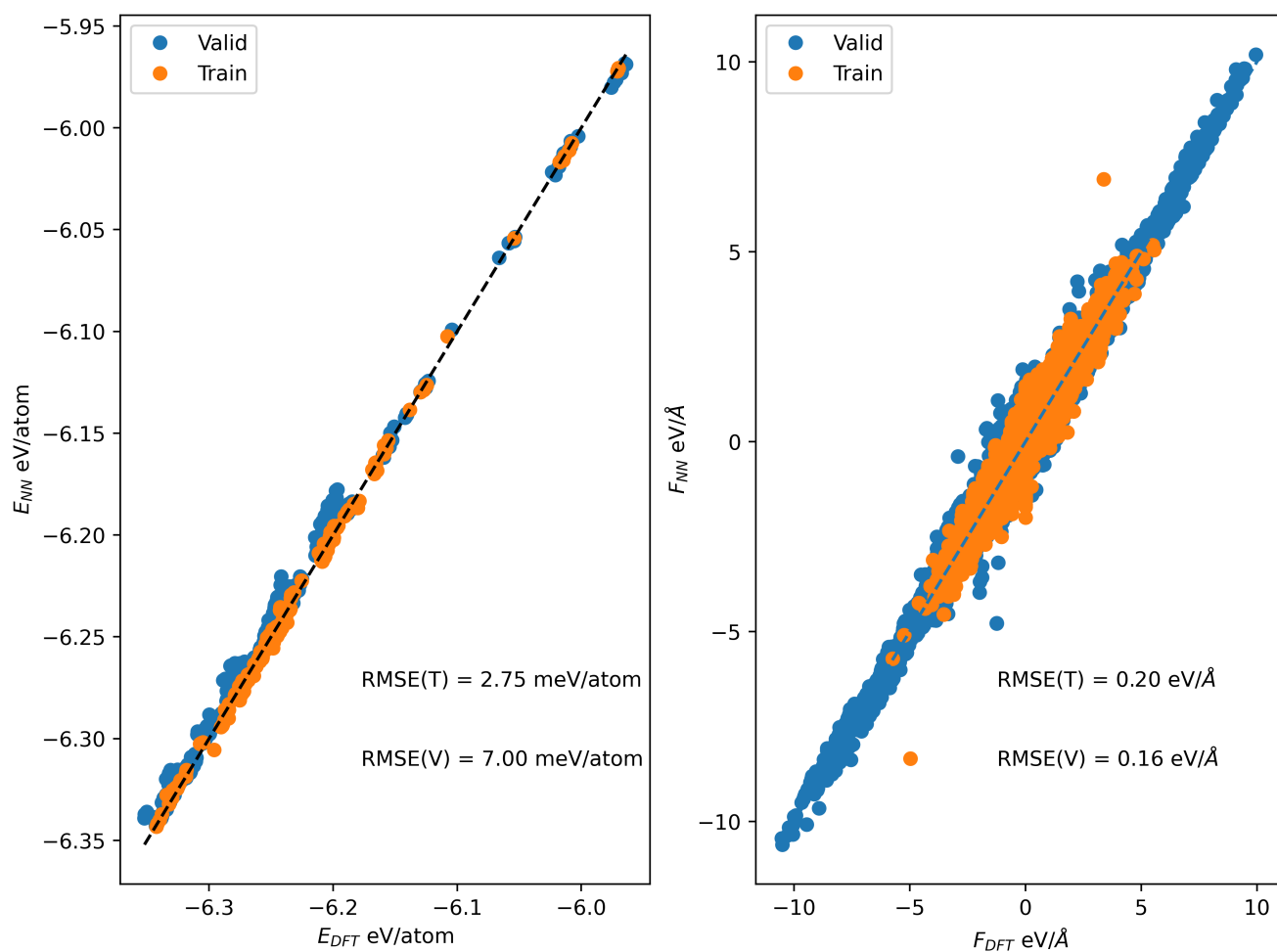


Figure B.5: Parity plot comparing the reference DFT energies and forces with the neural network estimates for Pt(643)

### B.3.4 Pt(111)

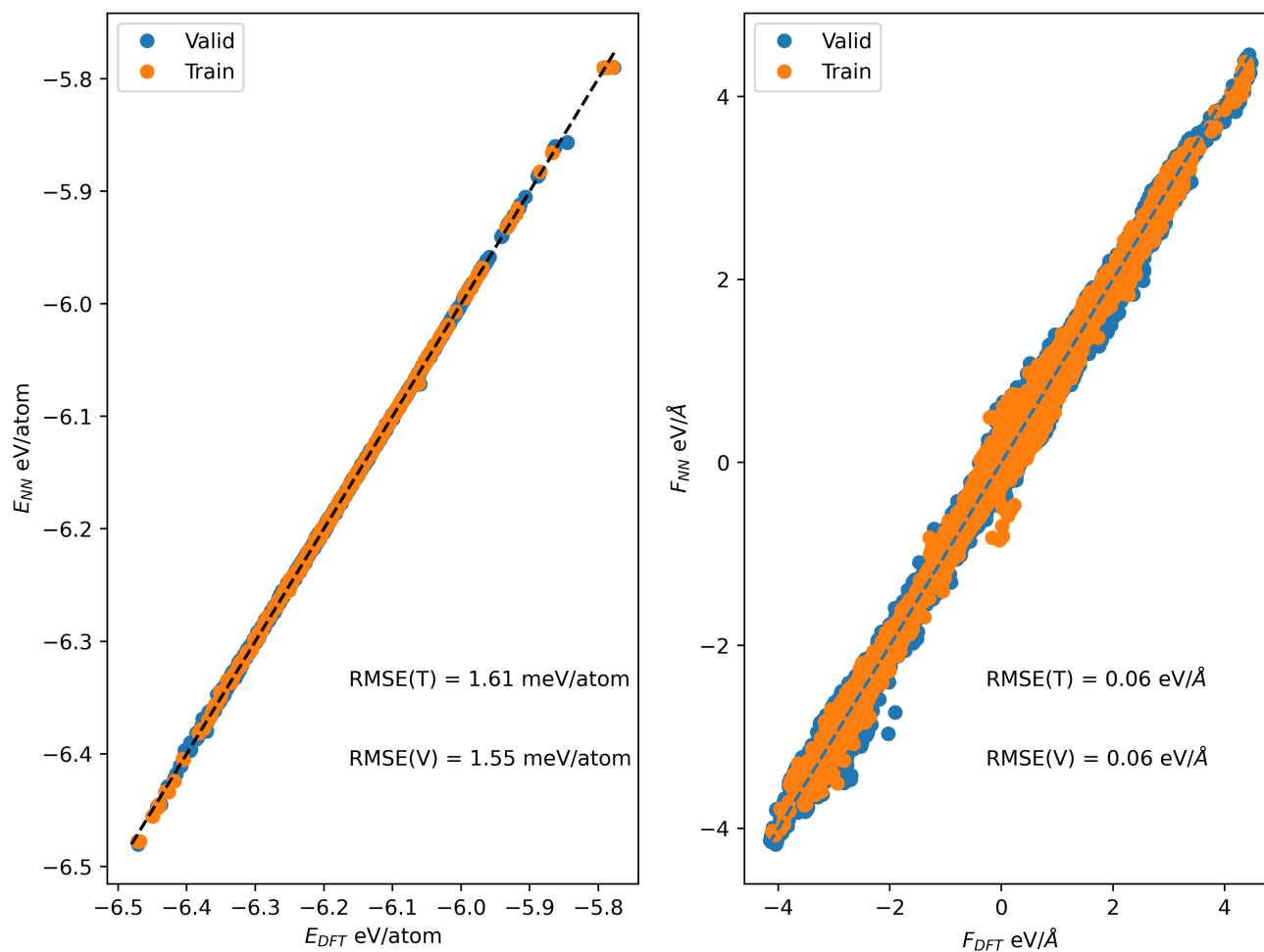


Figure B.6: Parity plot comparing the reference DFT energies and forces with the neural network estimates for Pt(111)

### B.3.5 Low Coordination adsorption sites

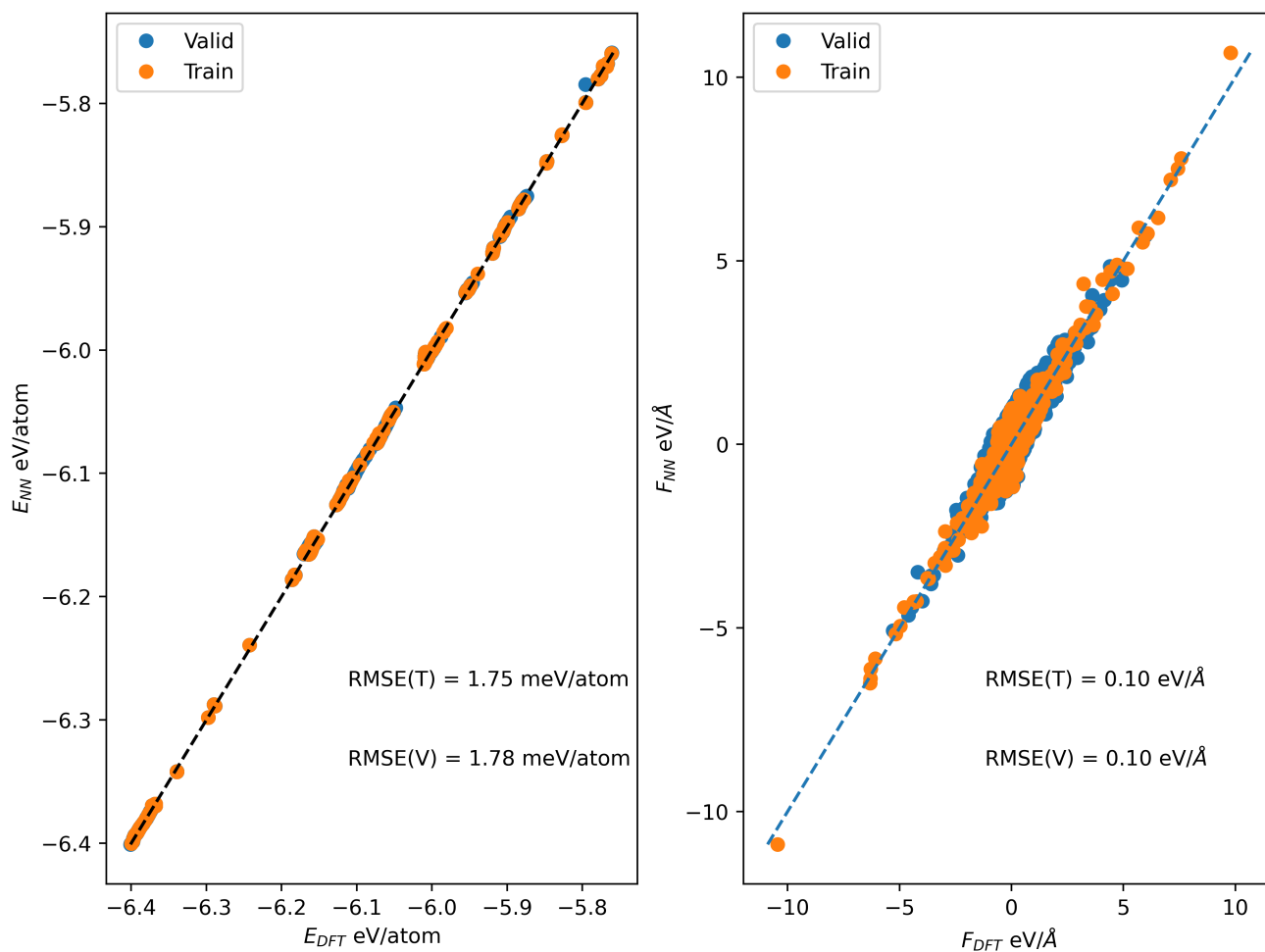


Figure B.7: Parity plot comparing the reference DFT energies and forces with the neural network estimates for structures with low coordination adsorption sites

## APPENDIX C

### Supplementary Information for Chapter 5

#### C.1 Stepped Surfaces

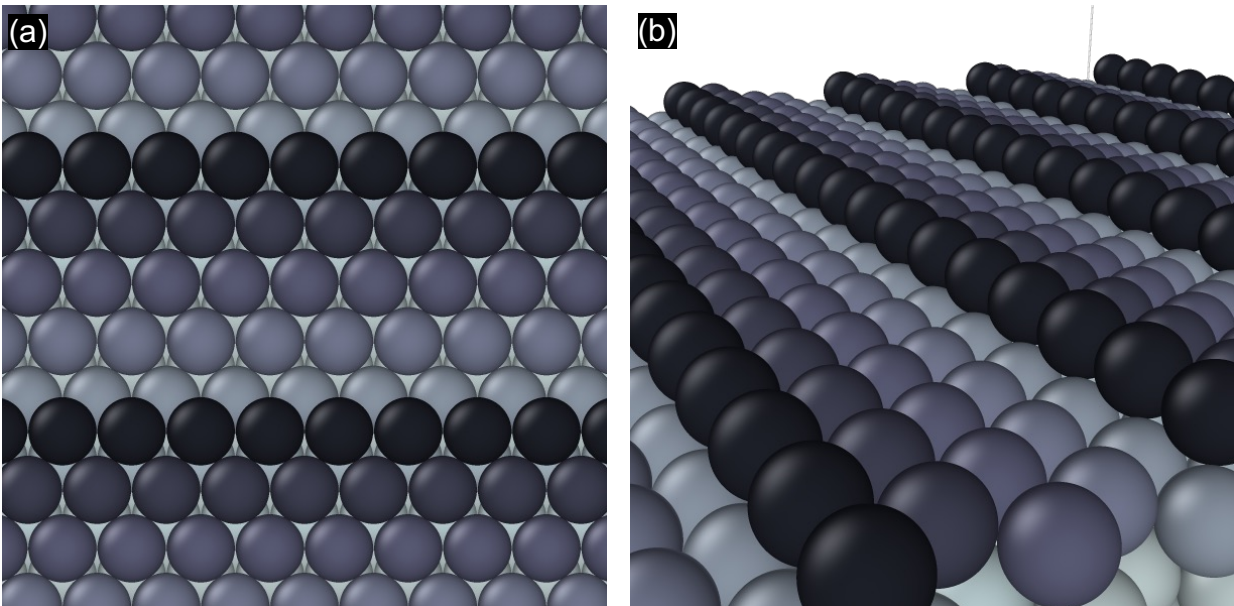


Figure C.1: Model showing clean Pt(553) surface with (111) terraced and (111) type steps. (a) Top view, (b) Side view

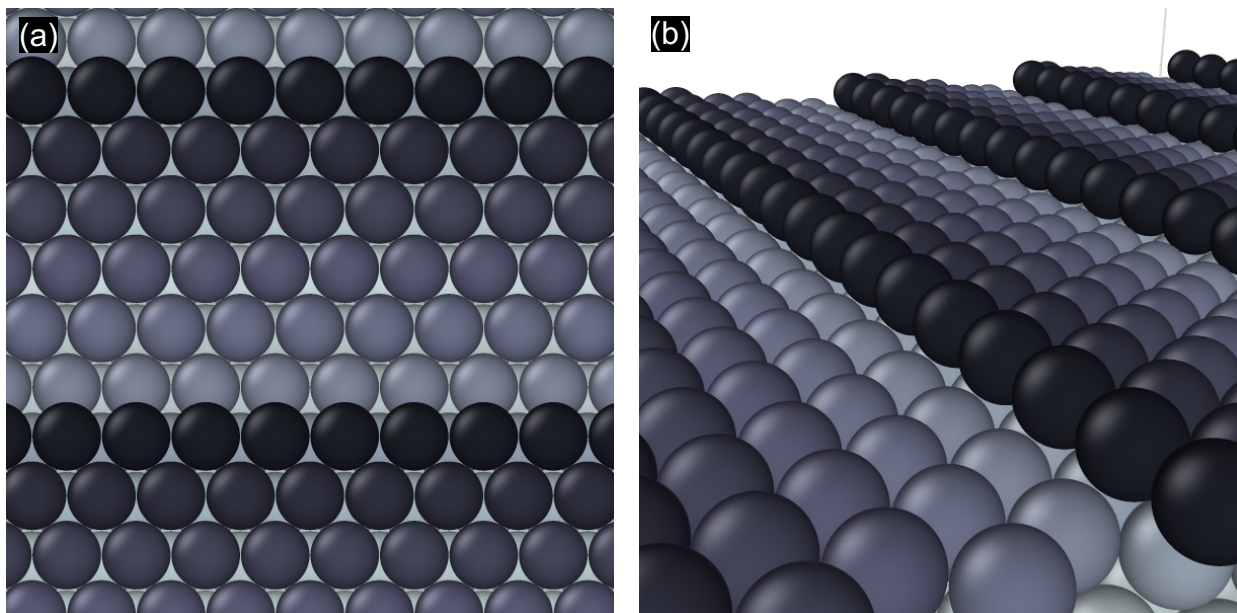


Figure C.2: Model showing clean Pt(557) surface with (111) terraced and (100) type steps. (a) Top view, (b) Side view

## C.2 STM images

Fig. C.3 shows the STM image of Pt(111) in Ultra High Vacuum (UHV) conditions ( $5 \times 10^{-8}$  Torr of CO). The width of terrace is in the range of 10-30 nm with the step height typically one atomic layer.

## C.3 Methods

### C.3.1 Density Functional Theory Calculations

Calculations were performed using the Vienna Ab-initio Simulation Package<sup>253-256</sup> using the general gradient approximation (GGA) Perdew-Burke-Erzenhof (PBE) functional.<sup>257</sup> Core electrons were described using the projector augmented wave potentials.<sup>258,259</sup> A k-spacing of 0.25 is used for all the calculations and the generated k-point grid is centered at the  $\Gamma$  point. Periodic slabs of Pt surface with CO are separated by 12 Å vacuum in the z direction.



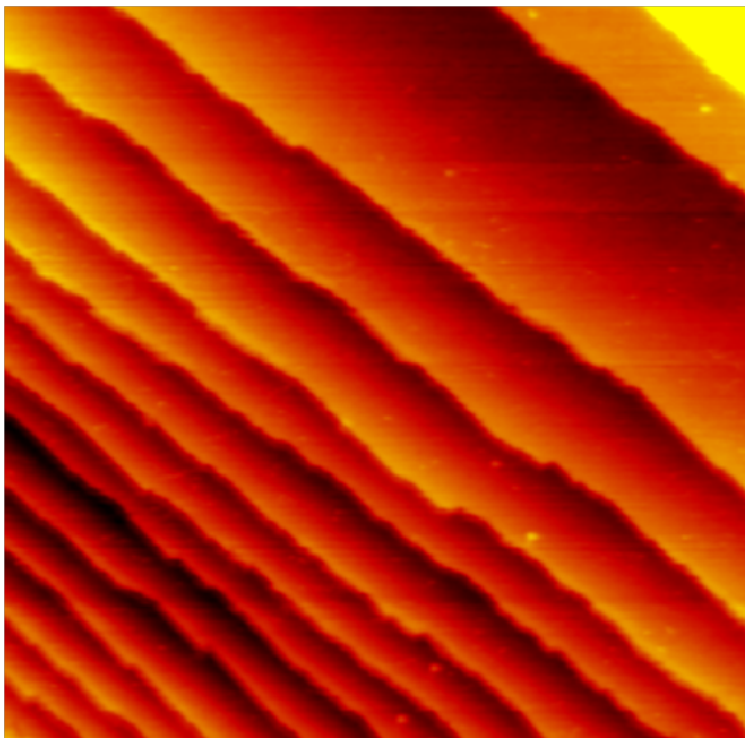


Figure C.3: Pt(111) in  $5 \times 10^{-8}$  Torr CO. Size: 100 nm x 100 nm.

A fermi smearing width of 0.2 eV was applied using the Methfessel-Paxton method (order 2). A cutoff energy of 400 eV is used. The known issue of over-binding of CO on Pt surfaces (“Pt(111)/CO Puzzle”) has been corrected using the CO bond distance-based correction developed by us.<sup>225</sup> The generalized correction is given as  $\Delta = 4.77 * d_{CO} - 5.37$ , where  $\Delta$  is the correction applied in (eV) and  $d_{CO}$  is the bond length of adsorbed CO in ( $\text{\AA}$ ).

### C.3.1.1 Symmetry Functions for High-Dimensional Neural Network Potential

The symmetry function (radial  $G^{rad}$  and angular  $G^{ang}$ ) hyper-parameters  $\eta$  and  $\mu$  defining the width and position of the Gaussian functions are determined automatically using the scheme described by Gastegger et al. (using N=6) and  $\lambda=[-1, 1]$ ,  $\zeta=[1, 4, 16]$  are chosen for descriptor generation..<sup>206</sup> This generates 14 G2 radial symmetry functions and 48 angular G3 symmetry functions for each element.

Table C.1: Symmetry functions used for HDNNP input layer generation

Radial			Angular			
$\eta$	$R_s$	$R_c$	$\eta$	$\lambda$	$\zeta$	$R_c$
0.0204	0	7	0.0204	-1	1	7
0.0356	0	7	0.0204	1	1	7
0.062	0	7	0.0204	-1	4	7
0.1082	0	7	0.0204	1	4	7
0.1886	0	7	0.0204	-1	16	7
0.3289	0	7	0.0204	1	16	7
0.5735	0	7	0.0356	-1	1	7
1	0	7	0.0356	1	1	7
6.0664	1.1667	7	0.0356	-1	4	7
3.3385	1.5727	7	0.0356	1	4	7
1.8372	2.12	7	0.0356	-1	16	7
1.0111	2.8577	7	0.0356	1	16	7
0.5564	3.8522	7	0.062	-1	1	7
0.3062	5.1929	7	0.062	1	1	7
			0.062	-1	4	7
			0.062	1	4	7
			0.062	-1	16	7
			0.062	1	16	7
			0.1082	-1	1	7
			49	1	1	7
			0.1082	-1	4	7
			0.1082	1	4	7
			0.1082	-1	16	7

			0.1082	1	16	7
			0.1886	-1	1	7
			0.1886	1	1	7
			0.1886	-1	4	7
			0.1886	1	4	7
			0.1886	-1	16	7
			0.1886	1	16	7
			0.3289	-1	1	7
			0.3289	1	1	7
			0.3289	-1	4	7
			0.3289	1	4	7
			0.3289	-1	16	7
			0.3289	1	16	7
			0.5735	-1	1	7
			0.5735	1	1	7
			0.5735	-1	4	7
			0.5735	1	4	7
			0.5735	-1	16	7
			0.5735	1	16	7
			1	-1	1	7
			1	1	1	7
			1	-1	4	7
			1	1	4	7
			1	-1	16	7
			1	1	16	7

### C.3.1.2 HDNNP Accuracy

The accuracy of HDNNP is represented by the energy and force prediction error with respect to the reference DFT data for both training and validation data. This is plotted as a parity plot show in Fig. C.4. We also show a histogram of energy errors showing the distribution of errors (Fig. C.5). 87.58% of training data and 84.75% of validation data have error below 1 meV/atoms. And, 97.12% of training data and 96.55% of validation data have error below 2 meV/atoms.

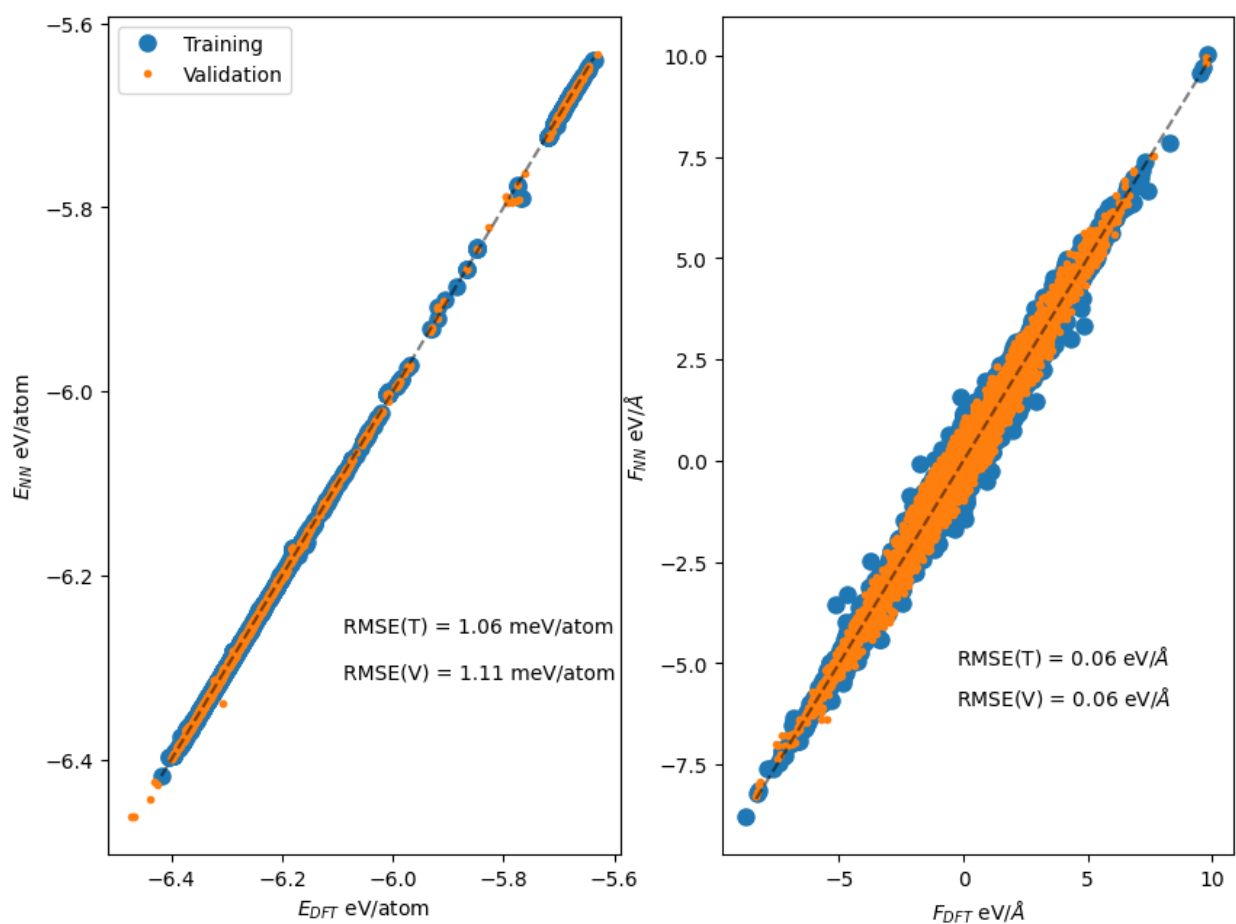


Figure C.4: Parity plot showing the training (6153 structures) and validation (13379 structures) data.

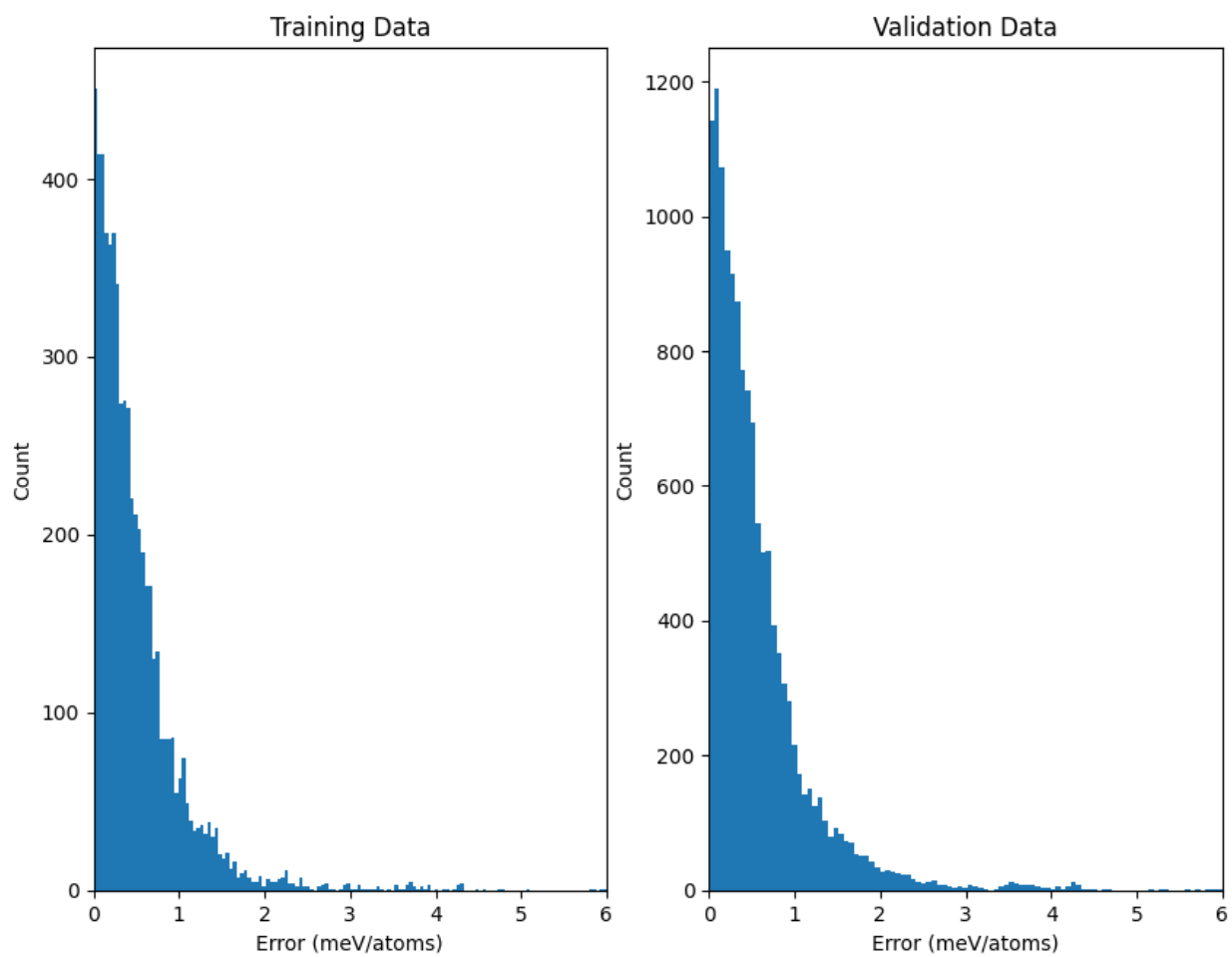


Figure C.5: HDNNP accuracy: Energy Error histogram.

## C.4 Effect of Pressure

### C.4.1 Pt(553)

Table C.2:  $\Delta E_{rec}$  separated into  $\Delta E_{metal}$  and  $\Delta E_{chem}$  at different CO pressures for various reconstruction models studied for Pt(553)

Pressure (Torr)		Step Wandering			Step atom extraction			Islands with NR step		
		1 at.	2 at.	3 at.	1 at.	2 at.	3 at.	1 at.	2 at.	3 at.
450	$\Delta E_{metal}$	0.91	1.10	1.66	1.71	2.69	3.70	1.30	2.41	2.97
	$\Delta E_{chem}$	-0.59	-0.59	-1.59	-1.04	-2.10	-2.71	-0.66	-1.94	-2.52
	$\Delta E_{rec}$	0.32	0.51	0.07	0.67	0.59	0.99	0.64	0.47	0.45
0.5	$\Delta E_{metal}$	0.91	1.10	1.66	1.71	2.69	3.70	1.30	2.41	2.97
	$\Delta E_{chem}$	-0.67	-0.68	-1.50	-1.04	-2.01	-2.70	-0.71	-1.85	-2.28
	$\Delta E_{rec}$	0.24	0.42	0.16	0.67	0.68	1.00	0.59	0.56	0.69
0.0007	$\Delta E_{metal}$	0.91	1.10	1.66	1.71	2.69	3.70	1.30	2.41	2.97
	$\Delta E_{chem}$	-0.74	-0.66	-1.36	-1.01	-1.85	-2.70	-0.53	-1.53	-2.21
	$\Delta E_{rec}$	0.17	0.44	0.30	0.70	0.84	1.00	0.77	0.88	0.76

Table C.3: Number of CO per unit cell on Pt(553) at different CO pressure and considered reconstruction models (SW - Step Wandering, SE - Step atoms Extraction, NR - Islands with NR step)

Structure	Pressure (Torr)		
	450	0.5	0.0007
0 at.	18	16	16
1at. SW	17	17	15
2at. SW	18	18	15
3at. SW	18	18	16
1at. SE	18	17	16
2at. SE	18	18	16
3at. SE	18	16	16
1ad NR	18	17	17
2ad NR	18	18	15
3ad NR	19	18	16

In the manuscript, we show the energetics of elementary surface reconstruction step at various temperatures but only show structures at high pressure (450 Torr). Reconstruction structures at 0.5 Torr and 0.0007 Torr have been shown here in Fig. C.6 and Fig. C.7 respectively.

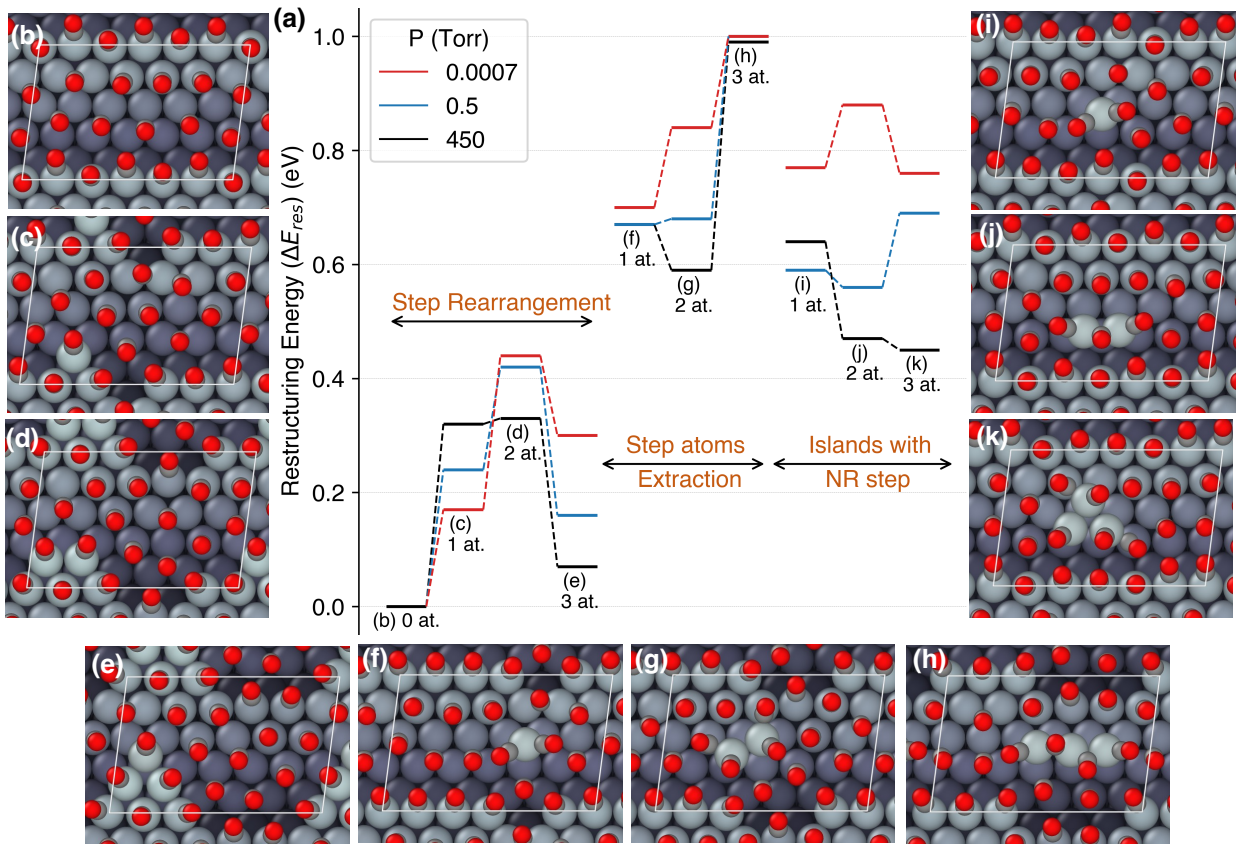


Figure C.6: (a) Energetics of elementary surface reconstruction steps explored for Pt(553) step edge including step wandering (b-e), step atom extraction (f-h) and island extraction from bulk (i-k). Structures shown at 0.5 Torr



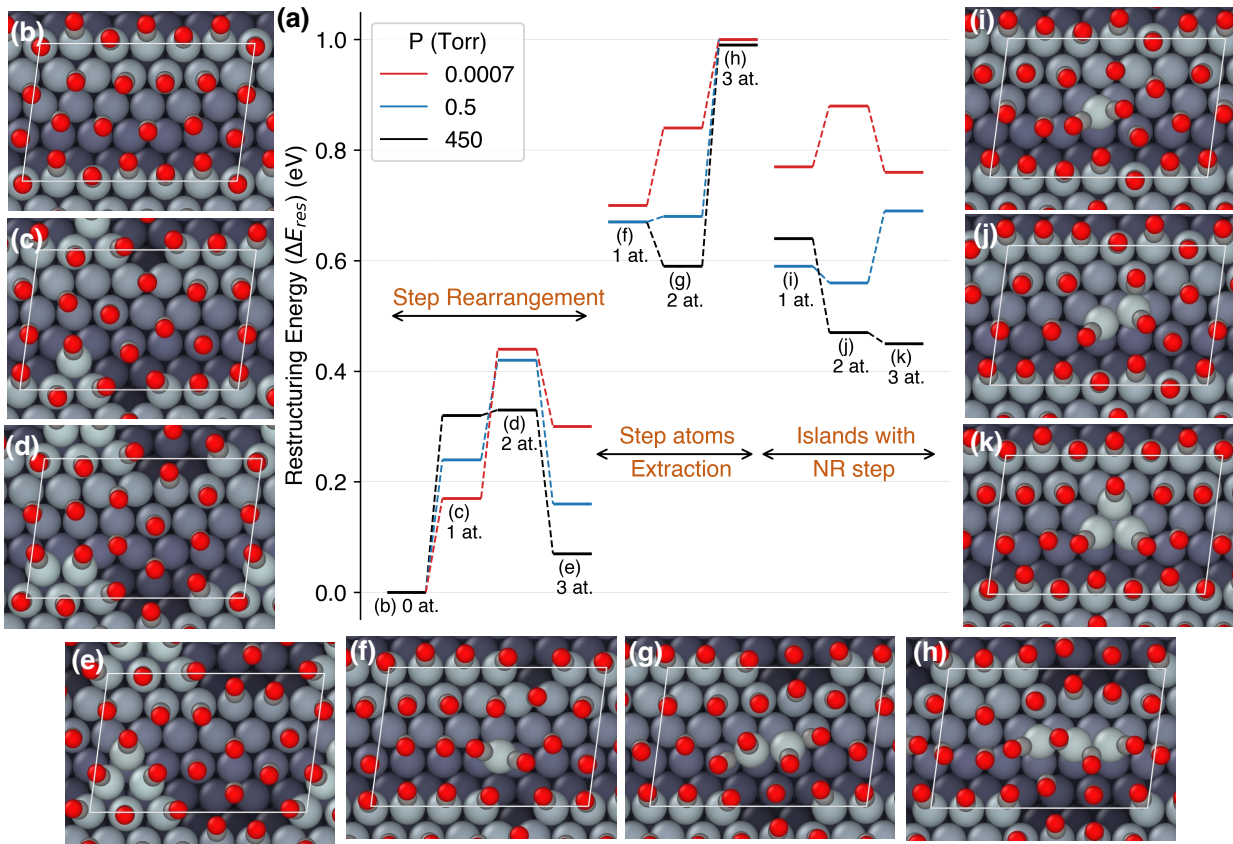


Figure C.7: (a) Energetics of elementary surface reconstruction steps explored for Pt(553) step edge including step wandering (b-e), step atom extraction (f-h) and island extraction from bulk (i-k). Structures shown at 0.0007 Torr

### C.4.2 Pt(557)

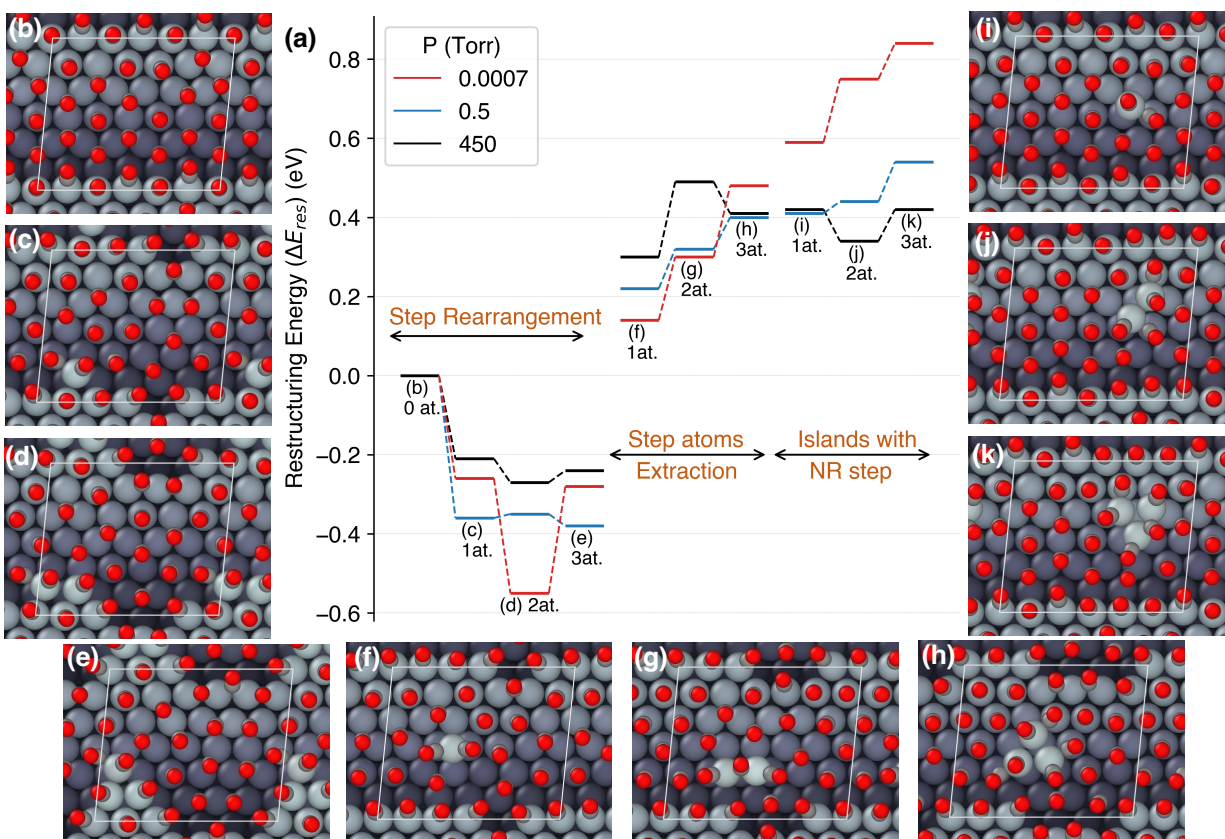


Figure C.8: (a) Energetics of elementary surface reconstruction steps explored for Pt(557) step edge including step wandering (b-e), step atom extraction (f-h) and island extraction from bulk (i-k). Structures shown at 0.5 Torr

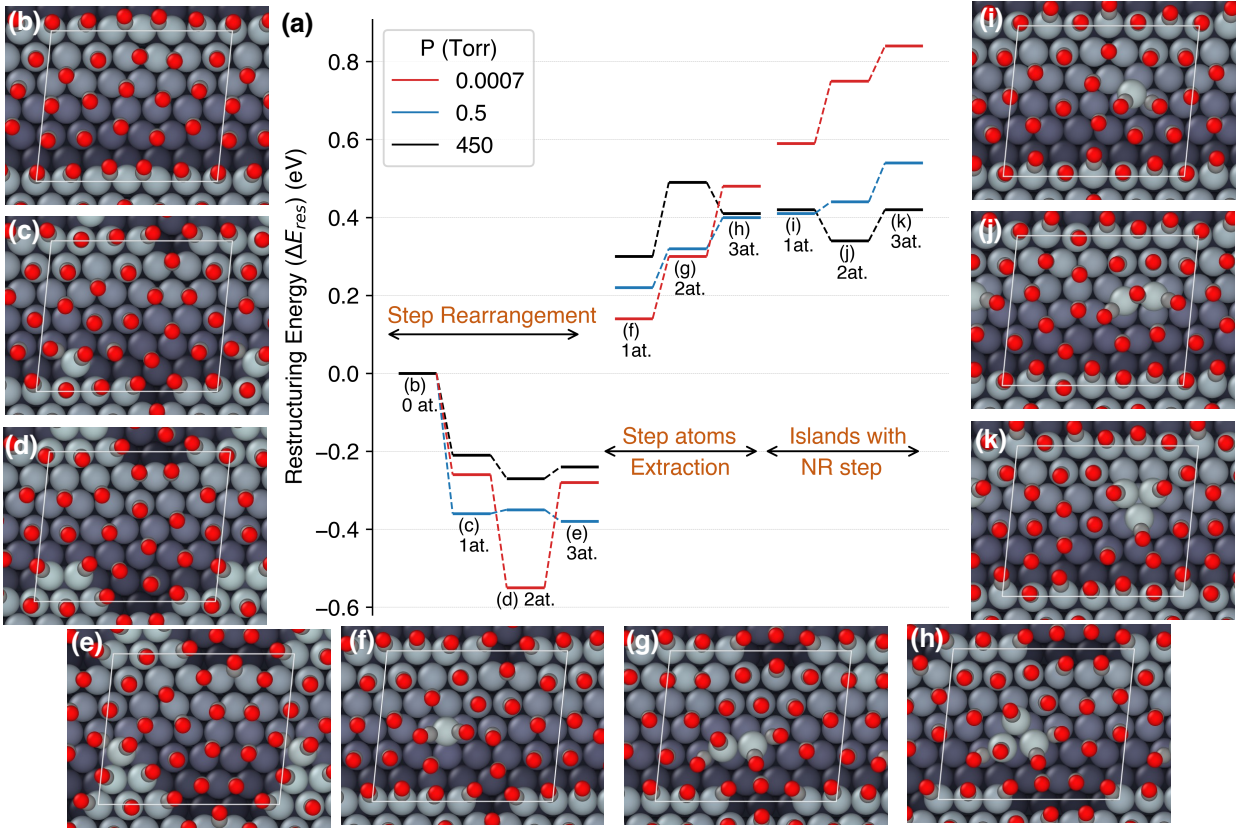


Figure C.9: (a) Energetics of elementary surface reconstruction steps explored for Pt(557) step edge including step wandering (b-e), step atom extraction (f-h) and island extraction from bulk (i-k). Structures shown at 0.0007 Torr

Table C.4:  $\Delta E_{rec}$  separated into  $\Delta E_{metal}$  and  $\Delta E_{chem}$  at different CO pressures for various reconstruction models studied for Pt(557)

Pressure (Torr)		Step Wandering			Step atom extraction			Islands with NR step		
		1 at.	2 at.	3 at.	1 at.	2 at.	3 at.	1 at.	2 at.	3 at.
450	$\Delta E_{metal}$	0.54	0.52	0.67	1.52	2.32	2.99	1.37	2.26	3.00
	$\Delta E_{chem}$	-0.75	-0.79	-0.91	-1.22	-1.83	-2.58	-0.95	-1.92	-2.58
	$\Delta E_{rec}$	-0.21	-0.27	-0.24	0.30	0.49	0.41	0.42	0.34	0.42
0.5	$\Delta E_{metal}$	0.54	0.52	0.67	1.52	2.32	2.99	1.37	2.26	3.00
	$\Delta E_{chem}$	-0.90	-0.87	-1.05	-1.30	-2.00	-2.58	-0.95	-1.82	-2.46
	$\Delta E_{rec}$	-0.36	-0.35	-0.38	0.22	0.32	0.40	0.41	0.44	0.54
0.0007	$\Delta E_{metal}$	0.54	0.52	0.67	1.52	2.32	2.99	1.37	2.26	3.00
	$\Delta E_{chem}$	-0.78	-1.07	-0.96	-1.38	-2.03	-2.51	-0.77	-1.51	-2.17
	$\Delta E_{rec}$	-0.24	-0.55	-0.28	0.14	0.30	0.48	0.59	0.75	0.84

Table C.5: Number of CO per unit cell on Pt(557) at different CO pressure and considered reconstruction models. (SW - Step Wandering, SE - Step atoms Extraction, NR - Islands with NR step)

Structure	Pressure		
	450	0.5	0.0007
0 at.	26	24	20
1at. SW	25	22	22
2at. SW	25	22	20
3at. SW	24	22	20
1at. SE	24	21	21
2at. SE	23	23	21
3at. SE	24	24	21
1ad NR	24	24	20
2ad NR	25	24	21
3ad NR	25	24	21



### C.4.3 Pt(111) + Islands

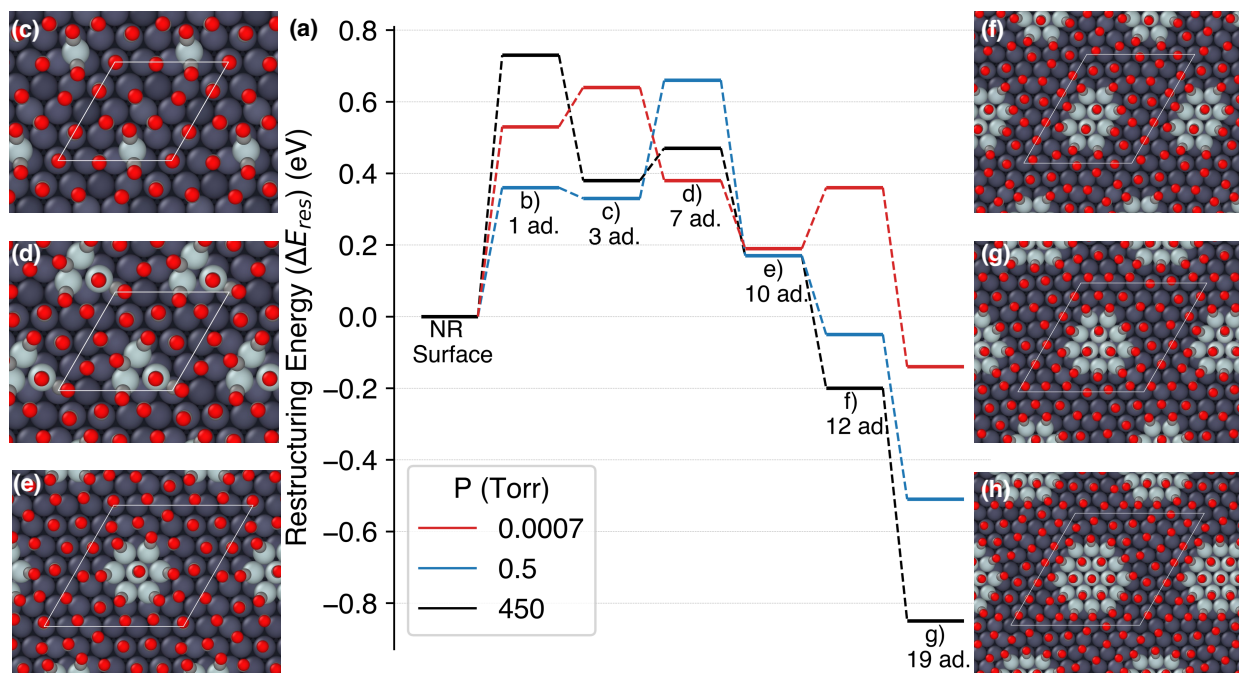


Figure C.10: (b) Comparing the formation energies of Pt islands of increasing sizes from 1 to 19 atoms on Pt(111) terrace. (b-e) Showing the representative structures at 0.5 Torr.

Table C.6:  $\Delta E_{rec}$  separated into  $\Delta E_{metal}$  and  $\Delta E_{chem}$  at different CO pressures for various reconstruction models studied for Pt(111) with different island sizes.

Pressure		1 at.	3 at.	7 at.	10 at.	12 at.	19 at.
450	$\Delta E_{metal}$	1.13	2.64	3.68	4.82	6.36	7.30
	$\Delta E_{chem}$	-0.40	-2.26	-3.20	-4.65	-6.56	-8.16
	$\Delta E_{rec}$	0.73	0.38	0.47	0.17	-0.20	-0.85
0.5	$\Delta E_{metal}$	1.13	2.64	3.68	4.82	6.36	7.30
	$\Delta E_{chem}$	-0.76	-2.31	-3.02	-4.65	-6.41	-7.82
	$\Delta E_{rec}$	0.36	0.33	0.66	0.17	-0.05	-0.51
0.0007	$\Delta E_{metal}$	1.13	2.64	3.68	4.82	6.36	7.30
	$\Delta E_{chem}$	-0.59	-2.00	-3.30	-4.62	-6.00	-7.44
	$\Delta E_{rec}$	0.53	0.64	0.38	0.19	0.36	-0.14

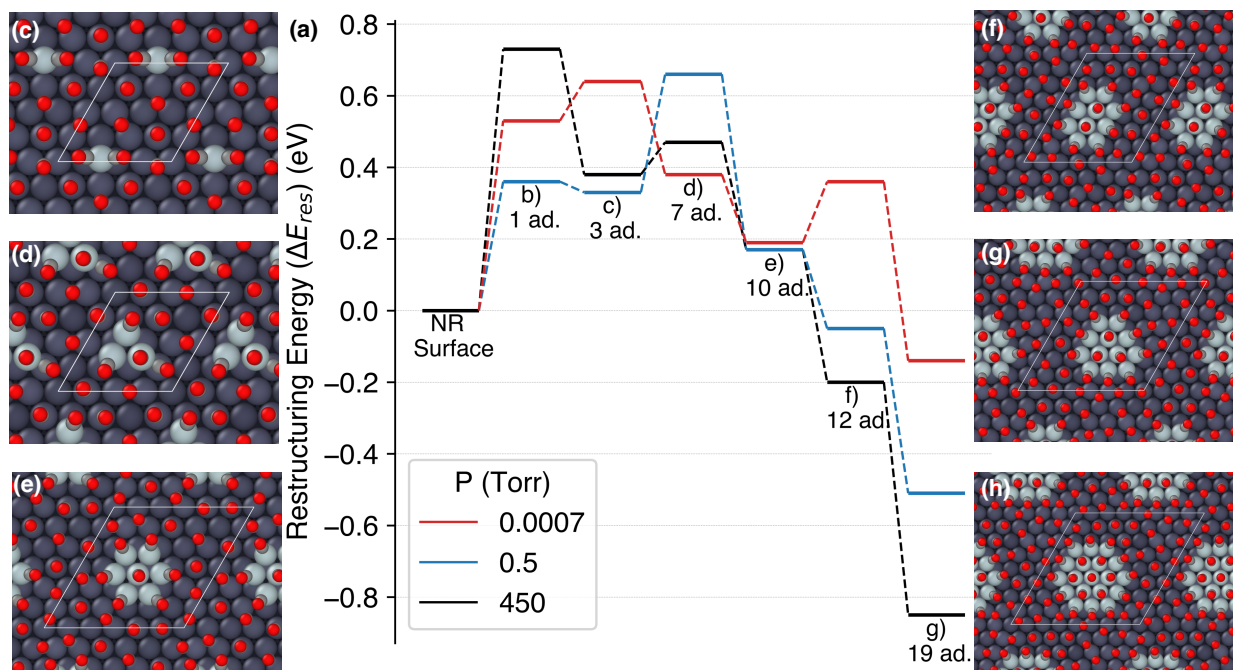


Figure C.11: (b) Comparing the formation energies of Pt islands of increasing sizes from 1 to 19 atoms on Pt(111) terrace. (b-e) Showing the representative structures at 0.0007 Torr.

Table C.7: Number of CO per unit cell on Pt(111) at different CO pressure and considered island sizes.

		Pressure		
Structure	Unit cell size	350	0.5	0.0007
1pt	4x4x4	12	10	9
3pt	4x4x4	11	11	9
7pt	6x6x4	25	24	20
10pt	6x7x4	27	27	25
12pt	7x7x4	33	32	30
19pt	8x8x4	43	43	42



## C.5 Reconstruction in absence on CO

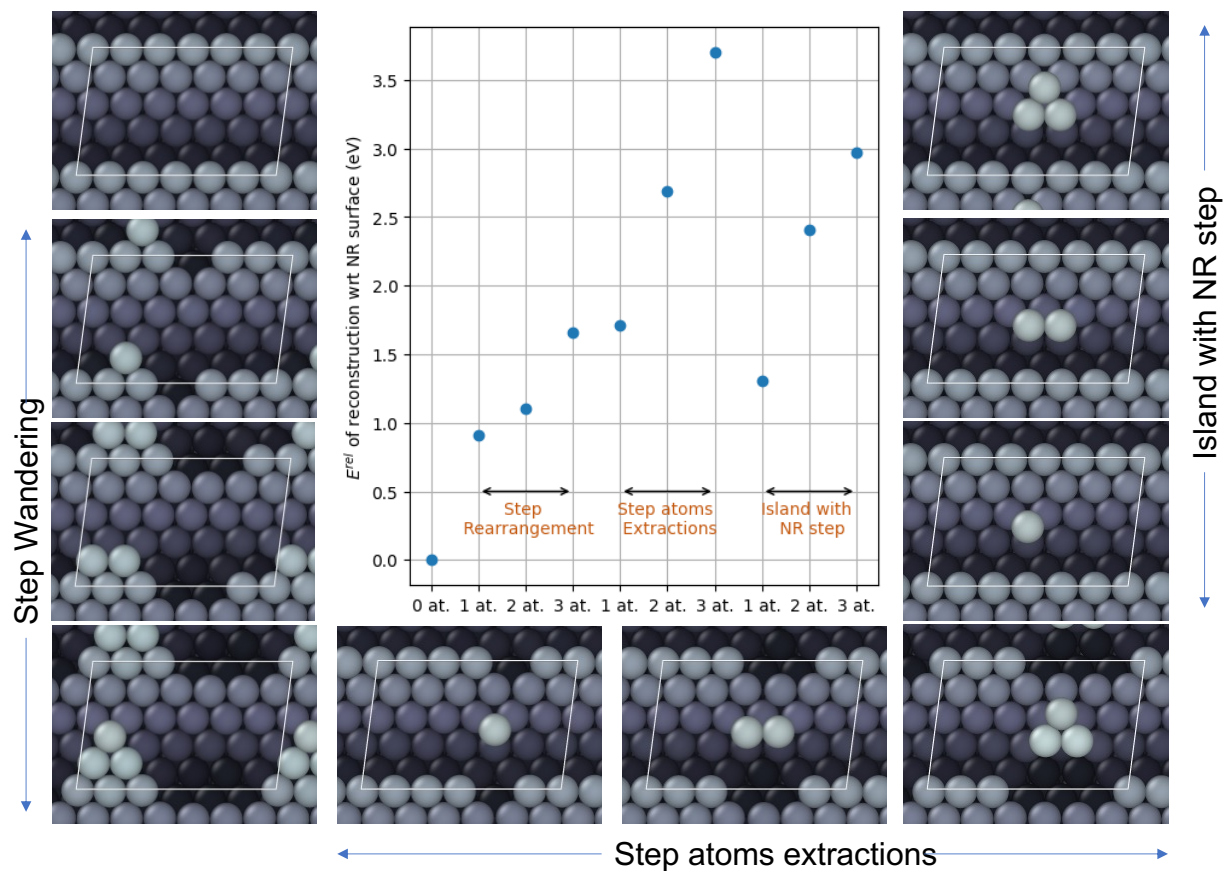


Figure C.12: Pt reconstruction energy for Pt(553) in absence of CO

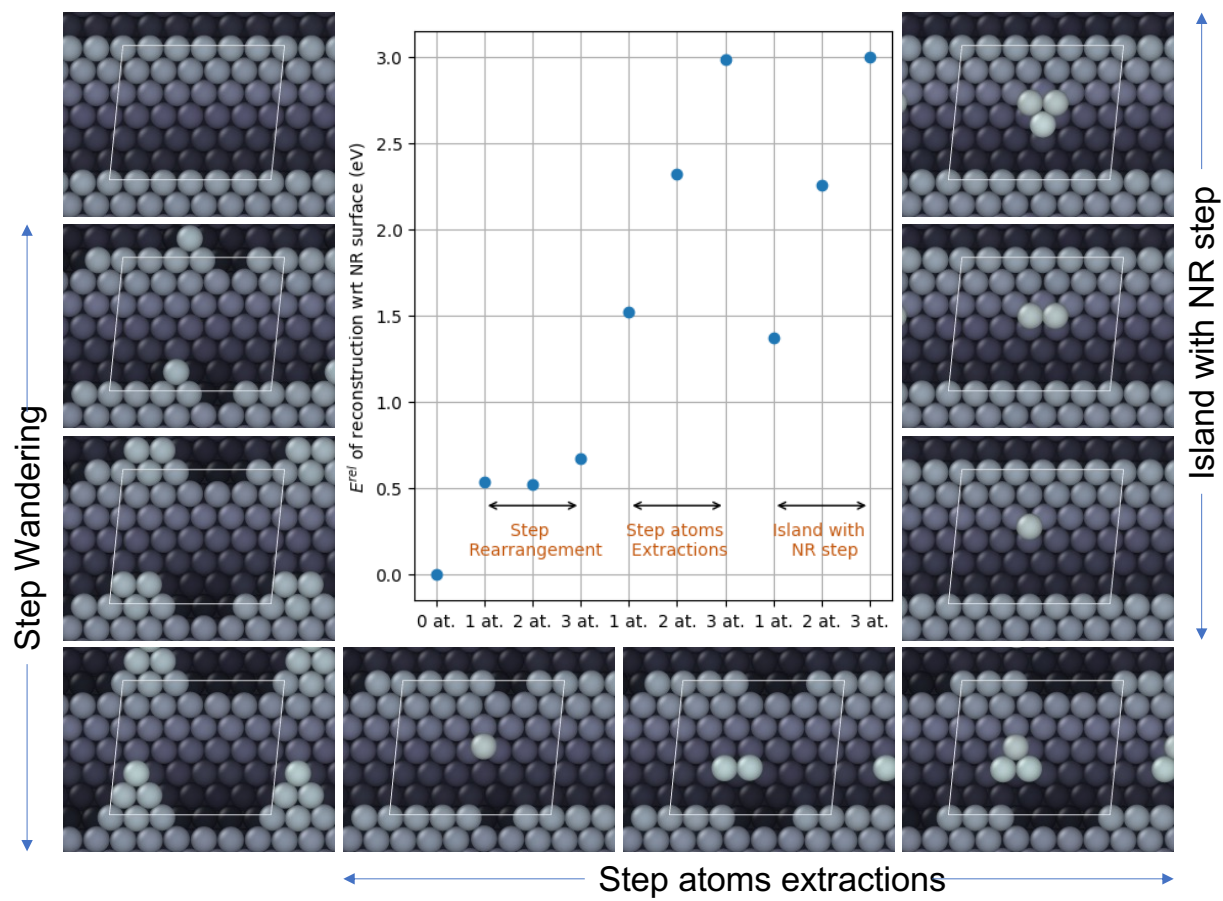


Figure C.13: Pt reconstruction energy for Pt(557) in absence of CO

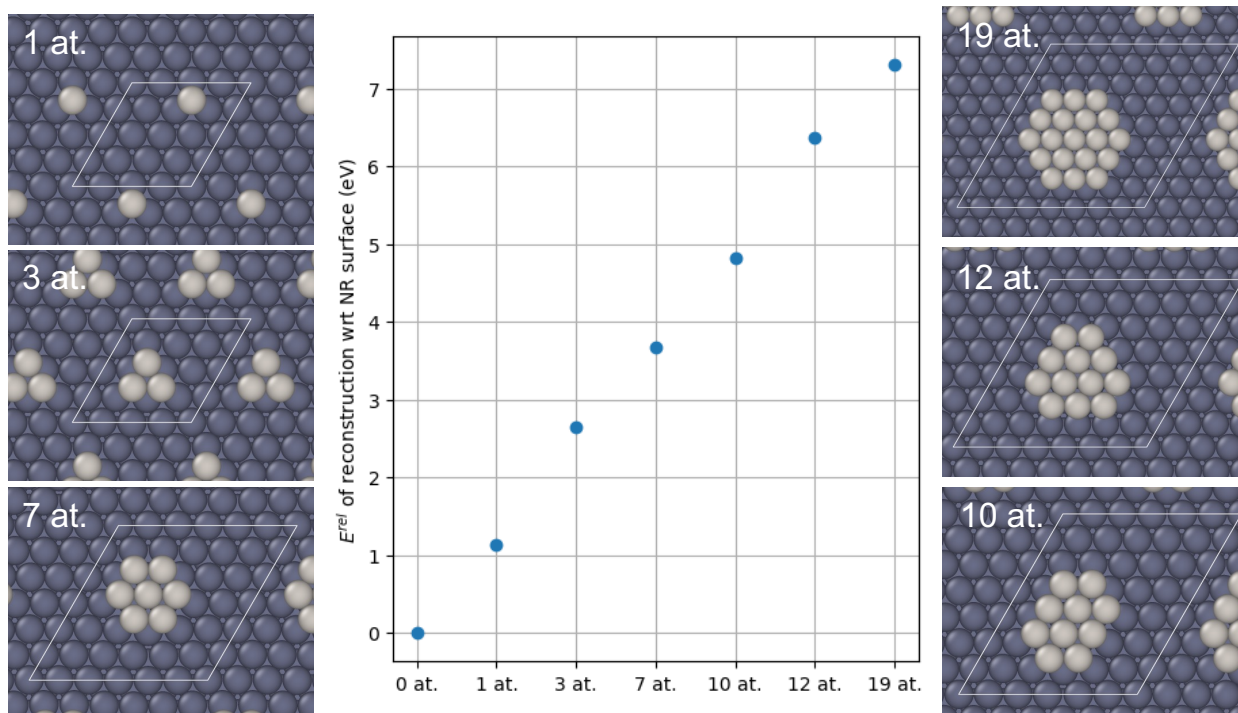


Figure C.14: Pt reconstruction energy for Pt(111) with islands in absence of CO

### C.6 $\Delta E_{chem}$ vs $\Delta E_{metal}$

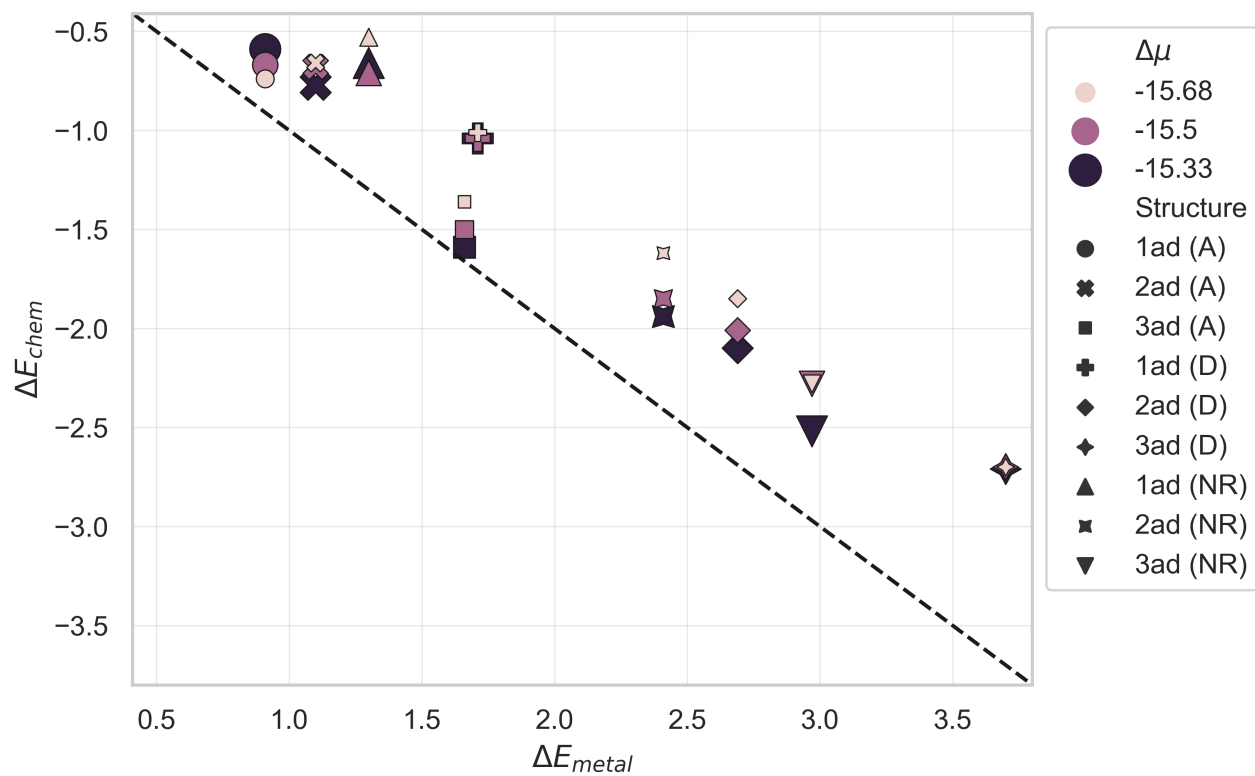


Figure C.15:  $\Delta E_{chem}$  vs  $\Delta E_{metal}$  for Pt(553). (A) - step wandering, (D) - Step atom extraction and (NR) - Island with NR step

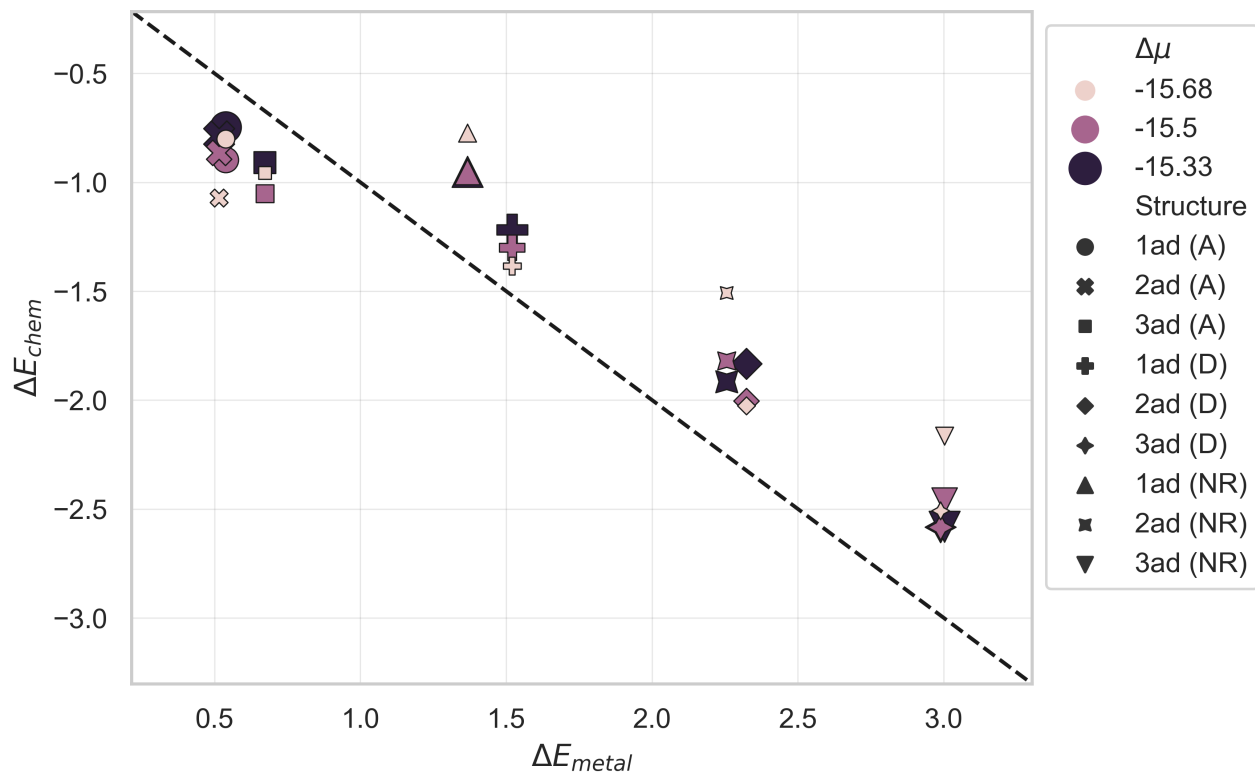


Figure C.16:  $\Delta E_{chem}$  vs  $\Delta E_{metal}$  for Pt(557). (A) - step wandering, (D) - Step atom extraction and (NR) - Island with NR step

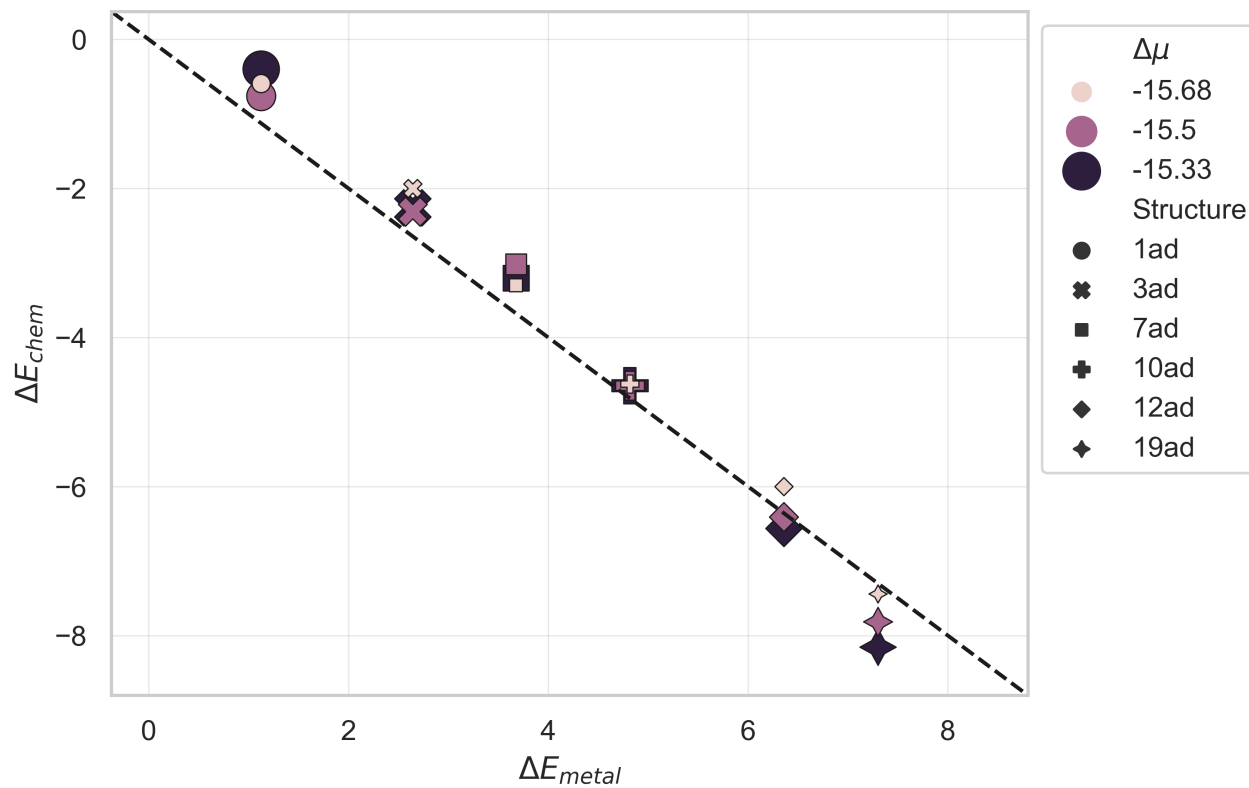


Figure C.17:  $\Delta E_{chem}$  vs  $\Delta E_{metal}$  for Pt(111). (A) - step wandering, (D) - Step atom extraction and (NR) - Island with NR step

## C.7 NEB - Diffusion

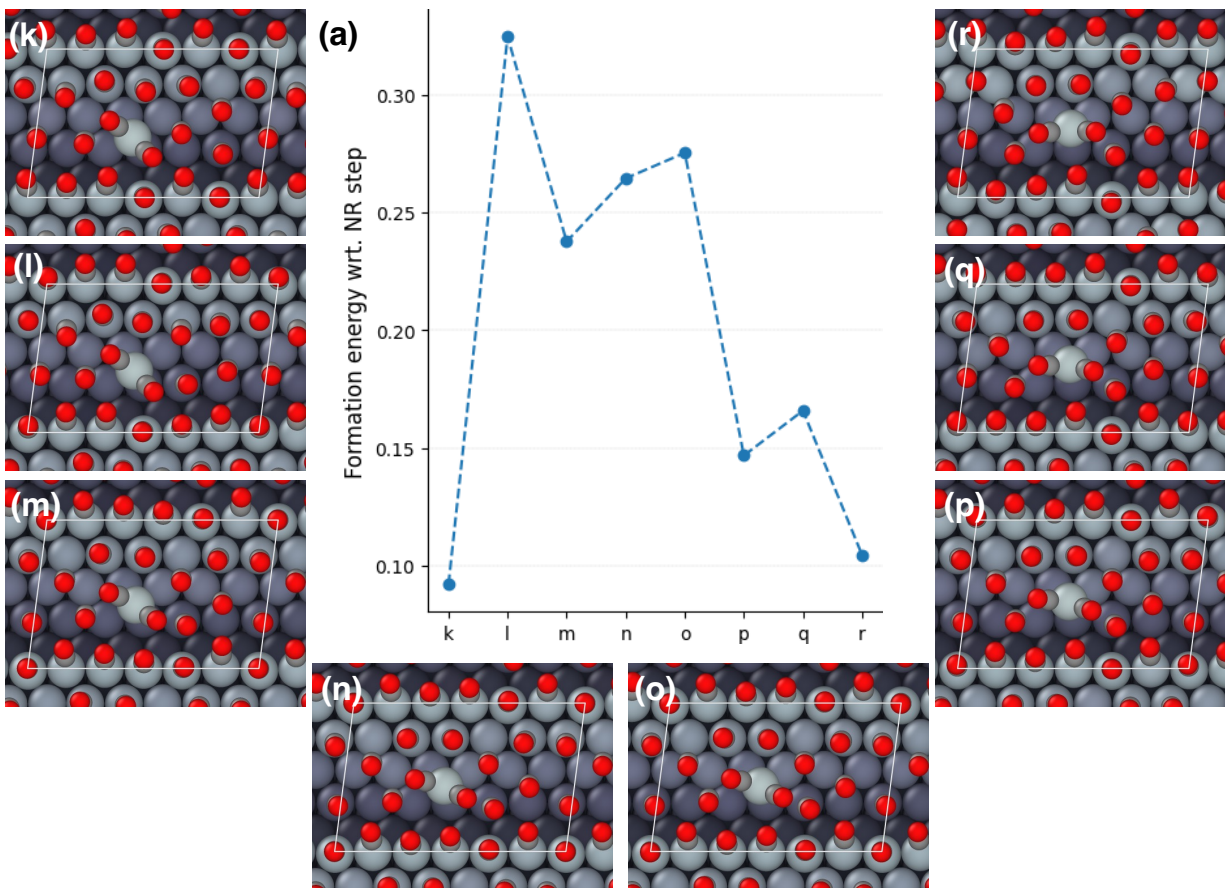


Figure C.18: Reaction energy diagram for 1 atom Pt diffusion on the terrace of Pt(553) at 450 Torr.

## C.8 Data Availability

The data used for this work is made available for recreation as a github repository: Click here to refer to the data or go to: [https://github.com/vsumaria/Pt\\_reconstruction/](https://github.com/vsumaria/Pt_reconstruction/)